

Forschungsbericht 2013-28

Development of a Kinematics Model for the Assessment of Global Crash Scenarios of a Composite Transport Aircraft Fuselage

Matthias Waimer

Deutsches Zentrum für Luft- und Raumfahrt
Institut für Bauweisen- und
Konstruktionsforschung
Stuttgart

D 93 (Dissertation Universität Stuttgart)

274 Seiten
173 Bilder
2 Tabellen
147 Literaturstellen



DLR

Deutsches Zentrum
für Luft- und Raumfahrt

Development of a Kinematics Model for the Assessment of Global Crash Scenarios of a Composite Transport Aircraft Fuselage

A thesis accepted by the Faculty of Aerospace Engineering and Geodesy of the
Universität Stuttgart in partial fulfilment of the requirements for the degree of
Doctor of Engineering Sciences (Dr.-Ing.)

by
Matthias Waimer
born in Schorndorf, Germany

Main referee: Prof. Dr.-Ing. Heinz Voggenreiter

Co-referee: Prof. Dr.-Ing. Martin Maier

Co-referee: Prof. Dr.-Ing. Peter Middendorf

Date of defence: 23rd September 2013

Institute of Aircraft Design
University of Stuttgart
2013

*Ohne **Ratgeber** sind Pläne zum Scheitern verurteilt,
aber wo man **gemeinsam überlegt**, hat man Erfolg.*

(Die Bibel - Sprüche 15,22)

*Without **counsel** plans fail,
but with **many advisers** they succeed.*

(The Bible - Proverbs 15:22)

Vorwort

Mein Dank gilt dem Deutschen Zentrum für Luft- und Raumfahrt e.V. - Institut für Bauweisen- und Konstruktionsforschung, namentlich Herrn Christof Kindervater, vormals Leitung der Abteilung Strukturelle Integrität, der mir eine spannende Forschungstätigkeit in einem interessanten Umfeld ermöglicht hat und dies weiterhin ermöglicht. Ebenso danke ich Frau Dr. Nathalie Toso, Leitung der Abteilung Strukturelle Integrität, für das Vertrauen in meine Arbeit besonders in der abschließenden Phase meiner Promotion.

Insbesondere gilt mein Dank meinem Doktorvater Herrn Prof. Dr. Heinz Voggenreiter, Direktor des DLR Instituts für Bauweisen- und Konstruktionsforschung, für die Ermutigung zur Promotion und die hilfreichen Wegweisungen zur Erreichung des Ziels.

Meinem Mitberichter Herrn Prof. Dr. Martin Maier, Technisch-Wissenschaftlicher Direktor am Institut für Verbundwerkstoffe GmbH, möchte ich danken für die Begutachtung und das Interesse an meiner Arbeit über die Begutachtung hinaus.

Meinem Mitberichter Herrn Prof. Dr. Peter Middendorf, Direktor des Instituts für Flugzeugbau der Universität Stuttgart, möchte ich herzlich danken für die offene Bereitschaft zur Begutachtung. In besonderer Weise bin ich dankbar für die konstruktiven und fruchtbaren Projektbesprechungen in den Anfangsphasen der Promotion.

Herrn Dr. Dieter Hachenberg, Airbus Operations GmbH, möchte ich in besonderer Weise herzlich danken für die anhaltend gute Zusammenarbeit sowie die Ermöglichung der Promotion in enger Kooperation mit Airbus. Mein Dank gilt insbesondere der offenen Kooperation zur Unterstützung der Promotion, den hilfreichen Beiträgen in zahlreichen Projektbesprechungen, sowie der Bereitstellung unterschiedlichster Daten. All diese Unterstützung hat bedeutsam zur Qualität der Arbeit beigetragen.

Mein ganz besonderer und herzlicher Dank gilt meinem technischen Betreuer Dieter Kohlgrüber, DLR Institut für Bauweisen- und Konstruktionsforschung, für die allumfassende Betreuung meiner Promotion, von den ersten Überlegungen zur Promotion bis zur finalen Ausarbeitung. Die Gründlichkeit, Schärfe und Tiefe der technischen Betreuung sind hier besonders zu erwähnen. Das hohe Engagement bei der Diskussion technischer Fragen, die unzählig hilfreichen Beiträge und letztlich die Ausdauer bei der akribischen Prüfung meiner Ergebnisse sind unschätzbar und haben auch mich persönlich vorangebracht. Vielen Dank Dieter, für alle Mühe und Zeit, die du in mich investiert hast!

Der größte Dank gilt meiner lieben Frau Nadine! Vielen Dank für deine große Unterstützung und deinen geduligen Verzicht auf viel gemeinsame Zeit. Von Herzen danke ich dir für deine unermüdliche Motivation und Ermutigung. Es ist ein Segen, dich an meiner Seite zu haben!

Meinem Schwager Johannes Wiedmann danke ich für die Ausdauerleistung, als erster und voraussichtlich auch letzter Nichtfachmann die Arbeit vollständig gelesen zu haben und anglistisch beratend zur Seite gestanden zu sein.

Schließlich gilt mein Dank noch meinen lieben DLR-Kollegen, die für eine sehr schöne Arbeitsatmosphäre sorgen und es regelmäßig schaffen, durch ein nettes Gespräch oder mit einer Tasse Kaffee mich aus meinem vertieften Arbeiten zurück ins Leben zu holen.

Stuttgart, im Oktober 2013

Matthias Waimer

Contents

ABBREVIATIONS	9
ZUSAMMENFASSUNG	11
ABSTRACT	13
1. INTRODUCTION	14
1.1. Objective and structure of the thesis	18
2. REVIEW ON CRASHWORTHINESS RESEARCH – STATE OF THE ART	21
2.1. Review on crashworthiness research	21
2.2. Review on simulation methodologies	31
2.3. Identification of open questions – definition of the thesis	36
3. ASPECTS OF THE KINEMATICS MODEL APPROACH	39
3.1. Basic approach of the Kinematics Model	39
3.2. Macro modelling of crash devices	41
3.2.1. Selection of a macro element	42
3.2.2. Macro architecture for axial crushing	43
3.2.3. Macro architecture for frame bending	45
3.2.4. Macro architecture for cargo-crossbeam failure	46
3.2.5. Macro architecture for the passenger crossbeam connection	47
3.3. Definition of Kinematics Model output data	48
3.3.1. Output definition of macro elements	49
3.3.2. Output definition of structural loads	50
3.3.3. Output definition of injury risks	51
3.4. Further modelling aspects	53
3.4.1. Refinement of the sub-cargo area modelling	53
3.4.2. Parameterisation of the Kinematics Model	55
4. DETAILED INVESTIGATION OF FRAME FAILURE MODELLING	57
4.1. Positioning of the ‘kinematic hinges’	58
4.2. Pre-failure behaviour of a frame-stringer-skin structure	65
4.2.1. Potential failure initiations of a frame-stringer-skin structure loaded under pure bending	66
4.2.2. Elastic behaviour of a frame-stringer-skin structure	69
4.3. Post-failure behaviour of a frame-stringer-skin structure	73
4.3.1. Frame failure of typical fuselage design	73
4.3.2. Frame failure of non-typical fuselage design	76

4.3.3.	Failure behaviour of CFRP frame structures	80
4.3.4.	Outcomes of the investigation of the post-failure behaviour	82
4.4.	Influence of the kinematic hinge architecture on lateral frame stability	83
4.5.	Influence of the discretisation	88
4.6.	Influence of the bending-compression ratio	94
4.6.1.	Identification of typical bending-compression ratios	95
4.6.2.	Influence of the bending-compression ratio on the kinematic hinge behaviour	97
4.6.3.	Influence of the bending-compression ratio on the failure behaviour of a frame-stringer-skin structure.....	102
4.7.	Summary – the final kinematic hinge macro architecture.....	103
5.	IMPLEMENTATION OF A USER ELEMENT FOR FRAME FAILURE MODELLING	106
5.1.	Requirements for an improved macro element	107
5.2.	Implementation of the user element.....	112
5.3.	Verification on the quasi-single element level	117
5.4.	Verification on the reference model level.....	120
5.5.	Summary and outlook.....	123
6.	DEVELOPMENT OF A CRASHWORTHY COMPOSITE FUSELAGE DESIGN – CRASH SCENARIO ASSESSMENT.....	124
6.1.	Natural crash kinematics	125
6.2.	Development of crash scenario A & B.....	129
6.3.	Assessment of crash scenario A & B.....	136
7.	DEVELOPMENT OF A CRASHWORTHY COMPOSITE FUSELAGE DESIGN – CRASH SCENARIO DEVELOPMENT	141
7.1.	Definition of structural allowables	142
7.2.	Analytical consideration of the crash zone.....	146
7.3.	Approach for the crash scenario development.....	149
7.4.	Crash scenario development	152
7.4.1.	Crash kinematics optimisation.....	153
7.4.2.	Structural adaptation.....	159
7.4.3.	Final crash scenario.....	163
7.5.	Modification of the final crash scenario – the ovalisation effect.....	166
7.6.	Summary - definition of the final macro input characteristics	171
8.	DEVELOPMENT OF A CRASHWORTHY COMPOSITE FUSELAGE DESIGN – EXPERIMENTAL INVESTIGATION ON THE DESIGN OF CRASH DEVICES	174
8.1.	Axial crushing tests	175
8.2.	Frame bending tests.....	184
9.	CONCLUSION AND OUTLOOK	192

9.1.	Methodology of the finite element modelling approach	192
9.2.	Methodology of the crash design process	194
9.3.	Outlook	195
A1.	APPENDIX OF CHAPTER 2.....	197
A1.1.	The finite element method in the scope of this thesis	197
A2.	APPENDIX OF CHAPTER 4.....	201
A2.1.	Analysis of pre-failure behaviour – description of the numerical model	201
A3.	APPENDIX OF CHAPTER 5.....	203
A3.1.	List of property parameters.....	203
A3.2.	List of solution-dependent variables (SDV)	206
A3.3.	Structogram of the calculation of internal forces	207
A3.4.	Definition of the reference model	214
A4.	APPENDIX OF CHAPTER 6.....	216
A4.1.	Definition of the fuselage design and the Kinematics Model used for the crash scenario assessment .	216
A4.1.1.	Assumptions for the macro input characteristics	218
A4.1.2.	Numerical parameters	220
A4.2.	Further simulation results of the assessment study of the crash scenarios	220
A4.2.1.	Change of sign of the moment load in the frame of scenario B	220
A4.2.2.	Rotation angle of the absorbing kinematic hinges in both scenarios	221
A4.2.3.	Structural load – frame inner flange strains of both scenarios.....	222
A4.2.4.	Tensile loads in the vertical support struts	222
A4.2.5.	Simulation results of the robustness cases for scenario A.....	223
A4.2.6.	Simulation results of the robustness cases for scenario B.....	230
A5.	APPENDIX OF CHAPTER 7.....	236
A5.1.	Definition of the fuselage design and the Kinematics Model used for the crash scenario development.....	236
A5.2.	Further results of the final crash scenario	239
A5.3.	Further results of the ovalisation effect	246
A5.4.	Further details of the metallic frame model.....	251
A5.5.	Determination of an optional trigger load level for the vertical support struts	252
A6.	APPENDIX OF CHAPTER 8.....	254
A6.1.	Remarks to the development of a test setup for axial crushing tests	254
A6.2.	Test matrix of the axial crushing test programme	258
A6.3.	Remarks to the development of a test setup for frame bending tests	259
A6.4.	Test matrix of the frame bending test programme.....	261
	BIBLIOGRAPHY.....	263

Abbreviations

ABAQUS/Explicit	Explicit FEM solver
ALLAE	Artificial strain energy (ABAQUS/Explicit)
ALLCW	Total work done by constraint penalties (ABAQUS/Explicit)
ALLFD	Total energy dissipated through frictional effects (ABAQUS/Explicit)
ALLIE	Total strain energy (ABAQUS/Explicit)
ALLKE	Total kinetic energy (ABAQUS/Explicit)
ALLPW	Total work done by contact penalties (ABAQUS/Explicit)
ALLWK	Total external work (ABAQUS/Explicit)
ANSYS	FEM software
APDL	ANSYS parameter design language
ASCII	American standard code for information interchange
CCB	Cargo-crossbeam
CFRP	Carbon fibre reinforced plastic
CID	Controlled impact demonstration (NASA full-scale crash test)
CPU	Central processing unit
CRASURV	Commercial Aircraft Design for Crash Survivability (European Community funded project)
CTF n	Connector total force component n (ABAQUS/Explicit)
CTM n	Connector total moment component n (ABAQUS/Explicit)
CU n	Connector relative displacement in the n -direction (ABAQUS/Explicit)
CUR n	Connector relative rotation in the n -direction (ABAQUS/Explicit)
DLR	Deutsches Zentrum für Luft- und Raumfahrt e.V. (Germany)
DOF	Degree of freedom
DRI	Dynamic response index
DRI-KRASH	Hybrid code (Dynamic Response Inc.)
EA	Energy absorption
EADS-IW	European Aeronautic Defence and Space Company – Innovation Works
ETOTAL	Total energy balance (ABAQUS/Explicit)
FAA	Federal Aviation Administration (U.S.)

FAR	Federal Aviation Regulations (U.S.)
FE(M)	Finite element (method)
FF	Frame flange
FORTTRAN	Programming language
FP	Frame pitch
HIC	Head injury criterion
IARV	Injury assessment reference values
IFF	Inner frame flange
IFW	Inner frame web
KH	Kinematic hinge
LCF	Integral frame design with LCF-shaped cross-section
LF	Lower flange
MFF	Middle frame flange
MIL-HDBK	Military handbook (U.S. Department of Defense)
NACA	National Advisory Committee for Aeronautics (U.S.)
NAL	National Aerospace Laboratory (Japan)
NASA	National Aeronautics and Space Administration (U.S.)
OFF	Outer frame flange
OFW	Outer frame web
ONERA	Office National d'Études et de Recherches Aérospatiales (France)
PAM-CRASH	Explicit FEM solver
PAM-OPT	Optimisation software
PAX	Passenger
PEEK	Polyether ether ketone
RF	Reserve factor
SDV	Solution dependent variable (ABAQUS/Explicit)
SECFO	Section force (PAM-CRASH)
SECTMESH	DLR in-house mesh generation tool (based on APDL)
SP	Seat pitch
UD	Uni-directional
UF	Upper flange
VUEL	user element (ABAQUS/Explicit)
VUMAT	user material (ABAQUS/Explicit)

Zusammenfassung

Die Verbesserung der Crashesicherheit von Passagierflugzeugen ist ein Thema, das zunehmend an Bedeutung gewinnt. Stetig steigende Zahlen im weltweiten Flugverkehr erfordern eine verbesserte Crashesicherheit, um einen Anstieg von Unfallopfern in gleichem Maße zu verhindern. Eine weitere wesentliche Herausforderung hinsichtlich der Crashesicherheit ist die gegenwärtige Entwicklung im Transportflugzeugbau, die eine Ablösung von metallischen Werkstoffen durch faserverstärkte Kunststoffe zeigt. Duktiles, und damit Energie absorbierendes, Materialverhalten wird abgelöst von hoch-elastischem jedoch sprödem Werkstoffverhalten mit vergleichsweise geringer Energieabsorption. Alternative Crashkonzepte unter Anwendung von diskreten Crashabsorbern müssen daher beim Designprozess von neuartigen Flugzeugstrukturen aus faserverstärkten Kunststoffen beachtet werden. Dabei hat der Designprozess für den Crashlastfall Einfluss auf das gesamte Rumpfdesign eines Transportflugzeuges und sollte demnach bereits in einer frühen Phase des Entwurfsprozesses berücksichtigt werden.

In diesem Zusammenhang entwickelt die vorliegende Arbeit in einem ersten Teil ein Vorentwurfstool für den Crashlastfall von Passagierflugzeug-Rumpfstrukturen unter Betrachtung einer Standard-Sektion. Auf Basis der expliziten Finite Elemente Methode wird ein Modellierungsansatz entwickelt, der eine effiziente Abschätzung des Strukturverhaltens ermöglicht. Der entwickelte Modellierungsansatz repräsentiert eine Kombination aus linear-elastischem Materialverhalten und der Beschreibung von Strukturversagen durch Makro-Modellierung. Die vorliegende Arbeit untersucht typische Versagensmechanismen einer Rumpfstruktur unter crashrelevanter Last und entwickelt daraus entsprechende Makro-Modelle. Insbesondere hinsichtlich der unter crashrelevanter Last dominierenden Spantstruktur wurden detaillierte Untersuchungen durchgeführt, um eine möglichst genaue Modellierung des realen Strukturverhaltens zu gewährleisten.

In einem zweiten Teil entwickelt die vorliegende Arbeit einen Designprozess unter Anwendung des neuartigen Modellierungsansatzes. Ausgehend von einer Bewertung von natürlichen Crashkinematiken wird ein Crashdesign auf Basis einer statisch vorausgelegten Rumpfstruktur entwickelt. Als Grundlage für die Entwicklung und Bewertung des Crashkonzeptes werden die Passagierlasten, die Strukturlasten sowie die Anforderungen an diskrete Crashabsorber definiert. Die Entwicklung des Designprozesses beinhaltet hierbei auch experimentelle Ansätze zur

Untersuchung von Crashabsorber-Konzepten. Quasi-statische sowie dynamische Komponententests unterschiedlicher Komplexität dienen dabei der Realisierung vorgegebener Absorber-Charakteristiken oder der Generierung von Eingabedaten für die Makro-Modellierung im Designprozess.

Abstract

Crashworthiness of transport aircraft is a topic that has gained more importance over the last decades and that will become even more relevant in the future. The increase of the worldwide commercial air traffic demands improved crashworthiness to avoid an increase of fatal accidents in the same magnitude. In addition, a substantial challenge is the today's trend in the aircraft industry to increasingly replace metallic materials by composite materials. Ductile, energy absorbing material behaviour is replaced by high-elastic but brittle material characteristics with comparably low energy absorption. Therefore, alternative crash concepts using discrete crash absorbers have to be considered in the design process of new aircraft structures made of composite materials. The crash design process will have an influence on the overall design of a transport aircraft fuselage structure, and hence should be considered in an early phase of the design process.

In this context, the present thesis develops in a first part a preliminary crash design tool for transport aircraft fuselage structures considering a standard section. A modelling approach is developed on the basis of the explicit finite element method which enables an efficient assessment of the structural behaviour. The developed modelling approach represents a combination of linear-elastic material behaviour and the description of structural failure by macro modelling. The thesis investigates typical failure mechanisms of a fuselage structure caused by crash related loads und derives appropriate macro models. In particular with respect to the frame that highly affects the structural behaviour of the fuselage in case of crash, detailed investigations are performed which ensure an accurate modelling of the real structural behaviour.

In a second part, the thesis develops a design process using the new modelling approach. After an assessment of natural crash kinematics, a crash design is developed on the basis of a statically pre-sized fuselage structure. Basis for the development and assessment of the crash concept are the passenger loads, the structural loads and the requirements for the discrete crash absorbers. The development of the design process also comprises experimental approaches for the investigation of crash absorber concepts. Quasi-static as well as dynamic component tests of different complexity provide a basis for the realisation of the required absorber characteristics or for the generation of input data for the macro models used in the design process.

1. Introduction

Occupant survivability and crashworthiness of transport aircraft is a topic that has gained more importance over the last decades and that will become even more relevant in the near future. In the last two decades the worldwide annual flight hours of commercial jet airplanes¹ has increased from about 22 million hours to 45 million hours. In the same period the number of such commercial jet airplanes has worldwide increased from about 10,000 to 20,000 [1]. Regarding this increase of commercial air traffic it is a widely recognized aim to avoid an increase of fatal accidents in the same dimension.

Occupant survivability is primarily a question of prevention of accidents. High effort is made to improve the safety standard of traffic operations that include in particular the air traffic management at and near the airport [131]. Besides the prevention of accidents the improvement of survivability in case of an accident is a continuous process in which the scientific world as well as the aircraft developers bring up high effort. Typically the focus with respect to survivability in case of aircraft accident is on fire and cabin safety. Non-flammable and non-toxic materials as well as the improvement of the burn-through behaviour are topics which have led to significant improvement of survivability in the past. Regarding the cabin safety, regulations for the seat design as well as safety devices such as seat belt systems or improved lighting systems of the escape route contributed to an enhanced survivability.

The role of the aircraft structure with respect to the occupant survivability was secondary in the past, especially regarding the certification rules. Nevertheless, accident statistics document the obvious influence of the aircraft structure on the survivability in an accident [2,3]. From 1983 to 2000, the U.S. national transportation safety board analysed accidents involving part 121 U.S. air carrier operations² [4]. 568 accidents were analysed in this study, 26 of these accidents were categorized as serious accident. In this context a serious accident is defined as one that involved fire, at least one serious injury or fatality, and either substantial aircraft damage or complete destruction. Seven of the 26 serious accidents were defined non-survivable due to the impact forces. In the remaining 19 serious but survivable accidents, 1523 (76.6 %) of the 1988 occupants survived. With respect to the 465 fatalities, 306 (66 %) occupants died from impact,

¹ Commercial jet airplanes heavier than 60,000 pounds maximum gross weight

² Air carrier operations performed under Title 14 Code of Federal Regulations Part 121

131 (28 %) died from fire and 28 (6 %) died from other causes. Figure 1-1 illustrates these values per year in the considered period 1983 – 2000. According to this study two-thirds of the fatalities resulted from impact. In contrast to this, only less than one-third of the fatalities resulted from fire.

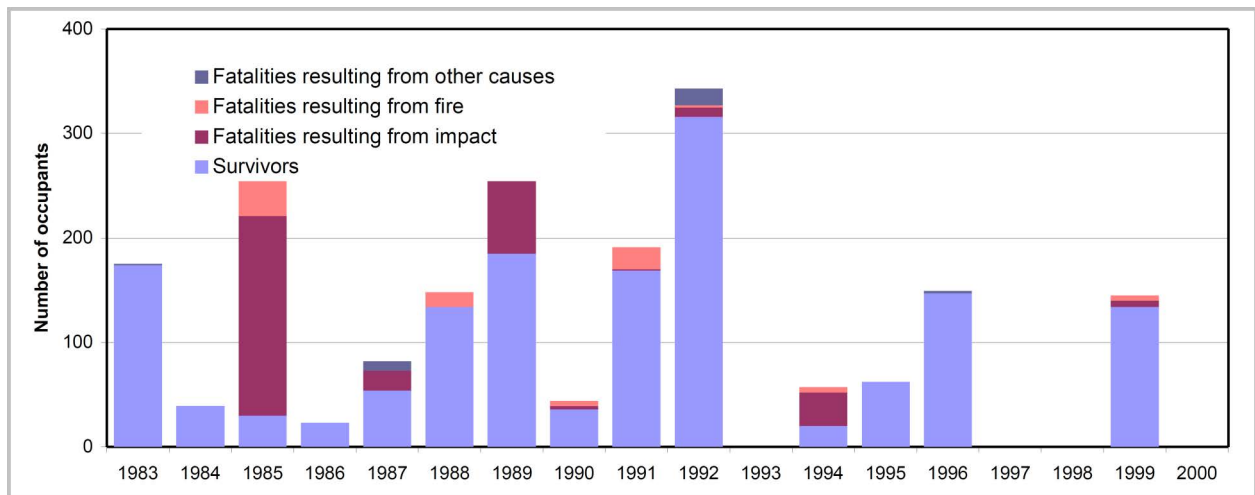


Figure 1-1: Number of survivors and fatalities for the serious but survivable accidents [4]

The role of the aircraft structure in accidents was considered in more detail in [5]. 153 impact survivable accidents were analysed in this study in the period of 1959 – 1979. Of these 153 accidents, 28 accidents experienced extensive damage and rupture of the fuselage lower surface – excluding fuselage break accidents. Eleven of these were fatal accidents with 27.7 % of the total onboard. On the one hand, these values emphasise that accidents with extensive damage of the fuselage structure can be survivable in general. On the other hand, the study identifies the potential to reduce the number of fatalities in such accidents by an improved crashworthiness of the fuselage structure.

This general outcome of the accident statistics - the aircraft structure plays a major role in the occupant survivability - is tightened by a change in the aircraft design which has arisen in the near past. Metallic materials are increasingly replaced by composite materials. Figure 1-2a) gives an overview on this change for military aircraft. The replacement of metallic parts by composite structures in commercial transport aircraft is illustrated in Figure 1-2b). In the transport aircraft category several advantages of composite material are discussed which push the increasingly usage of such materials [7-9]. The reduction of structural weight is the most important argument for the introduction of new composite materials. Further advantages are an improved fatigue performance as well as a better corrosion resistance. In addition, fabrication costs may be reduced by the usage of composite structures instead of metallic structures. In particular the manufacturing process of the fuselage structure could be improved significantly using composite materials. 33 % of the total parts of a metallic aircraft structure are installed in the fuselage, only

12 % in the wing structure. The relative costs per pound of structure are accordingly. The metallic fuselage structure identifies relative cost³ of 1.25, the metallic wing structure only 0.815 [8].

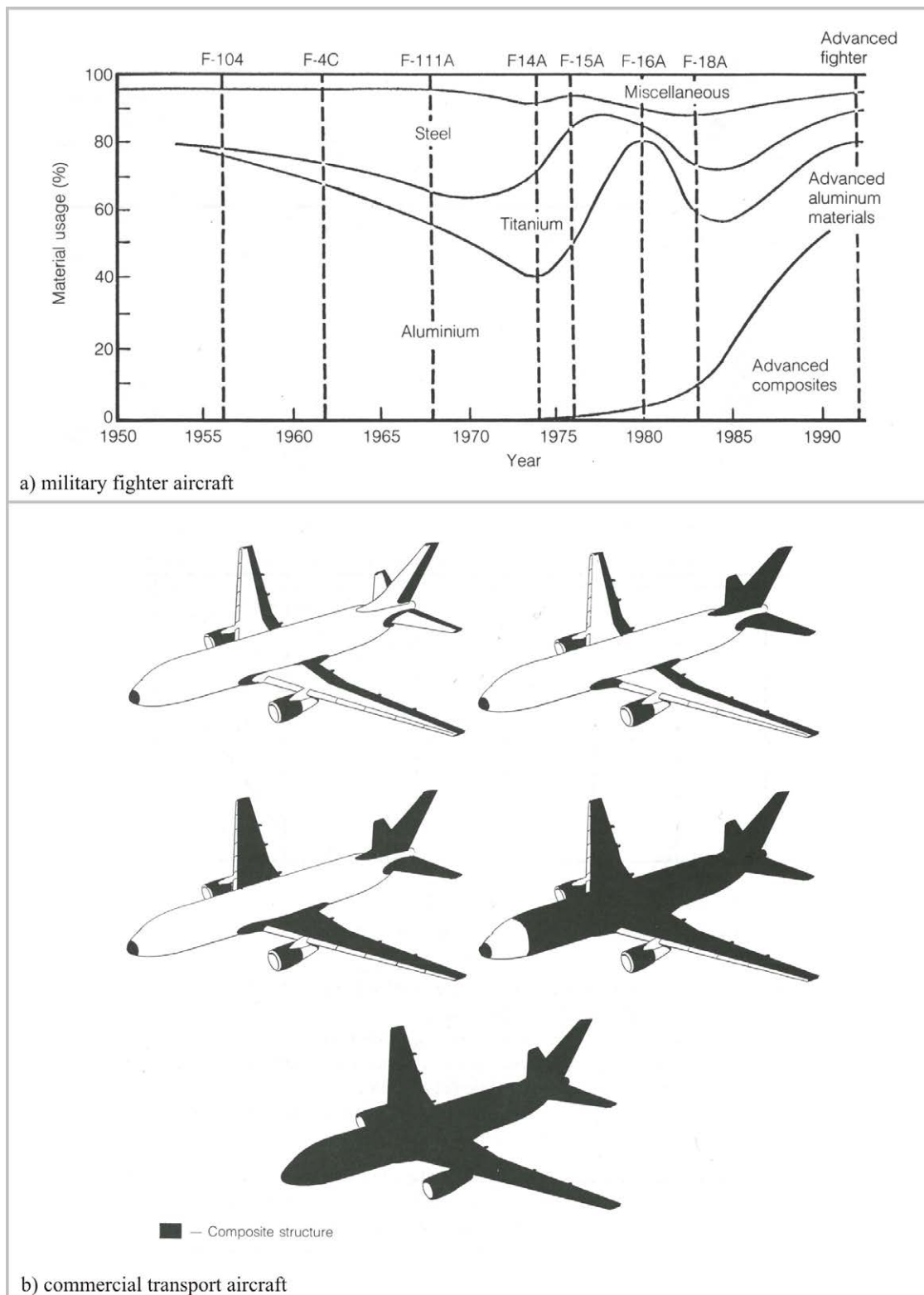


Figure 1-2: Progress in using composite material [6]

³ Relative cost for the overall airframe = 1.0

Besides these benefits of composite materials in the aircraft design there are also some drawbacks. One main drawback is the material failure behaviour. Composite materials, more precisely carbon-epoxy material, provides a negligible plasticity, the damage behaviour is very brittle. With respect to the failure characteristic, such materials provide significantly less energy absorption compared to typical metallic material. Figure 1-3 compares the stress strain relationship of carbon-epoxy material and aluminium which are typically used in an aircraft structure.

The significantly lower capacity of CFRP materials to absorb energy by damage and plasticity strengthens the influence of the aircraft structure on the occupant survivability in an accident. Especially a fuselage structure of a transport aircraft made of CFRP material may provide critical crash behaviour. Higher impact forces are expected compared to a metallic structure which potentially exceeds the human tolerances. In addition, the structural integrity is endangered. Uncontrolled fuselage fractures are critical with respect to occupant evacuation as well as intrusion of fire and smoke or water in case of ditching.

The failure behaviour of CFRP materials and its consequences for the crashworthiness of an aircraft is one main issue which leads to very high effort in the introduction of first full-composite fuselage structures for transport aircraft.

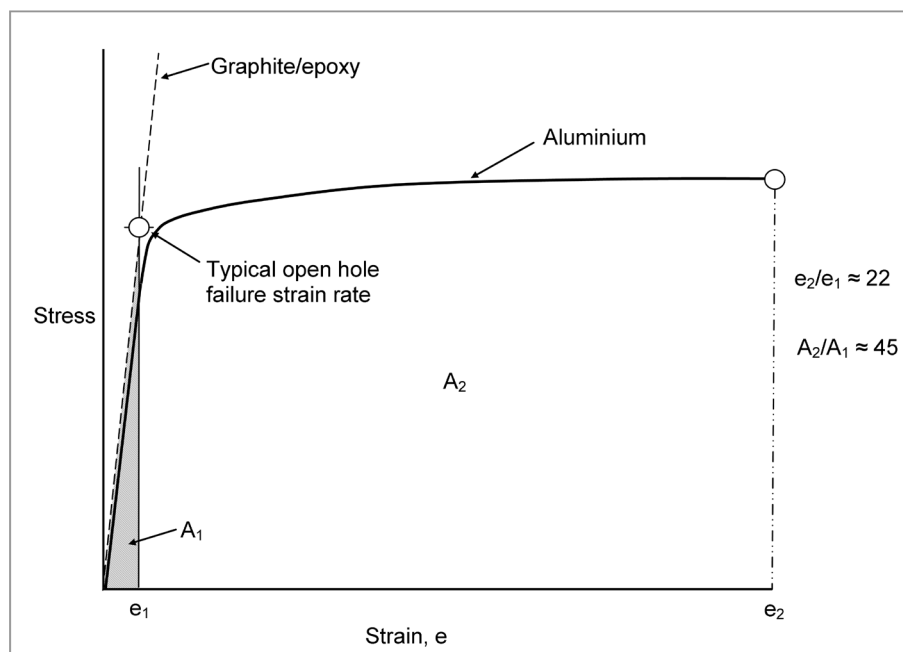


Figure 1-3: Stress strain relationship of graphite-epoxy material and aluminium [6]

Therefore, the increasing usage of composite materials has also shown an impact on the certification process of commercial transport aircraft. General certification regulations are given e.g. in the U.S. federal aviation regulations. Part 25 of these regulations defines the airworthiness standards for transport category airplanes [10]. The emergency landing conditions in section

25.561 define several load cases for which the aircraft design has to demonstrate every reasonable chance for the occupant of escaping serious injury. The load cases in this section are given by load factors which are equivalent to minor crash landing cases. More severe crash landing cases are not considered in the FAR25. In particular, limitations of impact forces acting on the occupant in specific crash cases are not defined. This is important with respect to new fuselage designs made of composite materials. Due to the limited energy absorption capacity discussed above, much higher impact forces on the occupants are expected for composite compared to metallic fuselage structures.

To cover all issues which arise in case of composite aircraft structures regarding certification, the U.S. federal aviation administration defines so called special conditions which are published specifically for each new aircraft model. Such special conditions may specify survivable crashworthiness characteristics that have to provide approximately the same level of safety as those of a similarly sized airplane fabricated from traditionally used metallic materials [11].

Currently, the developers of transport aircraft are working intensively on this huge challenge to fulfil such special conditions. In these development procedures crashworthiness has a completely different significance as it is known from former developments of metallic aircraft. The design of the fuselage structure has to be adapted to improve the poor crashworthiness characteristics of typical composite fuselage structures. Special crash concepts have to be integrated enabling the absorption of kinetic energy by absorber devices. Structural components in the fuselage have to be stiffened to carry typical crash loads and to avoid uncontrolled failure. Finally, the complete design of a composite fuselage structure is driven by the challenge to achieve crashworthiness characteristics which are similar or better compared to metallic designs where crashworthiness plays a negligible role in the design of a fuselage structure.

Looking back to the increasing traffic of commercial transport aircraft the global aim is to improve the occupant survivability similarly to the increasing amount of traffic. Hence, the final challenge is not only to achieve an equivalent level of safety for composite aircraft compared to nowadays aircraft but even to enhance it significantly.

1.1. Objective and structure of the thesis

The objective of this thesis is to contribute to the development of a crashworthy composite fuselage design of transport aircraft. A methodology is used which considers local crash devices that are installed in the critical areas of a fuselage structure. A new modelling approach on fuselage section level had to be developed, which is based on commercial explicit finite element method, and which is used to design the local crash devices. By modification of the devices'

characteristics the crash kinematics of the fuselage structure can be optimised. A desired crash kinematics can be realised by the definition of trigger load and absorption level in the individual crash devices. The aim of such a numerical analysis on the fuselage section level is the minimisation of crash loads and the avoidance of uncontrolled crash kinematics. Furthermore, the fuselage structure, and more precisely the critical frame structure, can be adapted to the improved crash loads to avoid any significant uncontrolled failure outside of the crash devices. Finally, the required characteristics of the individual crash devices, which were found in the numerical approach on the fuselage section level, can be used as a basis for the development of local trigger and energy absorbing concepts. The essence of this methodology is the usage of a numerical modelling which is well suited for a preliminary design process. In addition, the development of technological concepts can be performed on the component level and does not need the accomplishment of large and expensive tests. Figure 1-4 illustrates such a crash concept which is based on this methodology, covering energy absorption in the sub-cargo area, the lower side shell and the passenger crossbeam support struts.

The structure of the thesis provides two main aspects. The first aspect considers the methodology of the developed modelling approach and comprises chapters 2-5. The focus is on the numerical representation of typical frame failure mechanisms which is the most important one with respect to crash related loads on a fuselage structure.

Chapter 2 gives a review on the work which has been done in the field of aircraft crashworthiness in the past. The state of the art is discussed in this chapter with respect to technological as well as numerical methods. Based on this state of the art open questions are identified which define the objective of this thesis.

In chapter 3 the basic modelling approach of the developed Kinematics Model is presented. The macro modelling techniques as well as further modelling aspects are discussed.

Chapter 4 deals with the numerical representation of frame failure which is the main failure mechanism of a fuselage section crash kinematics. Several aspects are analysed in detail which contribute to a sufficiently accurate frame failure representation.

Chapter 5 describes the development of a user-subroutine for frame failure modelling. An advanced model of the frame failure macro representation was programmed in a user element which provides some improvements compared to the standard frame failure modelling discussed in chapter 4.

The second main aspect of the thesis considers the methodology of a crash design process that is based on the application of the Kinematics Model. Chapters 6-8 discuss the design process on the basis of an exemplary application.

In chapter 6 different natural crash kinematics of a typical fuselage section are analysed and assessed using the Kinematics Model. The preferred natural crash kinematics represents the basis for the development of the crash design.

In chapter 7 the selected crash kinematics, as an outcome of chapter 6, is applied on a statically pre-sized CFRP fuselage structure. A crash scenario was developed which includes the definition of local crash device characteristics as well as the sizing of a crashworthy frame structure.

Finally, chapter 8 deals with the development of different experimental test setups which were used to investigate local crash device concepts. A detailed crushing test setup was developed for the investigation of potential crush absorbers in the sub-cargo area. In addition, the development of a generic frame bending test setup is discussed with the focus on the investigation of general characteristics such as the energy absorption capacity.

Concluding remarks are given in chapter 9.

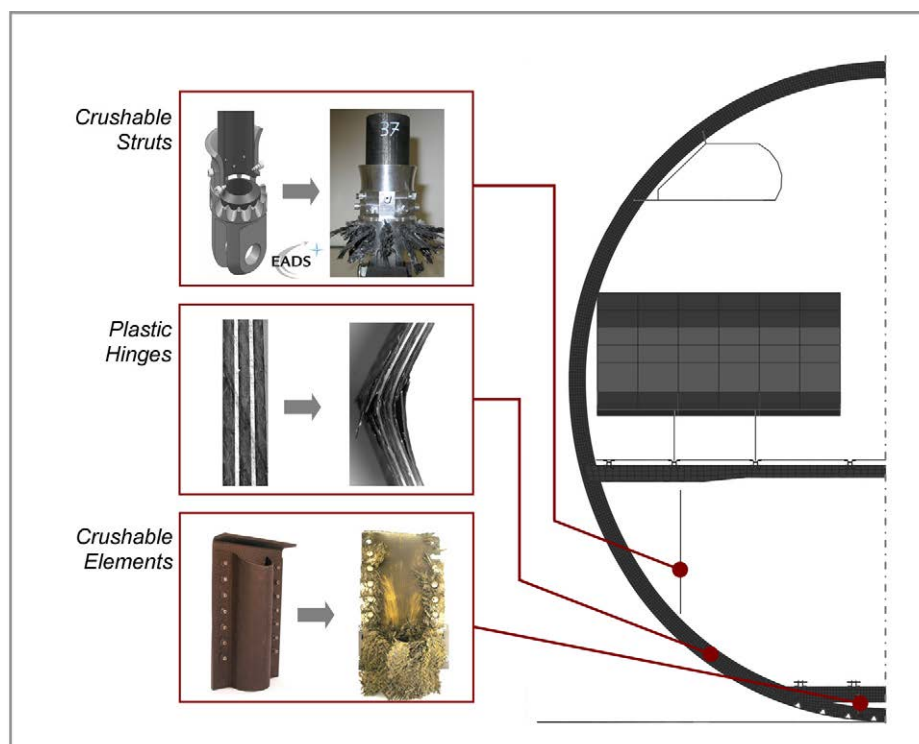


Figure 1-4: Crash design concept using local crash devices

2. Review on crashworthiness research – state of the art

This chapter deals with a review on research activities on the crashworthiness of aircraft. Experimental as well as analytical work is considered.

Paragraph 2.1 discusses the main topics which have been experimentally analysed in the past. A current state of the art of crashworthy aircraft design is outlined from these wide experimental database gained by the discussed research activities.

The focus in paragraph 2.2 is on the simulation methodologies which have been developed and used to investigate and improve the crashworthiness of aircraft. Different simulation methods are discussed and a state of the art in crash simulation of aircraft structures is outlined.

Finally, paragraph 2.3 identifies open questions regarding the development of crashworthy aircraft designs as well as simulation methodologies. Different topics are derived from these open questions which have to be investigated within this thesis.

2.1. Review on crashworthiness research

In the 1950s and 1960s the research activities on aircraft crashworthiness were affected by full-scale crash tests. In the 1950s the NACA performed seven full-scale crash tests of different aircraft types such as low-wing or high-wing configurations as well as aircraft designs with and without pressurised cabin [12]. In the 1960s two crash tests of larger aircraft were conducted on behalf of the U.S. federal aviation agency [13-14]. A Douglas DC-7 as well as a Lockheed 1649 were crash tested in a specific environment representing survivable or potentially survivable accidents of hard landing, wing low impact with the ground and impact into large trees in an off-airport forced landing. In Figure 2-1 the crash test of the Lockheed 1649 is depicted.

All these conducted crash tests were performed with the main velocity component in horizontal direction. The aircraft were mounted on a guide rail standing on their own landing gear. With its own propulsion the aircraft were accelerated and guided against several crash barriers, obstacles and impact hills, as exemplarily illustrated in Figure 2-1a). The aim of these full-scale crash tests performed in the 1950s and 1960s was mainly the generation of a crash load data base of survivable crash cases. None of the tested aircraft structures were of “jet size” and the design differed partly significantly from today’s aircraft designs.

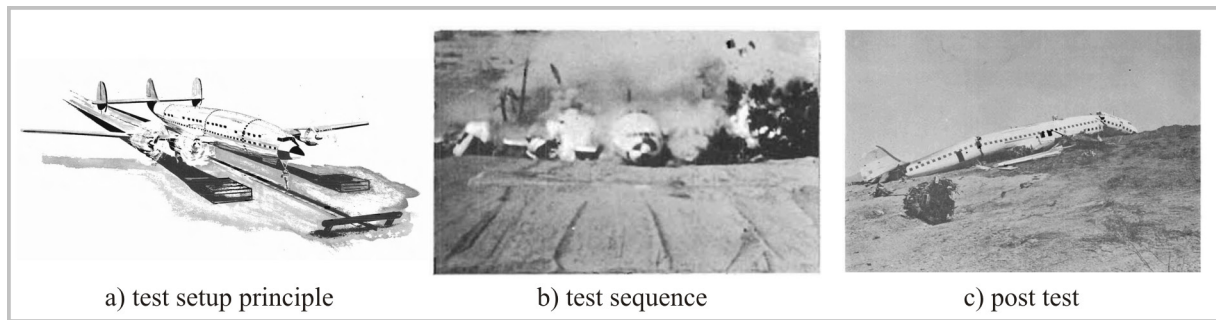


Figure 2-1: Full-scale crash test of the Lockheed 1649 [13]

In the 1980s an FAA crash dynamics research development program was initiated which was jointly sponsored by the NASA in some phases. Five vertical drop tests of B707 fuselage sections were conducted by the NASA and the FAA [15-19]. The lengths of the fuselage section were chosen to be between approximately 3 m and 4 m (10-13 ft). Soft sections, centre sections, conical sections and asymmetric sections with cargo door were tested. In addition to dummy or dummy ballast loading in the cabin, some of the sections were loaded with cargo. Figure 2-2a) depicts one of these B707 fuselage section drop tests. A further drop test was performed with a wide-body DC-10 fuselage section [20]. In these six fuselage section drop tests the initial velocity was defined between 6.1 m/s and 10.4 m/s (20-34 ft/s).

The research program culminated in the full-scale controlled impact demonstration (CID) test of a remotely piloted B720 airplane which was performed on December 1, 1984 [21-22]. Besides the generation of a good crash load data base a main interest of this test was the investigation on post-crash fire behaviour. Figure 2-2b) illustrates the B720 airplane shortly before impact on the wing opener barriers which were installed to enforce an extensive fuel spill with the danger of post-crash fire.

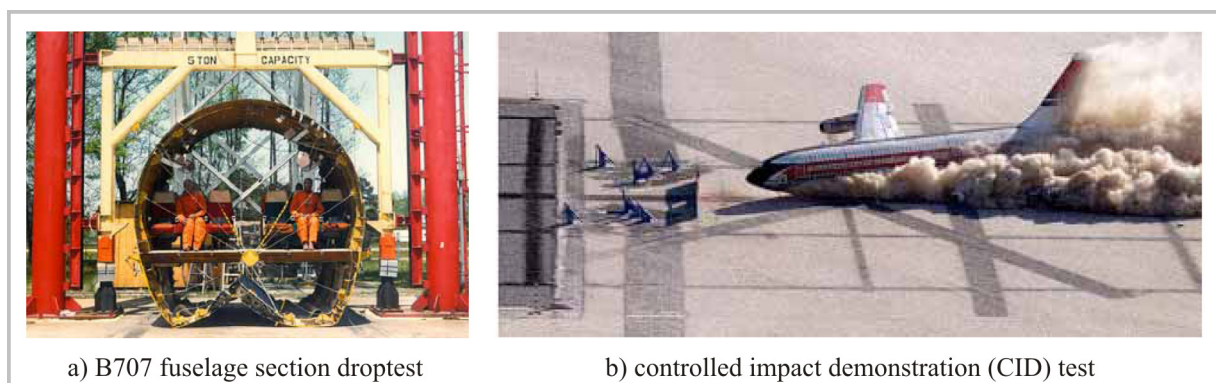


Figure 2-2: Crash activities of the FAA and the NASA in the 1980s [23]

In the scope of the FAA crash dynamics research development program three further vertical fuselage section drop tests were performed in the 1990s and beginning of the 2000s [24-26]. Besides a B707 fuselage section aft of the wing, two B737 fuselage sections forward of the wing

with a cargo door were drop tested. Both B737 sections were loaded with cargo, one section with luggage and the other section with an auxiliary fuel tank. Both sections were equipped with overhead stowage bins to investigate potential endanger of cabin safety by overhead masses that may fail. All three fuselage section drop tests were performed with an initial velocity of 9.1 m/s (30 ft/s). Figure 2-3 illustrates one of the B737 fuselage section drop tests.

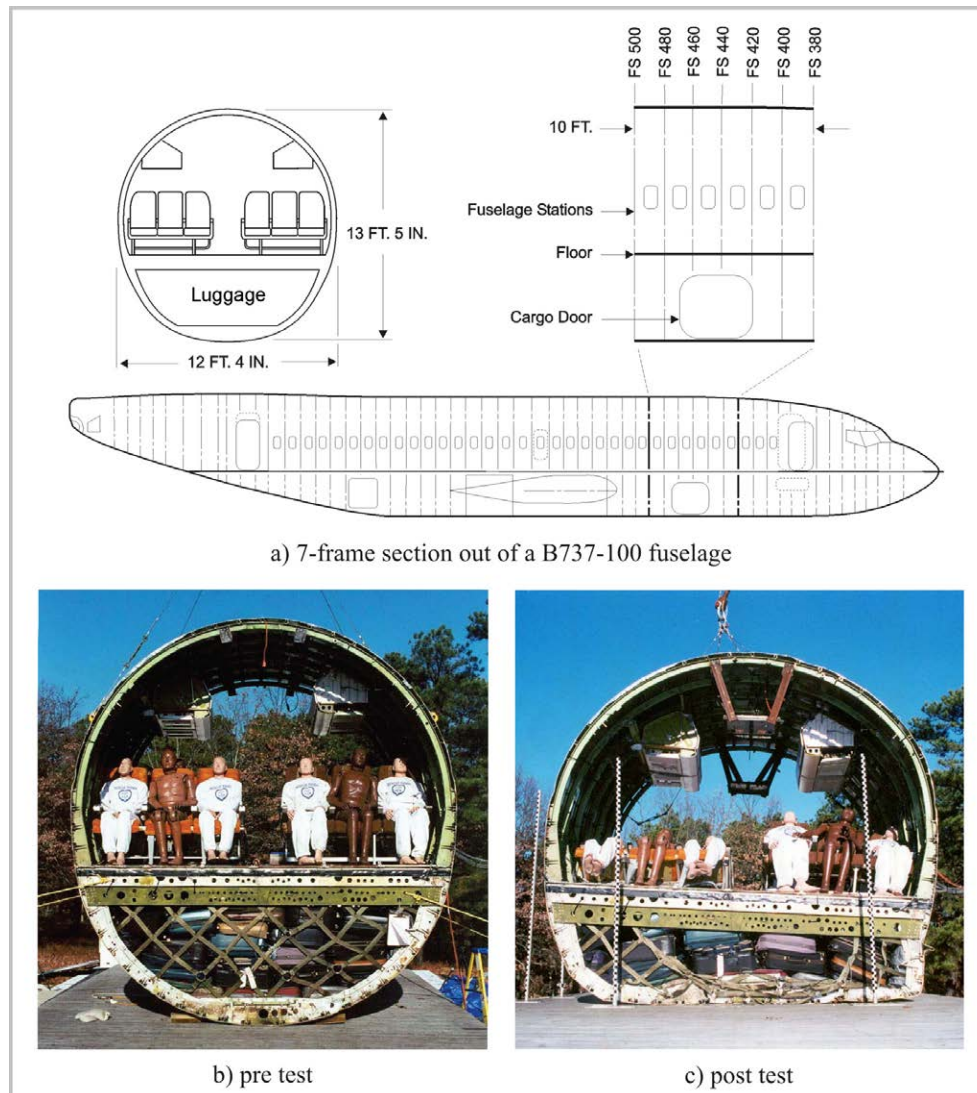


Figure 2-3: FAA drop test of a B737 fuselage section [24]

In the 1990s the European Community funded programme “crashworthiness for commercial aircraft” contributed to the investigation of the crash behaviour of metallic fuselage structures of transport aircraft. Besides quasi-static and dynamic sub-component tests of an A320 rear fuselage structure, an A320 fuselage section was drop tested [27-30]. The sub-component tests served for detailed investigations on the failure behaviour of the sub-cargo area as well as different located frame structures. The test results of the sub-component tests were intensively used to improve numerical modelling techniques. Different simulation methodologies were applied to perform pre-test simulations of the A320 fuselage section drop test. In 1995 the

research programme culminated in the drop test of a 6-frame section of an A320 rear fuselage. The drop test was performed with an initial velocity of 6.7 m/s (22 ft/s). In Figure 2-4, sub-component tests as well as the fuselage section drop test are depicted.

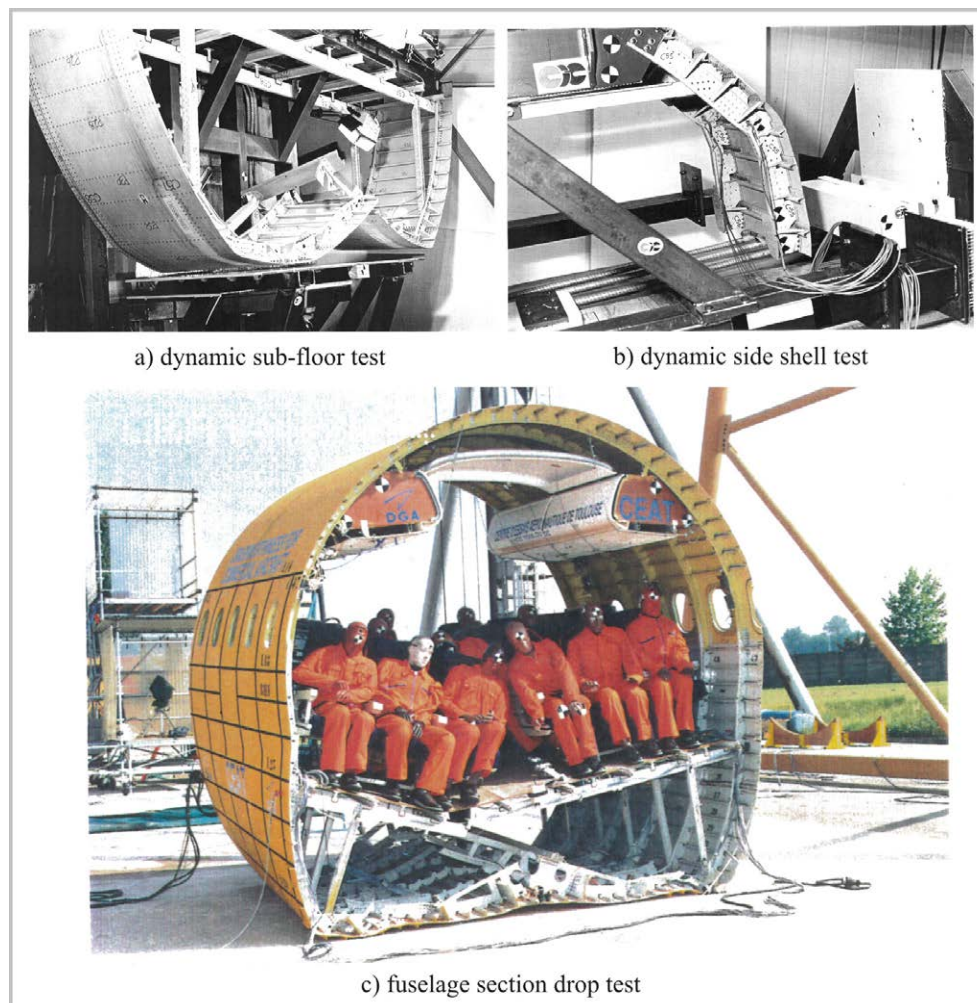


Figure 2-4: The European Community funded programme "crashworthiness for commercial aircraft" [28, 30]

Further research on crashworthiness of metallic transport aircraft structures was performed by the National Aerospace Laboratory of Japan (NAL) in the 2000s. A forward fuselage section with cargo compartment as well as an aft fuselage soft section of a YS-11 transport aircraft was drop tested with an initial velocity of 7.6 m/s (25 ft/s, forward fuselage section) respectively 6.1 m/s (20 ft/s, aft fuselage section) [31-32]. The NAL also performed about 40 drop tests of simplified structural aircraft fuselage models and analysed the influence of geometrical parameters on the crash behaviour, such as the position of the vertical support struts as well as the vertical location of the passenger crossbeam [132-133].

In the scope of an evaluation of the adequacy of current certification standards for seat and restraint systems for smaller commuter airplanes, the FAA initiated the commuter airplane crashworthiness program in the 2000s. Four different commuter category airplanes were tested in full-scale vertical drop tests [33-38]. Besides information on the fuselage accelerations which

contributed to the certification standards, valuable information of the structural crash behaviour of full-scale aircraft structures could be gained. In contrast to the design of large transport aircraft, these commuter airplanes provide no cargo floor area and are partly designed in a high-wing configuration. Nevertheless, information about local structural failure can be assigned also to the structural behaviour of large transport aircraft. Figure 2-5 depicts two of the tested commuter airplanes.

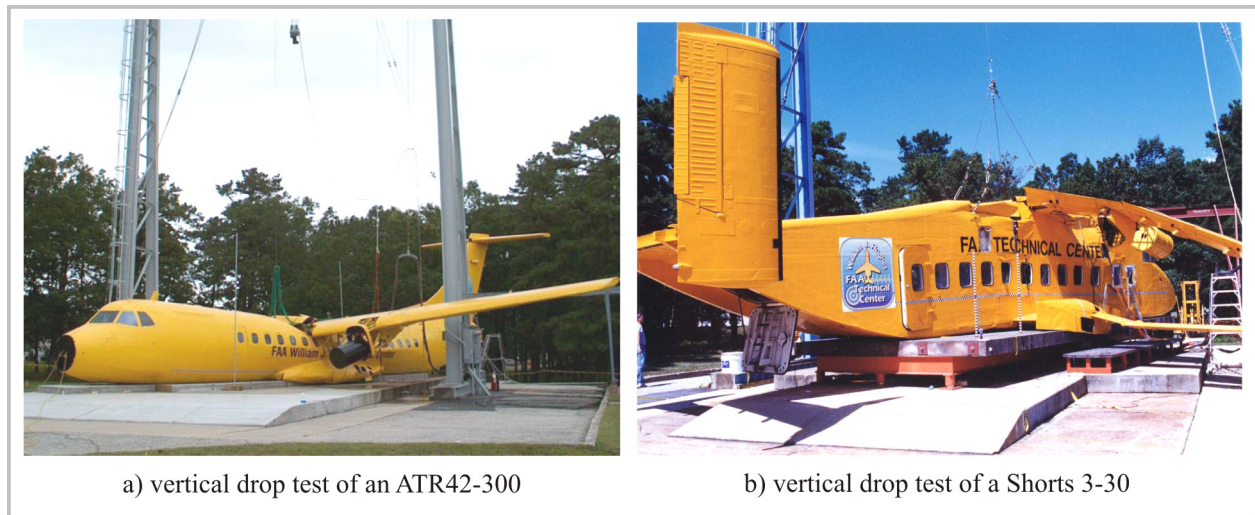


Figure 2-5: The FAA commuter airplane crashworthiness programme [37, 38]

All the work on crashworthiness of metallic aircraft structures, discussed above, contributes to the definition of a “metallic equivalent” as it is specified in the special conditions for the certification of new transport aircraft structures made of composite materials.

Crashworthiness research on composite structures

Crashworthiness research on composite aircraft structures is mainly driven by the challenge of controlled absorption of the kinetic crash energy. All known research in this field postulates local crash absorbers which have to be implemented in the structure to improve the crashworthiness of composite aircraft. The basis for such absorber concepts was developed in the research on helicopter structures. Several (metallic) sub-floor absorber concepts for a helicopter or a general aviation airplane structure were analysed by the NASA in the 1970s and 1980s [39]. Figure 2-6 depicts the main outcomes of this work. The principles of the NASA airframe crashworthy design concepts were adapted later to composite structures to benefit from the composites' high mass-specific energy absorption by crushing [40]. Although composite material, and in a narrower sense CFRP material, generally provides brittle failure behaviour with little energy absorption, a controllable progressive crushing process of such material can lead to a mass-specific energy absorption which is significantly higher than that obtained for metallic materials. Figure 2-7 compares the mass-specific energies absorbed by different materials in different

crushing processes. Wide-ranging research has been conducted in this field with the focus on the material behaviour under crushing which has been analysed by different specimens and components like tubes, half-tubes, cruciforms or corrugated beams [41-45].

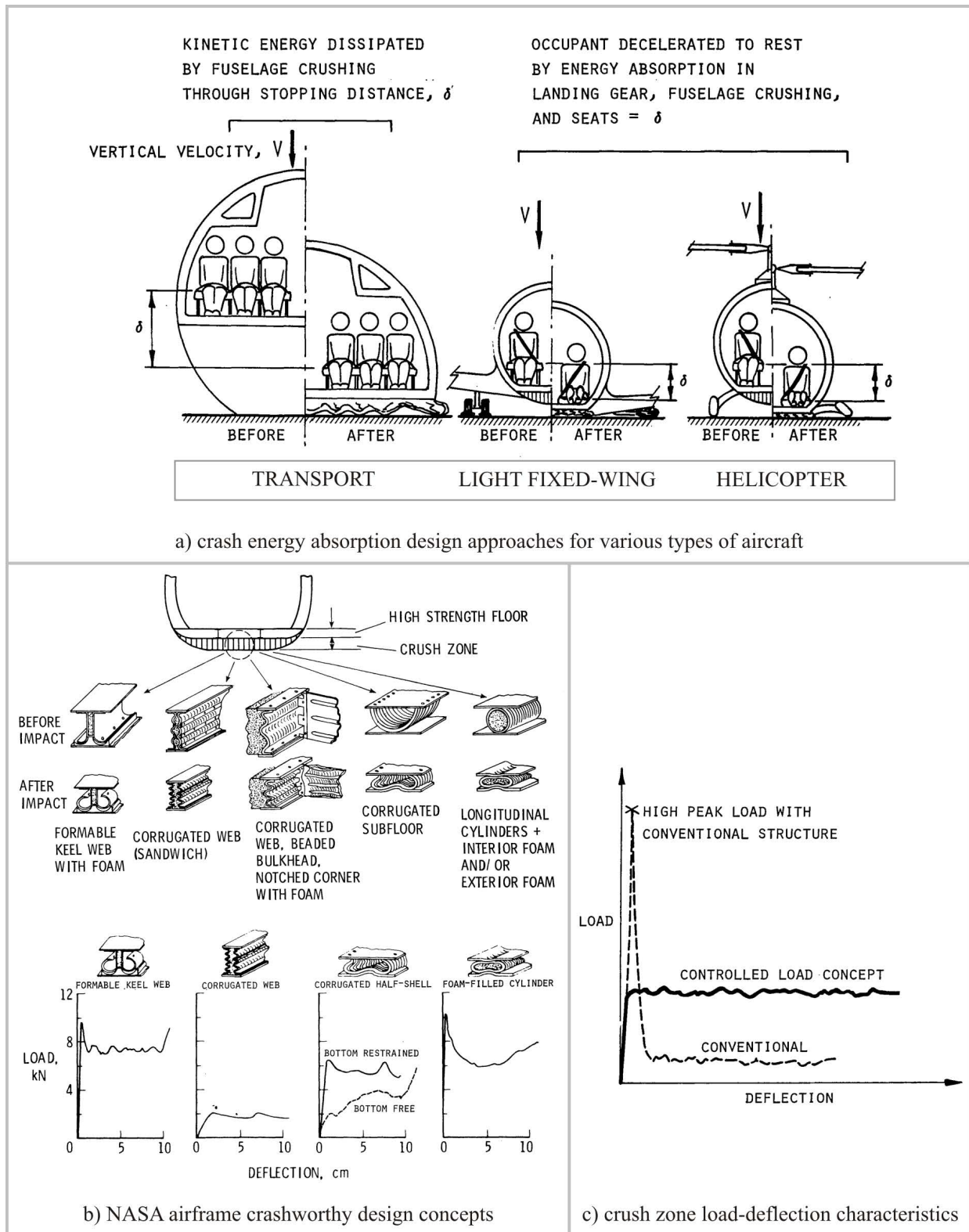


Figure 2-6: NASA research on crashworthy airframe design concepts [39]

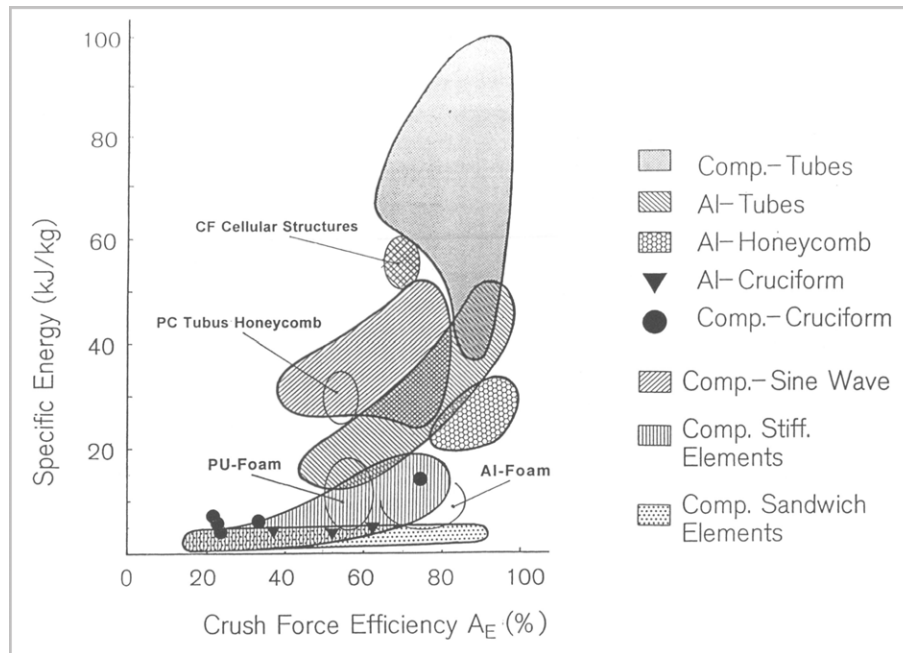


Figure 2-7: Crushing performance of generic structural elements [41]

Unfortunately, this wide-ranging research has its focus limited on the crushing of generic composite specimens to investigate the material behaviour. As a crashworthy composite transport aircraft design can not be reduced to one single failure mode of generic specimens, further research has to be conducted regarding other failure modes, such as bending failure of the frame structure. Figure 2-6a) depicts this case. Whereas a typical crashworthy helicopter design is defined by a stiff structure allowing extensive crushing of the sub-floor area, the failure behaviour of a transport aircraft structure in a crash event is dominated by frame bending failure.

In addition to the local failure modes, the overall crash behaviour of a composite aircraft structure has to be analysed.

Both topics were considered in research work which was conducted by the NASA in the 1980s [46-51]. Several composite aircraft structural components were tested to investigate the overall crash behaviour as well as the frame failure behaviour.

Composite fuselage frames with various cross-sectional shapes and a diameter of 1.8 m (6 ft) were drop tested. The drop tests were performed in a guiding system to constrain the single frames from out-of-plane rotation during the test. In addition, a skeleton and a skinned composite subfloor section was drop tested. All drop tests were performed with an initial velocity of 6.1 m/s (20 ft/s). Figure 2-8 shows examples of tested structural components. The main outcome of this study was a similar failure behaviour of these composite structures compared to the failure behaviour of metallic fuselage sections which was identified in the fuselage section drop tests discussed above. This failure behaviour was obtained for composite structures which have not been designed or optimized for energy absorption or crash loading considerations. The similar

failure behaviour is focused on the failure locations in a fuselage structure and not on the energy which is absorbed in the individual frame failure locations.

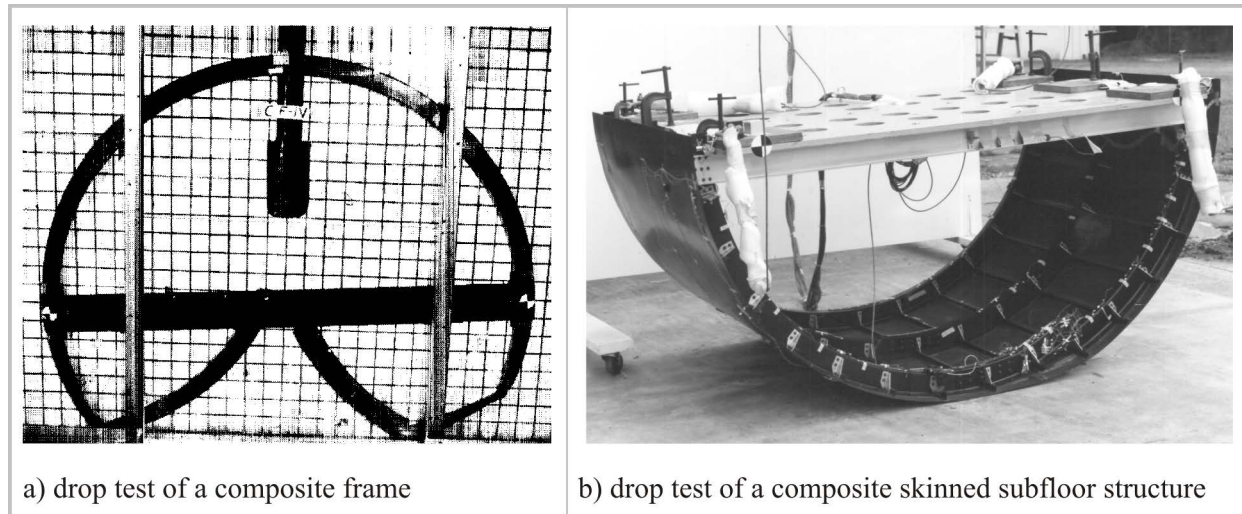


Figure 2-8: NASA research on composite aircraft structural components [47]

In the 1990s crashworthiness research for composite fuselage designs was conducted intensively in the European Community funded programme “CRASURV” (Crash Survivability). In the scope of this project a review on crashworthiness research of composite structures was performed. Well documented reference lists of this review are given in [52, 53]. The spectrum of the CRASURV project comprised the complete test pyramid from material coupon tests up to fuselage sub-floor drop tests, as illustrated in Figure 2-9. Composite absorber concepts such as corrugated beams or cruciform structures, depicted in Figure 2-9c), were tested [134-135]. The investigated absorber structures were integrated into composite fuselage designs of a commuter aircraft as well as a single-aisle transport aircraft. In a sub-floor drop test of the commuter structure the desired crash kinematics could not be obtained [54-56]. Uncontrolled failure of the absorber structures occurred with little energy absorption, Figure 2-9d). Regarding the composite single-aisle transport aircraft design a sub-cargo structure as well as a sub-floor structure was drop tested [57-59]. Neither the sub-cargo structure drop test nor the sub-floor structure drop test could demonstrate the functionality of the specified crash concept. In the sub-cargo structure drop test the absorbers, sine-wave beam structures, did not crush along its full length, Figure 2-9e). An improved design was implemented in the sub-floor structure. Nevertheless, this drop test again denied a successful functionality of the defined crash concept as the fuselage design above the absorber structure was not able to carry the crash loads. The cargo-crossbeam failed and prohibited the crushing of the sine-wave beam structure, Figure 2-9f). All three drop tests were conducted with an initial velocity of about 7 m/s. Despite of the non-successful drop tests a main outcome of the CRASURV project was the conclusion that an implementation of energy absorption devices is mandatory for a composite aircraft structure [61].

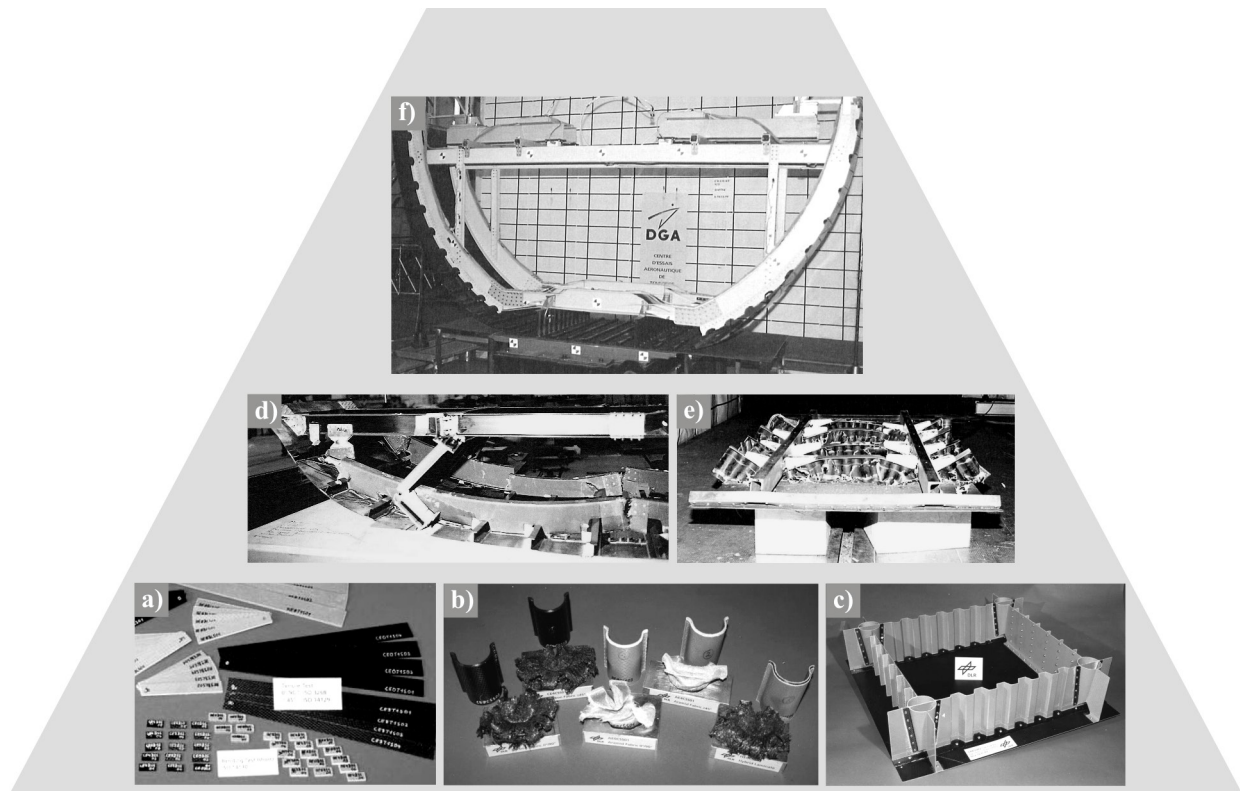


Figure 2-9: The European Community funded project "CRASURV" [56,57,59,136,137]

The crash concept of the CRASURV composite transport aircraft structure specified a crush zone which is located exclusively in the sub-cargo area. Further potential of energy absorption above that area was not considered. As the kinetic energy has to be absorbed along a comparably small crash distance, high crash forces can occur which lead to a massive design of the above fuselage structure. In case of the CRASURV transport aircraft structure the cargo-crossbeam as well as the frame structure had to be sized significantly stiffer compared to typical aircraft designs [60].

Further research on crashworthy composite fuselage design considered the cargo area as additional crash zone to increase the available crash height. This crash zone is mainly affected by frame bending failure. Research work was conducted in the 1990s to improve such bending failure characteristics of CFRP frame structures with respect to an increased energy absorption capacity [62-65]. Figure 2-10 depicts typical compression tests of curved frame components which were conducted in the scope of this work. In this study textile composite frame structures were investigated additionally, such as braided frames. Although an optimized design showed limited improvements of energy absorption in a bending failure process, significant increase in the post-failure energy absorption was not observed.

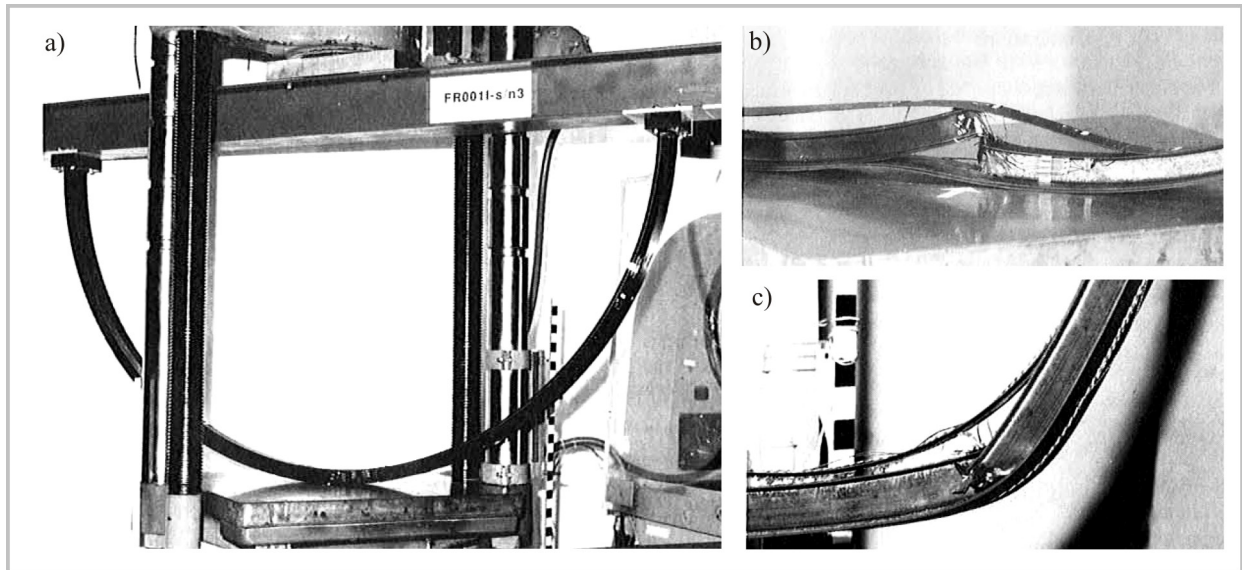


Figure 2-10: Research on improved energy absorption in CFRP frame structures [62]

Currently, transport aircraft developers work on new programmes of wide-body aircraft with primary structures made of CFRP. Boeing is certifying its new B787 model which provides a CFRP fuselage structure. Airbus is developing its A350XWB model which is planned to be fabricated with a high ratio of CFRP material. To fulfil an equivalent level of crashworthiness compared to metallic designs, as specified in the special conditions of the B787, Boeing has defined a crash concept for the sub-cargo area [66]. Massive stanchions made of CFRP shall be crushed in a progressive mode. In contrast to the stiff structure which was designed in the CRASURV transport aircraft fuselage section, the B787 fuselage structure provides much less stiffness above the sub-cargo area, as Figure 2-11 depicts. In crash cases without cargo loading, the comparably filigree cargo-crossbeams and frames have to carry the full crash load.

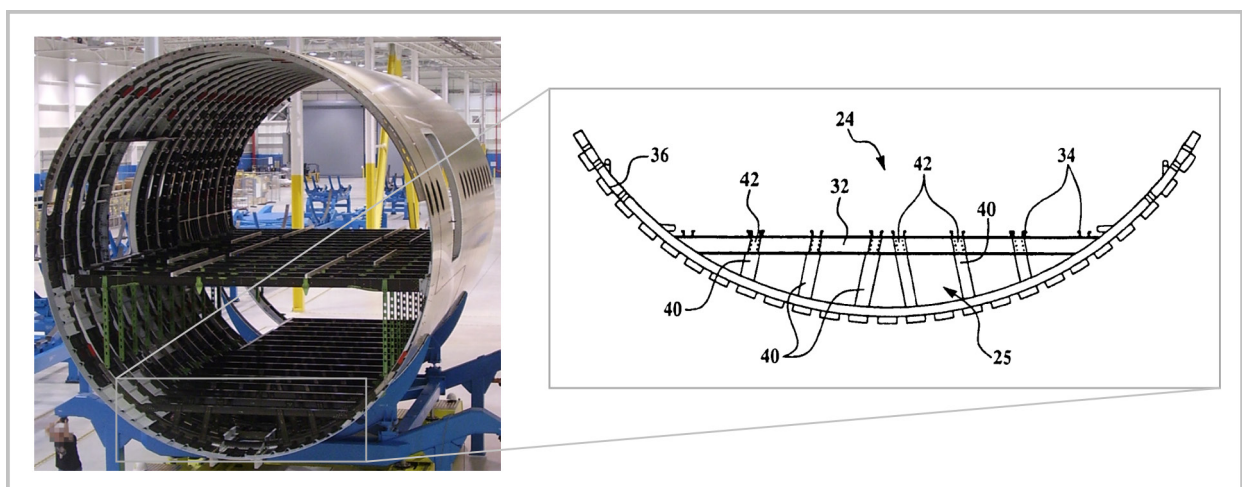


Figure 2-11: Boeing 787 crash concept (fuselage section 46) [66, 67]

2.2. Review on simulation methodologies

In general, crash dynamics of detailed structural designs are too complex for manual analysis. However, computer based modelling methods offer a capability that can provide a simulation of all important dynamic interactions. Numerous computer simulation models have been developed for use in simulation evaluations. And none of the developed modelling procedures is totally free of testing requirements and analytical judgement. The reason is the extremely complex process for the structural deformation under crash loading, which involves transient dynamic behaviour, complicated framework and shell assemblies, large deflections and rotations as well as extensive plastic deformation, damage and failure [5].

The multi-body approach, depicted in Figure 2-12, uses a very simple model to represent the considered structure, based on spring and beam elements as well as mass elements. In addition, plastic hinges can be defined to describe large rotational deformation. The equations of motion are solved numerically. Such models are very efficient due to their simplifications and are often used in the preliminary design phase of vehicles or trains to estimate the general crash characteristics [68-73].

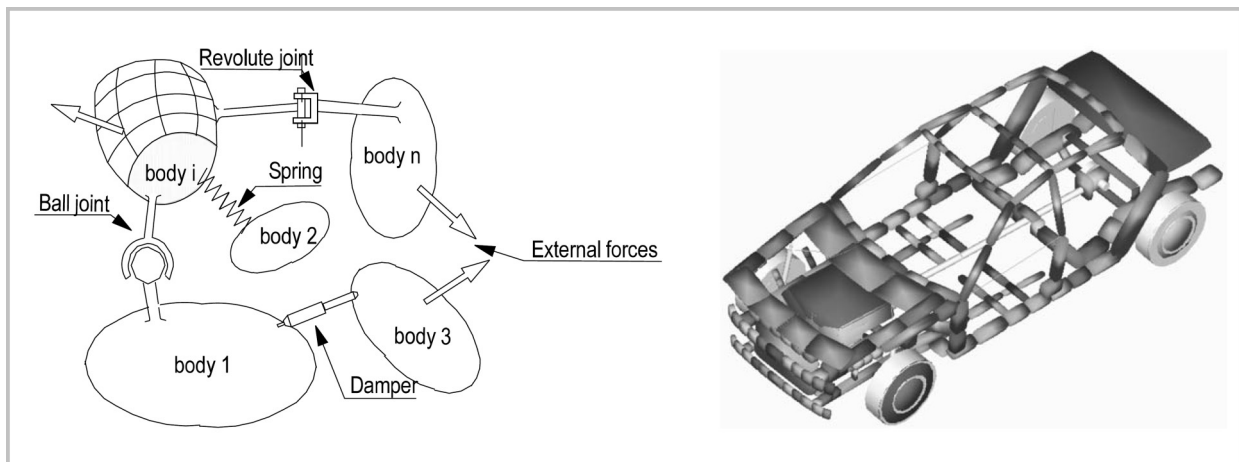


Figure 2-12: Multi-body system - generic model and vehicle model [70]

Hybrid models are based on the multi-body approach and use experimental test data as well as detailed finite element simulations to generate input data for the spring elements and the plastic hinges. A widely used hybrid modelling program in the field of aircraft crashworthiness is DRI-KRASH [145]. Several crash tests discussed in paragraph 2.1 were analysed with this code, examples are illustrated in Figure 2-13. The model efficiency can be used to simulate full-scale crash tests such as the controlled impact demonstration (CID). Test results of the fuselage section drop tests, which were conducted in advance of the CID test, could be used to calibrate the full-scale model and to predict the CID test. In addition, the hybrid full-scale model was used to perform sensitivity studies [74].

In the European Community funded project “Crashworthiness for commercial aircraft” the hybrid code DRI-KRASH was used to predict the drop test of an A320 fuselage section. The experimental test data of structural components of an A320 fuselage were used as characteristic inputs for spring elements and plastic hinges. Finally, a good prediction of the fuselage section drop test could be achieved [75].

In contrast to the usage of experimental test results, detailed finite element simulations can be performed to generate characteristic failure data of structural components which can be used as input for springs and plastic hinges in the hybrid model. An example of such an approach is given in [76] on the basis of a helicopter subfloor structure.

Further examples on hybrid code applications are given in [77].

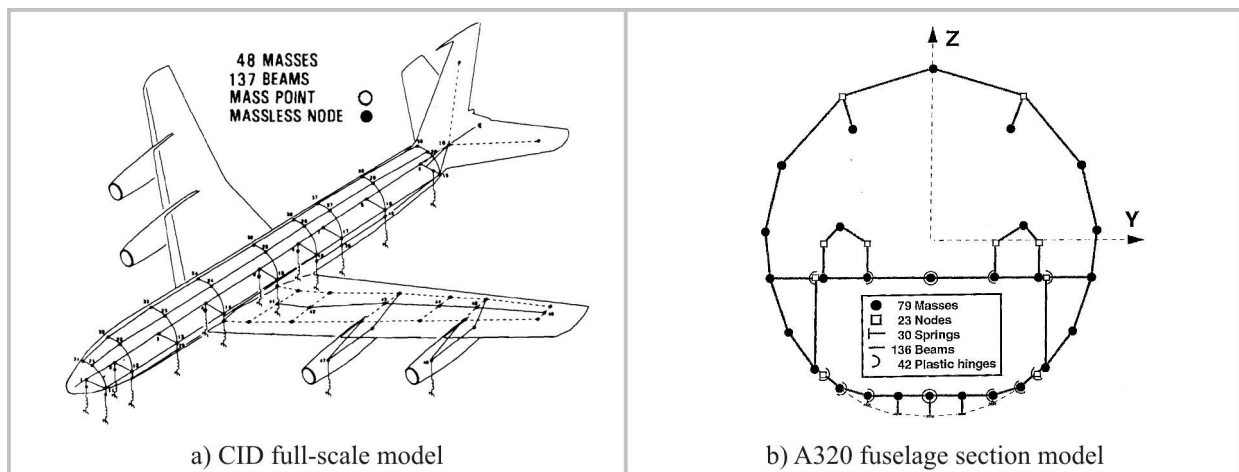


Figure 2-13: Hybrid code models (DRI-KRASH) [74,75]

The finite element method is a further analytical approach in which the structure is divided into appropriate structural units called elements. The deformation characteristics of each component are calculated from its material stress-strain curve. The structural mass is placed at nodes at each element boundary and is therefore distributed throughout the structure. The equations of motion of the elements are solved numerically. An overview on the finite element method and its integration schemes is given in Appendix A1.1.

The finite element method is used for detailed analysis of structural design or its failure behaviour particularly due to dynamic loads. Explicit finite element method for analysis of crashworthiness of aircraft structures is used extensively. A wide range of literature documents the use of FEM for crash analysis of aircraft structures [78-86]. Some of the fuselage section drop tests discussed in paragraph 2.1 were simulated using the finite element method, Figure 2-14b). Based on the experience gained with such simulations, the NASA prepared best practices for crash modelling and simulation [87]. The increased computational power allows the

simulation of larger models up to detailed full-scale models of aircraft crashes, as the NASA performed in the recent past of the full-scale drop test of an ATR42 aircraft [88], Figure 2-14a).

Nevertheless, the current state of the art in the FE simulation of aircraft crashworthiness is the consideration of a fuselage section instead of a full-scale model. The explicit finite element method limits its range of considered problems to short-time events. Long duration events, such as a real aircraft crash scenario lasting several seconds, would lead to unacceptable error propagation due to the enormous number of calculation cycles. Hence, typical FE simulations consider purely the vertical direction which shortens the crash event to few hundred milliseconds. The neglect of the horizontal component has minor influence on the structural damage and crash kinematics of an aircraft fuselage. In typical crash scenarios the aircraft slides on the ground and induces friction forces which are significantly below the impact loads of the vertical direction. Furthermore, the longitudinal forces of the aircraft sliding are mainly carried by the fuselage skin and the stringers whereas the vertical impact loads are carried mainly by the frame structure. For that reason, the consideration of a fuselage section under purely vertical crash loads is a sufficient approach for the development of crash concepts that have the aim to reduce the impact loads on the occupants. This approach is conducted in current development processes of new composite fuselage aircraft such as the Boeing 787 or the Airbus A350XWB.

Still, such simulation results are of generic manner and do not consider all potential loading conditions of a real crash situation. For example, the sliding of an aircraft against hills or on rough ground, which can lead to fuselage break events, is not considered. Again, such failure event has less influence on the vertical impact loads which are the major cause of death in aircraft accidents.

The consideration of a fuselage section in numerical analyses implicates another drawback which has to be discussed. A fuselage structure comprises several sections which differ significantly in their structural behaviour. Fuselage sections which include landing gear bays or the centre wing box provide much stiffer behaviour compared to the typical fuselage sections. In addition, the installation of cargo doors can lead to asymmetric crash kinematics caused by different stiffness of the lower fuselage side shells. The concentration on a typical fuselage section for the analyses of crash concepts can be critical. Nevertheless, it provides a sufficient generic basis for the development of such fuselage concepts in a preliminary design phase and it provides a basis for comparison of safety levels. On the basis of such analyses on the fuselage section level an equivalent level of safety compared to metallic airframes can be demonstrated in a certification process. However, it is obvious that the developed crash concept on the basis of a

typical fuselage section has to be adapted to the other fuselage sections to fulfil a real equivalent level of crashworthiness.

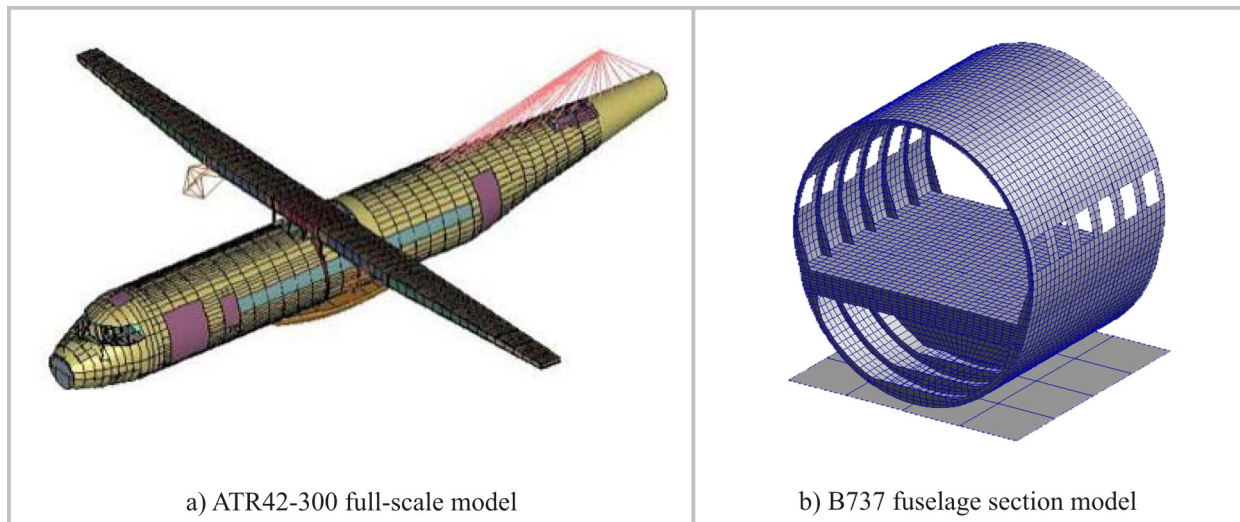


Figure 2-14: Finite element models [84,88] – in comparison to hybrid code models in Figure 2-13

A further point that has to be discussed in the scope of finite element modelling is the definition of material behaviour. In contrast to hybrid modelling, the FEM approach provides detailed models for the representation of material behaviour. With respect to the simulation of composite structures this is a huge challenge. The complex damage and failure behaviour of composite structures can not be modelled by characteristic curve inputs as it is the case in hybrid models.

High effort was raised in the European project “CRASURV” to develop improved formulations for composite materials [89-93]. The verification of such models was performed from the coupon level up to the fuselage section level. Figure 2-15 shows exemplary results of this research and compares the failure modes of composite cruciform and trapezoidal beam obtained by simulation and test.

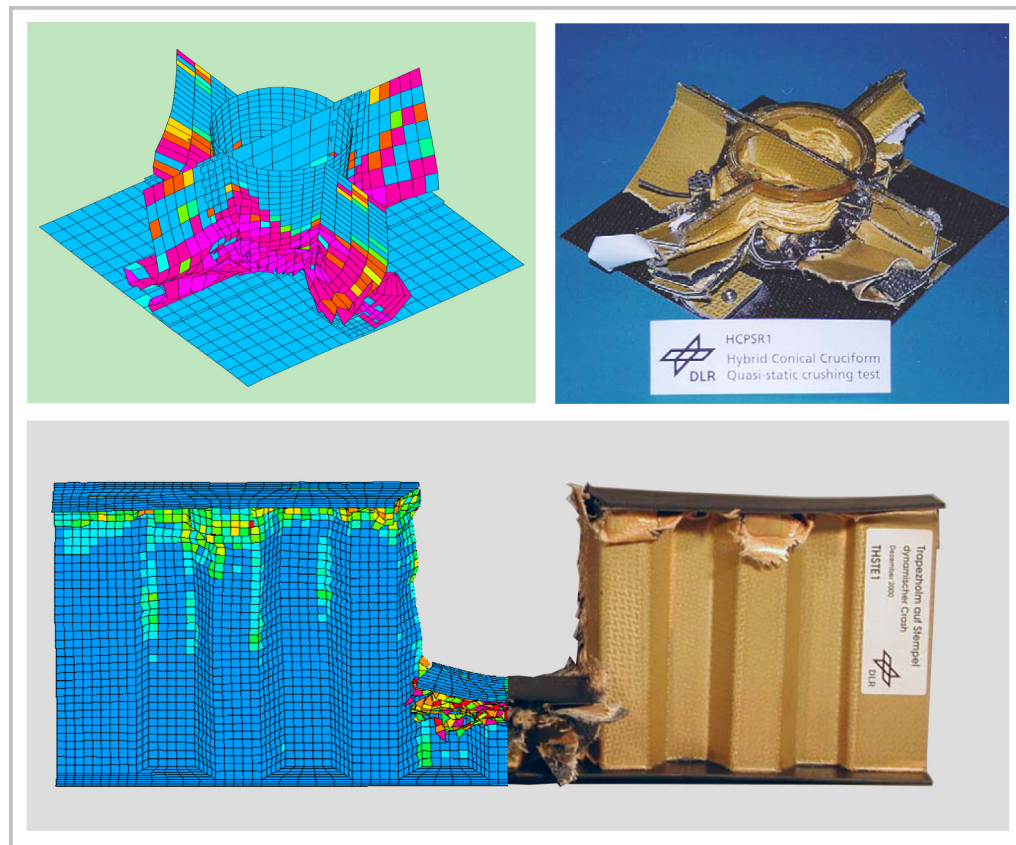


Figure 2-15: Composite material model validation [94,138]

The NASA performed simulations of composite aircraft structures as well. The simulation of a 1/5-scaled model composite fuselage concept as well as of a full-scale composite helicopter is documented in [95-98].

Further work on simulation of composite materials in finite element methods is documented in [99-102]. In particular [100,101] represents the current state of the art in composite modelling using the finite element method. In this work crushing tests of CFRP specimens were simulated using a stacked shell approach. The failure behaviour, and more important the failure load level, of the simulation agrees well with the test results, as depicted in Figure 2-16. Nevertheless, the presented results represent post-test simulations. With respect to the predictive capability of composite material models further research is required.

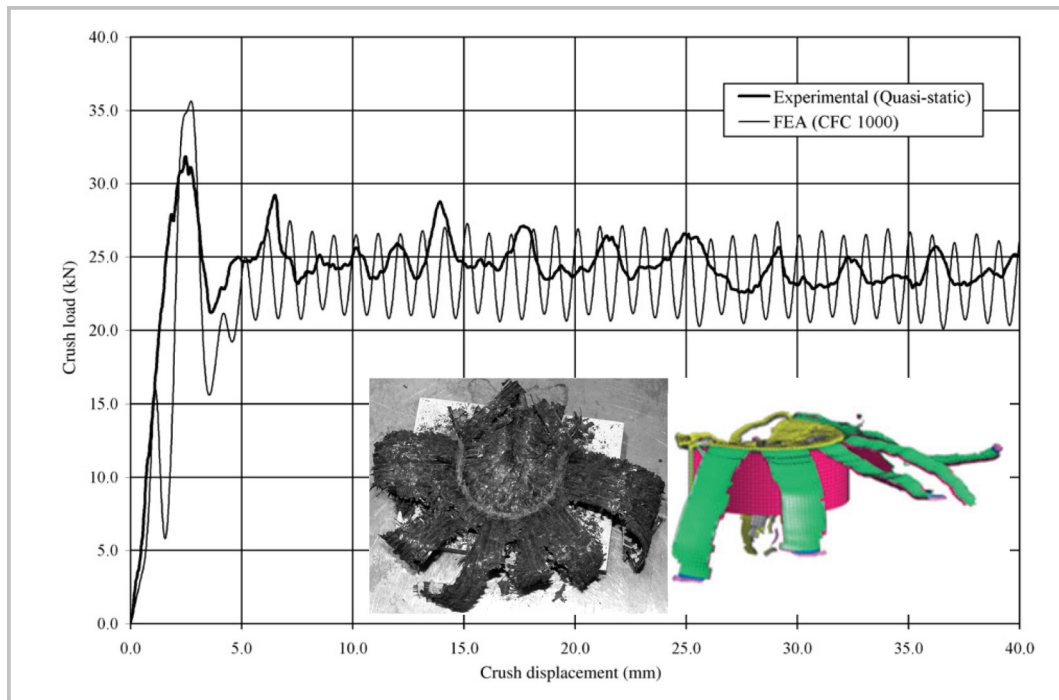


Figure 2-16: State of the art composite modelling in finite element methods [101]

2.3. Identification of open questions – definition of the thesis

The review on crashworthiness research in paragraph 2.1 identified that a wide basis of knowledge was gained in the past by several research programmes. The complete range from material tests up to full-scale crash tests was considered. In addition, the critical crash behaviour of composite structures was investigated in several research projects. Nevertheless, sufficient crashworthiness for composite fuselage structures could not be demonstrated until now. The research work identified, that crash concepts which were developed for composite helicopter structures can not be adapted directly to transport aircraft structures. The static sizing of helicopter structures provides already a stiff fuselage design as heavy masses – turbine and transmission - are installed above the cabin. A similar crash concept adapted to transport aircraft would lead to significant structural mass penalty compared to the static sizing, as demonstrated by the crash improved composite transport aircraft fuselage design in the project CRASURV. Composite fuselage designs of new wide-body aircraft which are currently being certified, such as the Boeing 787, specify a crash concept which is mainly similar to helicopter crash concepts. An equivalent level of safety compared to metallic designs is questionable in this aircraft model as the fuselage structure above the crash zone provides less stiffness. The outcome of the current state of the art is the need to develop crashworthy composite fuselage designs which provide an equivalent or even better level of safety compared to today's aircraft structures made of aluminium. Such crash designs have to specify additional crash devices which control a crash scenario and which absorb sufficient kinetic energy. The principle of these crashworthy designs

was already given in Figure 1-4. The crash devices have to be designed so that their activation corresponds to a controlled crash kinematics which should be a cascading scenario starting with failure and energy absorption in the lower fuselage area and progressing stepwise by the activation of other crash devices during the crash sequence. The design of trigger load and energy absorption level in the individual crash devices has to be performed on the fuselage section level considering the crash kinematics of the entire fuselage cross-section. In addition to the design of crash devices, the statically sized fuselage structure potentially has to be resized to sustain the crash loads.

Such a design process can be conducted numerically by the methods discussed in paragraph 2.2. Hybrid codes, for example DRI-KRASH, are efficient to analyse such problems. Failure is described using macro elements such as springs and plastic hinges. With respect to the design of crash devices this modelling approach is advantageous as the required characteristic of the individual crash device can be defined directly by the macro input. The main disadvantage of this approach is its coarse level of discretisation. Detailed conclusions about the structural behaviour are hardly possible as several structural parts are not modelled in detail. As an example, a re-sizing of the frame structure to consider the crash loads can not be performed accurately enough with the hybrid approach, as the structural interaction of frame and skin is not represented, which plays a major role in the bending behaviour of a frame structure. In the hybrid model, beam elements represent frames, stringers and the skin. Hence, the discretisation cannot resolve detailed structural design requirements.

In contrast to hybrid codes, the modelling approach of detailed finite element method offers the possibility of detailed structural analyses. The structure is modelled more accurately which allows the analysis of local effects and the re-sizing of structural parts due to the crash loads. However, the detailed modelling approach also implicates disadvantages. To represent the fuselage structure in sufficient detail a large amount of data is necessary to build up the model. As the crash aspect is typically analysed in the preliminary design phase of an aircraft development, these detailed data are partly not available. Assumptions can be used for the missing data, but finally these details may have an important influence in some crash events and have to be considered as critical. In addition, the detailed FEM approach uses material formulations for composites which are not fully predictive, especially with respect to failure and post-failure modelling. The results of such analyses will have a significant level of uncertainty.

The development of crash designs for transport aircraft fuselage structures requires an analytical approach which combines some advantages of hybrid codes and detailed FEM. The possibility to describe the required behaviour of crash devices by macro elements should be combined with a

more detailed modelling approach. The discretisation should be as detailed as necessary to represent all important structural effects and as coarse as possible to avoid the need of data which is not available in a preliminary design phase. Uncertainties caused by damage and failure representation of composite material formulations should be avoided by the usage of mainly linear-elastic material models. The main failure events should be described exclusively by macro elements. The analytical approach should provide the opportunity to completely design a fuselage structure for crash. This includes the required characteristics of the crash devices to achieve an optimum crash kinematics, their positioning in the fuselage structure as well as the design of the remaining structure to sustain the crash loads.

Definition of the thesis is the development of such an analytical approach. Besides the modelling approach itself a complete crash design methodology shall be developed and demonstrated. This includes the definition of a design process as well as the development of experimental test setups to investigate concepts for local crash devices. Such test setups can be used either to generate input data for the macro elements or to develop crash devices which fulfil the required characteristics of the crash design process.

3. Aspects of the Kinematics Model approach

This chapter deals with a crash design tool that was developed according to the requirements discussed in paragraph 2.3. Benefits of different established analyses techniques are combined to provide a preliminary design tool for the crash scenario development of a fuselage structure.

The general modelling technique of this so-called “Kinematics Model” is discussed in this chapter 3. Further detailed investigations, which were performed in the scope of the model approach development, are considered in chapter 4 and 5.

3.1. Basic approach of the Kinematics Model

Chapter 2 already discussed the circumstance that in a well-defined crash scenario of a composite fuselage structure main failure should occur exclusively in the crash devices. Failure outside of the crash devices could lead to uncontrolled crash kinematics of the brittle structure with the potential loss of any crashworthiness. Hence, the circumjacent structure of the crash devices has to remain intact. This requirement leads to a modelling approach where all failure is described by macro elements which represent the crash devices. The remaining structure, that is not allowed to fail, is modelled linear-elastically. Crash scenarios can be developed, assessed and optimised by modification of the macro characteristics. These modifications include trigger loads, energy absorption capacities or in general the capability of energy absorption (brittle or absorbing failure characteristics).

In general, the Kinematics Model is based on the commercial explicit finite element method. On the one hand, the model is discretised in such detail that all important structural effects are represented. Hence, the fuselage structure is represented using shell, beam and bar elements according to the common FEM approach. On the other hand, the discretisation is as coarse as possible to avoid the need of data which are not available in a preliminary design phase. Finally, the structure is modelled using mainly linear-elastic material characteristics. Uncertainties caused by damage and failure representation of CFRP material models are negligible in this approach.

Based on the linear-elastically modelled structure an increased element size can be defined for the representation of the fuselage structure, compared to classical explicit FE modelling approaches considering non-linear material behaviour. In the linear-elastically modelled parts,

the deformations of the finite elements are comparatively small, at least in the range of structural design allowables. Mesh refinement for representation of large deformation is not essential even though the elements typically used in explicit FEM use low-order shape functions of a linear form.

Additional model efficiency is obtained in a comparatively coarse model representation. Structural parts which do not contribute to important effects with respect to typical crash loads primarily have to represent their stiffness in an accurate way. For this reason, stringers are modelled using beam elements. Details such as clips and cleats are not modelled.

The Kinematics Model considers exclusively vertical crash loads on a fuselage section, similar to the current state of the art simulations of aircraft crashworthiness as discussed in paragraph 2.2. The crash concept, respectively the equivalent level of safety, is assessed on a 2-bay soft section. The generation of fuselage section geometries as well as the corresponding FE meshes was performed using the DLR in-house mesh generation tool 'SECTMESH' [103].

Figure 3-1 illustrates the modelling approach of the Kinematics Model. Potential crash devices respectively failure locations which are represented by macro architectures are highlighted in red colour.

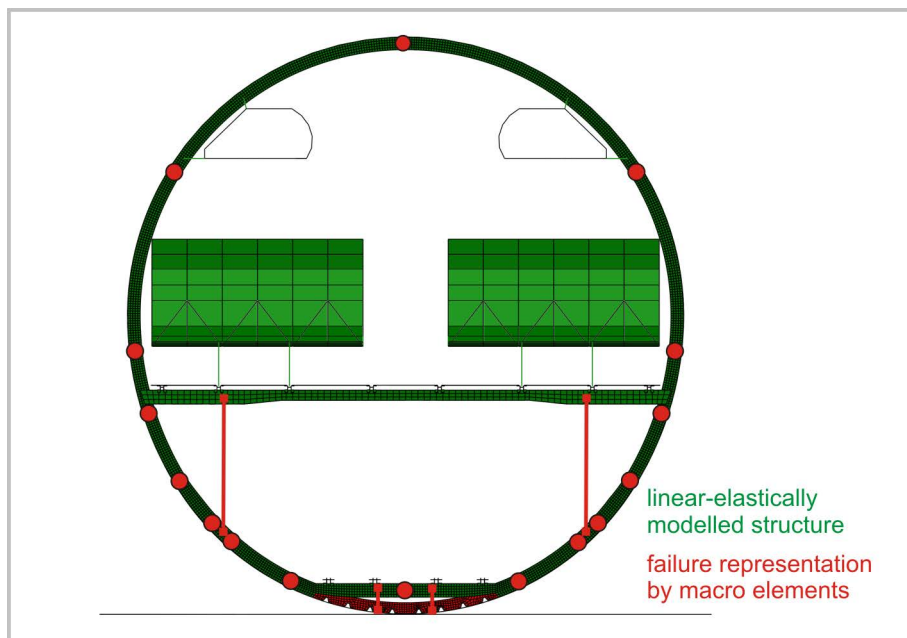


Figure 3-1: Modelling approach of the Kinematics Model

The macro elements are the central components of the Kinematics Model. They represent the main crash behaviour of the structure. An accurate modelling to represent realistic failure is of primary importance. In the following paragraph 3.2 different failure modes of a typical fuselage structure are discussed and compared to their developed macro architectures.

3.2. Macro modelling of crash devices

Chapter 2 highlighted the spectrum of experimental studies on crashworthiness of aircraft structures which were performed in the past. These valuable experimental results were analysed to identify typical failure mechanisms of fuselage structures under crash loads. The identified failure modes were graded in failure categories of primary and secondary importance. Failure modes of primary category represent main failure events which influence the crash kinematics significantly. These are failures of the main structural parts. In contrast to the main structural failures, the secondary category considers failure modes which have less influence on the crash kinematics. Moreover, this secondary category includes failure events which have to be avoided in a robust crash concept for a composite fuselage structure. Failures of overhead bin connections as well as of passenger crossbeams are events which are assessed critical for occupant survivability. Further failure events like disintegration of structural parts or other distributed extensive damages have to be avoided particularly for a composite fuselage design to achieve a controllable crash concept. Figure 3-2 gives an overview on typical failure events of a fuselage structure and highlights the failure modes of both categories.

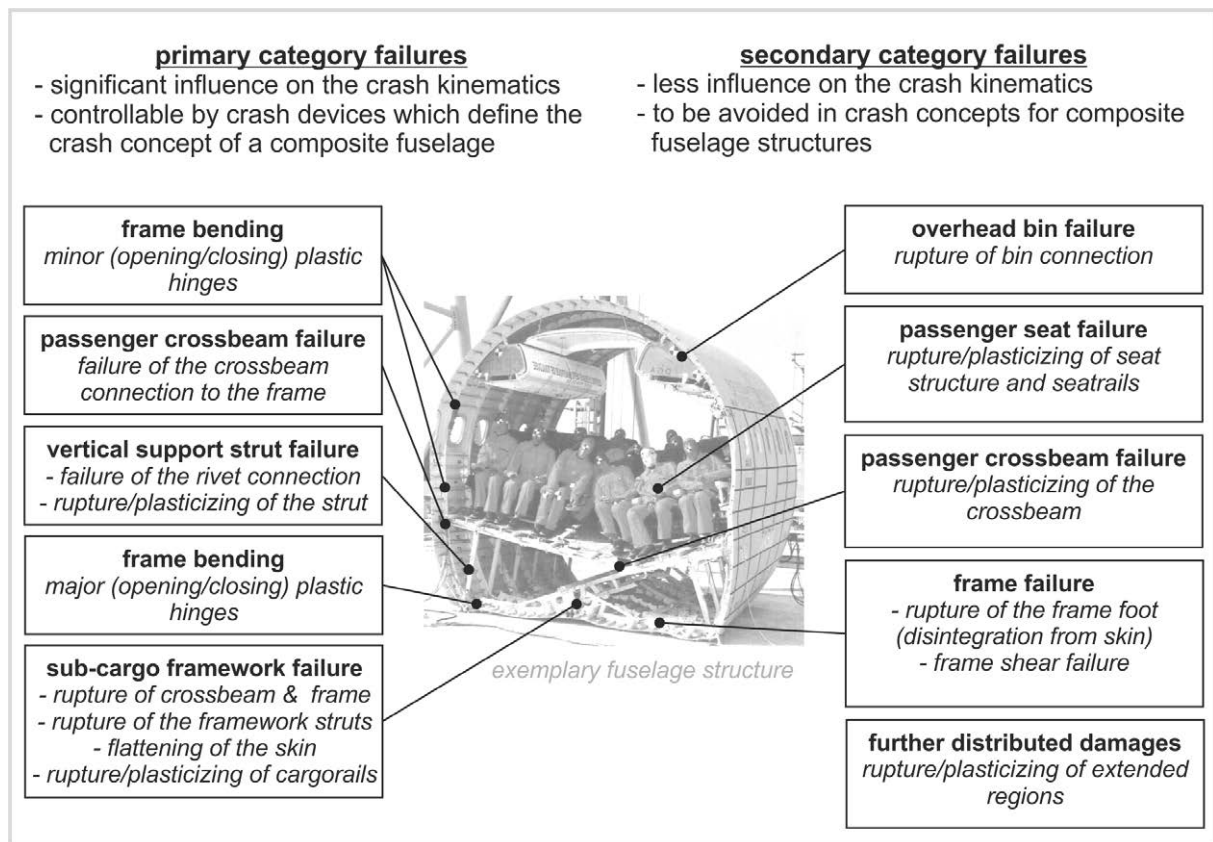


Figure 3-2: Typical failure events of a fuselage structure caused by crash loads

The identification of typical failure mechanisms is mainly based on metallic structures as very little experimental results are available of fuselage section drop tests of composite structures.

Nevertheless, all research on composite fuselage structures done in the past indicate that typical failure mechanisms of CFRP fuselage structures caused by crash loads are similar to that of metallic fuselage structures, although their behaviour is significantly more brittle [46-51].

With respect to the failure modes graded in the primary category, macro architectures were developed to describe these failure mechanisms in the Kinematics Model. The macro architectures represent typical failure events which have to be controlled in a crash concept using appropriate crash devices.

The following sub-paragraphs deal with the macro architectures of the individual failure modes.

3.2.1. Selection of a macro element

A macro architecture for failure representation is a formation of several finite elements which represents the failure kinematics of individual structural parts in an airframe. The definition and configuration of such architectures decides on the accuracy of the representation of structural failures. Besides an appropriate architecture the choice of the central macro element decides on the options to describe the structural failure behaviour under different loading conditions. In general, a macro element is used to describe individual behaviours between structural nodes. Figure 3-3 illustrates the general capabilities of macro elements. The range of available characteristics implicates the advantage of such elements.

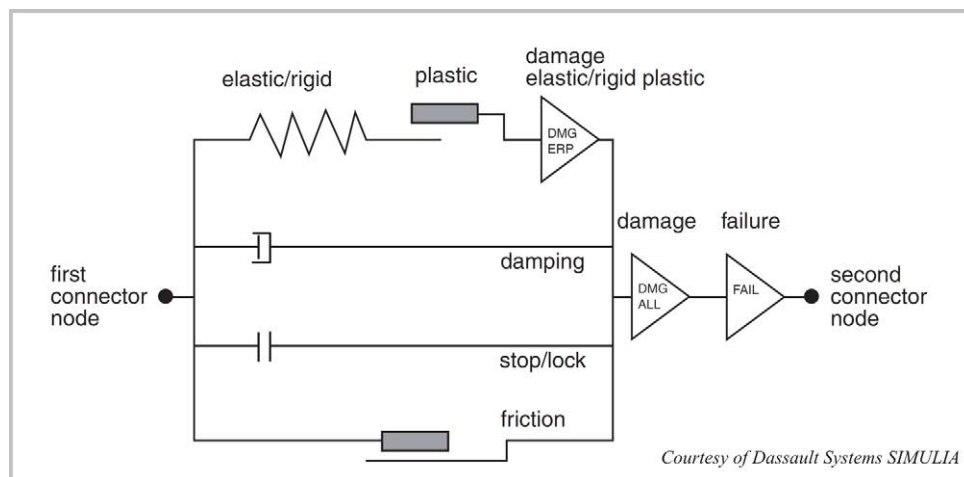


Figure 3-3: Conceptual illustration of the macro element behaviours [104]

With respect to the different macro architectures discussed in the following sub-paragraphs, the representation of failure and absorbing characteristics requires the possibility to define extensive input data for the macro element. Besides the main loading behaviour of a crash device several options for the description of unloading and reloading behaviour are essential. The preferred description of the macro behaviours is a load-deflection curve. Other descriptions, e.g. by damage and failure, can not be used directly for comparison of numerical crash device

characteristics with experimental test results. Hence, a tabular input format of the macro element behaviour is desired.

Several macro element types were assessed with respect to their functionalities and their applicability. Joint elements are typically preferred elements of finite element programmes which provide most options to define load-deflection behaviour for different loading conditions. An assessment of element types in the explicit FE code PAM-CRASH resulted in the selection of the 'kjoint' element. In the explicit FE code ABAQUS/Explicit the 'connector' element was selected which provides similar options. The 2-node 'kjoint' or 'connector' element is a macro type element which offers the independent description of all six degrees of freedom. It enables the definition of a main characteristic, as well as an unloading and reloading behaviour, by tabular curve input. The transition from loading to unloading respectively from reloading to loading is given by a slope which is a further input value. Figure 3-4 depicts this macro behaviour and gives exemplarily the keywords for the selected input options of the 'connector' element in ABAQUS/Explicit.

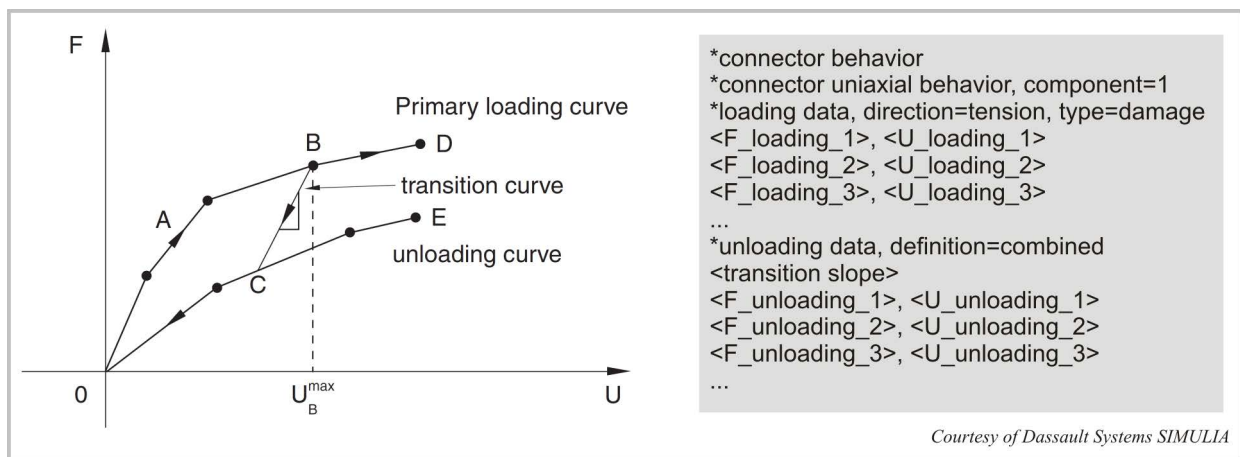


Figure 3-4: Tabular input options for the selected macro element [104]

3.2.2. Macro architecture for axial crushing

Structural failures in an airframe which occur in a crushing process are represented in the Kinematics Model by axial macro architecture. This type represents the crash devices in the sub-cargo area as well as in the vertical support struts. Although the energy absorbing concepts may be different in both applications, as illustrated in Figure 1-4, the axial failure kinematic is similar and can be described with the same macro architecture. The failure characteristic can be defined using a force-deflection curve, as shown in Figure 3-5. In this sample force-deflection graph brittle behaviour is defined for failure caused by tensile loads (positive deflection). With respect to failure caused by compression loads (negative deflection) the residual force plateau after triggering implicates energy absorption by crushing.

The connection of the macro element to the fuselage structure is realised by rigid bodies. Structural nodes of the linear-elastically modelled fuselage structure form a rigid body together with a non-structural reference-node which is allocated to the macro element.

With respect to the crash kinematics it is important to represent all released degrees of freedom of the considered structural part. For example, some designs of vertical support struts define an articulated connection to the fuselage structure using a pin joint. Moment loads around this pin axis cannot be transmitted by the vertical strut. For that reason, the macro architecture is modelled so that the crash device can be connected to the fuselage structure either fixed or articulated. This modelling option requires the definition of two serial macro elements. The need of two serial macro elements is founded in the definition of its degrees of freedom. All translational degrees of freedom are described with respect to the first macro element node. The rotational degrees of freedom are defined regarding the second element node. As the macro element represents crash devices of finite length rotational motion may only be considered at one end of the element, at node 2. Hence, a second macro element defined serial to the first one but in opposite direction enables a rotation at a second location. This second macro element was defined at the position of node 1 with a zero length. The crash device characteristic is defined in the first macro element with its finite length whereas the second macro element has rigid behaviour and offers exclusively the option of free or fixed rotation. Figure 3-5 illustrates this macro architecture.

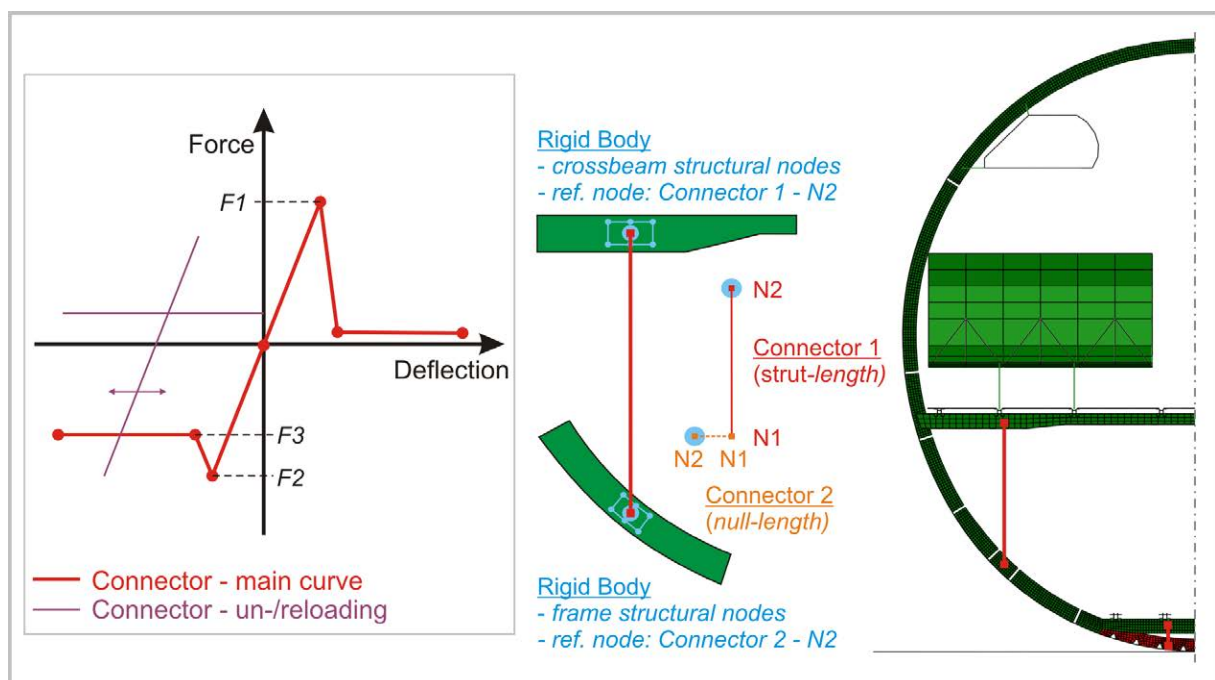


Figure 3-5: Macro architecture for axial failure

3.2.3. Macro architecture for frame bending

Frame bending representation is described by a rotational motion and represents the bending failure mechanism of the frame structure. These ‘kinematic hinges’ provide a complex failure behaviour which is caused amongst others by the interaction of the frame structure with the fuselage skin. In addition, it is the main failure event in a typical fuselage crash scenario as a large crash distance is affected by the frame bending mechanism, absorbing a significant amount of the total kinetic energy.

The input format for the description of the frame failure characteristic is a moment-rotation curve, as illustrated in Figure 3-6. The sample graph shows brittle failure behaviour for a so-called opening hinge rotation, which is characterised by tensile load in the inner frame flange (negative rotation). Different moment plateaus for a closing hinge rotation (positive rotation) represent the energy absorption capability of this frame failure characteristic.

The macro architecture defines a cut in the linear-elastically modelled frame with rigid bodies enforcing the free ends of the frame. Both frame parts are connected with the macro element which describes the frame failure behaviour. This macro element is positioned in the skin plane. The nodes of the macro element are connected to the rigid bodies of both frame sections. The macro element, respectively the cut in the frame, has a finite length. All degrees of freedom are fixed except the frame bending rotational degree of freedom. This rotation is defined at the second node of the macro element. As the ‘kinematic hinge’ length is negligible small compared to the frame length, the rigid behaviour of the macro architecture in the fixed degrees of freedom has marginal influence on the overall stiffness. Figure 3-6 depicts this macro architecture.

Several detailed investigations were performed to analyse the frame bending behaviour and to derive this present macro architecture which accurately represents frame bending behaviour. These investigations are discussed in chapters 4 and 5.

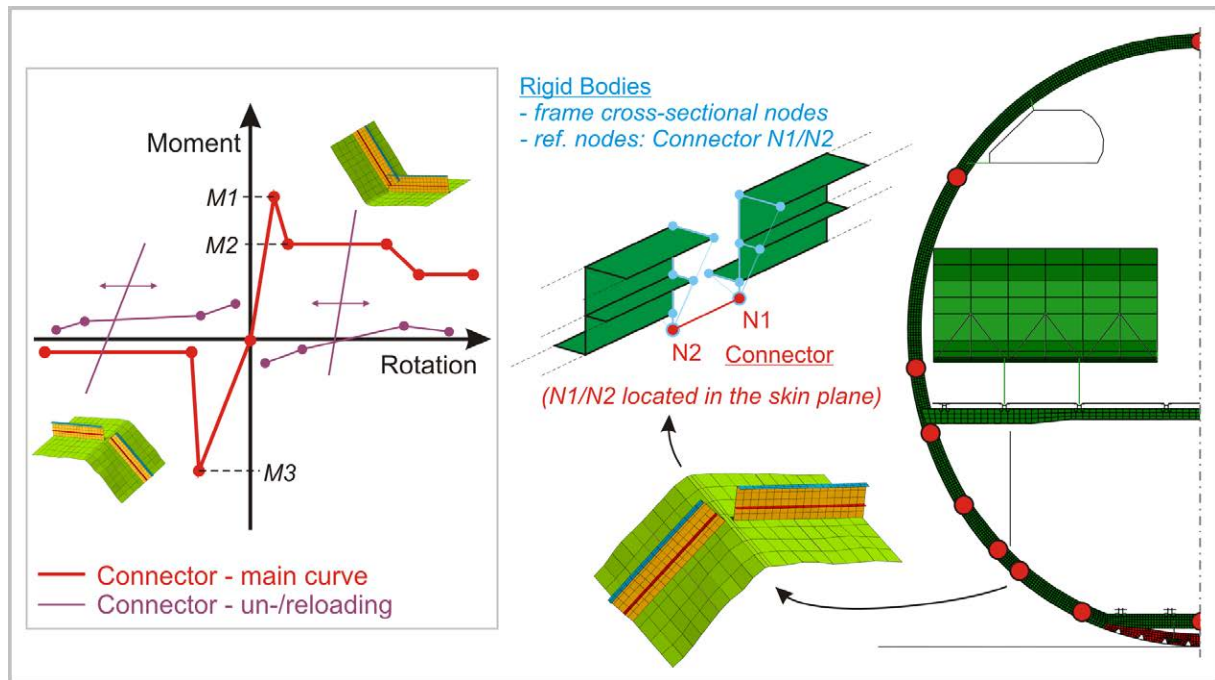


Figure 3-6: Macro architecture for rotational failure in the frame

3.2.4. Macro architecture for cargo-crossbeam failure

Another structural failure which was assigned to the primary category is failure of the cargo-crossbeam. The bending failure mechanism of this crossbeam has a significant influence on the crash behaviour of a fuselage section and can even decide on the general crash kinematics. With respect to a crash concept for a composite fuselage this failure has to be controlled by a crash device.

In contrast to the frame bending failure, the cargo-crossbeam bending failure is less complex as structural interaction with other parts is less significant. Nevertheless, the macro architecture is defined analogue to that of the frame bending failure. A cut separates the elastically modelled cargo-crossbeam in two parts. The nodes of each free end in the cut of the crossbeam form a rigid body together with a non-structural node which is allocated to the macro element. The macro element connects both rigid bodies and describes the failure behaviour of the crossbeam. The non-structural nodes of the macro elements are positioned in the centre of area of the cargo-crossbeam section. One simplification in this approach is the assumption that the elastic centre of the crossbeam cross-section corresponds with the centre of area. Regarding a crossbeam structure made of composite with typically complex layup the elastic centre does not necessarily correspond to the centre of the cross-sectional area. Still, it is very close to the centre of area as a typical layup definition does not differ significantly from a symmetric composition.

In Figure 3-7 the macro architecture of the cargo-crossbeam failure is given.

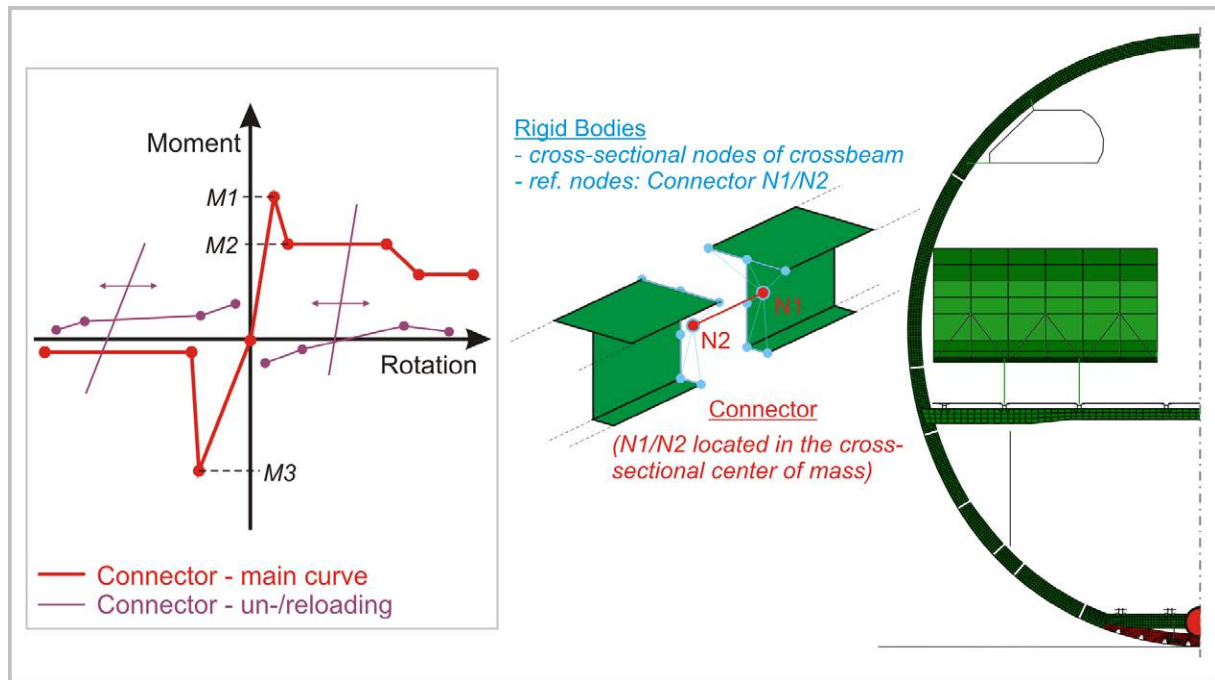


Figure 3-7: Macro architecture for rotational failure in the cargo-crossbeam

3.2.5. Macro architecture for the passenger crossbeam connection

The connection of the passenger crossbeam to the frame was generally identified as non-critical. In none of the experimental results discussed in chapter 2 this connection failed. Nevertheless, failure close to this connection occurred due to the loads introduced by the passenger crossbeam.

An additional crash device in the connection of passenger crossbeam and frame could reduce these loads by a certain flexibility. This flexibility would enable an extensive ovalisation of the whole frame structure utilising the comparably high failure strain of composite material. Besides the smoothening effect of an ovalisation further energy could be absorbed in the passenger crossbeam connection by a simple tensile absorber.

To analyse the effect of such an ovalisation concept, a macro architecture was defined for this structural connection. Instead of a tied connection, the macro element connects the passenger crossbeam with the frame structure. The load introduction in both elastically modelled parts is defined by rigid bodies which describe a similar region as given by typical rivet fields of such connections. The structural nodes inside of this region form the rigid bodies together with a non-structural node which is allocated to the macro element.

Whereas the macro architectures discussed above are defined with one active degree of freedom, there are two active degrees of freedom in this case. In addition to the translation in lateral direction a rotational motion around the longitudinal axis (flight direction) is defined to enable further ovalisation by unconstrained relative rotation between frame and passenger crossbeam.

Figure 3-8 depicts the macro architecture and illustrates exemplary characteristics of such a crash device.

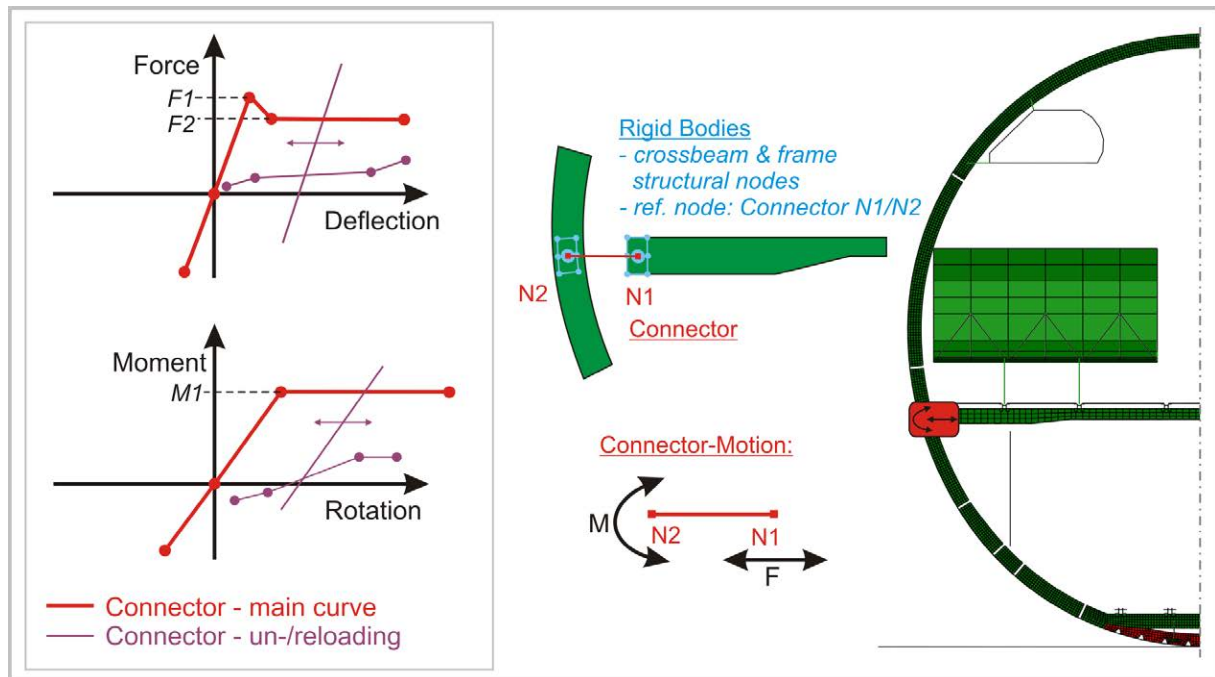


Figure 3-8: Macro architecture for the passenger crossbeam connection

3.3. Definition of Kinematics Model output data

Output definition has to be defined with respect to the specific modelling approach. Appropriate criteria have to be specified to assess crash scenarios which are analysed using the Kinematics Model.

Typical output definitions are energies of the whole model as well as of specific parts or structural regions. Whole model energies like total, kinetic or internal energy give information about the overall behaviour of the simulation model. Output of numerical energies indicates the quality of the numerical model. Internal energy output of individual structural parts give information about the distribution of absorbed or elastically stored energy.

Section forces and moments are additionally used to explicitly analyse the load acting in several structural parts. Cutting surfaces are defined along the whole frame structure as well as along the crossbeam structures. This section output can be used to analyse specific load ratios such as the bending-compression or the shear-compression ratio. These values can further be used for the definition of boundary conditions in the analyses of local components.

Besides these general output definitions three main types of output data are defined in the Kinematics Model. This additional output is the basis for an assessment of crash scenarios and provides information about the macro element characteristics, about the structural loads of the

fuselage section and about the crash loads on the passengers. In the following sub-paragraphs these specific output definitions are discussed.

3.3.1. Output definition of macro elements

Output definition of the macro elements provides valuable information about the crash device characteristics which are necessary to achieve a desired crash scenario. Several values are of interest. The time of activation of the individual crash devices is an important output to understand the general kinematics of a crash scenario. Therefore load-time and deflection-time output is essential. In addition, the amount of energy which is absorbed in the crash devices is of interest. Furthermore, maximum deformations in the individual crash devices play an important role, especially with respect to the realisation of crash concepts. All this information can be used as requirements for a sub-sequent development of local crash concepts, as depicted in Figure 3-9.

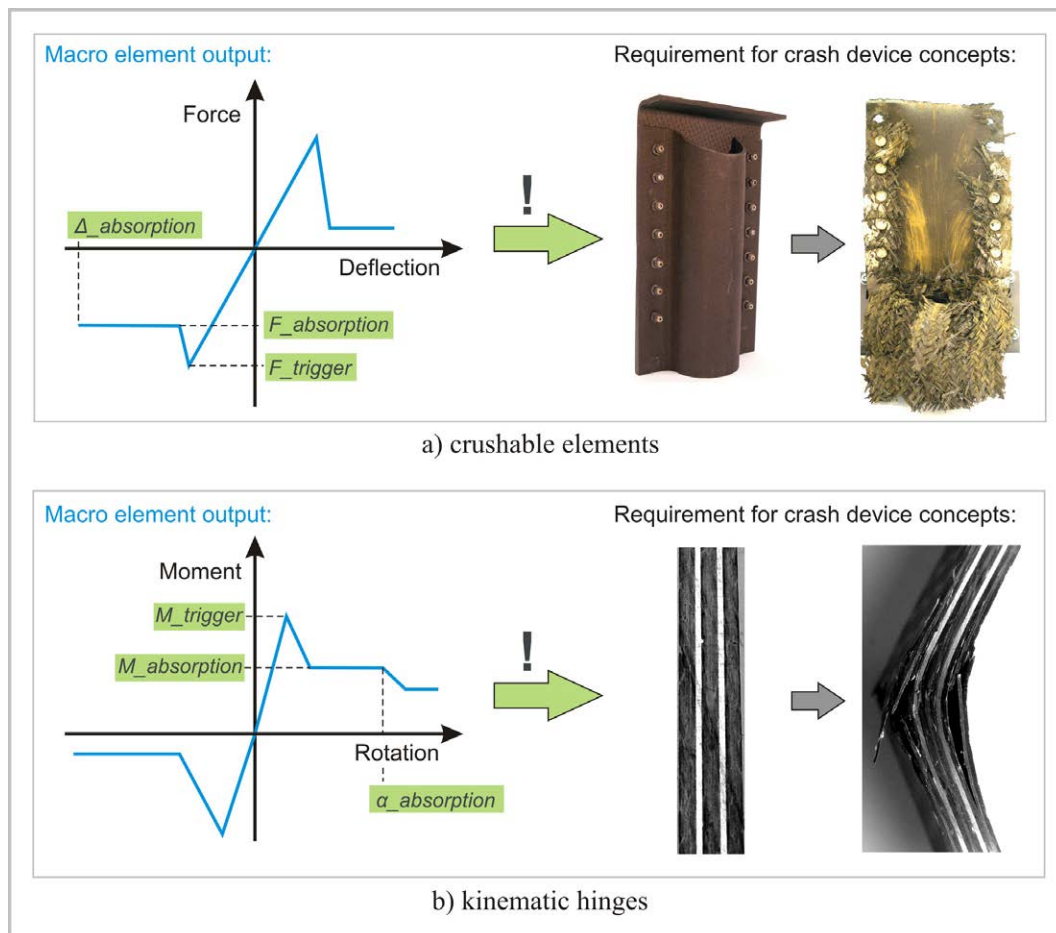


Figure 3-9: Output data of the macro elements - requirement for the development of local crash devices

The macro elements provide output options for each of its six components. The active component(s) is of prime interest as it describes the load-deflection characteristic of the crash device. In addition, output of the passive components can be used to check the loads which are

caused by constraints to fix these components. That output helps to check the model approach against non-accuracy caused by high constraint loads in the passive degrees of freedom.

3.3.2. Output definition of structural loads

Research on aircraft crashworthiness in the past, as discussed in chapter 2, identified the frame structure as the most critical part of a fuselage section. In addition, the crossbeams are critically loaded in a crash event. Both structures, frames and crossbeams, have to carry the vertical crash load which is the main component of the total crash load.

In contrast to this, the fuselage skin as well as the stringers are loaded uncritically. In case of a real crash event these structural parts carry the longitudinal crash loads which are significantly lower than the vertical ones as a typical full-scale crash scenario allows sliding of the aircraft on the ground which induces comparably low friction forces in longitudinal direction.

Hence, the verification of structural loads concentrates on the frame as well as on the crossbeam structure. An appropriate criterion was defined for the assessment of frame and crossbeam loads. This criterion aligns to the model approach of a preliminary design tool with its requirement of a coarser discretisation.

One requirement is the concentration on global loads with respect to a frame section. Detailed information on the ply level of a frame section laminate is not convenient with respect to the global frame sizing. Furthermore, a load based criteria such as section forces and moments does not consider the load carrying capacity of the frame profiles in the individual frame regions. Additional formulations would be necessary to define load limits of the individual frame designs. Such a formulation is complex as the influence of the skin has a major effect. The skin can be described as an additional flange with an unknown flange width. The determination of load limits for such an unknown structural combination is not efficient.

For that reason the criterion of the Kinematics Model is based on global strains which are measured and assessed along the frame. Bar elements with negligible stiffness are modelled along the frame and crossbeam flanges to measure the strain distribution. These strain values can be checked against analytical or empirical strain limit criteria such as limits against crippling failure of compressive loaded frame flanges. Figure 3-10 shows an example of the Kinematics Model with highlighted bar elements for the strain assessment. Exemplary bar element output in Figure 3-10 clarifies the efficiency of such an approach to check the loads along a frame or crossbeam structure against limit strain criteria. The exceeding of the strain limit of a large number of strain bar elements can be checked with a single graph.

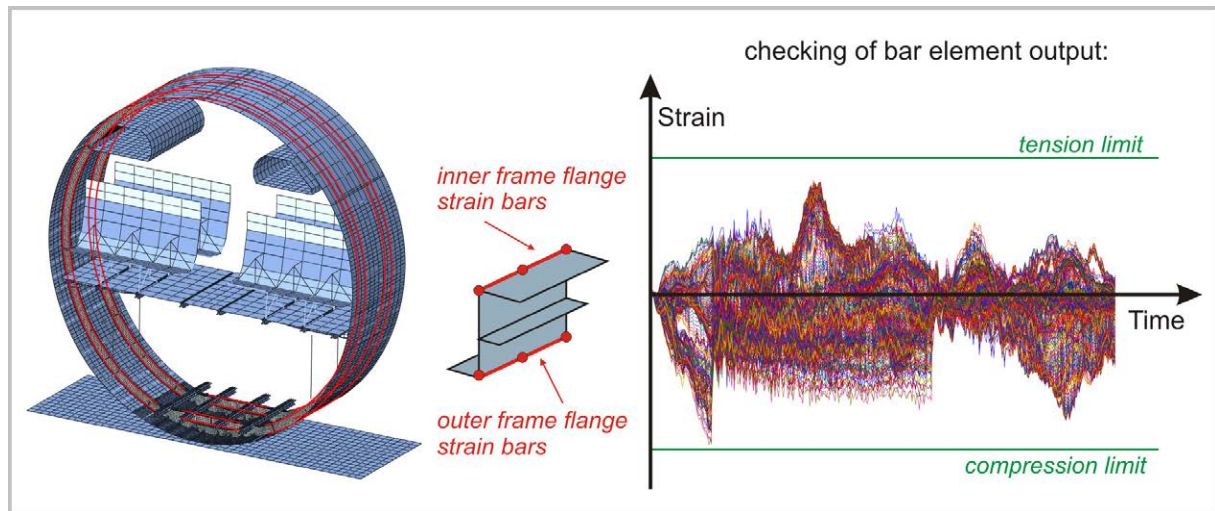


Figure 3-10: Bar elements for strain measurement

3.3.3. Output definition of injury risks

Loads on occupants are one of the main criteria for the assessment of a crash scenario. Different injury criteria can be used to analyse the occupant response in a crash event [105-107,139]:

- The dynamic response index (DRI) is derived from a simple one-dimensional lumped-mass spring damper system and was developed to estimate the probability of compression fractures in the lower spine due to acceleration in a pelvis-to-head direction.
- The FAR Part 27.562 (c) (normal category rotorcraft) specifies that the spinal load should not exceed 6672 N (1500 lb.) [109]
- A head impact tolerance specification is the Head Injury Criteria (HIC) which is based on the resultant accelerations measured at the centre of gravity of the head.
- Injury Assessment Reference Values (IARVs) are defined for restrained Hybrid III dummy occupants. These assessment reference values specify injury guidelines for several parts of the body such as head, head/neck interface, chest and knee.
- Finally, the whole-body acceleration tolerance curve was established by Eiband [108]. The Eiband acceleration tolerance levels were determined from sled tests on human volunteers, pigs, and chimpanzees that were conducted for a single input acceleration pulse.

In the Kinematics Model the whole-body acceleration tolerance curve according to Eiband is used to assess the passenger loads. The selection of this criterion is based on the modelling of seat and passenger. A simplified seat-passenger model is used which represents the passenger with a single mass element. Macro elements between mass element and seat structure represent

the seat cushion stiffness and the harness system. The seat structure is modelled with shell and beam elements. The seat-passenger model was calibrated based on experimental test data [110]. These test data comprise load-deflection curves of seat cushion and harness system as well as data about the seat structure. Figure 3-11 illustrates the simplified seat-passenger model used in the Kinematics Model.

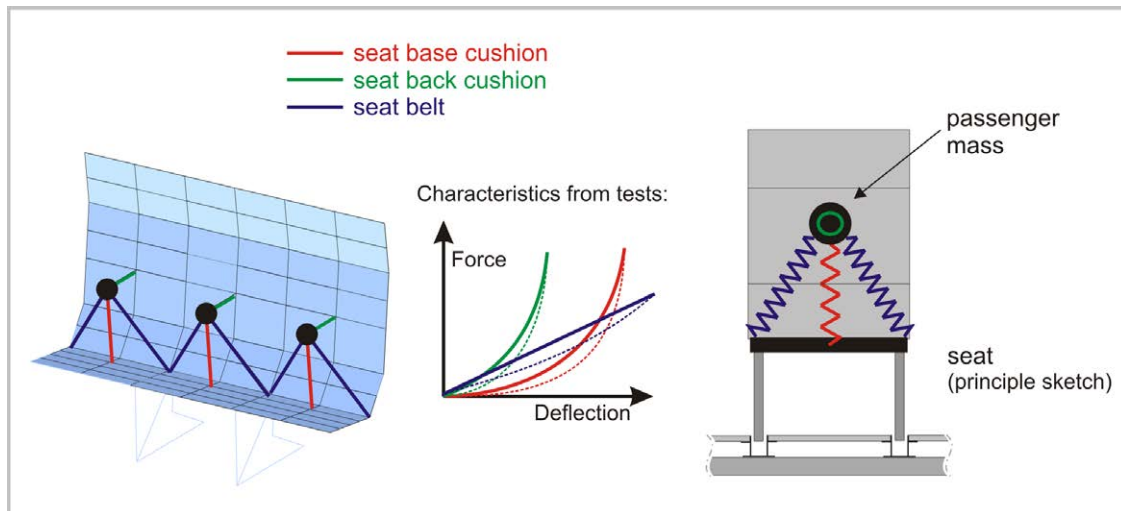


Figure 3-11: Simplified seat-passenger model (triple seat)

Occupant modelling with a single-mass element is an appropriate modelling technique for a preliminary design tool. Two of the above described injury criteria can be used in case of single-mass representation of occupants, the dynamic response index (DRI) as well as the Eiband criterion. Whereas the DRI defines one index value, a complete acceleration curve over the pulse duration provides more detailed information about the occupant loads. The DRI represents a better quantitative criterion, the Eiband curves provide the better qualitative criterion.

With respect to the assessment of crash scenarios the more qualitative Eiband criterion provides better information on the occupant loads. Hence, the Eiband whole-body tolerance curves of positive, vertical acceleration are used for the assessment of passenger loads in the Kinematics Model. This criterion is valid as the passengers typically experience one-dimensional loads in a drop test. In case of combined loading the Eiband criterion is not recommended as there are no tolerance curves for combined loading.

In the Eiband diagram plots of the vertical acceleration versus the pulse duration for the passenger masses are given. This 'acceleration - pulse duration' graph is compared with two Eiband curves of vertical loading direction, the limit curves to moderate and severe injury. This type of diagram gives a good overview on the load levels of different passengers and indicates potential injury. Figure 3-12 shows the principle of the Eiband diagram.

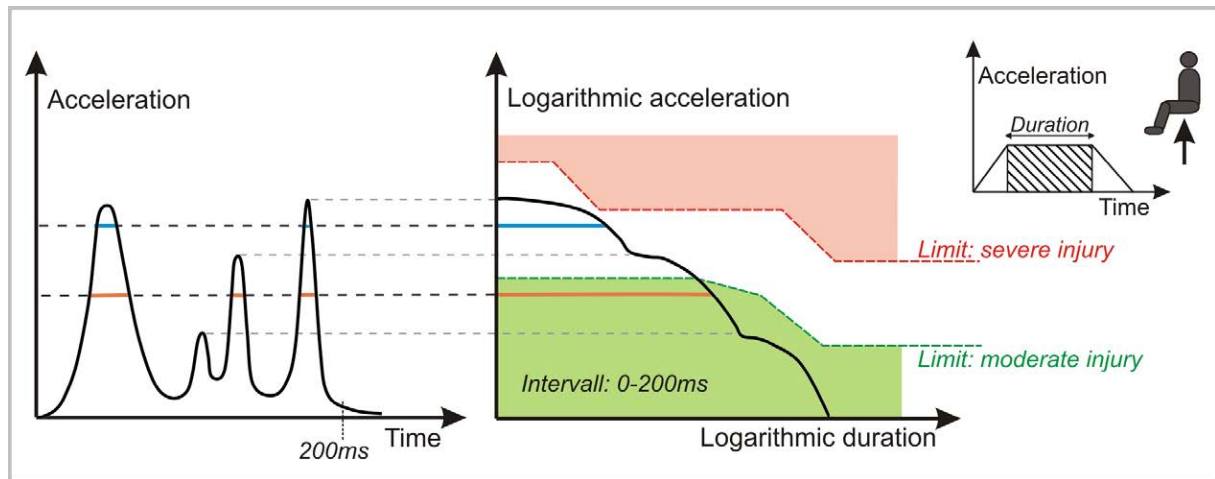


Figure 3-12: Principle of the Eiband diagram

3.4. Further modelling aspects

Further aspects of the modelling approach are discussed in the following sub-paragraphs and conclude the discussion of general aspects of the Kinematics Model approach.

3.4.1. Refinement of the sub-cargo area modelling

The representation of failure exclusively by macro elements with a linear-elastically modelled structure identified limitations in a first verification loop. In the area below the cargo-crossbeam, significant kinematic constraints were identified. In this sub-cargo area, a complex combination of crushing and other failure mechanisms leads to extensive failure of the sub-cargo structure. This effect is even more evident in case of a crash concept that specifies crushing of this structure using a comparably stiff cargo-crossbeam (bendframe concept). Such complex structural failure mechanisms cannot be clearly divided in categories of failure locations as well as of remaining undamaged structures. Damage and failure can occur along the whole lower frame structure. In addition, the stringer structure can be destroyed by the crushing of lower frame, cargo-crossbeam and the framework struts. If failure in this area is exclusively represented by macro elements which allow one-dimensional or two-dimensional failure modes, kinematic constraints may occur that influence the crash kinematics of the whole fuselage section. Such constraints are shown exemplarily in Figure 3-13. Although kinematic hinges are positioned in the lower frame structure, high compression forces lead to frame buckling which induces the formation of elastic hinges. Unrealistically high normal forces as well as a large amount of elastic energy which is stored in these parts falsify the crash behaviour of such a model.

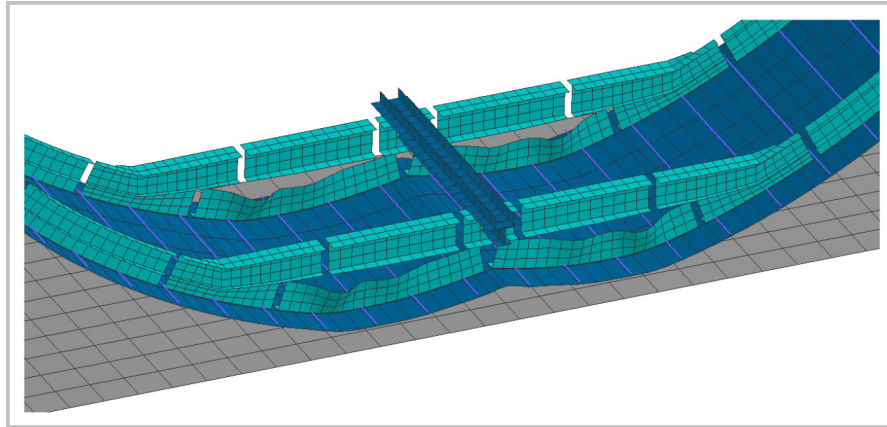


Figure 3-13: Kinematic constraints in the sub-cargo area with a kinematics modelling

A solution for this issue was found in a mixture of kinematics modelling and detailed FEM where the main crash characteristic of the sub-cargo area is furthermore described by macro elements. This solution represents all structural parts which could lead to kinematic constraints in a detailed modelling with material damage and failure. These parts are the fuselage skin, the stringers and the frames of the sub-cargo area. The remaining structure is modelled by the kinematics modelling approach described above. These are the cargo-crossbeam, the cargo floor and the framework of the sub-cargo area. Macro elements are positioned in the cargo-crossbeam to represent bending failure. The framework is modelled by macro elements which describe the failure mode and potential energy absorption of these struts. Figure 3-14 depicts the refined sub-cargo area, where structural details such as mouseholes in the frames are modelled, too. The stringers are modelled in detail using shell elements. The typical element size in this area is $L_e = 10 \text{ mm}$ which is about 50 % of the element size used in the Kinematics Model approach. The connection of the fuselage skin of sub-cargo area and upper fuselage part with its different mesh sizes is realised using a tied connection. In the frame a kinematic hinge is positioned at the transition of sub-cargo area and upper fuselage section. It is important to note that material damage and failure of the detailed modelled parts influence the crash kinematic of the fuselage section not in a significant way, except the avoidance of highly elastic loading which would lead to the kinematic constraints discussed above. The main crash behaviour of this area is still represented by macro elements.

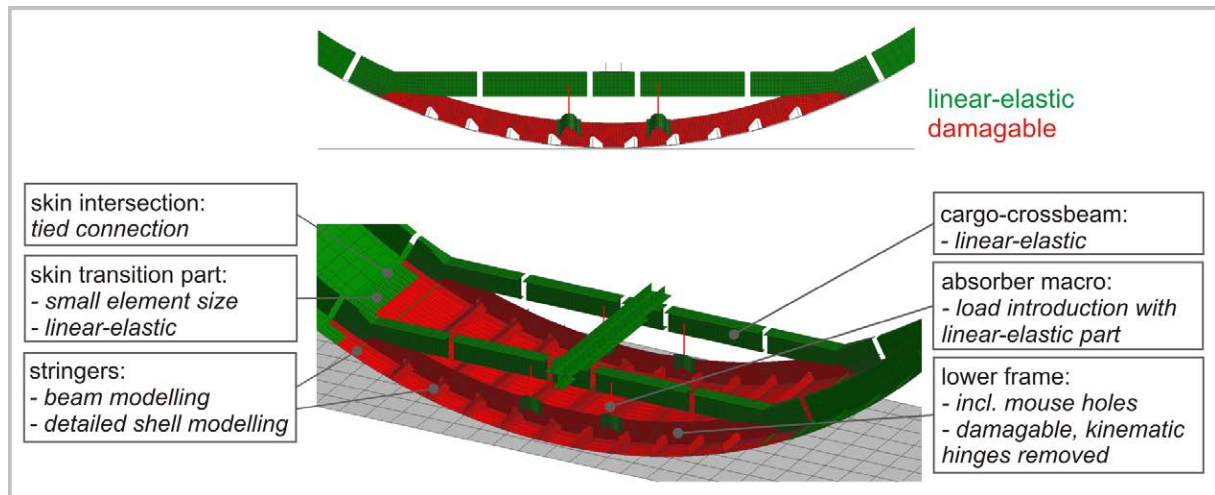


Figure 3-14: Mixed modelling in the refined sub-cargo area

3.4.2. Parameterisation of the Kinematics Model

One requirement for the development of the Kinematics Model is a flexible and effective assessment of crash concepts regarding global crash aspects on the fuselage section level. The assessment of crash concepts considers different load cases besides a reference crash case, the so-called ‘standard crash case’¹, to get information about the robustness of a crash concept. In addition, the development of a crash scenario implicates extensive adaptation of macro characteristics as well as of the fuselage structure.

Therefore, the input definition of the Kinematics Model is parameterised which comprises the model geometry but also the model properties which are the macro characterisation of the crash devices, the definition of loading cases for robustness analyses as well as the definition of numerical parameters.

With respect to the model geometry the mesh generation was embedded in the DLR in-house fuselage mesh generation tool SECTMESH, which is based on ANSYS APDL [103]. Additional subroutines were programmed to generate mesh modifications for the macro architectures of the Kinematics Model such as cuts in the frame and the crossbeam or generation of reference nodes for the macro elements. Another subroutine defines bar elements along the frames which are used for the measurement of strains, as discussed in paragraph 3.3. Further options were defined in additional subroutines such as renumbering of reference nodes for section output definition or the model refinement of the sub-cargo area.

¹ Within this thesis, the ‘standard crash case’ specifies impact conditions of a vertical impact with $v_i = 6.7$ m/s, fully loaded overhead bins, occupied seats, zero pitch and roll angle. Cargo loading is not considered in this case.

With respect to the model properties all essential input data for the FE solver were parameterised. Input data for macro element characterisation were defined using several parameters. By default, the tabular input of the primary loading curve offers 10 data points in each loading direction. The tabular input for the un-/reloading curve offers 7 data points. The parameterisation can additionally be used to define dependent parameters. Standard macro curve characteristics with main properties such as stiffness, trigger and absorption load can be specified. In an optimisation process these main properties can be used in the parameter variation whereas the tabular input parameters are calculated automatically.

With respect to the assessment of crash scenarios under different loading conditions, several loading parameters were defined such as passenger and overhead bin masses, the initial velocity, definition of cargo loading or the definition of roll angles.

In an exemplary analysis model of a single aisle 2-frame fuselage section with a total of 46 macro definitions, a total number of 870 parameters is used for the description of the model properties, exclusively discretisation parameters which are defined in SECTMESH.

4. Detailed investigation of frame failure modelling

The discussion of different macro models of crash devices in chapter 3.2 identified the frame bending as the most complex and most important failure mechanism of a fuselage structure under crash loads. Whereas other crash devices are located at specific structural connections or even represent complete structural parts, the macro architecture of the frame bending mechanism is highly integrated in the fuselage shell structure. Structural interactions which result from this high integration have to be represented accordingly by the macro architecture. In addition, the frame is the primary fuselage structure which is most affected in a crash event. Especially with regard to single-aisle aircraft a large amount of available crash height of the fuselage section is influenced by the frame. Approximately 70 % of a typical fuselage section crash height up to the vertical support struts is influenced by frame failure mechanisms. Only about 30 % of the crash height is influenced by the sub-cargo area.

Further investigations were performed to understand the structural behaviour of the frame under crash loads in more detail and to derive a macro modelling from these results that is accurate enough and appropriately defined for the usage in a preliminary design tool.

The present chapter deals with these investigations and will discuss several issues in the following paragraphs which affect the structural behaviour of the frame. Figure 4-1 gives an overview on the investigations and the corresponding paragraphs of this chapter. The outcomes of these investigations were integrated into the final kinematic hinge macro architecture which is discussed in paragraph 4.7.

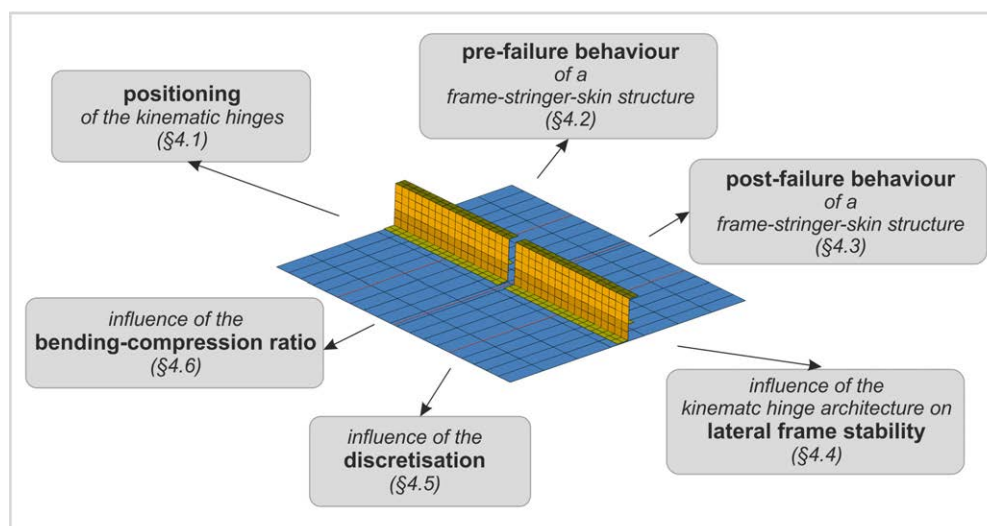


Figure 4-1: Overview on the investigations presented in chapter 4

4.1. Positioning of the ‘kinematic hinges’

Frame bending failure is a mechanism which is generally not limited to specific locations but can occur at positions along the whole frame. In contrast to this frame mechanism with firstly unclear distributed failure locations, all other macro elements discussed in chapter 3.2 represent individual crash devices with a clearly defined location. Axial crush absorbers represent crash devices in the sub-cargo framework or in the vertical support struts. The macro model for cargo-crossbeam failure is typically located in a centre position where the highest moment load is expected. And finally the crash device of a passenger crossbeam connection is located at the connection points to the frame.

The unclear distribution of potential frame failure locations affects the positioning of the kinematic hinges in the fuselage section model which represent such frame bending failure mechanisms. To resolve this uncertainty typical frame failure behaviour was analysed to conclude to potential frame failure locations in a fuselage section. A combined procedure was established for this investigation. Firstly, typical failure locations were identified by an empirical method that evaluates the frame failure behaviour of fuselage sections which were drop tested in the past. Secondly, an additional analytical method was used to conclude to potential frame failure locations of individual fuselage section designs by numerical simulation. In the scope of this thesis, the procedure considers a typical transport fuselage design of narrow-body aircraft size.

In the empirical method, typical frame failure locations were identified by the evaluation of fuselage section drop tests which were performed in the last decades [15-19,24-26,30-31]. Figure 4-2 shows exemplary results of some of the evaluated drop tests. Different loading conditions were considered in this empirical evaluation. Besides the fully loaded condition of seats and overhead bins, partly occupied conditions as well as several cargo loading conditions were tested in the considered drop tests. In addition, different initial velocities between $v_1 = 6.1$ m/s (20 ft/s) and $v_2 = 9.1$ m/s (30 ft/s) were regarded. Finally, the evaluated drop tests provide fuselage structures of different designs. For instance, the shape of a B707 fuselage, Figure 4-2a)-d), provides less curved side shells compared to an A320 fuselage, Figure 4-2f). Furthermore, the B707 and B737 fuselages, Figure 4-2a)-e), are designed without vertical support struts whereas the A320 and the YS-11 fuselages provide such struts¹. Variations of the general fuselage section size are given by the difference of B707, B737, A320 and YS-11 cross-sections, in the scope of

¹ Further detailed investigations about the influence of the support strut position on the location of a plastic hinge formation are given in [115].

narrow-body fuselage designs. Further variations in the fuselage design exist by additional cargo door or tapered rear fuselage section.

In the scope of the regarded narrow-body fuselage size, this range of considered fuselage section designs under vertical crash loads provides a sufficient empirical basis for the definition of potential frame failure locations of typical fuselage structures, which are depicted in Figure 4-2i). According to this empirical basis, typical main frame failure occurs below the passenger crossbeam between an angle of $\alpha_3 \approx -50^\circ$ and $\alpha_3 \approx +50^\circ$. In this area, the frame failure locations strongly depend on the crash scenario. Gathering all failure locations independent of the crash scenario the locations in this area are the following: At $\alpha_3 \approx \pm 50^\circ$ typical frame failure occurs in a closing motion. This is close to but below the location of the vertical support strut, if such a strut is defined in the fuselage design. Without vertical support strut, frame failure typically occurs at a same position. Further failure location was observed below α_3 , near the connection of the cargo-crossbeam at an angle of about $\alpha_2 \approx \pm 25^\circ$. This failure is typically of opening motion. Finally, typical frame failure occurs in the lower centre potentially together with failure of the cargo-crossbeam at an angle of $\alpha_1 \approx 0^\circ$. This failure at the point of the first impact is of opening motion.

In most of the considered tests, failure between $\alpha_3 \approx \pm 50^\circ$ and $\alpha_7 \approx \pm 90^\circ$ was not observed. In this area, frame failure may occur in case of higher energetic crashes or other specific load cases. In case of frame failure in this area, three potential failure locations have to be considered. The first one is located directly below the passenger crossbeam connection at $\alpha_6 \approx \pm 85^\circ$. The second location is at an angle of about $\alpha_5 \approx \pm 65^\circ$. The third location is very close to α_3 but above a potential vertical support strut at $\alpha_4 \approx \pm 55^\circ$. Dependent on the fuselage design α_4 can coincide with α_3 . The potential crash kinematics develops such that at α_6 opening frame bending occurs and accordingly at α_5 closing frame rotation. Hence α_4 is of opening motion. An example of this frame failure formation is given in Figure 4-2e) at the right lower fuselage shell. In general, this local crash kinematics depends strongly on the fuselage design as well as the loading condition. Under specific conditions this local kinematics can develop with inverse frame bending rotations at $\alpha_4 - \alpha_6$.

The drop test results of the A320 fuselage structure, Figure 4-2f), show additional frame failure which is located directly above the passenger crossbeam at an angle of about $\alpha_8 \approx \pm 95^\circ$. Such a frame failure mechanism is highly influenced by the passenger crossbeam. In case of the A320 section drop test, the crossbeam failed and induced high moments in the frame location near the crossbeam connection. A further potential failure location of the frame is the region below the overhead bins at an angle of about $\alpha_9 \approx \pm 145^\circ$. In this area, the inertia loads of the stowage bins

induce high stresses in the frame. At the A320 frame structure, shown in Figure 4-2f), as well as at the B737 frame structure, given in Figure 4-2e), frame failure was identified in this area. Finally, another potential failure location is the upper central area of the fuselage structure at $\alpha_{10} \approx 180^\circ$. Load oscillations caused by the overhead bin mass on both sides of the fuselage section as well as by the overall crash kinematics can superpose in this area and subsequently exceed the frame strength.

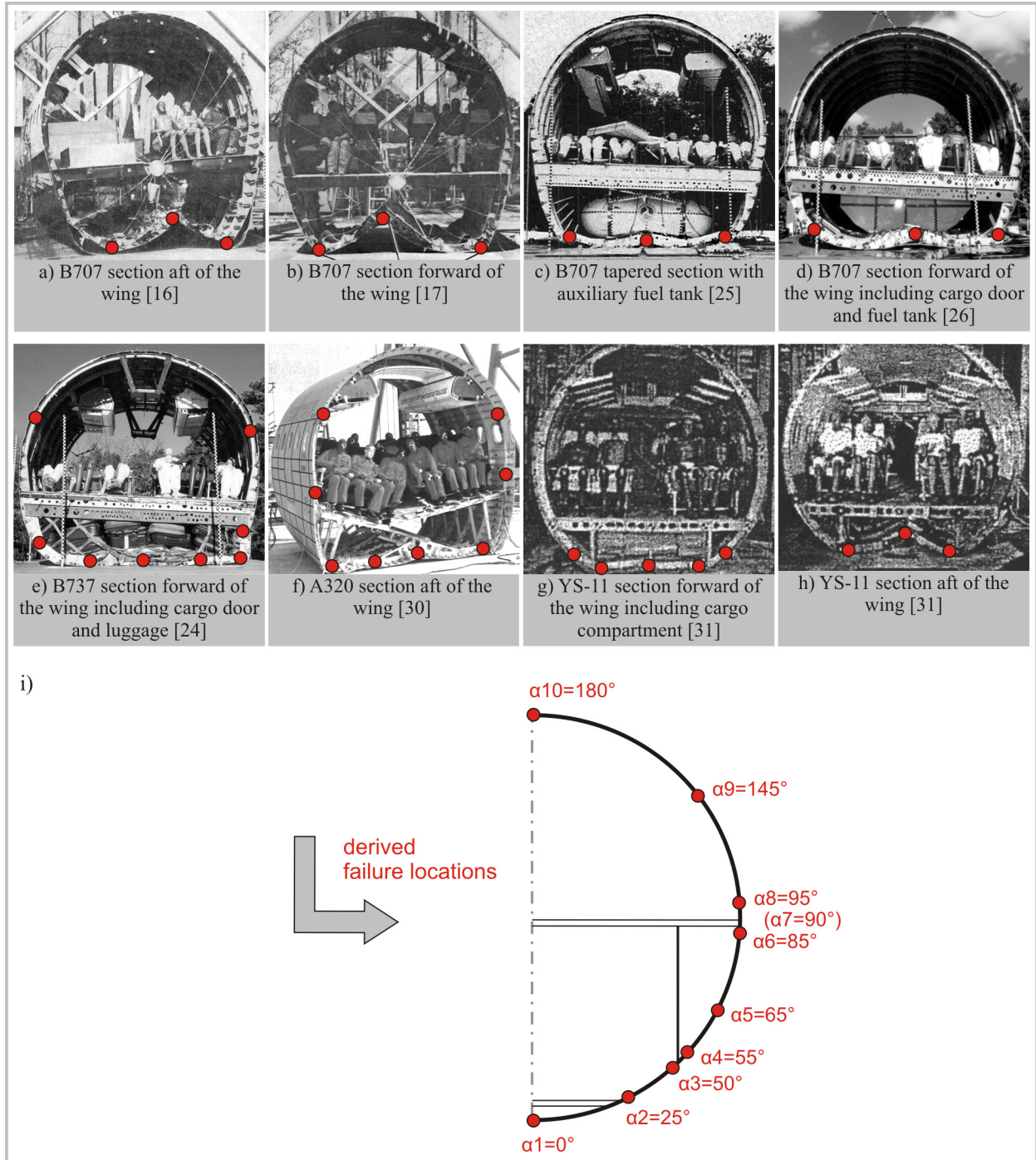


Figure 4-2: Frame failure locations of typical fuselage section drop tests

The considered fuselage section drop tests of this empirical evaluation represent fuselage structures exclusively of metallic material. Until now, there is no full-section structure made of

CFRP material which was drop tested. Nevertheless, and as mentioned in chapter 2, research work done on CFRP structures in the past, identified frame failure locations which are similar to metallic fuselage structures. In the following, the test results of the research work on composite frame structures are evaluated additionally in the scope of this empirical method.

Valuable results with respect to potential failure locations of composite frames were obtained by several tests on frame components in the scope of a joint NASA-US-Army programme [46-51]. Generic CFRP frame structures with a diameter of $D = 1.8 \text{ m}$ (6 ft) were tested statically and dynamically. Single frame tests were performed with different configurations and loading conditions. The configuration of the centre restraint which simulated the passenger crossbeam varied significantly. Steel cables simulated exclusively tensile restraint, aluminium tubes effected also constraint in compression load direction. Another variant with massive steel bars provided additional restraint of rotations in the passenger crossbeam connection. In this case bending moments were carried by the crossbeam. Different impact velocities between $v_1 = 6.1 \text{ m/s}$ (20 ft/s) and $v_2 = 8.4 \text{ m/s}$ (27.5 ft/s) as well as different added masses between $m_1 = 9.1 \text{ kg}$ and $m_2 = 45.4 \text{ kg}$ were defined in the tests. The masses were installed at the crossbeam. The location of splice plates which connected four 90° -frame components to a circumferential frame was positioned either at $\beta_1 = 0^\circ/90^\circ$ or at $\beta_2 = \pm 45^\circ$. The frame structures were constrained during the test in lateral direction to avoid out-of-plane bending.

In Figure 4-3 some of these results are summarised. Figure 4-3a) depicts failure locations of a static single frame test which was performed with splice plates at $\beta_1 = 0^\circ/90^\circ$ and a massive steel bar as centre restraint. The first frame failure occurred in the lower centre at an angle of $\alpha_1 = -18^\circ$ and $\alpha_1 = 7^\circ$. Typically, one failure location is expected in this lower centre area. The occurrence of two failure locations was potentially caused by the splice plate at $\beta_1 = 0^\circ$ which influenced the failure mechanism in this area. Further frame failure occurred at $\alpha_2 = -58^\circ$ and $\alpha_2 = +54^\circ$.

The dynamic single frame tests with steel bar as centre restraint (two tests) were conducted with higher kinetic energy. The resulted failure locations are given in Figure 4-3b) & 4-3c). With the same initial velocity, both frame tests differ in the mass which was additionally installed at the steel bar. In the first test of frame #4, an added mass of $m_{\#4} = 45.4 \text{ kg}$ (100 lbs) was installed. In the second test of frame #5, an added mass of $m_{\#5} = 42.2 \text{ kg}$ (93 lbs) was mounted on the steel beam. In these tests, first frame failure occurred in the lower centre at $\alpha_1 = +1^\circ$ (frame #4) respectively at $\alpha_1 = +6^\circ$ (frame #5). Further failure developed at $\alpha_2 = -59^\circ$ and $\alpha_2 = +68^\circ$ (frame #4) respectively at $\alpha_2 = -62^\circ$ and $\alpha_2 = +62^\circ$ (frame #5). In frame #4 additional failure occurred at $\alpha_2 = +38^\circ$. In both frames the splice plates were positioned at $\beta_2 = \pm 45^\circ$. Hence, all second frame failures are located above respectively directly below a splice plate.

In addition to the single frame tests, static and dynamic tests of sub-floor sections with similar frame size were performed. Skeleton sections (frames and stringers) and a skinned floor section (frames, stringers and skin) were tested in a two-bay configuration (3-frames). The splice plates were located in these tests at $\beta_1 = 0^\circ$. The skeleton tests showed mainly consistent frame failure locations in the static and dynamic test. Regarding the dynamic test, the resulted failure locations are depicted in Figure 4-3d). The first failure was located in the lower centre at an angle of $\alpha_1 = +11.3^\circ$. The second failure occurred at $\alpha_2 \approx \pm 45^\circ$. Further failure was located at an angle of $\alpha_3 = \pm 78.3^\circ$ for the dynamic test. In the static test this third failure location occurred one-sided. In general, the skeleton tests were influenced by out-of-plane bending and twisting, as boundary conditions were not defined to constrain these motions. This circumstance as well as the absence of the skin led to extensive failure of the skeleton with a third failure location.

Compared to the skeleton tests the skinned section test results showed less distinct failure behaviour. After a non-destructive static test, the destructive dynamic test identified three frame failure locations at the skinned section, which are illustrated in Figure 4-3e). The first failure in the lower centre is located at $\alpha_1 = +11.3^\circ$. Further failure developed at $\alpha_2 = \pm 56.3^\circ$. The first frame in the front of the skinned section differed from these failure locations as the section first impacted in the front with a slight pitch angle.

All frame failures of skeleton and skinned section started at notched stringer locations. The normalized circumferential strain values measured at the outer and inner frame flange showed similar strain distributions for skeleton and skinned section. The circumferential strain values of the dynamic test of the skinned section are given in Figure 4-3f). These strain distributions clearly show the locations of potential frame failure. In the lower centre at $\alpha_1 = 0^\circ$ strain maximum at the inner frame flange and strain minimum at the outer frame flange indicate potential frame failure in the opening direction. Between $\alpha_2 = \pm 50^\circ$ and $\pm 55^\circ$, strain minimum at the inner frame flange and strain maximum at the outer frame flange identified potential frame failure in closing direction.

Summarising these test results of the CFRP frame components, main failure regions can be identified as depicted in Figure 4-3g). In the lower centre, opening frame bending failure is located between $\alpha_1 = \pm 12^\circ$. Above, closing hinge locations are located between $\alpha_2 = \pm 45^\circ$ and $\pm 60^\circ$. Frame components with splice plates located at $\beta_2 = \pm 45^\circ$ showed closing hinge locations above the splice plates at slightly increased angles up to $\alpha_2 = \pm 68^\circ$. The third failure location of the skeleton tests indicates potential frame failure behaviour in cases of higher energetic crashes similar to the aforementioned discussions on the metallic fuselage section level.

In general, the discussion of drop test results of CFRP frame and subfloor structures identified similar frame failure locations as observed in the evaluation of metallic fuselage section drop test results. However, the fuselage sections represent significantly more structural details compared to the considered generic CFRP structures wherefore further failure locations were identified in the evaluation of fuselage section drop test results.

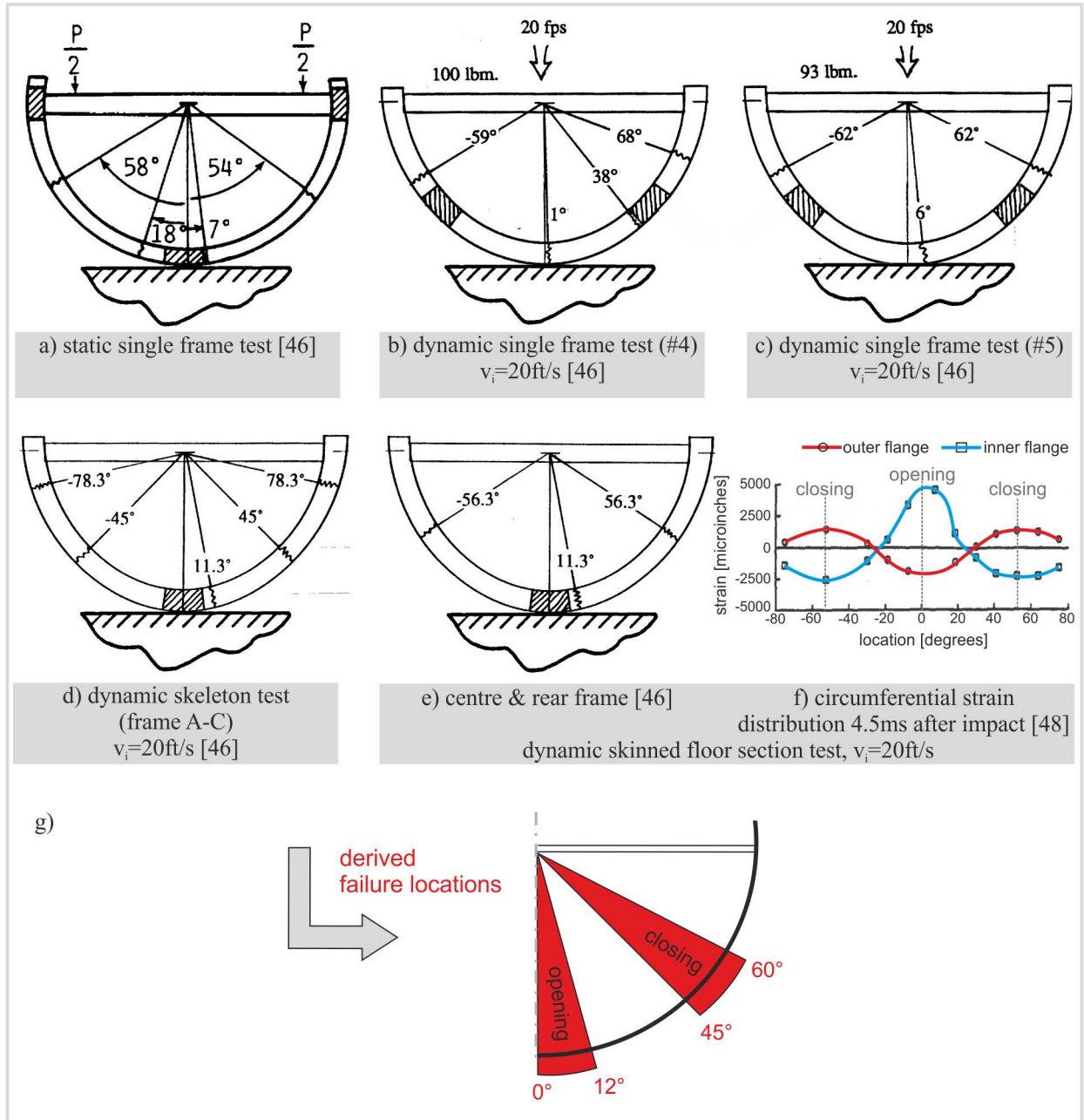


Figure 4-3: Frame failure locations identified in the CFRP frame component tests

The empirical method of evaluating test results concluded to frame failure regions of typical fuselage structures. With respect to the positioning of kinematic hinges in a fuselage section model more accurate information is required to determine detailed hinge locations, especially with respect to individual fuselage designs. This requires a further analytical method to conclude to detailed locations and to position the kinematic hinges accordingly. In the analytical method

the circumferential strain along the frames is measured in the fuselage section model. In a first step, the Kinematics Model is calculated without any kinematic hinge in the linear-elastically modelled frames. Figure 4-4 illustrates results of such a model variant at $t = 20$ ms after the first impact. The graphs show the strain distribution of the inner and outer frame flange in the critical fuselage side shell. The strain distributions show an extremum at $\alpha_3 = -41^\circ$ and $\alpha_3 = +42^\circ$ which indicate potential closing hinge failure. In the further procedure of this analytical method, additional kinematic hinges can be positioned at locations where strain exceeding occurs respectively where the strain distribution of inner and outer frame flange indicates potential failure.

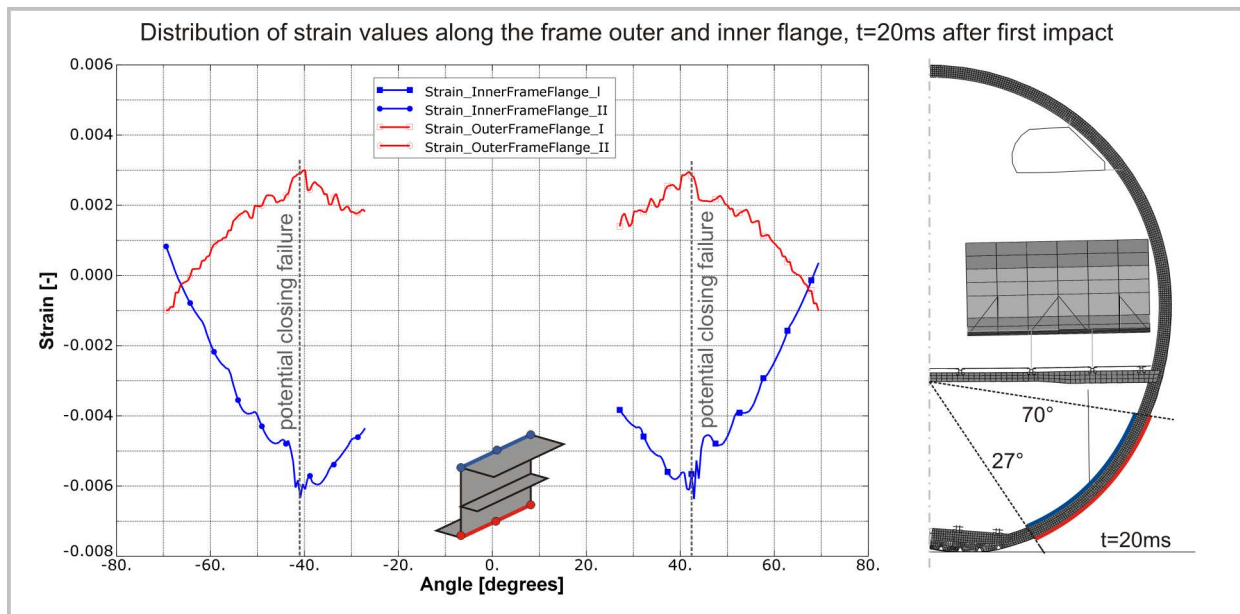


Figure 4-4: Determination of potential frame failure locations by simulation

Summarising the investigation on the positioning of the kinematic hinges, an evaluation of several fuselage section drop test results was conducted to conclude from experimental results of realistic structures to typical frame failure locations. A further evaluation of drop tests of generic CFRP frame components identified comparable failure behaviour of metallic and CFRP frame structures, with respect to the failure locations. Hence, the outcomes of the above discussed evaluation of section drop tests of metallic fuselage sections can be transferred to the consideration of CFRP fuselage structures.

With respect to a detailed positioning of kinematic hinges in the Kinematics Model an analytical method was demonstrated. In this method, the strain distribution along the frame is measured to conclude to potential frame failure locations. This approach allows to determine failure locations of the specific fuselage design that is considered.

4.2. Pre-failure behaviour of a frame-stringer-skin structure

The behaviour of a frame structure up to failure initiation shows significant influence in crash events of fuselage structures and has to be considered in crash analyses accordingly. Therefore, the pre-failure behaviour of a generic frame-stringer-skin structure was analysed with respect to two problem definitions. Firstly, the elastic behaviour of such a structural component was investigated to define a macro architecture that enables an appropriate elastic representation. Secondly, potential structural instabilities of a frame-stringer-skin structure were considered to derive simplified failure criteria. These criteria can be used in the Kinematics Model to define trigger values for the kinematic hinges as well as to determine reserve factors or potential exceeding in the frame structure apart from the kinematic hinges.

Both problem definitions were investigated numerically with a generic frame-stringer-skin model. Several reasons led to the decision to concentrate on numerical simulation and not to consider analytical methods. One reason is the effective width of the skin that contributes to the global bending stiffness and which is complex to be determined analytically. There are formulations which define an effective width for high bending beams, such as a frame-skin component, assuming a constant stress-based effective width along the beam [140]. However, such assumptions can lead to discrepancies in the stiffness calculation and in the definition of the elastic centre. Other reasons which contributed to the abandonment of analytical methods are structural details that significantly influence the elastic behaviour but cannot easily be considered in an analytical approach. Such details are mouseholes in the outer frame web as well as cleats which provide lateral frame support.

The numerical model that was used in this investigation is illustrated in Figure 4-5a). A detailed description of the model is given in Appendix A2.1. To identify the structural behaviour in dependence of different frame stiffness, several LCF-shaped frame designs were analysed. The considered frame designs represent extreme cases with respect to the expected stability behaviour of different frame stiffness and comprise variations of frame height as well as of frame thickness. The four extreme cases which were analysed numerically are depicted in Figure 4-5b) – 4-5e). The smallest frame section, Figure 4-5e), represents a statically pre-sized frame design of a generic CFRP standard fuselage with respect to the complete envelope of flight and ground load cases, which was given by the project partner Airbus. Increased frame stiffness has to be potentially provided for a robust crash design. Hence, this investigation also considers massive frame designs and covers the full spectrum of frame profiles which are expected to be used in the scope of a crash design for a CFRP fuselage structure.

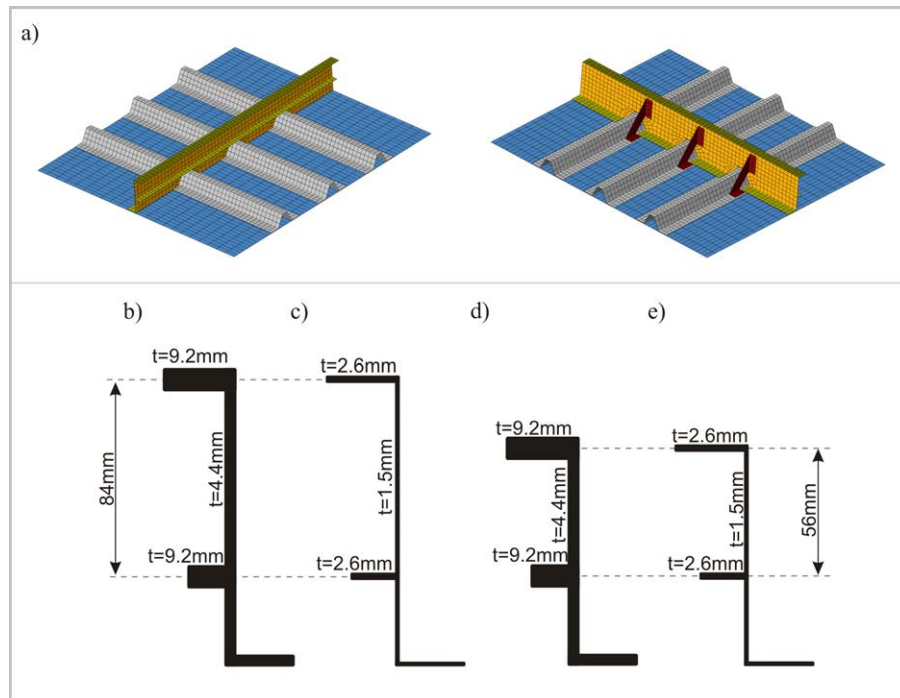


Figure 4-5: Numerical investigation of a frame-stringer-skin structure

4.2.1. Potential failure initiations of a frame-stringer-skin structure loaded under pure bending

In a first investigation potential failure initiations were considered to derive simplified failure criteria for the Kinematics Model. Thin-walled structures are typically affected by stability limits. Hence, structural instabilities have to be considered besides limitations of material strain. Three main instability failure initiations were identified and analysed. Figure 4-6 shows simulation results which illustrate these instability modes and which are discussed in the following.

In case of closing frame bending the inner frame flange is loaded in compression with a risk of potential instability in this structural part. Analyses results discussed later in paragraph 4.2.1 will show, that the inner frame flange and the middle frame flange are loaded in the same direction for all considered LCF-shaped frame designs. According to the stress distribution of the moment-loaded frame cross-section, the inner frame flange is generally loaded more critically compared to the middle frame flange and local instabilities are expected at this inner flange. Figure 4-6a) illustrates the frame-stringer-skin component, with a filigree frame design according to Figure 4-5e), in a closing bending mode. Buckling of the frame inner flange is obvious. In addition, the interaction of frame inner flange buckling and frame inner web buckling is visible. The diagram depicts the longitudinal strains along frame inner, middle and outer flange. Additional strain output is given for the outer side of the frame inner flange. Bar elements for strain measurement were positioned between the flange nodes along the whole

frame. Good correlation of strain values in the individual flanges illustrates the constant moment load along the frame. After a linear increase the initiation of buckling is clearly indicated in the frame inner flange strains. The strains along the outer side of this flange reduce whereas further increase of strain occurs at the web side of the inner flange. Oscillations in the curves after initiation of buckling are caused by dynamic effects. As the simulations were performed using explicit time integration, the moment load was applied dynamically to limit the total simulation time.

A further instability mode is lateral frame buckling which can occur in case of stiff frame designs under closing moment loads. Figure 4-6b) shows global lateral frame buckling in the frame-stringer-skin model with the highest frame stiffness considered in this investigation according to Figure 4-5b), despite of cleats which provide lateral frame support. In the diagram of Figure 4-6b) the strains indicate the initiation of frame buckling in a fan-shaped curve progression along the frame inner flange, at inner and outer side of this flange. The strain distribution clearly illustrates a most critical loading of the inner frame flange for this instability mode. According to this strain distribution, tensile failure in the frame outer flange is not expected. Instead, failure of the highly loaded cleats has to be considered that would lead to the loss of lateral frame support inducing a significant increase of lateral frame buckling. Load shifting in the frame inner flange that occurs in conjunction with extensive lateral frame buckling leads to increased strain values at the web side of the inner flange. Hence, potential failure of the lateral support would lead to more distinct lateral frame buckling and subsequently can be observed as instability of the web-sided frame inner flange strain.

The third instability mode that was identified and analysed with the numerical model is skin buckling which can occur under opening bending loads. In this loading condition, the frame inner flange is loaded in tension whereas the frame outer flange respectively the skin is loaded in compression. Figure 4-6c) shows the frame-stringer-skin model in an opening bending mode with extensive skin buckling. The initiation of this instability mode is observable by (dynamic) oscillations in the strain graphs along frame inner, middle and outer flange. In general, buckling of the skin is allowed and does not necessarily lead to failure initiation. But in case of extensive skin buckling other failure effects can be initiated. The rivet connections of stringer and frame to the skin are at risk. In addition, potential crippling failure of the frame outer flange has to be considered. Furthermore, after initiation of buckling in the skin potential failure could occur in the frame outer web which is weak because of the mousehole sections. These potential failure modes can be covered by a strain limit criterion of the longitudinal frame outer flange strain. In a preliminary design phase such a strain based failure criterion can not be derived from detailed

failure effects as such detailed structural data are usually not available. Hence, a simplified criterion has to be defined to cover such potential failure modes in an appropriate way. This criterion considers the crippling strain limit of the frame outer flange and defines this value as maximum allowed strain along the outer frame flange.

In Figure 4-6c) the strain distribution shows a frame inner flange that is loaded much higher in opposite load direction than the frame outer flange. Hence, tensile strain limit in the frame inner flange has to be considered in addition to the crippling strain limit of the frame outer flange in case of opening bending.

Summarising the discussion of potential failure initiation modes of a frame-stringer-skin structure, the identified structural behaviour can be checked for potential failure by appropriate criteria regarding the strains at the frame inner and outer flange. Based on the required accuracy for a preliminary design tool, the strain values measured in these flanges can be checked for (compressive) crippling strain limits as well as for (tensile) material failure strain limits. These criteria are used in the Kinematics Model to identify potential failure of the frame respectively to define appropriate trigger criteria for the kinematic hinge macros.

The above discussion of potential failure modes is based on numerical investigations which consider pure moment loads. Paragraph 4.6 considers the influence of additional load components in normal direction. Nevertheless, the validity of the above defined failure criteria can be extended similarly to combined bending-compression loads. Regarding the frame cross-section under combined loads, the most critical region will similarly be at the frame inner and outer flange. Especially with respect to typical LCF-shaped frame designs the middle flange is designed similar to the inner flange and therefore remains less critical.

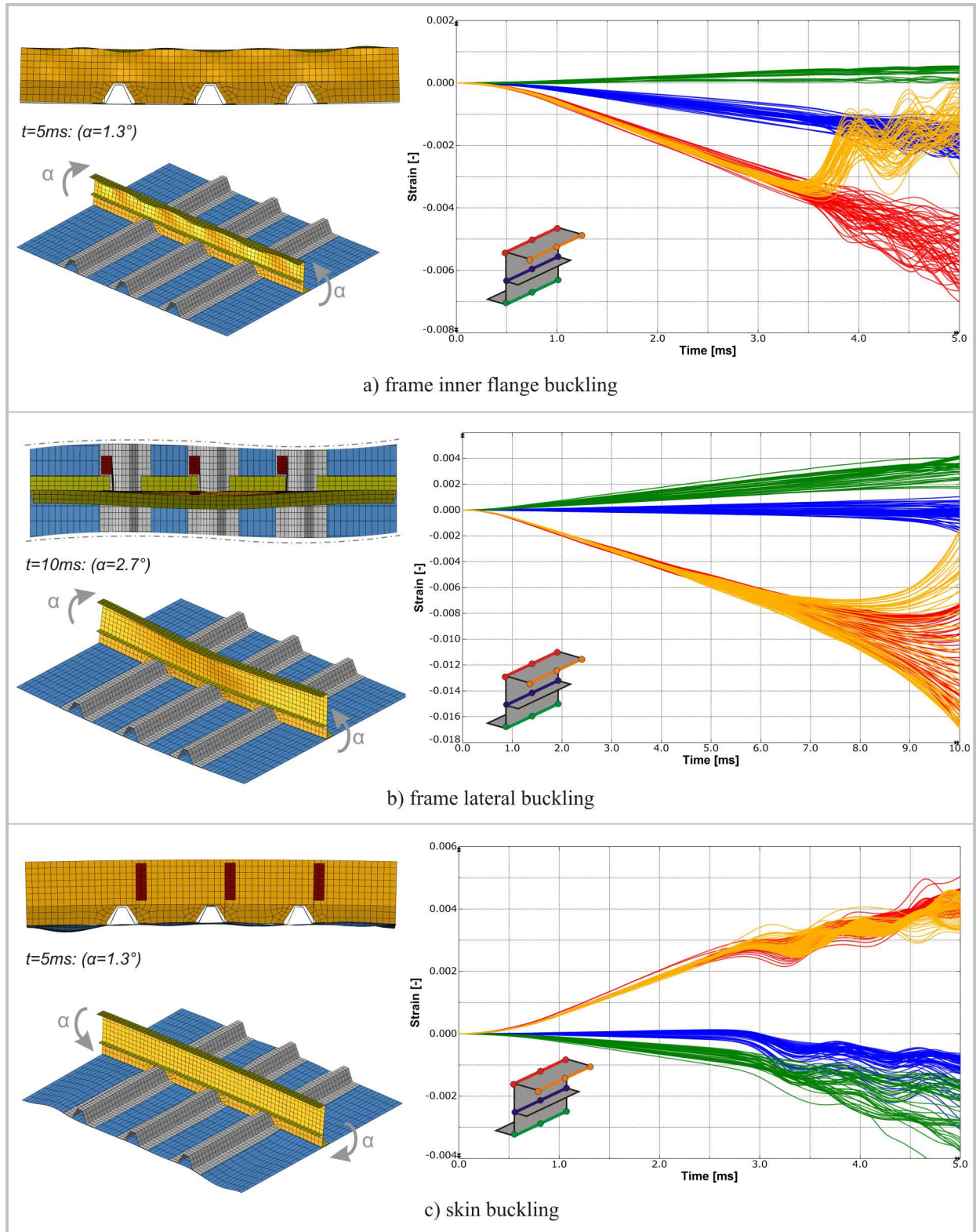


Figure 4-6: Consideration of instability modes of a frame-stringer-skin structure

4.2.2. Elastic behaviour of a frame-stringer-skin structure

A further investigation in the scope of the pre-failure analysis of a frame-stringer-skin structure regarded the elastic behaviour up to failure, to derive an appropriate kinematic hinge architecture from the identified characteristics. Considering again the four extreme cases of LCF-shaped

frame designs, the numerical frame-stringer-skin model was analysed regarding the strain distribution over the frame height to conclude to the elastic centre of the frame-stringer-skin component in dependence of the frame stiffness. The numerical model corresponds to the one used in paragraph 4.2.1 and is described in detail in Appendix A2.1.

The macro architecture as described in chapter 3.2 defines the frame bending mechanism by the rotational degree of freedom of the macro element. With respect to the elastic behaviour of a frame-stringer-skin structure under bending load, the pivot point of this rotation has to be positioned in the elastic centre to ensure accurate representation by the macro architecture.

Pure bending load is considered in this investigation although the typical crash load in a fuselage frame structure is a combined moment-compression load. The normal load ratio in a combined loading shifts the neutral axis compared to pure bending loading, nevertheless the bending mode acts with respect to the elastic centre. Applying a pure moment load on the frame-stringer-skin model, the neutral axis corresponds with the elastic centre. Hence, the location of the elastic centre can be identified directly by the consideration of the longitudinal strains in the frame flanges.

Figure 4-7 illustrates the ‘average strain - rotation’ graphs of the frame-stringer-skin model with the four frame designs, which were presented in Figure 4-5b) – 4-5e). The average strain is the average value of all strain bar elements along the frame. Hence, the set of strain curves for each frame flange, as illustrated in Figure 4-6, is replaced by their average value. The rotation which is plotted in the diagrams corresponds to the rotation angle that is applied at each end of the model. Thus, the bending angle is of twice this value. Strain graphs are depicted for opening and closing bending motion.

In all four diagrams of different LCF-shaped frame stiffness in Figure 4-7 a symmetrical strain distribution can be identified for opening and closing bending in the range of linear-elastic behaviour. In Figure 4-7a) the strain magnitude in the frame outer flange is very small. With this frame design of typical static sizing the elastic centre is close to the skin. Looking at cases with an increased frame stiffness, Figure 4-7b) and 4-7c) show the elastic centre between frame outer and middle flange. Figure 4-7d) represents the massive frame design with a total frame height of $h_F = 120$ mm and a flange thickness at the inner and middle flange of $t_{IFF/OFF} = 9.2$ mm. Such an extreme frame design shifts the elastic centre to the frame middle flange as it is obvious in this diagram. Here, the strain magnitude in the frame middle flange is close to zero.

An important outcome of this comparison is the fact that regarding all conceivable LCF-shaped frame designs the elastic centre is positioned between frame outer and middle flange. Consequently, the inner and middle flange is loaded in all considered variants in the same

direction and leads to a generally more critically loaded inner flange. With respect to the discussion of potential failure initiations in paragraph 4.2.1, this result proves the definition of failure criteria which are based purely on the consideration of failure at outer and inner frame flange.

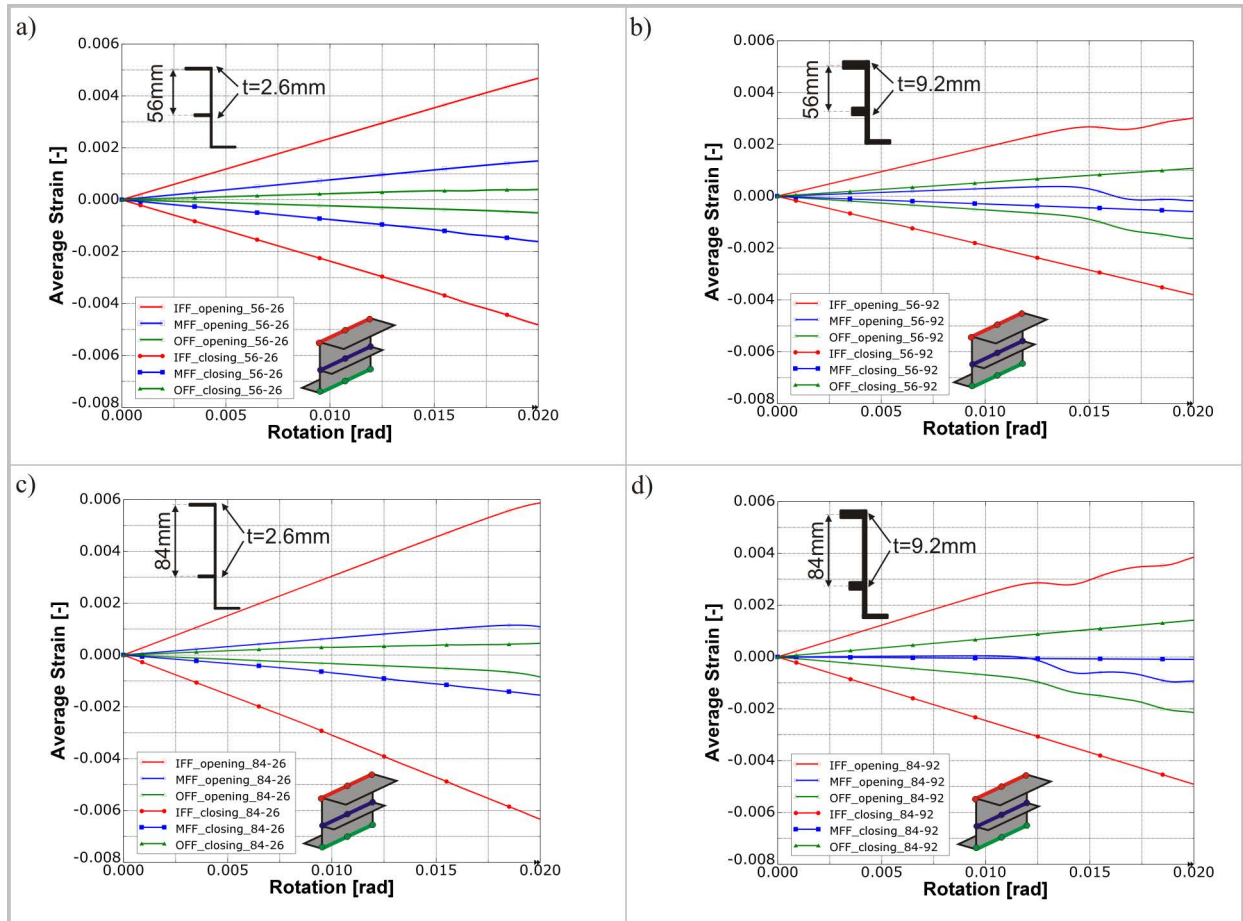


Figure 4-7: Longitudinal strain distribution in a frame-stringer-skin component with different frame stiffness

As a further result, the graphs in Figure 4-7 illustrate the dependence of the elastic centre position on the frame stiffness, which is in the range between outer and middle flange. Whereas the typical frame design of a static sizing has its elastic centre located very close to the skin, the most massive frame design holds its elastic centre close to the frame middle flange. Regarding the kinematic hinge architecture the positioning of the macro element would depend on the frame stiffness if the elastic bending should be represented accurately with respect to the elastic centre.

Such an accurate representation of the pre-failure behaviour is one requirement of the kinematic hinge architecture. A further requirement is a realistic representation of the post-failure behaviour. The following paragraph 4.3 discusses the post-failure bending mechanism of a frame-stringer-skin structure and identifies a mandatory position of the bending pivot point that is located in the skin plane. Considering both, the pre-failure and the post-failure representation

of a frame-stringer-skin bending mechanism, a compromise was defined which specifies the macro element position in the skin plane. With this approach the pre-failure behaviour is described accurately for typical frame designs and sufficiently for massive frame designs. The post-failure bending mechanism is represented accurately independent from the frame stiffness.

Based on this kinematic hinge architecture with a bending rotation axis that is located in the skin plane, a method had to be defined to calibrate the elastic stiffness of the macro element. As mentioned at the beginning of paragraph 4.2, the analytical analysis of the elastic behaviour of a frame-stringer-skin structure is not trivial. To enable an efficient method for the calibration of the kinematic hinge bending stiffness, the macro element is calibrated numerically with respect to the strain along the frame inner flange. Analogously to the strain bar elements along the frame flange, the bending stiffness of the kinematic hinge is measured with a strain bar element that bypasses the cut of the kinematic hinge in the frame. Figure 4-8 compares these strain values and plots the strain along the frame inner flange as well as of the kinematic hinge. The illustrated simulation models in Figure 4-8 show a simplified structural model according to the Kinematics Model approach. This procedure of equal discretisation level ensures the calibration of the kinematic hinge similar to the simplified represented frame structure of the preliminary design tool. The diagrams in Figure 4-8a) and 4-8b) of typical and massive frame design illustrate a good correlation of frame structure and calibrated kinematic hinge. Good correlation was achieved similarly for the massive frame design with an elastic centre of the surrounding frame structure that is located near the frame middle flange whereas the macro element is positioned in the skin plane.

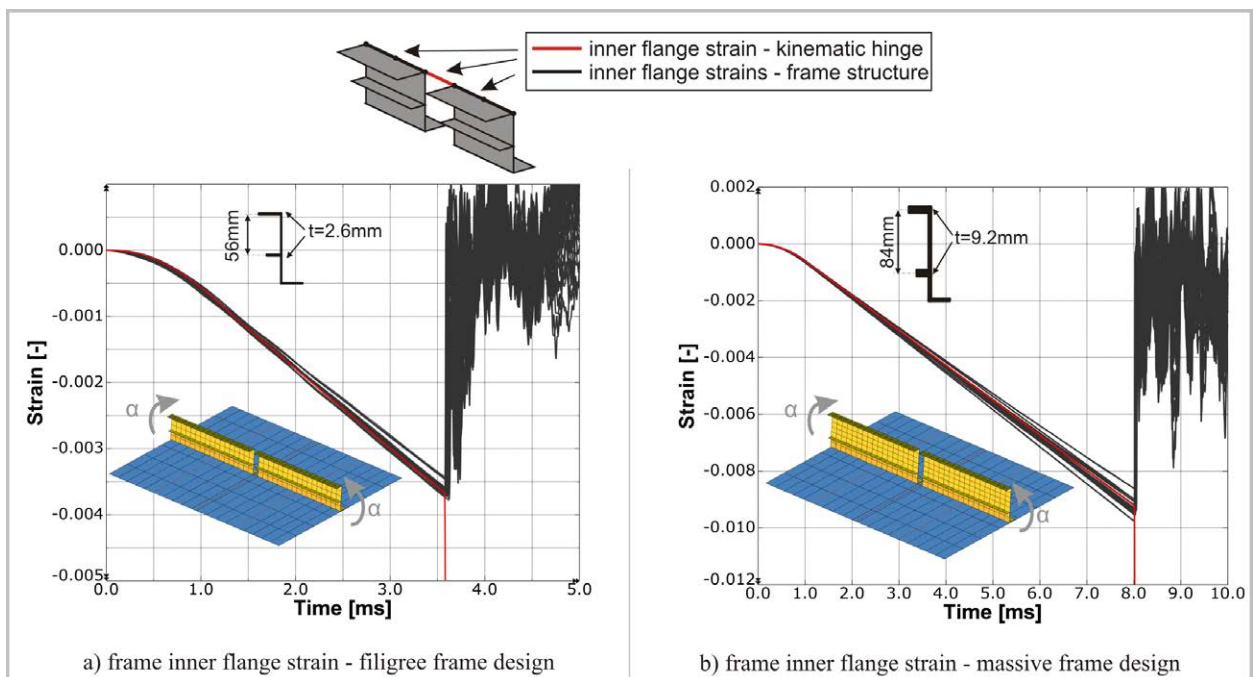


Figure 4-8: Calibration of the kinematic hinge bending stiffness

4.3. Post-failure behaviour of a frame-stringer-skin structure

The behaviour of a frame structure after failure initiation is the main mechanism that has to be represented by the kinematic hinge architecture. This post-failure mechanism has to be modelled by the macro architecture in a way that typical frame failure is represented and global crash kinematics can be simulated accurately.

The definition of appropriate kinematic hinge architecture for the representation of the post-failure behaviour was investigated on the basis of experimental tests which were performed in the past. Sub-structure level tests as well as fuselage section and full-scale drop tests were considered [15-19,24-26,28-38,46-51,56,62-65,134]. Post-failure damages of frame-stringer-skin structures were analysed to conclude to the spectrum of potential failure mechanisms. Based on the captured frame failure modes, the mechanisms were classified. Typical frame failure behaviour could be derived from this classification. Besides typical frame failure, several other failure mechanisms were identified which generally occur under specific conditions that differ from typical fuselage design.

4.3.1. Frame failure of typical fuselage design

In the following, examples of frame failures are presented and discussed. Figure 4-9 gives examples of the so-called typical frame failure mode. Basis of the typical frame failure mechanism is the structural interaction of the frame with the fuselage skin. Frame failure initiated by tensile rupture or compressive buckling reduces the frame stiffness so that the elastic centre shifts to the skin plane. The frame-skin component provides a significantly reduced bending stiffness which is in the final case of total frame rupture defined by the bending stiffness of the skin. Therefore flexion is concentrated in this failure location that forms a hinge whereas the circumjacent frame structure remains intact. In the hinge location, the skin with its comparably small thickness bends up to very high curvatures without exceeding the material failure strain. Thus, the skin provides structural integrity and forms the hinge. According to this effect, typical frame failure describes a bending mechanism with a pivot point that is finally located in the skin plane.

Figures 4-9a) – 4-9e) show examples of typical frame failure in a closing bending condition. The examples illustrate typical closing failure that is initiated by compressive buckling of the frame flanges. Figures 4-9a) and 4-9b) depict results of dynamic tests on sub-structure level. A320 fuselage panels in a 2-frame configuration were tested under crash relevant loads. Results of fuselage section drop tests are given in Figure 4-9c) and 4-9d). Finally, Figure 4-9e) depicts results of the ATR 42-300 full-scale drop test. Notable in Figure 4-9e) is the comparison of

typical frame and massive wing frame of this high-wing aircraft design. Similar hinge kinematics developed in both frame designs.

In Figures 4-9f) – 4-9j), examples of typical frame failure in an opening bending condition are given. Typical opening failure is initiated by tensile rupture of the frame inner flange that propagates through the frame cross-section. Figures 4-9f) – 4-9h) show different opening hinge locations of the drop tested A320 fuselage section. Similar hinge kinematics is given in Figure 4-9i) for the drop tested B707 fuselage section. Finally, typical opening frame bending failure of the ATR 42-300 structure is given in Figure 4-9j).

Notable in this selection of frame failure examples in Figure 4-9 is the occurrence of similar frame failure kinematics despite of different frame and stringer designs in an A320, B707 and ATR42 fuselage structure. The illustrations in Figure 4-9k) and 4-9l) depict the schematic failure modes in closing and opening bending condition.

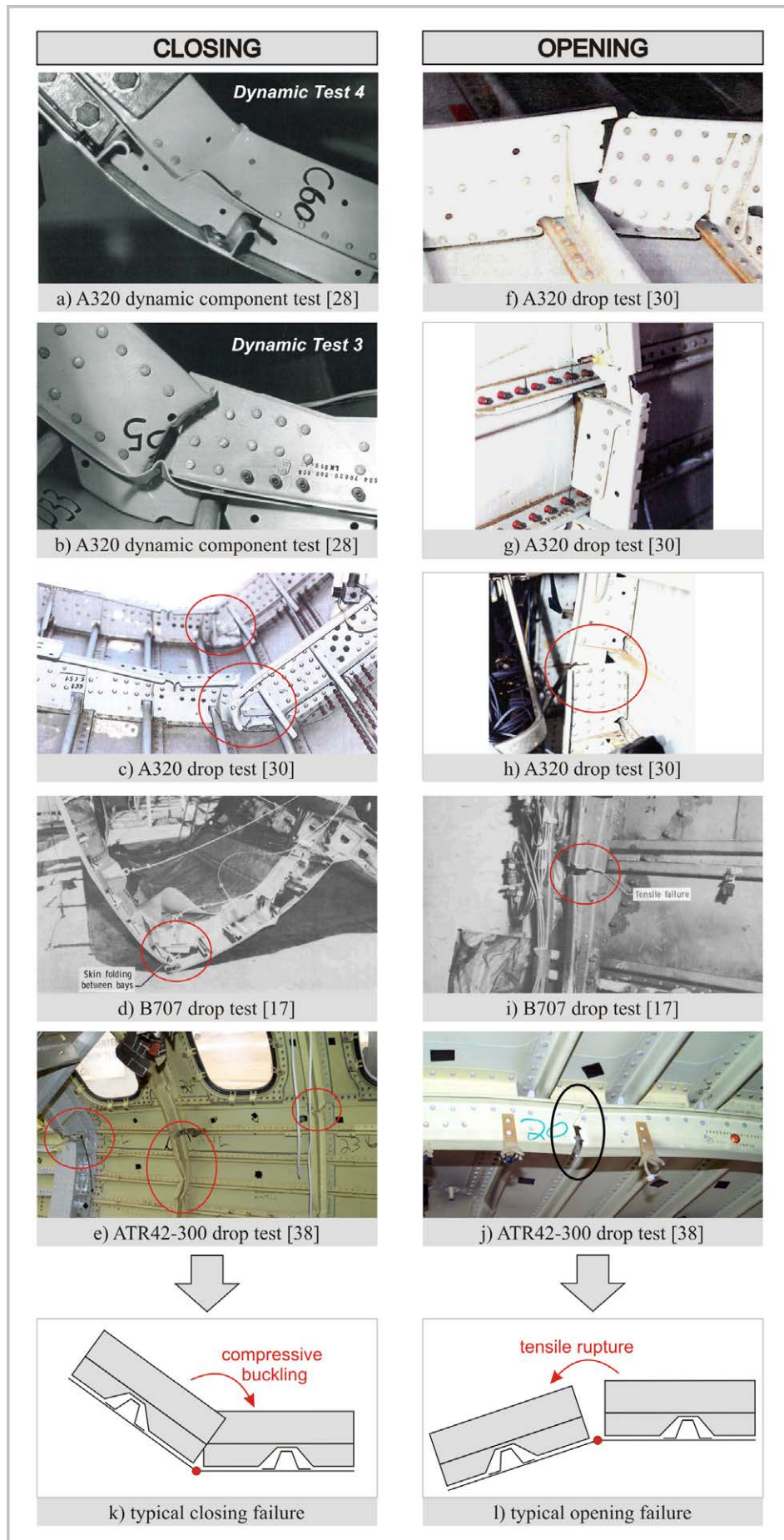


Figure 4-9: Typical frame failure mechanism

4.3.2. Frame failure of non-typical fuselage design

Regarding post-failure damages in regions of the fuselage that differ from the typical fuselage section, further frame failure mechanisms were identified which can not be categorized to the typical frame failure discussed above. These additional failure modes are illustrated in Figure 4-10. In Figures 4-10a1) and 4-10a2) results of the drop tested ATR 42-300 are shown. The complete area of the wing-fuselage interaction is depicted. In this high-wing aircraft configuration high crash loads acted during the drop test on the massive wing frames and led to complete rupture at five of the six wing frames. Separation of the skin in the frame failure location prohibited the formation of a hinge kinematics. High stiffness in the upper fuselage area, provided by the wing structure, hindered the massive wing frames from an inwards closing hinge rotation. Instead, high inertia loads of the wing led to a vertical shift of the upper frame parts including the separation of the skin. One wing frame experienced a closing hinge kinematics according to the typical frame failure mode, which is already illustrated in Figure 4-9e).

Results of a drop tested B707 fuselage section are given in Figures 4-10b1) and 4-10b2). This airframe test section is tapered and provides a cargo door at one side. In addition, the cargo area was loaded with bulk luggage. Asymmetry of the fuselage section in longitudinal (tapered section) and lateral (cargo door) direction as well as high interaction of the fuselage structure with cargo loading led to an asymmetric global crash kinematics and untypical frame failures. The flattening effect of the fuselage section caused skin folding inside the frame hinge location at the left fuselage side, Figure 4-10b1). At the opposite side, Figure 4-10b2), the frame ruptured at two locations. The frame part between both failure locations shifted outwards and enabled the skin to fold.

Drop test results of a tapered B707 section with an auxiliary fuel tank that was installed in the cargo floor are depicted in Figures 4-10c1) and 4-10c2). This fuselage section without cargo door provides symmetry in lateral direction. On both sides of this section, frame shear failure is visible. The frame ruptured and shifted in vertical direction which was enabled by additional skin separation. The cause of such frame shear failure can be found in the tapered geometry of the fuselage section. This asymmetric fuselage structure leads to asymmetric impact loads during the crash sequence with the first impact at the front end of the section.

Results of a drop tested B737 fuselage section with cargo door and conformable fuel tank in the cargo floor are depicted in Figures 4-10d1) and 4-10d2). On the left (cargo door) side, Figure 4-10d1), a closing hinge rotation of the frame is visible. This hinge kinematics differs slightly from typical hinge failure mechanism as lateral frame bending led to an enlarged area of the failure location. On the opposite side, Figure 4-10d2), closing hinge failure is visible. In this failure

location the frame ruptured completely. Due to the asymmetry, caused by the cargo door, and the flattening effect, caused by the fuel tank, the skin folded extensively in this frame failure location.

Figures 4-10e1) and 4-10e2) illustrate drop test results of a further B737 fuselage section with cargo door that was loaded with bulk luggage. Typical asymmetric crash kinematics is visible, which is caused by the structural asymmetry introduced by the cargo door. Opening and closing hinges developed similar to the test results shown in Figures 4-10d1) and 4-10d2). Here, a global view shall be given on this asymmetric crash kinematics.

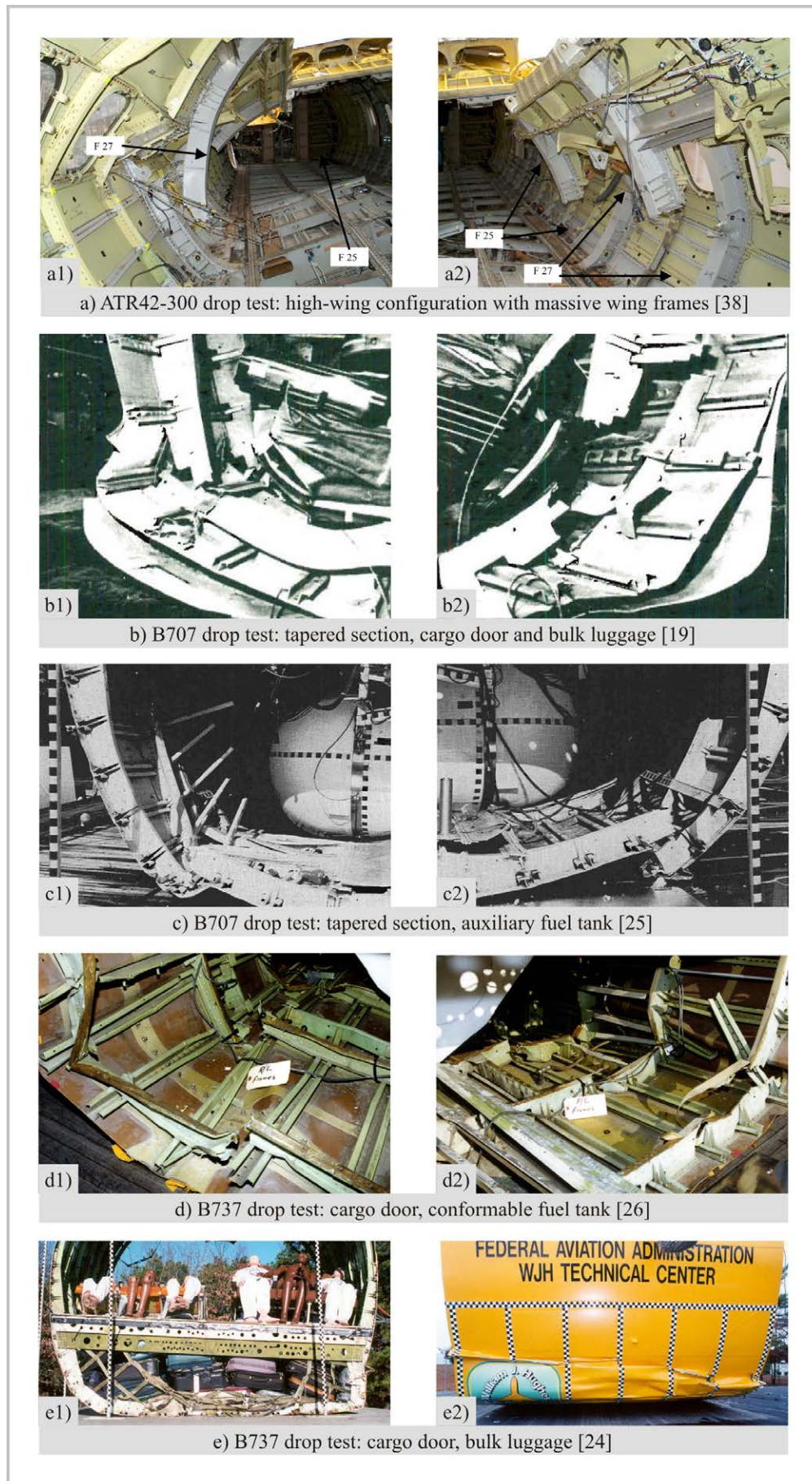


Figure 4-10: Further frame failure mechanisms (non-typical fuselage design)

Two additional main failure mechanisms can be derived from the captured frame failures discussed in Figure 4-10: Frame shearing and skin separation. Both failure mechanisms differ significantly from the typical frame failure kinematics. Both additional failure mechanisms are caused by structural designs which differ from the typical fuselage design. Such differences are high-wing aircraft design, tapered fuselage section or the existence of a cargo door, for instance. In the considered test results, the effect of these design variants was partly intensified by different cargo loadings. Such cargo loading avoids an unrolling of the lower fuselage shell and leads to higher constraints in the structure.

With respect to the development of a kinematic hinge macro architecture the selection of failure modes that have to be represented has to be discussed. In general, representation of complex failure mechanisms by simplified macro models can not consider the full spectrum of potential failure effects. Different macro architectures would be necessary in dependence of the individual failure mode. Nevertheless, besides typical frame failure, the need of representation of frame shearing and skin separation has to be assessed on the basis of the definition of the Kinematics Model. As a preliminary design tool for composite fuselages, crashworthy designs shall be assessed and developed with the Kinematics Model. According to the basics for crashworthy composite designs all failure occurrences have to be controlled by crash devices to avoid uncontrolled crash scenarios. Hence, the kinematic hinges represent crash devices in the frame which avoid uncontrolled failure. Potential energy absorption and structural integrity has to be ensured by such crash devices.

Typical frame failure as identified above is a frame bending mode that enables a controlled failure motion. In contrast to this, frame shearing leads to a separation of the frame structure that can hardly be controlled. Consequently, frame shearing should not be considered in a robust crash design. Skin separation is a failure mechanism that can occur even in combination with the typical frame failure mode. Especially in case of an opening hinge rotation, risk of skin separation is supposable. Tendencies of this combined effect are visible in Figure 4-9g). Nevertheless, skin separation is a failure mode that is hardly controllable. Propagation of rivet failure can lead to uncontrolled skin separation that induces further failure location outside of crash devices. For that reason, the philosophy for crashworthy design specifies the avoidance of skin separation wherefore this failure mode is not considered in the kinematic hinge architecture.

The specification of the kinematic hinge architecture - to represent exclusively typical frame failure - is well sufficient and effective regarding its usage in a preliminary design tool on the typical fuselage section level. Nevertheless, further natural frame failure mechanisms of non-

typical fuselage sections can not be represented with that macro modelling approach, which is why the usage of the Kinematics Model is generally limited to typical fuselage design.

4.3.3. Failure behaviour of CFRP frame structures

The previous discussion about the post-failure behaviour of a frame-stringer-skin component considered failure mechanisms of metallic structures. In the following, failure behaviour of CFRP frame structures was analysed to conclude to potential differences in the frame failure mode compared to metallic structures. Several tests of CFRP frame structures under crash relevant loads were conducted in the past. These results are discussed in the following.

Valuable results were generated in the past by drop tests of CFRP frame components as well as a skeleton subfloor section and a skinned subfloor section, which were already discussed in paragraph 4.1. The generally observed failure pattern for the tested CFRP frames and sections was similar to the drop test results of metallic transport fuselage sections [46]. Especially in the drop test of the skinned subfloor section typical frame failure behaviour could be identified. Due to the brittle material behaviour of CFRP the frames partly failed more distinct, but the skin remained intact and served as less stiff boundary condition for the broken frames. The CFRP skin provided structural integrity and generated the hinge rotation.

Further results of CFRP frame structures tested under crash related loads are depicted in Figure 4-11. Test results of semi-circular CFRP frame structures are given in Figures 4-11a1) and 4-11a2). A CFRP skin with a width of 1.4 times the frame outer flange width was co-cured with the graphite/epoxy I-shaped frame. The tests were performed quasi-statically. Again, the CFRP skin did not fail in the test but served as integer part and formed the hinge between the ruptured frame parts. In Figure 4-11a1) opening frame failure is illustrated at the lower centre ($\alpha_1 = 0^\circ$) of the semi-circular frame. In addition, skin delamination from the frame is visible at this opening bending failure. A closing hinge at the same frame-skin specimen is shown in Figure 4-11a2) which occurred at an angle of $\alpha_2 = 50^\circ$.

Further test results of a similar semi-circular CFRP frame-skin component are pictured in Figures 4-11b1) and 4-11b2). The quasi-statically loaded semi-circular frame-skin component shows an opening hinge with delamination of the skin in Figure 4-11b1). In Figure 4-11b2) a closing hinge is pictured. In both frame failure locations the skin remained intact.

Another example of CFRP frame failure is given in Figures 4-11c1) – 4-11c4). Results are presented of a commuter sub-passenger floor structure in a 2-frame configuration made of CFRP, that was drop tested with an initial velocity of $v_i = 7$ m/s. Figures 4-11c1) and 4-11c2) illustrate an opening hinge that developed in the lower centre of the structure at both frames. At

this location a splice plate connects two frame parts to the full frame length. The splice plate ruptured across the complete cross-section. The skin remained intact and formed the opening hinge. Figure 4-11c3) gives an overview on the left part of the sub-floor specimen. The opening hinge is visible on the right side of this picture. Figure 4-11c4) shows the right side of the specimen. High curvature of the CFRP skin with an angle of about 90° is observable. This test result demonstrates the capability of the skin to provide structural integrity and to generate a hinge formation, even if the skin is made of CFRP.

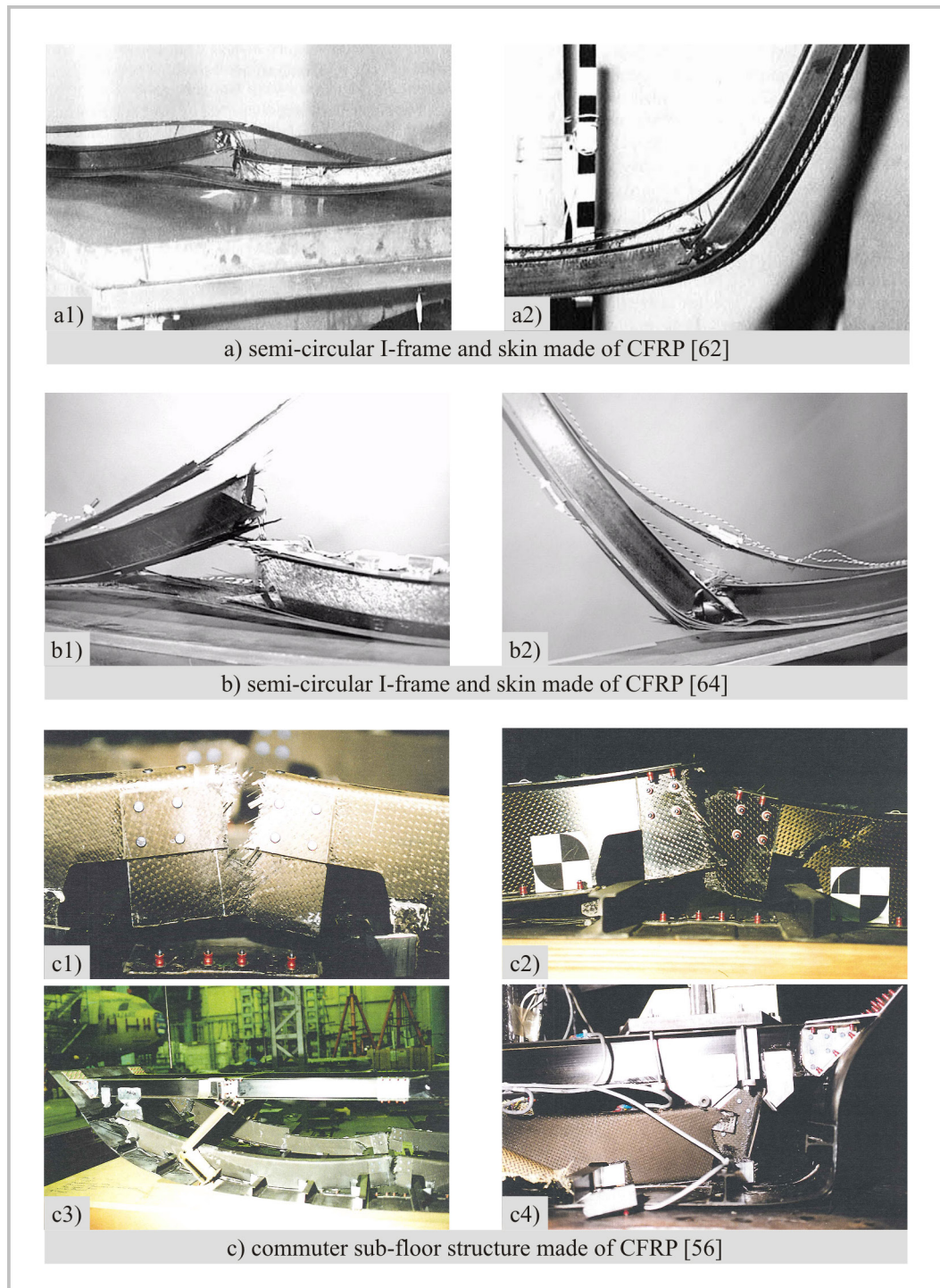


Figure 4-11: Failure behaviour of CFRP frame structures

4.3.4. Outcomes of the investigation of the post-failure behaviour

Summarising the discussion of the post-failure behaviour of a frame-stringer-skin component, several test results on frame structures were evaluated to identify the spectrum of frame failure mechanisms. Besides several other frame failure modes, a typical frame failure mechanism could be identified. The concentration on this typical frame failure mode with respect to the definition of a macro architecture was stated reasonable. Further evaluation of test results of CFRP frame structures identified very similar frame failure hinge kinematics compared to the previous discussion of metallic structures.

Based on this investigation on frame failure mechanisms, the kinematic hinge macro architecture was defined in a way that typical frame failure is represented accurately. As the skin described the integrating structural part and frame bending rotation occurs with a pivot point that is located in the skin, the macro element was positioned in the skin plane. Similar to the discussed test results of typical frame failure this macro element describes the frame failure behaviour respectively the behaviour of a frame crash device by a moment-rotation relation. The (CFRP) skin is modelled linear-elastically as this structural part remains inside of its material failure strain. The element size of the discretised skin was adapted so that element edges correspond with the length of the macro element respectively the length of the kinematic hinge gap. At least one element row is positioned inside the hinge gap. This enables the skin elements to experience high curvatures with its typical linear shape functions. Figure 4-12 illustrates the kinematic hinge mechanism and compares this hinge kinematic with typical frame failure of CFRP and metallic frame structures.

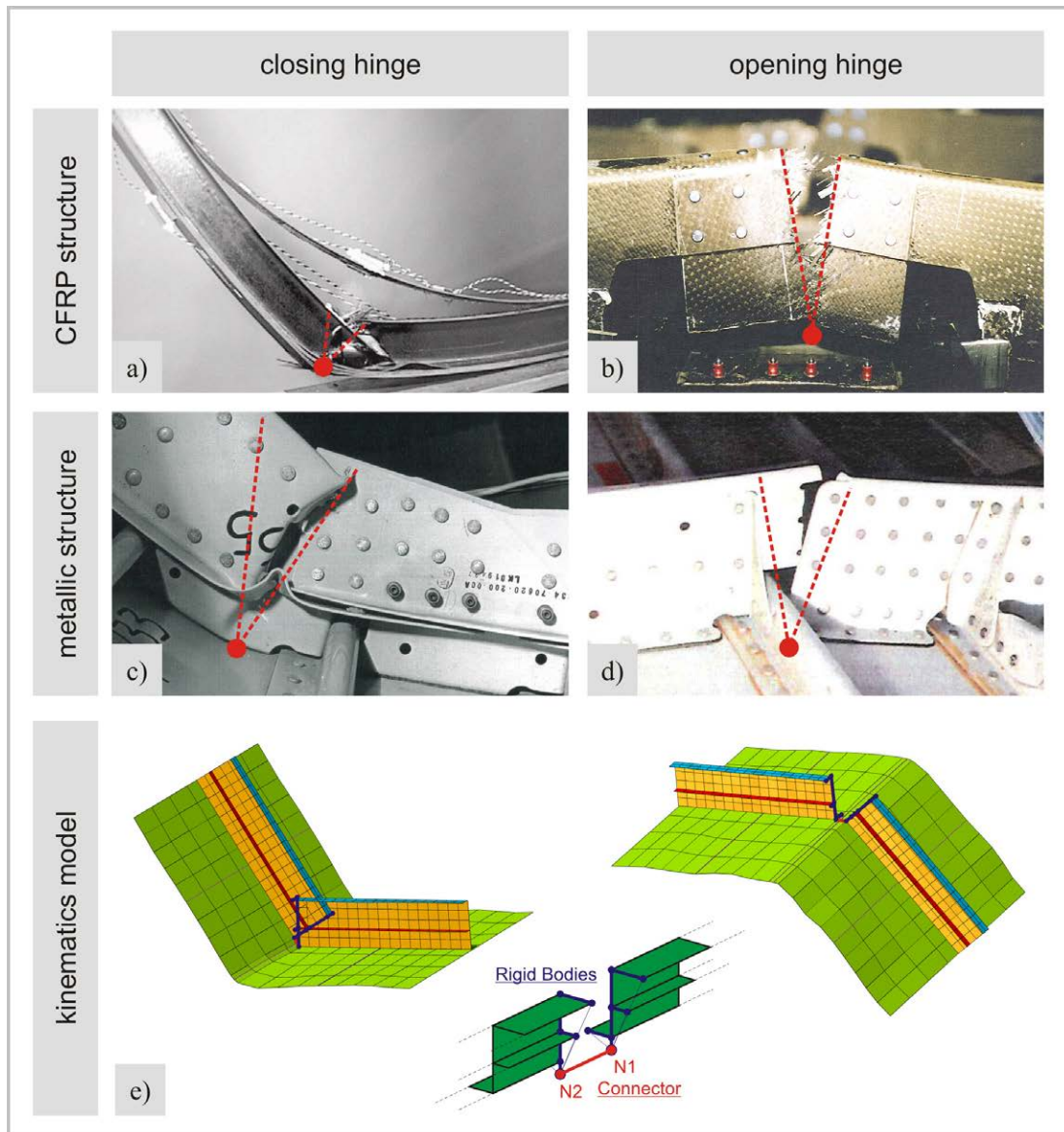


Figure 4-12: Kinematic hinge architecture for representation of typical post-failure behaviour

4.4. Influence of the kinematic hinge architecture on lateral frame stability

A typical design of an aircraft fuselage structure provides cleats for lateral support of the frames. Cleats increase the lateral frame stiffness significantly. Hence, potential lateral frame buckling occurs at higher loads, or vice versa frames can be designed lighter when support by cleats is provided. As mentioned in chapter 3.1 the Kinematics Model does not provide the modelling of cleat structures. These structural details are not considered in a preliminary design phase. On the other hand, the neglect of lateral support may lead to an over-dimensioned frame design. Especially in case of crash, the frame structure is typically loaded with high compression and bending loads which leads to an increased risk of lateral frame buckling. Hence, assumptions have to be defined to consider appropriate lateral frame support.

Furthermore, the influence of the frame cross-sections reinforced by rigid bodies in the kinematic hinge architecture has to be analysed. It has to be ensured that the kinematic hinges do not provide unrealistically stiff lateral frame support. Otherwise, this could lead to a non-conservative frame design.

The numerical frame-stringer-skin model as well as the Kinematics Model on the fuselage section level was used to investigate the lateral frame behaviour. Typical frame behaviour of detailed numerical models was compared to the behaviour of a coarse structural representation according to the Kinematics Model approach. In the following, this investigation is discussed.

The numerical frame-stringer-skin model which was used in this investigation was already discussed in paragraph 4.2. A detailed model description is given in Appendix A2.1. Three different model variants were analysed to investigate the lateral frame stiffness of different modelling techniques. Figure 4-13 illustrates these model variants. A detailed FEM model, pictured in Figure 4-13a), represents the reference with a typical structural design. In this variant cleats are modelled in detail. Typical cleat design was assumed with a thickness of $t = 2.5$ mm and a material stiffness based on aluminium material data. The variant in Figure 4-13b) corresponds to the Kinematics Model approach and provides a kinematic hinge in the centre of the frame segment. Cleats are not modelled in this approach. Figure 4-13c) represents a variant with a coarse discretisation according to the Kinematics Model. Neither a kinematic hinge nor lateral frame support by cleats are modelled here.

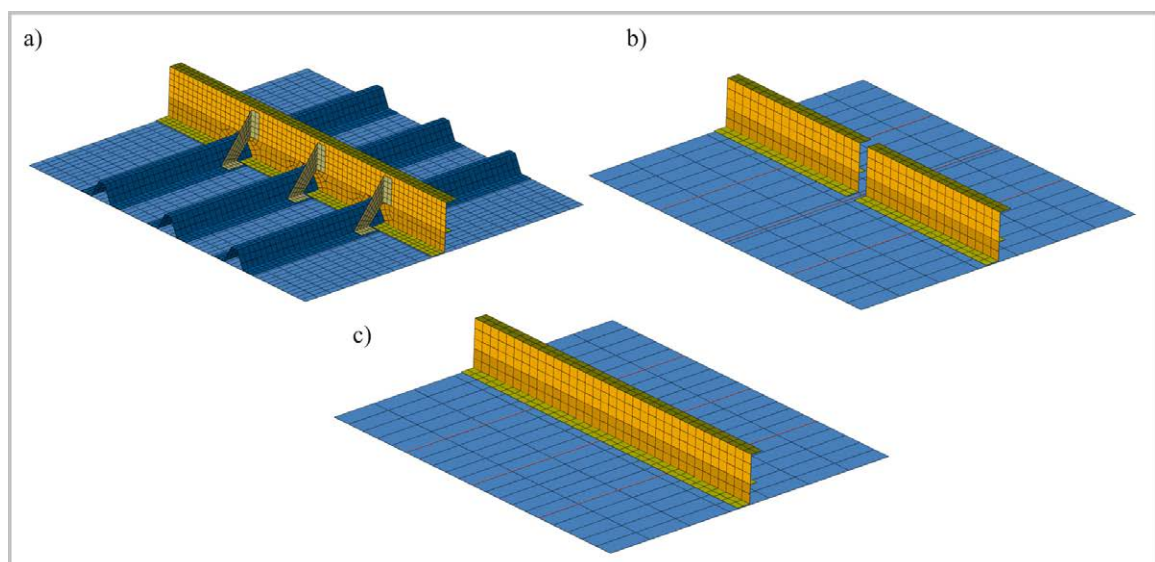


Figure 4-13: Frame-stringer-skin model variants used in the investigation on lateral frame stiffness

Similar to previous investigations different LCF-shaped frame designs were analysed to consider the whole spectrum of frame sizing which will potentially be used in a crash design process.

These designs represent the extreme cases with respect to instability modes and were already pictured in Figure 4-5b) – 4-5e). Pure moment load was considered in this investigation.

As expected, a general outcome of this investigation identified that filigree frame designs with thin flanges are less affected by the design of lateral frame support. Flange buckling is the major mode of instability for such filigree designs. In contrast to this, high influence of lateral frame support was identified for massive frame designs. Here, lateral frame buckling is the major mode of instability, as discussed in paragraph 4.2.1. For that reason, the discussion of simulation results concentrates in the following on the massive frame designs. In Figure 4-14 the graphs illustrate the strain along the frame inner flange of the variant with the most massive frame design, which corresponds to Figure 4-5b). A comparison of the modelling technique variants obviously shows that the neglect of lateral frame support leads to extensive frame buckling. The detailed FEM model variant as well as the Kinematics Model variant show similar strain distributions. The magnitude of both graphs is at a strain level between $\varepsilon_1 = -7000$ microstrain and $\varepsilon_2 = -8500$ microstrain. The crippling strain limit of this frame design is $\varepsilon_{cc} = -8290$ microstrain. Thus, the graphs represent the strain distribution at a maximum allowed load level at which the crash devices in the frames have to trigger at the latest. At this state the strain distribution of the variant without lateral support indicates strain exceeding up to $\varepsilon_3 = -12,300$ microstrain. As a result of this exceeding, modelling approaches without consideration of lateral frame support would lead to over-sized frame designs.

Compared to the variant without lateral support, the detailed FEM variant and the Kinematics Model variant correspond well. Small curvatures in both graphs indicate lateral frame buckling between the cleats respectively between boundary condition and the kinematic hinge. Strain oscillations in the centre of the graph of the Kinematics Model variant indicate little influence of the kinematic hinge on the strain distribution.

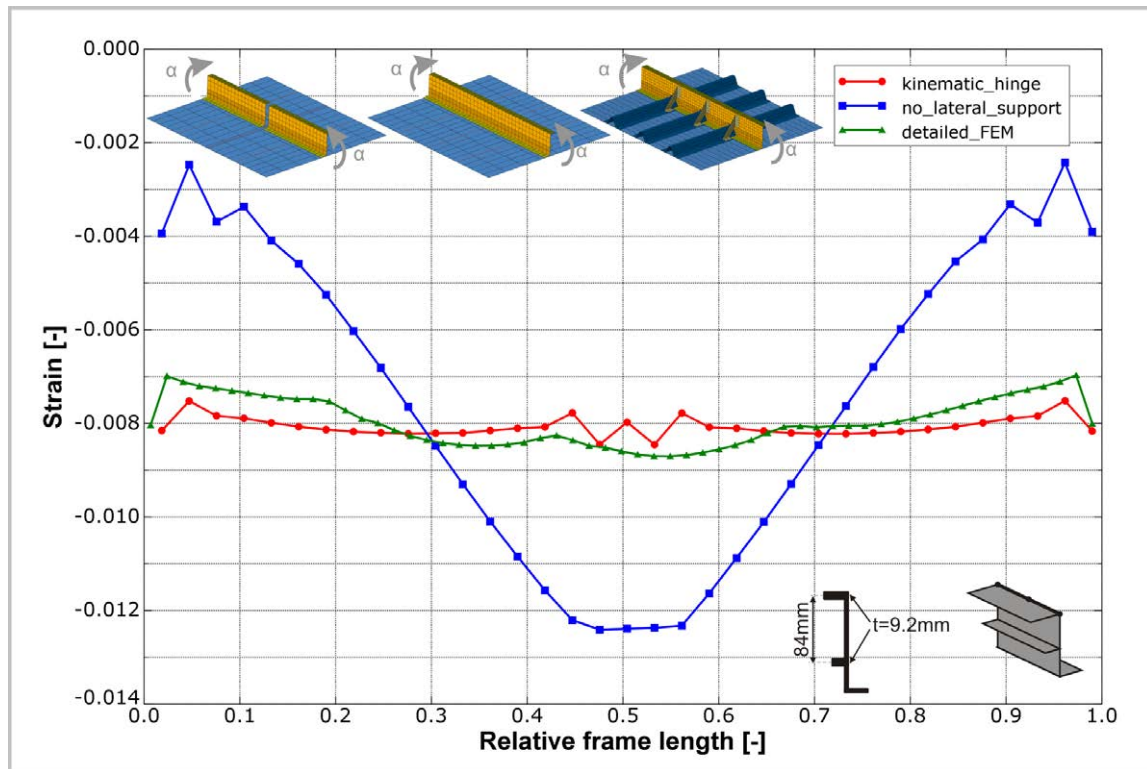


Figure 4-14: Strain along the frame inner flange with different frame lateral supports

After the investigation on generic fuselage sub-structure level, a similar investigation was performed with numerical models on the fuselage section level which were drop tested with an initial velocity of $v_i = 6.7$ m/s (22 ft/s). The basis of this investigation is a generic CFRP standard fuselage structure with a massive frame design. In contrast to the frame-stringer-skin model analyses more realistic loading of combined compression and bending will occur in the frame structure of these fuselage section analyses. In addition, a curved frame structure and more realistic boundary conditions can be found in these models. Figure 4-15 depicts the section model variants. All three variants provide the same discretisation. The reference variant in Figure 4-15a) provides artificial lateral support by constraints of frame inner flange nodes at each stringer position. These constraints in lateral direction represent an ideal cleat like frame support. The Kinematics Model is illustrated in Figure 4-15b) with a kinematic hinge distribution according to the outcomes of paragraph 4.1. A third section model without lateral frame support is pictured in Figure 4-15c). In this model, lateral frame support of the lower side shell structure between passenger crossbeam and cargo-crossbeam is given exclusively by the lower vertical support strut connection which is modelled using a rigid body.

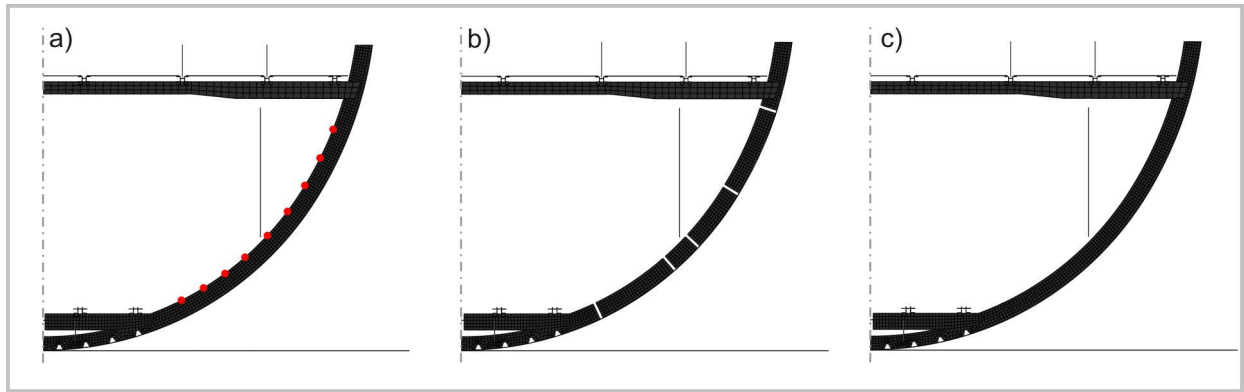


Figure 4-15: Fuselage section model variants used in the investigation on lateral frame stiffness

The results of this investigation on the fuselage section level are comparable to the results of the frame-stringer-skin model presented above. The strain along the frame inner flange of the lower fuselage side shell is depicted in Figure 4-16 at $t = 20\text{ms}$ after the first impact. At this state, the crushing of the sub-cargo area is nearly completed and the frame is loaded highly up to failure. The graphs illustrate the strain along the frame between cargo-crossbeam and passenger crossbeam. The frame coupling as well as the vertical support strut connection provides certain lateral support. Thus, the graph illustration concentrates on the regions between these structural supports. The region between cargo-crossbeam and vertical support strut is obviously the most critical one. The graph of the variant without lateral frame support indicates extensive lateral frame buckling in this region. The strain distribution of the Kinematics Model variant shows minor frame buckling whereas the variant with frame support by nodal constraint indicate negligible frame buckling. Regarding this critical region between cargo-crossbeam and vertical support strut, maximum strain level of the variant without lateral frame support reached high values of up to $\epsilon = -7600$ microstrain. The maximum strain values of the Kinematics Model variant is $\epsilon = -6200$ microstrain. The variant with frame support by nodal constraint reached a maximum strain level of $\epsilon = -6000$ microstrain. Hence, the Kinematics Model variant provides a lateral stiffness behaviour that is comparable to variants with exclusively defined lateral support.

The graphs in the region between vertical support strut and passenger crossbeam show similar strain distributions for all variants. Here, the loading is not critical at this state. Thus, extensive lateral frame buckling does not occur.

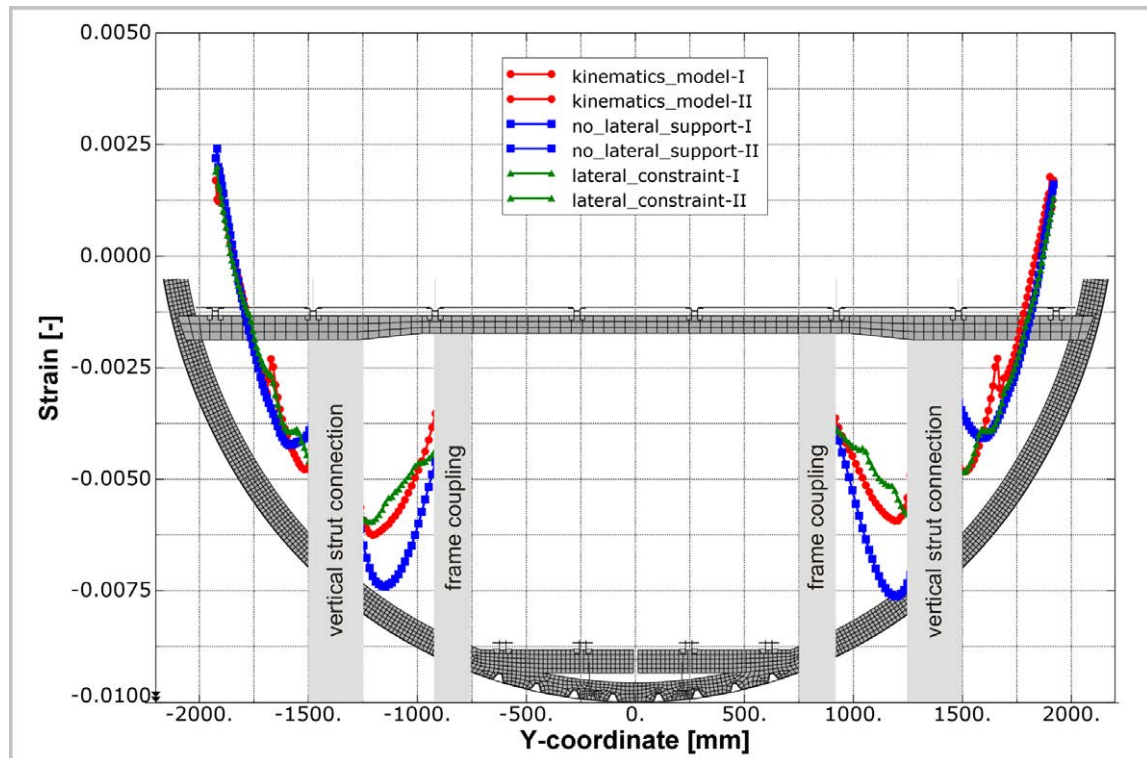


Figure 4-16: Strain along the frame inner flange of different frame lateral supports in the section model

Summarising the investigations on lateral frame stability, analyses on the sub-structure level as well as on the fuselage section level identified good agreement of the Kinematics Model approach with more detailed model representations of lateral frame support. The investigations showed that appropriate lateral frame support is provided by the kinematic hinges and vice versa the rigid body modelling in the kinematic hinges does not influence the lateral frame stiffness in an unrealistic manner.

To achieve this good agreement an appropriate density of kinematic hinges along the frame structure is required. Especially with regard to the upper fuselage, potential need of additional lateral frame support by nodal constraints has to be considered. In this area, the number of installed kinematic hinges is typically much lower compared to the lower fuselage and comparably long frame segments without any lateral frame support are at risk to buckle laterally. The definition of additional lateral support by nodal constraints can be specified individually in dependence of the occurrence of potential buckling events.

4.5. Influence of the discretisation

The basic idea of the Kinematics Model, which was described in chapter 3.1, specifies a coarse modelling for representation of the fuselage structure. Based on the linear-elastic material formulations an increased element size can be defined as structural deformations of the finite elements are comparatively small, at least in the range of structural design allowables.

In addition, the coarse modelling can be applied to the layup definition. Simplifications in the stacking sequence by merging of identical layers will reduce the number of integration points through the thickness of a finite element. Furthermore, as the material behaviour is reduced to linear-elastic formulation the number of integration points through the thickness of each layer could be reduced.

Finally, a reduced integration of the shell elements would significantly reduce the number of integration points in an element compared to fully integrated elements.

All these modelling aspects lead to a significant reduction of calculation time. This is of prime importance as modifications and adaptations are typical for a preliminary design phase and various simulation runs are necessary to finally result in a crash optimised design.

In this paragraph the aspects of coarse modelling are discussed to ensure an accurate model representation of the fuselage structural behaviour.

At first, the influence of the element size was analysed. Based on the frame-stringer-skin model, which is described in detail in Appendix A2.1, four representative LCF-shaped frame designs were calculated on different discretisation levels. The LCF-shaped frame designs correspond to the profiles which are illustrated in Figure 4-5b) – 4-5e). Pure moment load was assumed in this investigation.

In a first analysis, a fine discretised variant with an element size of $L_{e1} = 12$ mm was compared to a coarse modelled variant with an element size of $L_{e2} = 39$ mm. In addition to a large element size, the coarse model provides a simplified structural representation according to the Kinematics Model approach. The stringers are represented by beam elements. Mouseholes are omitted in this variant. In Figures 4-17 and 4-18 results of this comparison are given for the small, filigree frame design (Fig. 4-17) as well as the large, massive frame design (Fig.4-18). The strains along the frame inner flange are depicted over the time, respectively over the moment load. Both diagrams obviously show discrepancies between fine and coarse discretisation. In Figure 4-17, the set of graphs of the fine discretised variant approximately describes a unique slope up to initiation of flange buckling which is indicated in the graph oscillations starting at a strain level of about $\varepsilon = -3500$ microstrain. The set of graphs of the coarse modelled variant shows a fan-shaped distribution with significant differences in the slope. Oscillations which indicate potential flange buckling are visible at significantly higher loads compared to the fine modelled variant. In Figure 4-18, results of the large, massive frame design are given. A similar discrepancy between the fine and the coarse modelling variant is obvious. Here, a spread in the set of graphs of the fine modelled variant indicates frame buckling. The graphs of the coarse modelling variant show a fan-shaped distribution.

In this investigation the coarse model was discretised with one element over the width of all frame flanges. The frame inner web provides two elements over the height, the frame outer web provides one element over the height – in case of small frame design. In these explicit numerical simulations typical shell elements with linear shape functions are used. Such coarse discretisation in combination with linear interpolation of the elements results in significant constraint effects. The frame flanges, discretised with one element over their width, can not resolve the natural buckling mode of the filigree frame design and constraint such instability modes. The constraint of flange buckling results in an early frame buckling mode indicated by the fan-shaped strain distribution.

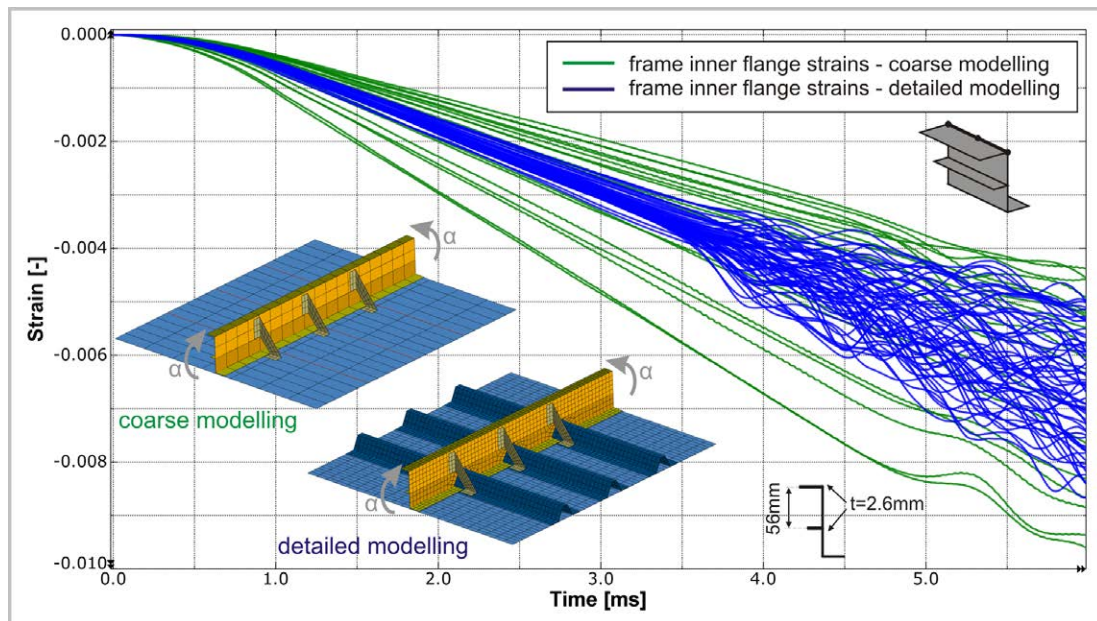


Figure 4-17: Strain along the frame inner flange with different discretisation level – small, filigree frame design

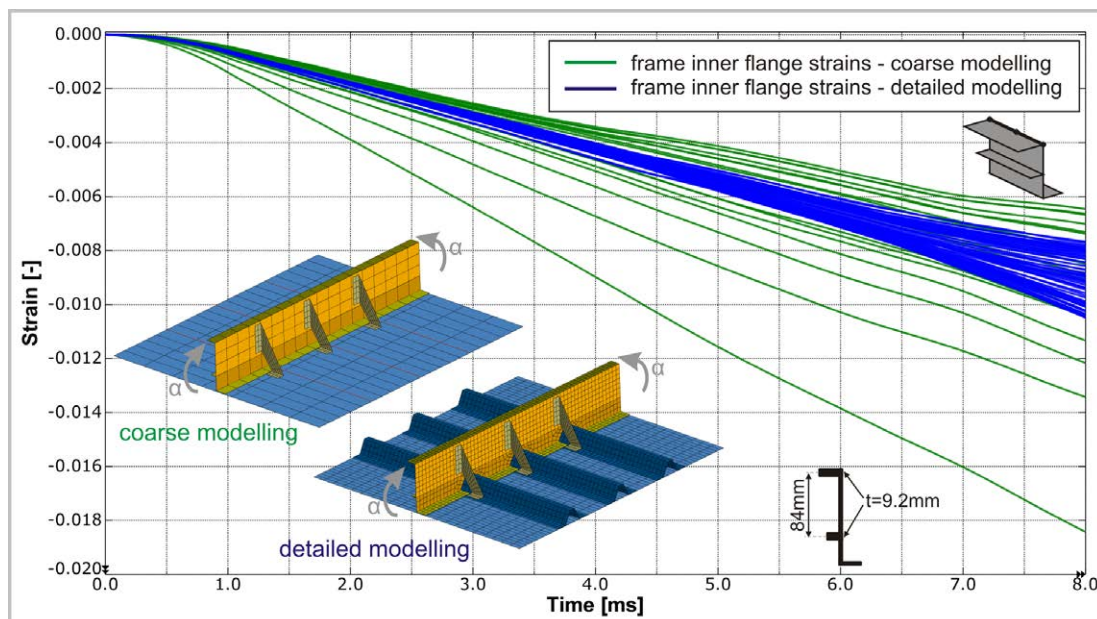


Figure 4-18: Strain along the frame inner flange with different discretisation level – large, massive frame design

In the following, the element size in the coarse variant was reduced in a way that the frame flange width was discretised with two element rows. Three element rows are modelled over the frame inner web height, two element rows over the frame outer web height – in case of the small frame design. With this mesh refinement constraint effects could be avoided and an accurate elastic behaviour was achieved, as the results in Figures 4-19 and 4-20 illustrate. Here, the fine modelled variant is compared with the refined Kinematics Model variant. Both diagrams illustrate good agreement in the elastic behaviour.

With respect to initiation of instabilities the filigree frame design as well as the massive frame design show a slightly delayed initiation of flange buckling respectively frame buckling for the Kinematics Model variant. This small discrepancy has no influence on the model accuracy as strain limit criteria in the Kinematics Model are not defined by the FE model, but according to the empirical handbook criteria.

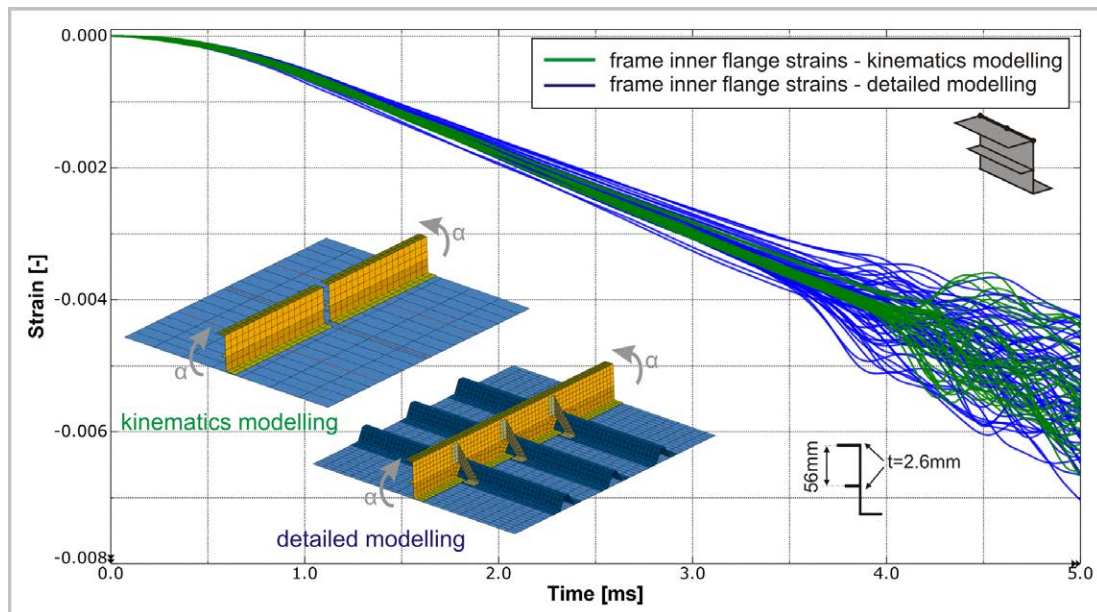


Figure 4-19: Strain along the frame inner flange, kinematics and detailed modelling – small, filigree frame design

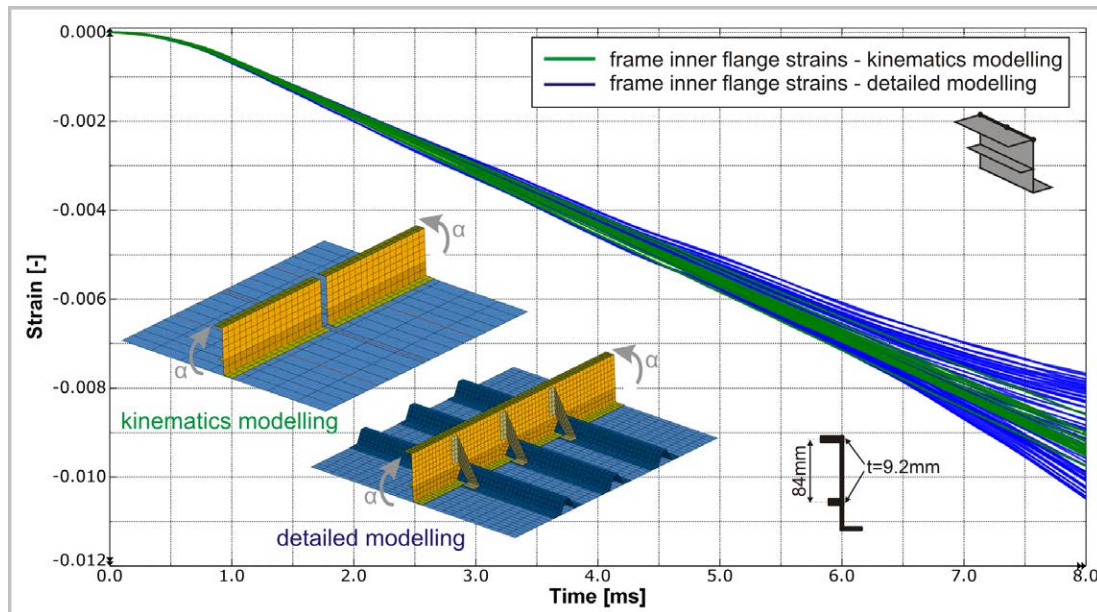


Figure 4-20: Strain along the frame inner flange, kinematics and detailed modelling – large, massive frame design

As an outcome of this study, a maximum reasonable element size can be defined so that at least two elements are modelled over the flange width of frame inner and outer flange. Such an element size leads to five elements over the frame height for the considered small frame profile (typical design). Up to seven elements over the frame height are modelled in this discretisation level for the large frame profile (massive design).

A further aspect regarding efficient calculation schemes is the usage of reduced integration for the shell elements. With reduced integration, one section point is used instead of four section points in the fully integrated shell element. This effect can reduce the calculation time significantly. Nevertheless, the combination of reduced-integration elements with a coarse regular mesh under bending loads is critical. Excessive hourglassing can increase the artificial energy of the hourglass control which is provided by the FE solver. Therefore, at least four elements through the section of bending regions are recommended when reduced-integration elements are used [111,112]. With respect to the frame web this recommendation is satisfied with the refined Kinematics Model variant discussed above. But the frame flanges are modelled in the refined variant with only two elements over the flange width. In case of frame buckling, the elements of the frame flanges experience in-plane bending loads. In this special case the recommendation to use at least four elements through the section is not satisfied. It is obvious that a mesh refinement is not reasonable. This would lead to a significant increase of calculation time caused by a comparably fine FE mesh which is not acceptable for an efficient preliminary design tool. Instead, the elements of frame inner and middle flange are calculated fully integrated. Hourglass modes can not occur with fully integrated elements. Hence, potential increase of artificial energy by hourglass control is avoided. The frame outer flange is

furthermore modelled with reduced-integration elements as this flange is connected to the skin by tie constraints which avoid the occurrence of hourglass modes. In addition, potential in-plane bending loads in this outer flange are negligible.

Further calculation efficiency was realised by a reduction of the number of layers as well as by the reduction of the number of integration points through the thickness of each layer. Potential influence of both simplifications was analysed with the frame-stringer-skin model considering the four representative LCF-shaped frame designs which are illustrated in Figure 4-5b)-e). Pure moment load was assumed in this investigation.

The investigation of effects caused by the merging of stacking sequences identified no influence on the elastic behaviour for all considered frame designs. Reasonable merging was conducted in this study which considered the fusion of similar plies.

The reduction of the number of integration points through the thickness did not show observable influence on the elastic behaviour, either. In this study, the number of integration points was reduced from three points per ply to one point per ply. With respect to the initiation of instabilities small effects were observed. In one frame design variant, flange buckling occurred marginally later with reduced layup and one integration point per ply. Once more, the initiation of instabilities has no effect on the accuracy of the Kinematics Model as empirical handbook criteria for failure initiation are used.

Summarising the investigation on the influence of the discretisation, several discretisation parameters were analysed with the focus on a maximum coarse structural representation to achieve model efficiency without the loss of model accuracy.

Investigations of the required mesh size led to a model efficient compromise that specifies a minimum number of elements along the frame height and uses fully integrated elements in the inner and middle flange to ensure model accuracy without further mesh refinement. Further model efficiency could be achieved by reasonable merging of the layup stacking sequence as well as by the reduction of the number of integration points per layer. Figure 4-21 compares the model efficiency of typical detailed modelling with the final kinematics modelling on the basis of the frame-stringer-skin simulation model with the small, filigree frame design. Summarising the discretisation aspects discussed above the model efficiency of the final kinematics modelling approach provides a factor of $f = 0.034$ relative calculation time compared to detailed modelling.

Minor discrepancies in the initiation of instability modes compared to detailed modelling will have no influence on the model accuracy as the initiation of instabilities is defined in the Kinematics Model by empirical handbook criteria.

Hence, the finally defined discretisation for the Kinematics Model significantly improved the model efficiency without the loss of accuracy.

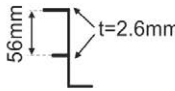
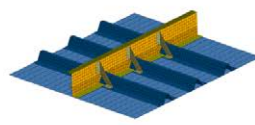
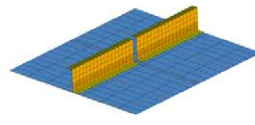
 <i>small, filigree frame design</i>	 detailed modelling	 kinematics modelling
frame discretisation (typical element size)	8mm x 12mm	12.5mm x 20mm
initial time increment	1.75e-04ms	4.51e-04ms
number of elements (frame-stringer-skin model)	4756	650
element integration	full integration	reduced integration (except the frame inner and middle flange)
number of integration points (through thickness per layer)	three	one
layup definition	full layup	reasonable merging
modelling <ul style="list-style-type: none"> - of the stringers - of the mouseholes 	detailed shell modelling considered	simplified beam modelling omitted
Calculation time	63:14min	02:09min
Relative calculation time	1.0	0.034

Figure 4-21: Model efficiency of the final kinematics modelling

4.6. Influence of the bending-compression ratio

In some of the investigations discussed in the paragraphs above, generic frame-stringer-skin models were analysed with pure moment load. The concentration on pure moment load should focus on the individual targets of the above investigations. In realistic crash scenarios a combined load of moment and normal force acts on the frame-stringer-skin structure. Depending on the location in the fuselage section and the crash phase, high normal forces can act on the structure. Especially in the critical sub-passenger floor area the normal forces are generally in compression direction. In this area, high compression forces can lead to small bending-compression ratios which influence the failure behaviour of the fuselage structure.

In this paragraph typical bending-compression ratios are discussed which act on a frame structure of a fuselage section during a typical crash event. The influence of these bending-compression ratios on the behaviour of the kinematic hinge architecture is highlighted. Finally, the influence of the bending-compression ratio on the failure behaviour of a frame-stringer-skin

structure is discussed and assessed with the failure criteria which were defined for pure moment loads in paragraph 4.2.1.

4.6.1. Identification of typical bending-compression ratios

The frame structure of the sub-passenger floor area can be divided in two different regions which experience different maximum loadings at different phases during a typical crash event. The frame region between cargo-crossbeam and vertical support strut is one of these frame regions. After the failure of the sub-cargo area first frame failure typically occurs in this region. The crash phase which is of interest to analyse the bending-compression ratio in this region is the period between the first impact of the fuselage and the failure of the frame, respectively the triggering of the kinematic hinges. With respect to a standard crash scenario² of a typical single-aisle transport aircraft this period is approximately between $t_1 = 0$ ms and $t_2 = 50$ ms. Figure 4-22 illustrates the bending-compression ratio during this period in two cutting surfaces which are positioned in this critical frame region at $\alpha_1 = 25^\circ$ and $\alpha_2 = 34^\circ$. The depicted results were generated in a simulation of a generic CFRP single-aisle fuselage section. The bending-compression ratio is defined as

$$r = \text{bending moment} / \text{normal force [mm]}.$$

The moment load was analysed with respect to a reference point that is located in the centre of the cross-section area. The cutting surfaces include the frame as well as the skin structure. Caused by the dynamic nature of a crash event the bending-compression ratio tends to high oscillations. Therefore, the graphs in the diagrams of Figure 4-22 are filtered with a butterworth filter and a cut-off frequency of $f = 180$ Hz. The raw data graphs, with a sampling frequency of $f = 2$ kHz, are additionally illustrated in grey colour.

Figure 4-22a) depicts the measured bending-compression ratio of cutting surface CS-02. A mean value of $r_2 = 400$ mm can be identified for the considered crash phase. The ratio in cutting surface CS-01 is illustrated in Figure 4-22b). The graph shows values which are mainly above a ratio of approximately $r_1 = 200$ mm.

In general, a bending-compression ratio higher than $r = 150$ mm was identified in the frame region between the sub-cargo area and the vertical support strut.

² Within this thesis, the ‘standard crash scenario’ specifies impact conditions of a vertical impact with $v_i = 6.7$ m/s, fully loaded overhead bins, occupied seats, zero pitch and roll angle. Cargo loading is not considered in this case.

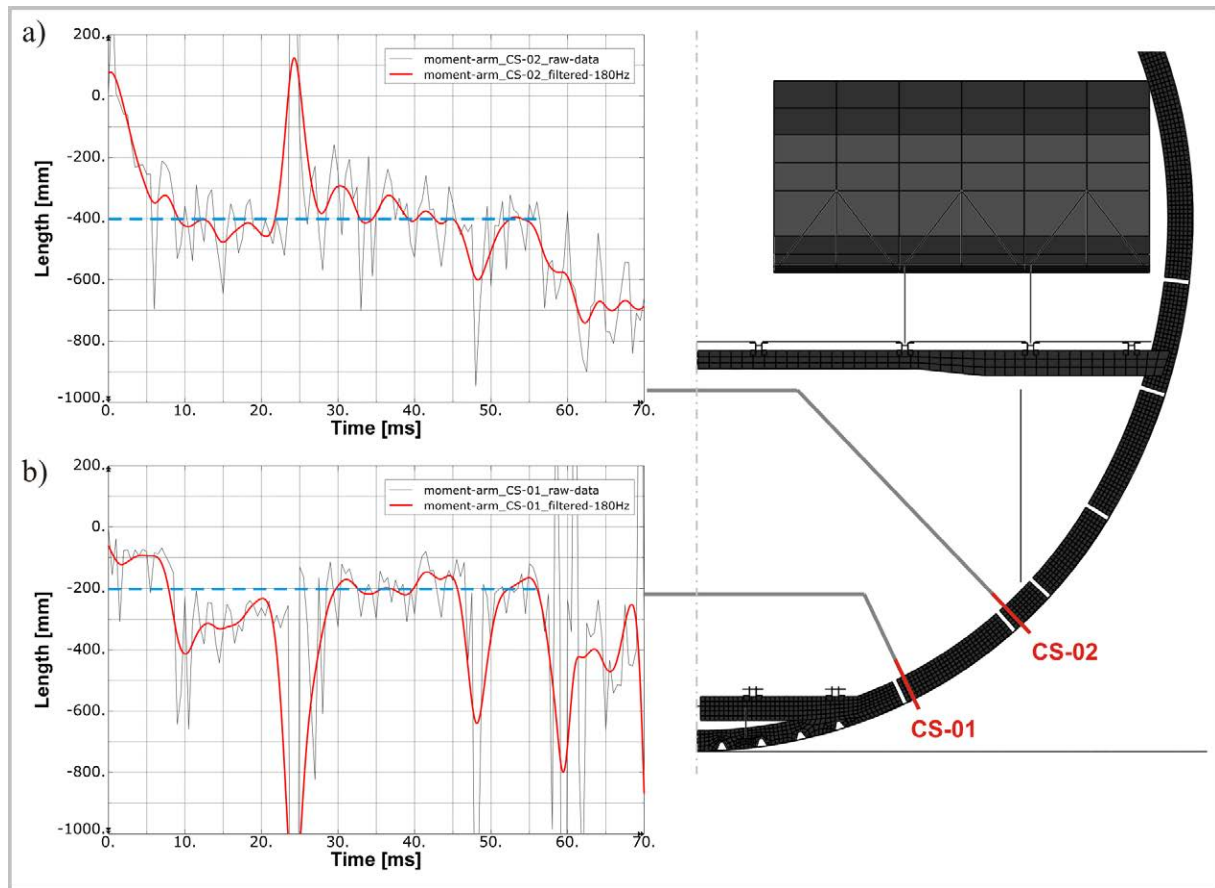


Figure 4-22: Typical bending-compression ratios in the lower side shell

The second frame region of the sub-passenger floor area is the frame part between vertical support strut and passenger crossbeam. Here, the crash load typically reaches its maximum at a later state of a crash event, when the vertical struts hit the ground. With respect to a standard crash scenario of a typical single-aisle transport aircraft this period is approximately between $t_1 = 80$ ms and $t_2 = 140$ ms. Figure 4-23 illustrates the bending-compression ratio of two cutting surfaces which are located in the so-called “Bermuda triangle” at $\alpha_3 = 49^\circ$ and $\alpha_4 = 60^\circ$. Similar to the graphs in Figure 4-22 a butterworth filter with a cut-off frequency of $f = 180$ Hz was used to filter the raw data which were sampled with a frequency of $f = 2$ kHz. Both graphs in Figure 4-23a) and 4-23b) show the typical plateau of a low bending-compression ratio which is caused by high compression forces during the impact of the Bermuda triangle. The results depicted in Figure 4-23 are based on a load case with a high initial velocity of $v_i = 9.1$ m/s (30 ft/s). In such a crash scenario, a certain amount of kinetic energy is still in the fuselage structure when the Bermuda triangle impacts on the ground. This leads to minimum values of the bending-compression ratio in both cuttings surfaces of $r = 75$ -100 mm.

In general, a bending-compression ratio higher than $r = 50$ mm was identified in the frame region of the Bermuda triangle. In a few crash cases, ratios lower than $r = 50$ mm could be identified for short durations.

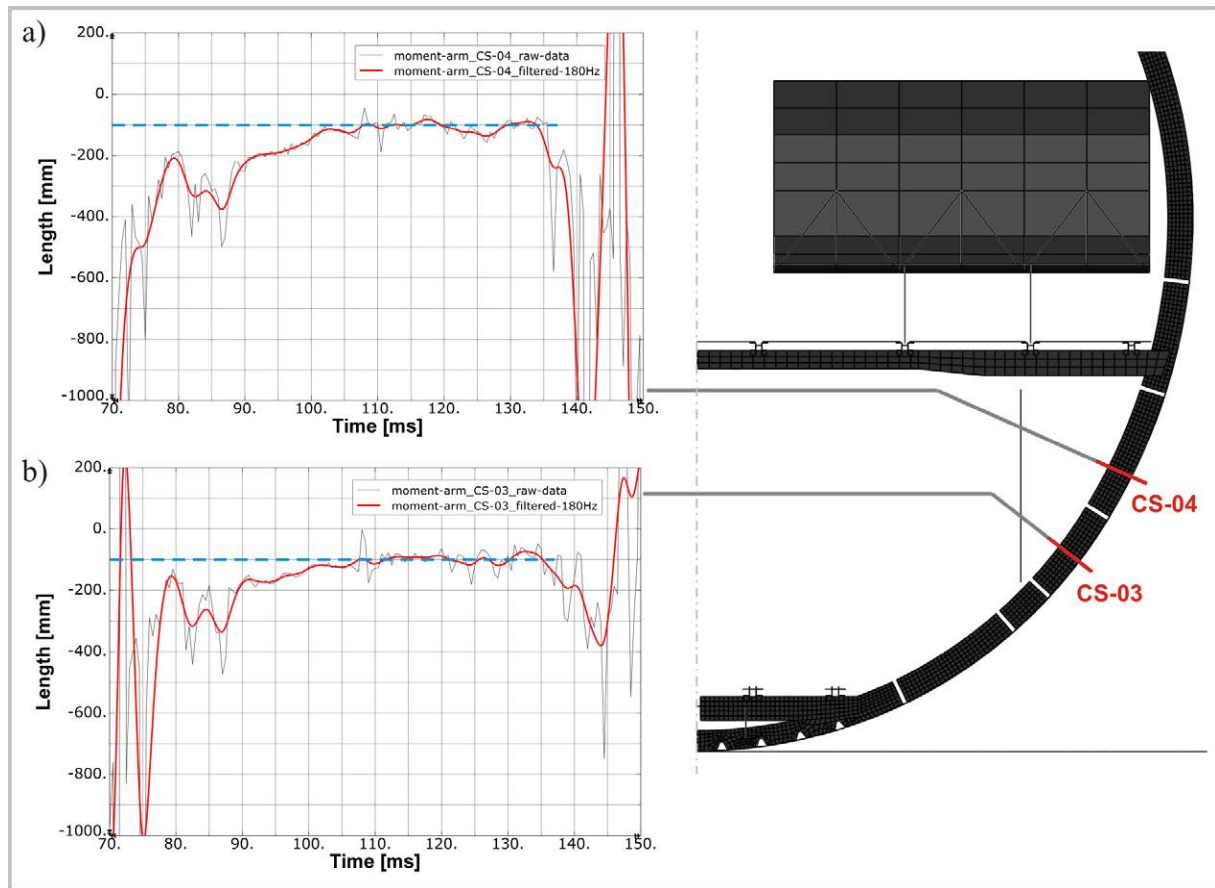


Figure 4-23: Typical bending-compression ratios in the Bermuda triangle

4.6.2. Influence of the bending-compression ratio on the kinematic hinge behaviour

The investigation on typical bending-compression ratios identified values of $r > 150$ mm in the critical frame region between cargo-crossbeam and vertical strut and $r > 50$ mm in the region of the Bermuda triangle. In the following, the influence of these bending-compression ratios on the behaviour of the kinematic hinges is investigated.

The investigation on the bending-compression ratio is based on the generic frame-stringer-skin model that was simulated with different frame profiles according to Figure 4-5b) – 4-5e). The generic simulation model represents the frame-stringer-skin structure in the Kinematics Model approach and is illustrated in Figure 4-24a). A kinematic hinge is positioned in the centre of the frame segment. The stiffness of the kinematic hinge was calibrated under pure moment load with respect to the frame inner flange strain, as discussed in paragraph 4.2.2. After the calibration under pure moment load different bending-compression ratios were applied on the model. Results with filigree as well as with massive frame design are depicted in Figure 4-24b) and 4-24c). In the diagrams the strains along the frame inner flange are illustrated over the simulation time respectively over the moment/compression load.

Under pure moment load ($r = \infty$) both model variants (filigree and massive frame design) show good correlation between the flange strain and the kinematic hinge strain. With a bending-compression ratio of $r = 150$ mm a small derivation of the kinematic hinge strain is visible. Significant discrepancy between the kinematic hinge strain and the strain along the frame inner flange can be identified with a bending-compression ratio of $r = 50$ mm for both model variants. Furthermore, in case of $r = 50$ mm higher deflection of the kinematic hinge strain can be identified for the massive frame design compared to the filigree frame design.

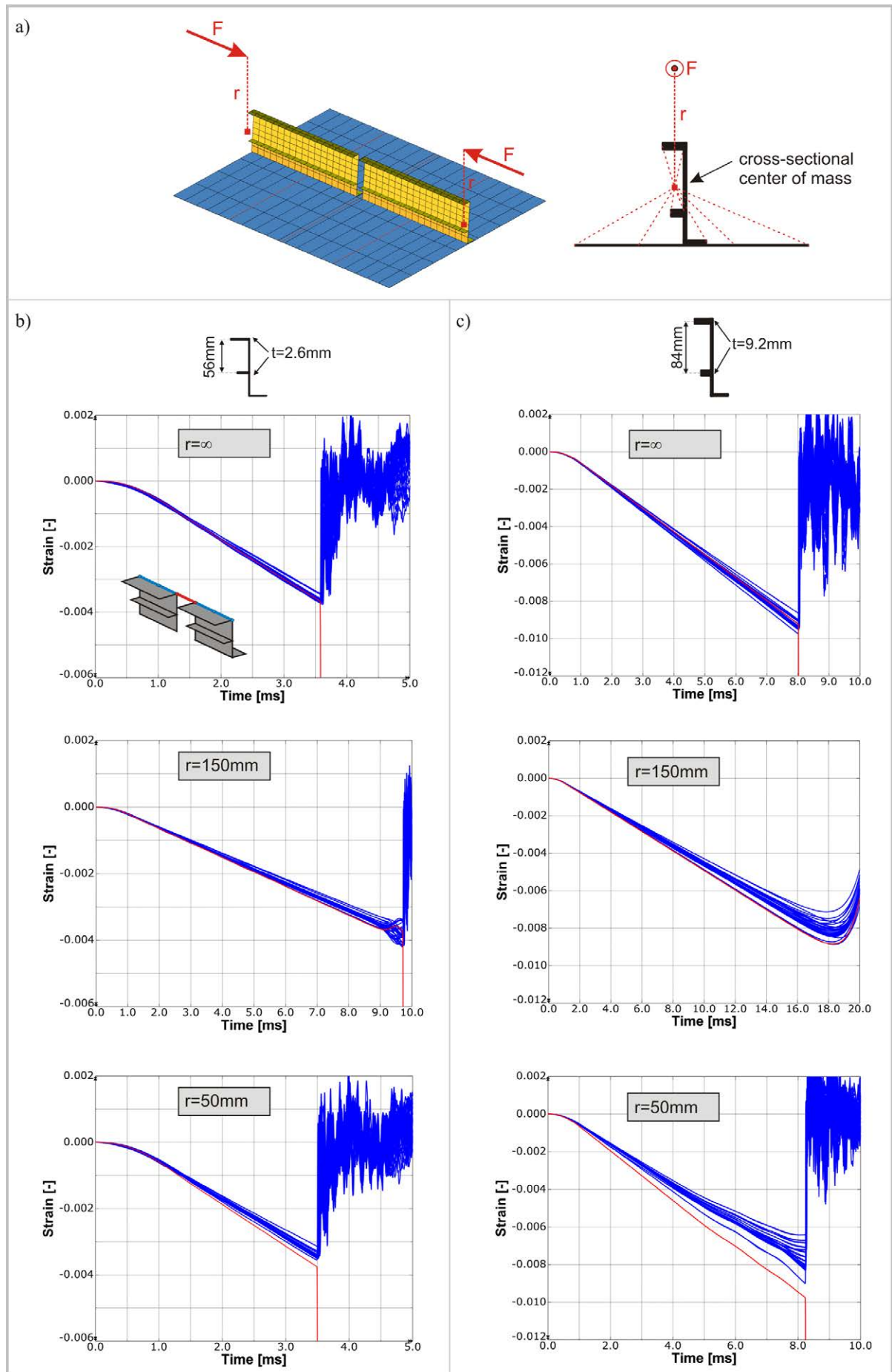


Figure 4-24: Elastic behaviour of the kinematic hinge in dependence of the bending-compression ratio

The effects that lead to the observed differences of kinematic hinge stiffness and frame stiffness with decreasing bending-compression ratio are explained in the following. Exemplarily, the strain graphs of Figure 4-24c), for $r = \infty$ and $r = 50\text{mm}$, are plotted again in Figure 4-25. Here, the mean value of the frame inner flange strains as well as the kinematic hinge strain is plotted over the frame inner flange displacement. For $r = \infty$ good correlation of the linear slope can be identified between the mean values of the frame inner flange strains as well as the kinematic hinge strain. In contrast to this, the kinematic hinge strain of $r = 50\text{ mm}$ clearly differs. Besides the discrepancy in the elastic slope a small difference in the trigger strain of the kinematic hinge of $\Delta\varepsilon \approx 0.5\text{e-}03$ can be identified.

The small difference in the trigger strain is caused by the kinematic hinge architecture. The characteristic of the kinematic hinge is described by a moment-rotation relation. The translational degrees of freedom are constrained. These numerical constraints in the connector element are not infinitely rigid. In case of high normal forces a marginal displacement in the translational degree of freedom leads to this small difference in the trigger strain.

The more significant deflection in the elastic slope of the kinematic hinge strain is caused by different locations of the elastic centre of the frame-skin cross-section and the pivot point of the kinematic hinge. The positioning of the macro element in the kinematic hinge architecture was already discussed in paragraph 4.2 and 4.3 with respect to the pre- and post-failure behaviour of a frame-skin structure. The position of the macro element in the skin plane is essential with respect to the post-failure behaviour. The drawback of this location is a load-dependent elastic behaviour of the kinematic hinge. In case of a combined loading of moment and normal force, the normal force acts in the elastic centre of the frame-skin cross-section. With respect to the kinematic hinge pivot point positioned in the skin plane this normal force induces an additional moment on the rotational degree of freedom of the macro element. Figure 4-26 illustrates this relation. The effect is a higher strain in the kinematic hinge compared to the frame inner flange strain. The higher the distance between elastic centre and pivot point the more this effect is observable. Hence, low bending-compression ratios in combination with a massive frame design leads to higher deflection of the kinematic hinge behaviour compared to a filigree frame design, as observed in Figure 4-24.

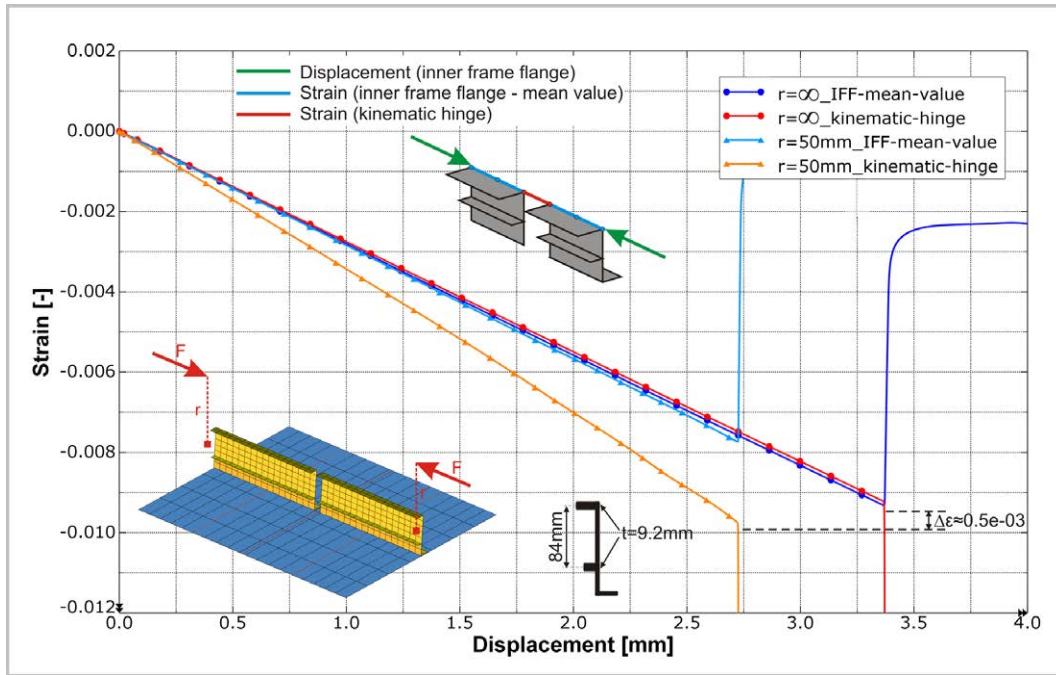


Figure 4-25: Strain along the frame inner flange for different bending-compression ratios

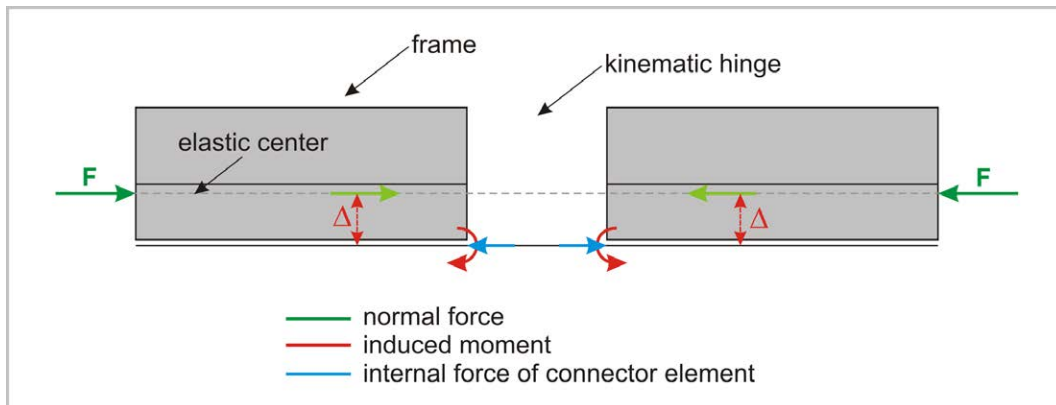


Figure 4-26: Additional moment load caused by different locations of the elastic centre and the pivot point

The comparison of the kinematic hinge accuracy in dependence of the bending-compression ratio in Figure 4-24 generally shows an acceptable behaviour up to a ratio of $r = 150$ mm. Ratios smaller than $r = 150$ mm lead to a significant loss of the kinematic hinge accuracy. The investigation discussed in paragraph 4.6.1 highlighted that a ratio smaller than $r = 150$ mm typically occurs in the region of the Bermuda triangle when high compression forces are induced by the impact of the vertical struts. With respect to such cases, the kinematic hinges in that region should be calibrated for low bending-compression ratios instead of pure moment load. This calibration would represent too stiff kinematic hinge behaviour during the first crash phases. But during the critical crash phase, when triggering of the kinematic hinges is expected, good correlation can be achieved.

Summarising the above discussed investigation, typical bending-compression ratios were identified and the kinematic hinge behaviour was analysed for different ratios. In general, good

accuracy of the kinematic hinge was identified for typical bending-compression ratios. With respect to very low bending-compression ratios, the kinematic hinge showed inaccurate tendencies. Potential calibration based on lower bending-compression ratios may compensate this effect.

4.6.3. Influence of the bending-compression ratio on the failure behaviour of a frame-stringer-skin structure

In the following, the influence of the bending-compression ratio on the validity of failure criteria is discussed. In paragraph 4.2.1 failure criteria were defined with respect to pure moment load on a frame-stringer-skin structure. The strain along the frame inner flange as well as along the frame outer flange of a LCF-shaped frame was identified to serve as failure criteria for opening and closing bending failure. In case of additional normal load the same failure criteria are still valid for the indication of potential frame failure. The frame middle flange remains uncritical in all load variations.

In the extreme case of pure normal load ($r = 0$ mm) the frame middle flange experiences the same strain magnitude compared to frame inner and outer flange. Typical LCF- shaped frame design defines the frame inner and middle flange of higher stiffness, respectively thickness, compared to the frame outer flange. The crippling strain criteria are more critical for the frame outer flange as for the frame middle and inner flange. Hence, the frame middle flange is uncritical in all loading conditions. To illustrate this effect, simulations were performed of different LCF-shaped frame profiles and different loading conditions ($r = \infty$, $r = 50$ mm). Figure 4-27 provides the simulation results and depicts the mean value of the frame flange strains plotted over the frame inner flange displacement. Exemplarily, the filigree frame design, Figure 4-27b), and the massive frame design, Figure 4-27c), are given. The diagrams illustrate opening bending in case of positive frame inner flange displacement and closing bending in case of negative frame inner flange displacement. The diagrams of the variant $r = 50$ mm illustrate a combined loading of bending and compressive normal force. In the diagram $r = 50$ mm, Figure 4-27c) shows that frame middle and outer flange strains are close to each other. This is one of the cases when the frame middle flange experiences nearly the same strain magnitude than the frame outer flange. Nevertheless, the crippling strain limit of the frame outer flange is generally more critical which is why even in such cases the frame middle flange is not critical. Hence, the general validity of the frame failure criteria, defined in paragraph 4.2.1, could be proved even in case of untypical high normal load.

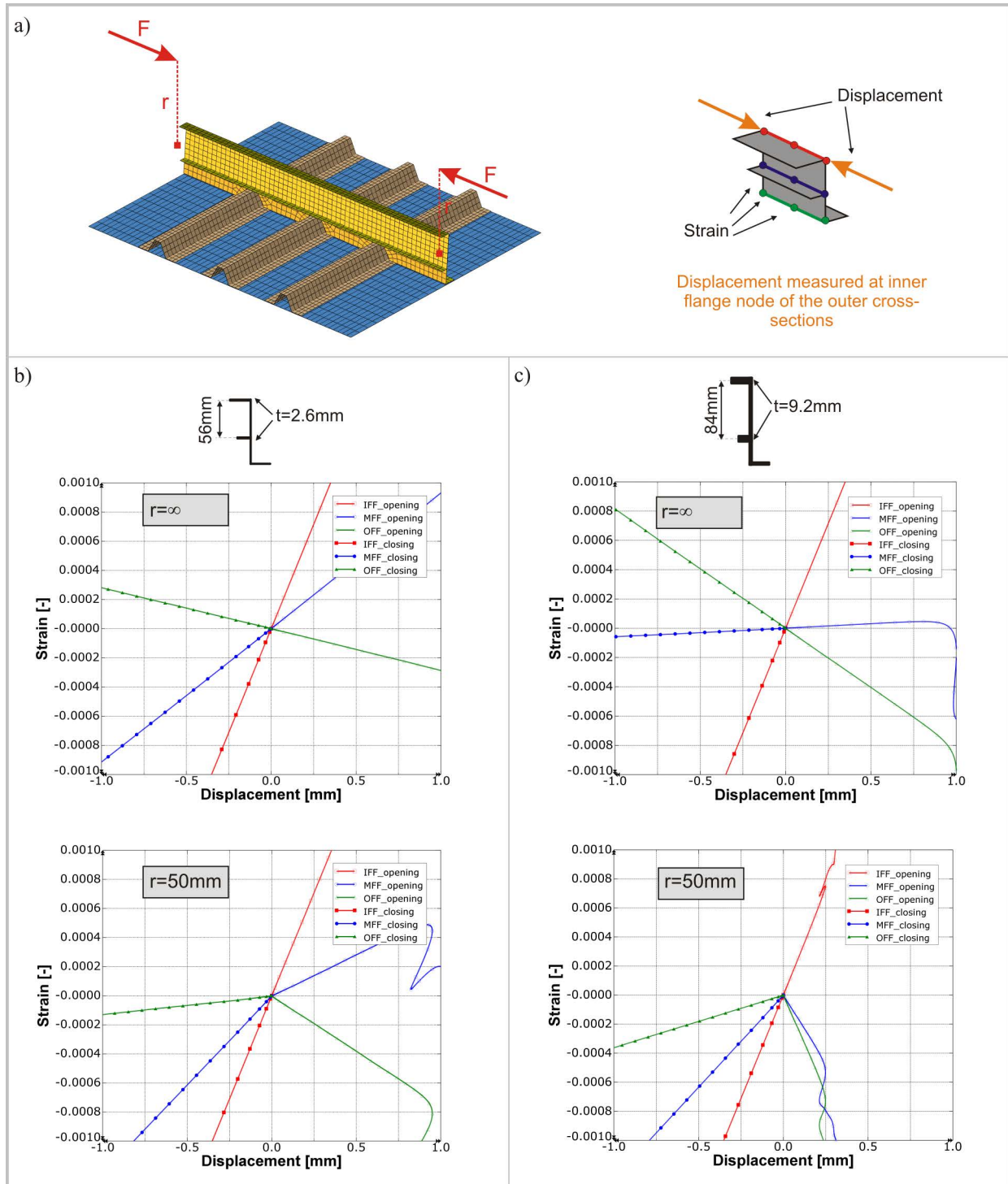


Figure 4-27: Influence of the bending-compression ratio on the elastic behaviour of a frame-stringer-skin structure

4.7. Summary – the final kinematic hinge macro architecture

The final macro architecture of the kinematic hinge is based on the investigations discussed in the previous paragraphs. In chapter 3.2.3 the basic macro architecture was already presented. In the following the main properties of the kinematic hinge, which were derived from the detailed investigations, are summarised. Figure 4-28 illustrates the properties of the final kinematic hinge architecture.

The positioning of the kinematic hinges in a model of a fuselage section is firstly defined according to the data basis of known experimental test results. Secondly, the positioning is defined according to the strain distribution in the frame flanges which are derived from numerical simulation of a preliminary Kinematics Model without kinematic hinges in the frame.

Lateral frame support is effected sufficiently by the kinematic hinge itself, as discussed in paragraph 4.4. Potentially, additional lateral support by nodal constraints can be defined in regions of the fuselage section where long frame segments are defined without kinematic hinge. This is potentially the case in the upper fuselage area where frame failure is expected only at few locations.

The kinematic hinge architecture is described mainly based on the discussion of pre- and post-failure behaviour of a frame-stringer-skin structure. A cut in the frame represents the discontinuity of the elastically modelled frame structure. Both free cross-sections of the frame are reinforced by rigid bodies. The macro element, a connector element in case of the FE code ABAQUS/Explicit, is positioned in the skin plane and connects both rigid bodies of the frame cross-sections. The connector element describes the frame pre- and post-failure characteristic by a moment-rotation curve. In this macro element the rotational degree of freedom is the only active one. In particular, the degree of freedom in the longitudinal frame direction is constraint. Due to the small length of the kinematic hinges compared to the total frame length in a fuselage section this rigid behaviour has no significant influence. With respect to the kinematic of such a hinge the longitudinal displacement in the skin plane respectively in the frame outer flange is fixed whereas the longitudinal displacement in the frame inner flange is described by the moment-rotation curve. Hence, calibration of the initial slope in the moment-rotation curve, which represents the elastic frame behaviour, is defined with respect to the frame inner flange strains. In addition, the trigger moment is generally calibrated with respect to a limit strain in the frame inner flange. This definition is conform to typical trigger mechanisms which are specified and located in the frame inner flange. Nevertheless, potential failure of the frame outer flange has to be checked besides the kinematic hinge by empirical strain criteria, as discussed in paragraph 4.2.1.

In addition to that, Figure 4-28 illustrates some properties of the kinematic hinge with the focus on model simplifications. For an improved simulation performance a coarse modelling is desired. In paragraph 4.5 minimum modelling refinements were identified to ensure adequate accuracy. These minimum refinements are a discretisation with at least two shell elements along the frame inner flange width to allow the formation of instability modes. At least five shell elements over the frame height are required to avoid the risk of extensive generation of hourglass

energy. In addition, reduced element integration, merged layup definition as well as a reduced number of integration points through the thickness were identified as a proper method to improve simulation performance within an adequate accuracy. With respect to the frame inner and middle flange, full element integration is used in favour of a relatively large element size.

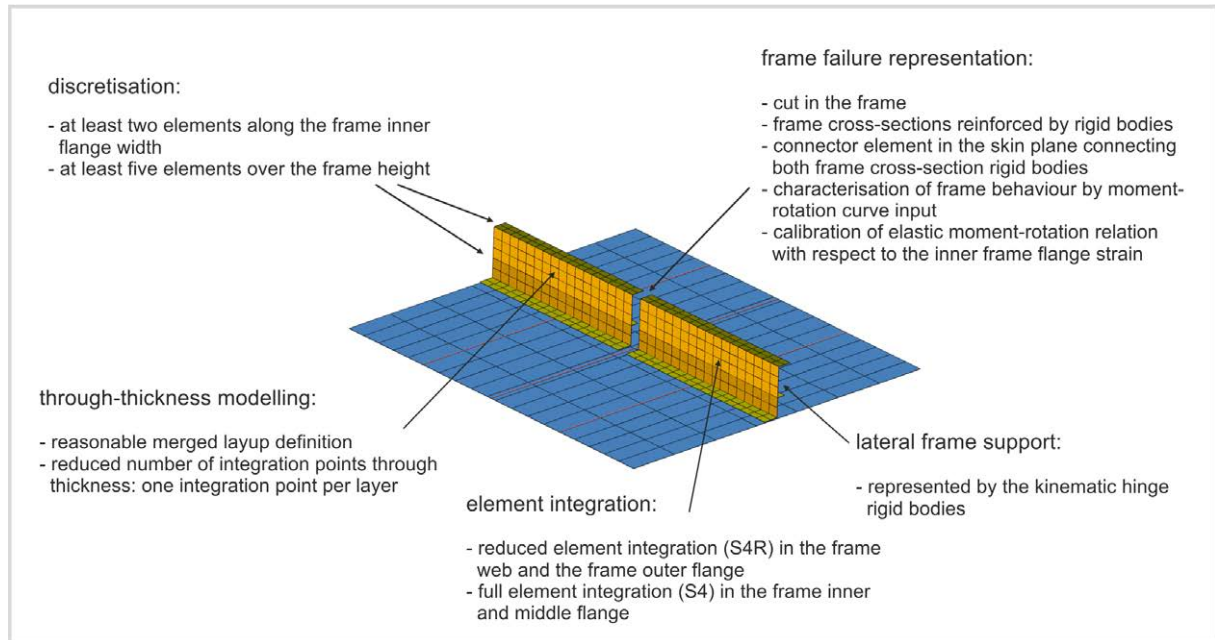


Figure 4-28: Final kinematic hinge macro architecture

5. Implementation of a user element for frame failure modelling

The development of the kinematic hinge architecture, discussed in chapter 4, was performed on the basis of standard macro elements which are provided by the commercial FE solver. The selection of an appropriate standard macro element was described in chapter 3.2.1. Outcome of this development is the final kinematic hinge architecture that is described in paragraph 4.7. This macro architecture enables the representation of typical frame failure mechanisms in a realistic and adequately accurate way. Although this failure representation is well sufficient with respect to a preliminary design tool, some limitations in the kinematic hinge architecture were the motivation to raise some effort for further improvement of the frame failure representation. In paragraph 5.1 a discussion of these limitations will identify that some of them are caused by restrictions of the standard macro element which is used in the kinematic hinge. The absence of proper standard macro elements, which are able to overcome these restrictions, led to the consideration of the development of a specific user element.

Implementation of user subroutines in an explicit finite element code is a decision which has to be balanced carefully. High effort is essential to obtain a qualified user element. Besides the programming of the subroutine an extensive verification is essential. In addition, the performance of element calculation is very important in an explicit code. Hence, the source code has to be written primarily with respect to efficient calculation, otherwise the user element is not suitable due to high costs of CPU time.

The weighting of arguments finally resulted in the decision to program such a user element. Paragraph 5.1 discusses the requirements which were gathered with respect to an improved macro element in the kinematic hinge. These requirements are mainly based on some limitations of the standard connector element which is used in the final kinematic hinge architecture according to chapter 4.7.

The following described work is based on the explicit finite element code ABAQUS/Explicit. A user element interface for explicit time integration is available in ABAQUS since the version V6.7 [104,116]. The implementation of the user element was performed based on ABAQUS versions V6.7, V6.8 and V6.9. Due to the recent option of a user element interface, the implementation was affected by several bugs which were partly solved in later versions (V6.9) of

ABAQUS. Some issues in the ABAQUS subroutine interface are still present for what reason the user element could finally not be implemented in the fuselage section model. Nevertheless, the implementation of the user element is completed and all functionalities could be proved.

In the following, paragraph 5.1 discusses requirements for an improved macro element. Paragraph 5.2 describes the programming of the user element. The verification process is documented in paragraphs 5.3 and 5.4 whereas paragraph 5.5 gives an outlook due to unsolved issues in the considered FE solver versions.

5.1. Requirements for an improved macro element

A catalogue of requirements was prepared which represents the basis for the development of a user element subroutine. A critical review of the final kinematic hinge architecture based on standard finite elements identified some limitations which shall be solved by the user element. Some additional requirements define the format of input definition as well as further improvements of the kinematic hinge options.

As discussed in paragraph 4.6 the kinematic hinge provides limited accuracy in case of low bending-compression ratios smaller than $r = 150$ mm. These low ratios can occur in case of high compression peaks, for instance when the vertical support struts hit the ground. The main reason for a deflection in the kinematic hinge accuracy in case of such low bending-compression ratios is the representation of frame longitudinal stiffness located exclusively in the skin plane. Due to this offset with respect to the elastic centre an additional moment is induced which leads to higher displacement in the kinematic hinge at the frame inner flange. This circumstance was discussed in paragraph 4.6 and is illustrated again in Figure 5-1a). To improve the kinematic hinge accuracy in case of low bending-compression ratios, the frame longitudinal stiffness has to be defined uniformly over the frame height. Hence, additional forces of the kinematic hinge macro element have to be applied at the frame inner flange, as displayed in Figure 5-1b). The ratio of applied force at the frame inner and outer flange has to be defined in a way that equilibrium of moment is given with respect to the elastic centre. A consequence of this requirement is the definition of a 4-node user element instead of a 2-node element, like the standard connector element, to apply the required forces in the frame inner flange.

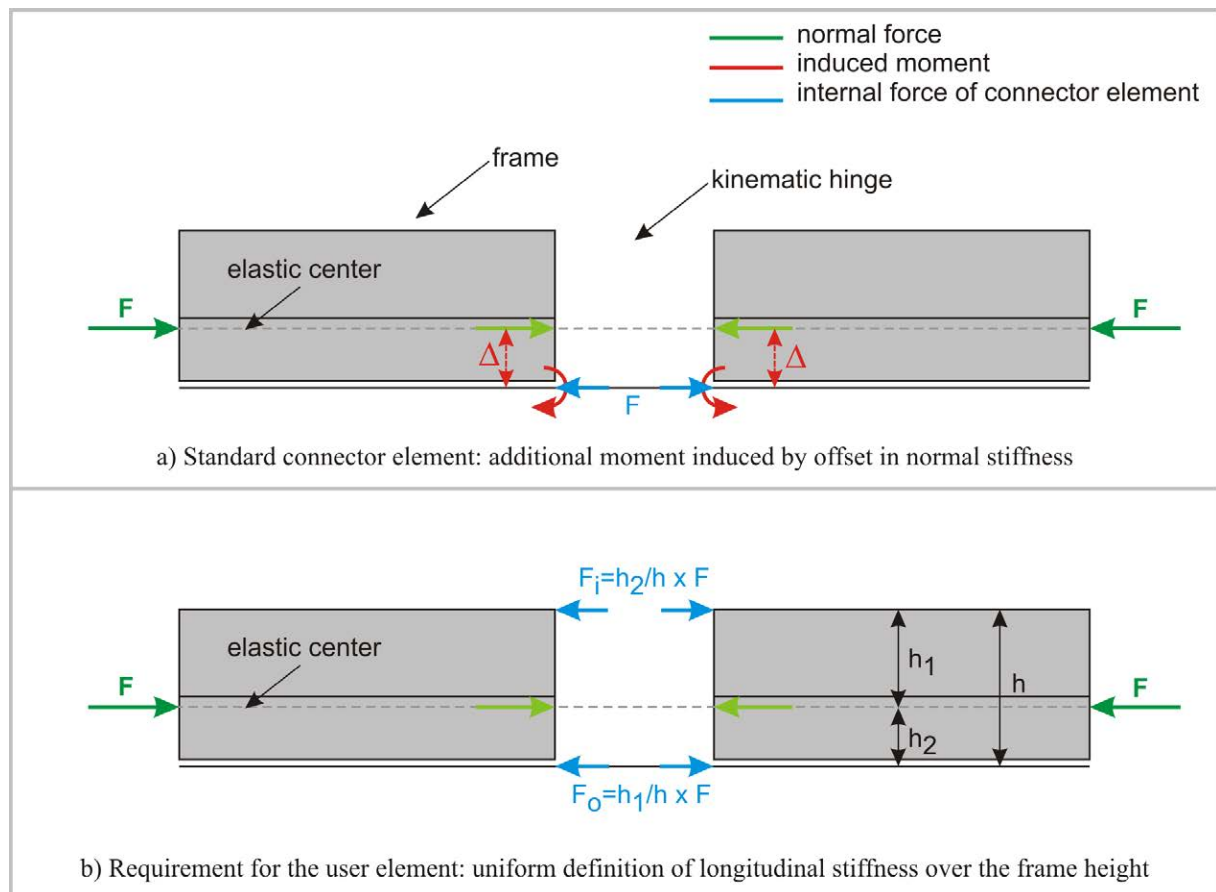


Figure 5-1: Applied forces of normal stiffness in the kinematic hinge

In addition, the discussion in paragraph 4.6 identified a small discrepancy in the trigger strain of the kinematic hinge in case of low bending-compression ratios. This discrepancy is caused by a finite stiffness of the fixed translational degree of freedom in the standard connector element. A trigger criterion based on strain instead of moment load would enable accurate triggering with respect to a strain failure criterion defined in the frame inner flange. In Figure 5-2 this trigger concept is compared to the trigger procedure of the standard connector element. Using the connector element, the trigger moment in the moment-rotation input curve is defined by calibration with a frame-stringer-skin reference model. The trigger moment is calibrated such that the desired strain in the frame inner flange is reached in the reference model. In contrast to this, the user element shall directly measure the strain in the frame inner flange and initiate triggering when the measured value exceeds the defined trigger strain criterion. A consequence of this requirement is again a 4-node user element. Additional element nodes in the frame inner flange are necessary to obtain the nodal displacement respectively the strain in the frame inner flange.

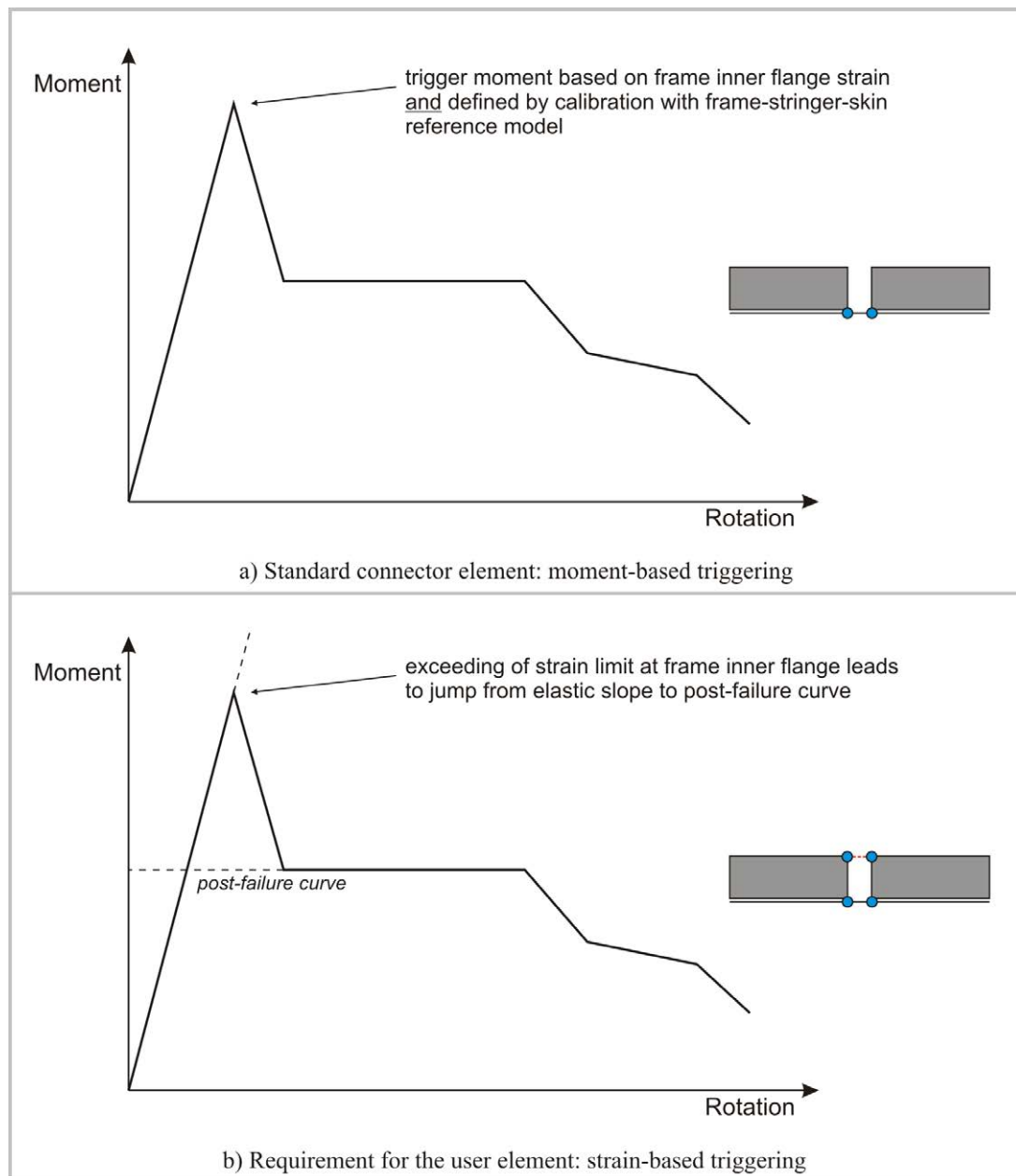


Figure 5-2: Comparison of trigger concepts in the kinematic hinge

A further requirement was identified in the critical review of the kinematic hinge architecture based on the standard connector element. The unloading and reloading characteristic of the connector element can be defined in the tabular input version with an unloading curve as well as a slope which defines the transition between main curve and unloading curve. Reloading behaviour of the connector element follows the unloading curve backwards and finally along the slope to the point at the main curve where unloading started. Physically more correct with respect to the unloading/reloading behaviour is the characterisation of a hysteresis. Especially in dynamic problems numerous unloading/reloading cycles are expected so that hysteresis effects can have influence on the kinematic hinge behaviour. Figure 5-3 illustrates this unloading behaviour and compares the hysteresis approach with the standard connector element behaviour.

Another requirement with respect to the unloading/reloading characterisation is the behaviour after zero crossing. The standard connector element behaviour during unloading follows the defined unloading input curve up to the main curve of opposite direction loading. Further unloading follows this main curve input. In Figure 5-3a) this behaviour is displayed. With respect to the physical behaviour of frame failure this characterisation is not correct. Although such a large unloading is expected only in very few cases, the user element shall provide physically correct behaviour in this item. Figure 5-3b) illustrates the unloading behaviour which is required for the user element.

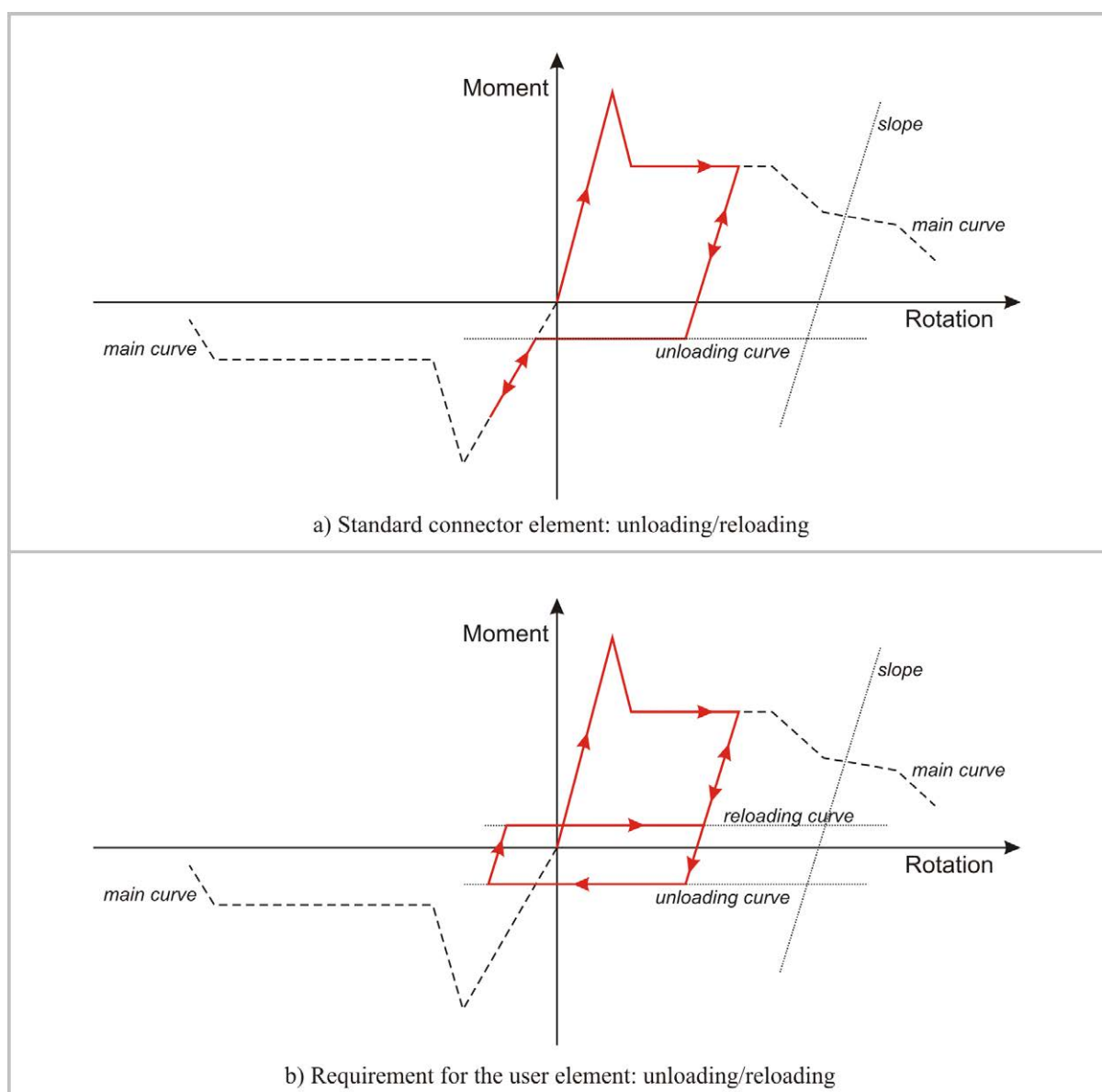


Figure 5-3: Comparison of unloading/reloading concepts in the kinematic hinge

Finally, requirements for the user element were defined with respect to the input format. Several input options are possible to define failure behaviour. Failure definition by damaging or plasticity parameters are conceivable as well as tabular curve input. Characterisation by tabular input is advantageous in this case as the failure behaviour can easily be described by a moment-

rotation relation. This is even more favourable when the kinematic hinge input is based on component test data or the final hinge characteristic defines the basis for the development of a crash device in the frame. Nevertheless, pure tabular input does not offer the possibility of strain based triggering. Hence, a combined input format is required for the user element. Elastic behaviour shall be defined by a stiffness value whereas tabular curve input is required for the description of the post-failure behaviour. The strain based trigger criterion initiates the transition from the elastic behaviour to the post-failure characteristic. The slope of this transition shall be definable by a stiffness value. With respect to the unloading behaviour the slope between main curve and unloading curve shall similarly be defined by a stiffness value. The unloading as well as the reloading curve shall be assumed to be constants. Figure 5-4 illustrates these input parameters which shall be individually definable for the opening and the closing bending direction.

Additional input parameters shall be defined for the normal stiffness in tension and compression for consideration of normal loads. Finally, the interval for history output of the element variables shall be defined in the input deck. In contrast to the output frequency, the list of element variables to be output shall be defined directly in the subroutine and not in the ABAQUS input deck of the user element.

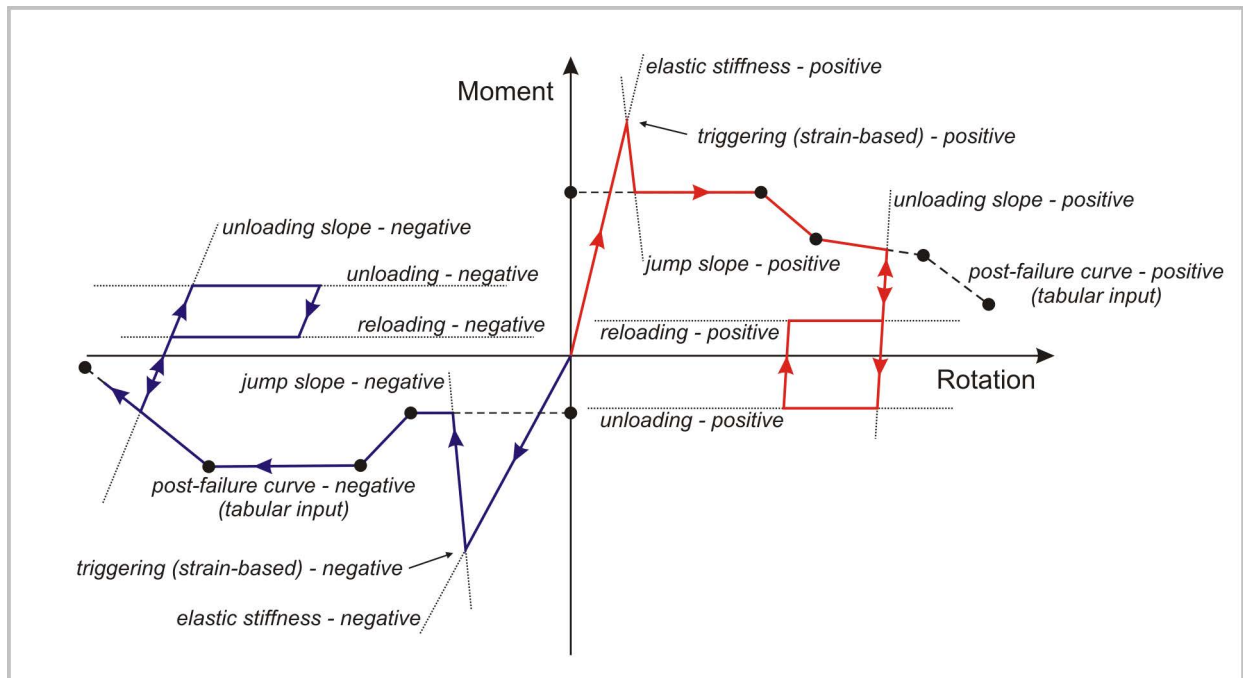


Figure 5-4: Required input parameters of the user element for the description of the moment-rotation behaviour

5.2. Implementation of the user element

The user element subroutine, called VUEL, was written as FORTRAN code and included in the kinematic hinge model using the Intel FORTRAN Compiler version 10.1.014 as well as the ABAQUS/Explicit versions V6.7-3, V6.8-1 and V6.9-1 on a Microsoft Windows machine. The interface which is used to implement the user subroutine in an ABAQUS analysis is given in [116].

In the following the description of the user element programming is organized chronologically to discuss the routine of the user element step by step. Figure 5-5 gives an overview of the user element architecture. The individual aspects of the source code architecture are discussed in this paragraph with the focus on the calculation of the internal loads which represent the user element behaviour respectively the frame failure characteristic of the kinematic hinge.

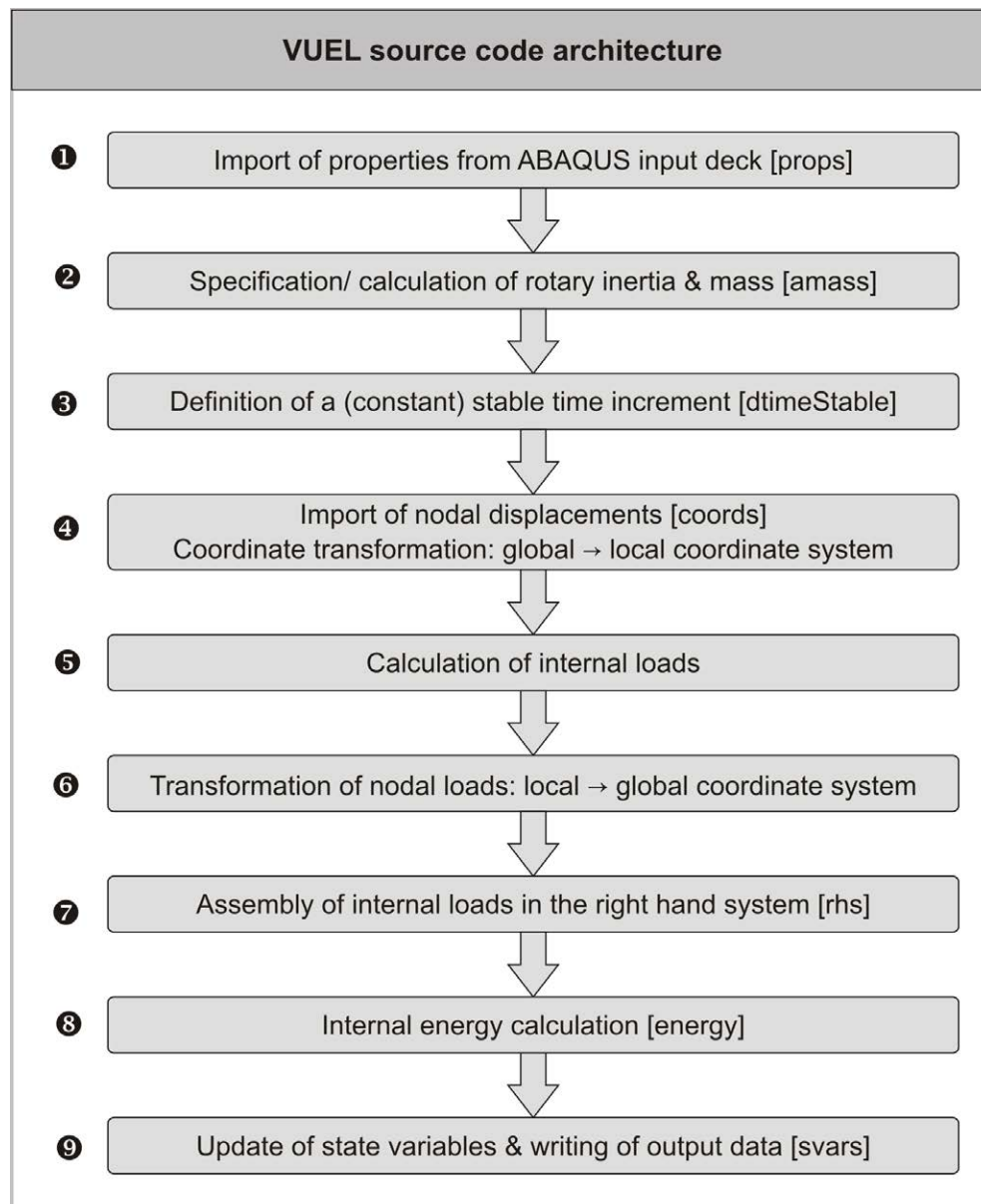


Figure 5-5: User element (VUEL) architecture

The ABAQUS input deck provides an interface for the user element where element data (*user element) as well as data of the element behaviour (*uel property) can be defined. The element data contain:

- Number of nodes of the element
- Number of property parameters to describe the element behaviour
- Number of coordinates at each element node
- Number of solution-dependent state variables to be stored within the element

The input deck of the user element is given in Appendix A3.1.

Based on the requirements of paragraph 5.1 a 4-node user element was developed. With respect to the kinematic hinge architecture this user element substitutes the standard connector element in one rotational (frame bending) as well as in one translational (frame normal compression) degree of freedom. Both degrees of freedom are used to describe the main crash behaviour of a frame structure. All other degrees of freedom are still constraint by a connector element that is installed in the kinematic hinge in parallel. The outer nodes of the user element are positioned in the skin plane and share these nodes with the standard connector element. The inner nodes are positioned at the frame inner flange in the frame web plane and share these nodes with the structural shell elements. All four user element nodes are included in the rigid bodies which reinforce the frame cross-sections. Each element node is defined with three translational and three rotational degrees of freedom. Figure 5-6 illustrates the kinematic hinge architecture with the user element as well as the definition of nodal degrees of freedom in the user element. Whereas nodal forces of frame normal stiffness is applied to all user element nodes, the moments of the rotational degree of freedom are applied exclusively to node 1 and 2, similarly to the standard connector element.

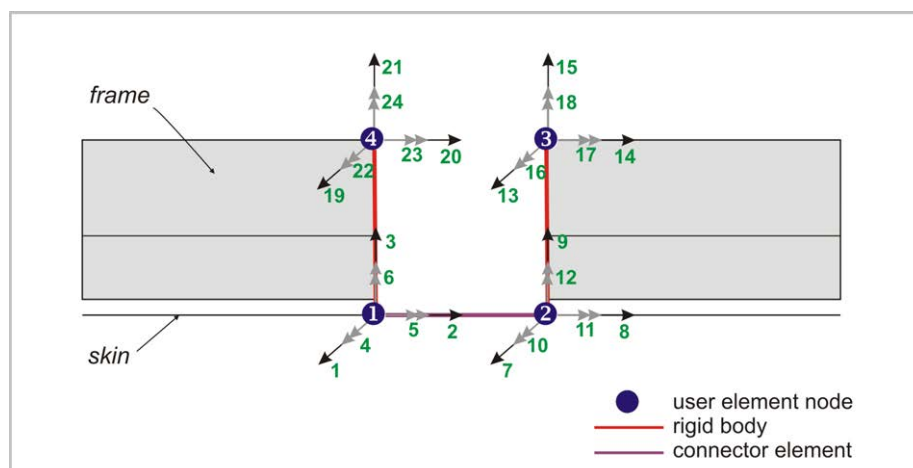


Figure 5-6: Kinematic hinge architecture with the user element

In the element behaviour definition of the ABAQUS input deck (*uel property) all property parameters can be specified. In the user element subroutine these property parameters are imported from the ABAQUS input deck in a first step. In Figure 5-4 of paragraph 5.1 the required moment-rotation behaviour is described which had to be developed. Most of the property parameters are illustrated in this Figure. In total, 47 property parameters are necessary to describe the element behaviour and which are imported in the user element. In this configuration the post-failure curve of each loading direction can be defined with eight pairs of values. An overview of these parameters is given in Appendix A3.1.

In a second step, nodal rotary inertia and mass are specified. The user element developed for the kinematic hinge is a macro element and not a structural element. Material density is not specified. Hence, definition of rotary inertia and mass does not represent structural mass but is important to ensure stable numerical calculation. As all user element nodes are coupled to rigid bodies in the kinematic hinge, small values for rotary inertia and mass can be defined here.

In a third step, a constant stable time increment has to be defined for element calculation. The stable time increment of a macro element strongly depends on the input characteristic defined by the user. The elemental time increment cannot be defined as the user element is not a structural element. Nevertheless, the critical time increment can be calculated based on the nodal time increment.

$$\Delta t \leq 2 \cdot \sqrt{\frac{m}{k}}, \quad k = 2 \cdot \frac{E \cdot A}{L} \quad (5.1)$$

The critical spring stiffness k is defined by the highest slope ($E \cdot A$) in the input property definition as well as the element length (L). Although a nodal stable time increment could be defined based on nodal mass and spring stiffness, the definition of a user-defined stable time increment was preferred here. This procedure is used similarly in standard macro elements of some commercial explicit finite element codes. In this procedure, the user is responsible for stable element calculation with respect to the time increment.

The interface between finite element code and user element is based on global coordinates. In a further step a coordinate transformation from a global to a local system has to be conducted after the import of the nodal displacements. With respect to the application of the user element in a fuselage section model, the coordinate transformation was simplified so that the yaw angle is assumed to be negligible ($\Psi = 0$). This simplification is reasonable in a fuselage section model with symmetry boundary conditions. The transformation as well as the definition of the local coordinates in the kinematic hinge is illustrated in Figure 5-7.

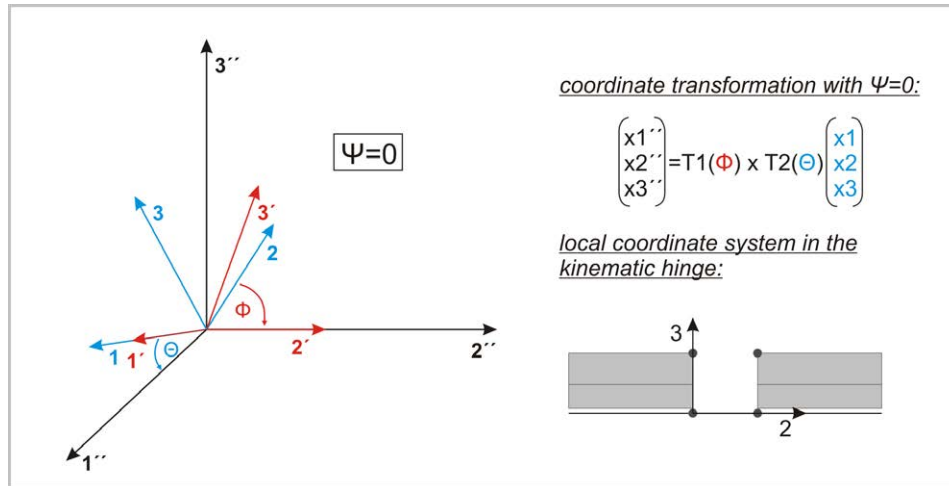


Figure 5-7: Coordinate transformation and local coordinate definition

The calculation of internal loads in a subsequent step is the main part of the element calculation. The calculation of this element behaviour needs several solution-dependent variables which are stored within the element. A total number of 15 solution-dependent variables are defined to calculate the required moment-rotation as well as force-displacement behaviour. A list of all solution-dependent variables is given in Appendix A3.2. Most of the variables of moment-rotation calculation are illustrated in Figure 5-8. The pictured variables are used to store the history load path and to find the correct load path of the current increment. The ‘salph_sX’ variables store the rotational displacements at which a change of sign in the loading direction leads to individual transition in the load path. For instance, ‘salph_s1’ stores the rotational displacement at which unloading was initiated. With the stiffness of the unloading slope, the variables ‘salph_s3’ and ‘salph_s2’ can be directly calculated. In a subsequent reloading the element behaviour has to pass ‘salph_s3’ and ‘salph_s1’ again to continue the loading along the post-failure curve. In addition, the ‘loadflag’ variable indicates the loading status of the last increment and defines along which load path the current increment has to be calculated.

Two assumptions in the calculation of the moment-rotation behaviour are given to limit the complexity of element calculation particularly with respect to element performance. The unloading slope has to be defined with a stiffness value which is equal or higher than the elastic slope. Otherwise, an unloading can lead to the crossing of the elastic slope which requires further loops in the element calculation. Another simplification requires constant moments in the post-failure curve between the first and the second pair of values. The transition-slope has to cross the post-failure curve in this constant segment.

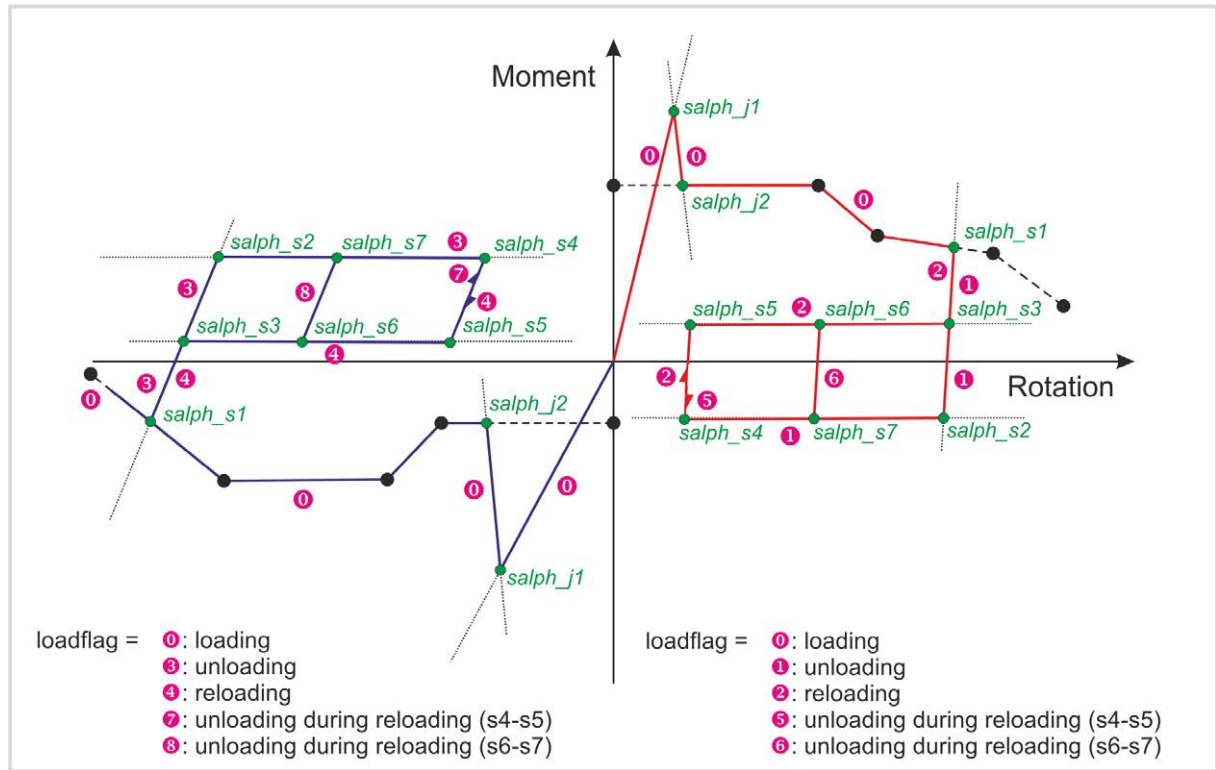


Figure 5-8: Solution-dependent variables for the element calculation

Two additional state variables are used for normal stiffness calculation. The normal forces are calculated as required in paragraph 5.1 and are applied to the element nodes as pictured in Figure 5-1b).

More details on the calculation of the internal loads are given in Appendix A3.3, where an extraction of the structogram is documented.

After calculation of the internal loads, these values have to be transformed from the local to the global coordinate system to assemble the nodal loads in the right hand side vector. This vector is the interface for the export of nodal loads to the solver.

Finally, the internal energy has to be calculated and exported to the solver. The determination of the user element internal energy is essential with respect to the conservation of energy of the whole model. Internal energy calculation considers the rotational as well as the translational degree of freedom and is defined as follows:

$$energy|_t = energy|_{t-\Delta t} + \left[\frac{sM1|_t + sM1|_{t-\Delta t}}{2} \cdot (salph1|_t - salph1|_{t-\Delta t}) + \frac{sF2|_t + sF2|_{t-\Delta t}}{2} \cdot (seps2a|_t - seps2a|_{t-\Delta t}) \right] \quad (5.2)$$

Whereas the energy calculation for the translational degree of freedom is trivial due to the purely elastic behaviour, the summation of internal energy for the rotational degree of freedom is

depicted in Figure 5-9 for a better understanding. In this figure the graph clearly illustrates the unloading/reloading hysteresis with its additional energy absorption effect.

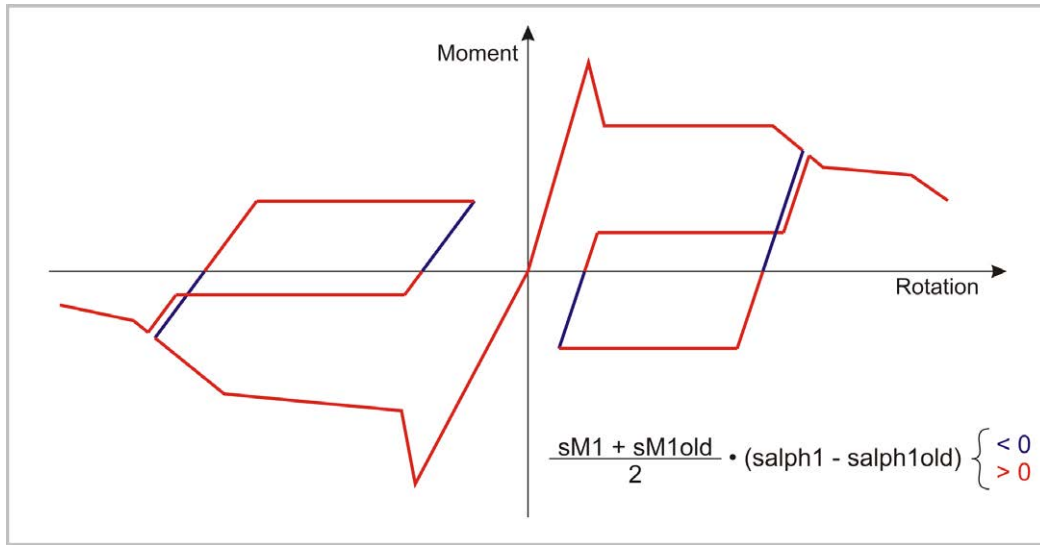


Figure 5-9: Internal energy calculation of the rotational degree of freedom

In the final step of the element calculation the state variables are updated and data are written to the output data file. Unfortunately, solution-dependent state variables of user elements can not be written to the ABAQUS output database (.odb) file [141]. Hence, these variables are written in a separate ASCII-file and can additionally be imported in a postprocessor. The element output is defined in a way that all 15 state variables as well as 'time' and 'internal energy' are written to the output data file, with an output frequency that can be defined by the property variable 'history_interval' in the ABAQUS input deck.

5.3. Verification on the quasi-single element level

Extensive verification of a user subroutine is essential to ensure a correct functionality for all potential loading conditions. After the implementation of the user element, the verification firstly concentrated on the internal element calculation, more precisely on the calculation of internal loads and internal energy as well as on the coordinate transformation. This verification was conducted on a quasi-single element level. As the user element was developed exclusively for implementation in the kinematic hinge, a simplified model of the kinematic hinge was built up which is equivalent to the single element level. Figure 5-10 illustrates this verification model. In this model the frame structure is represented by rigid bodies consisting of both user element nodes at one side and an additional node to apply external loads on the kinematic hinge.

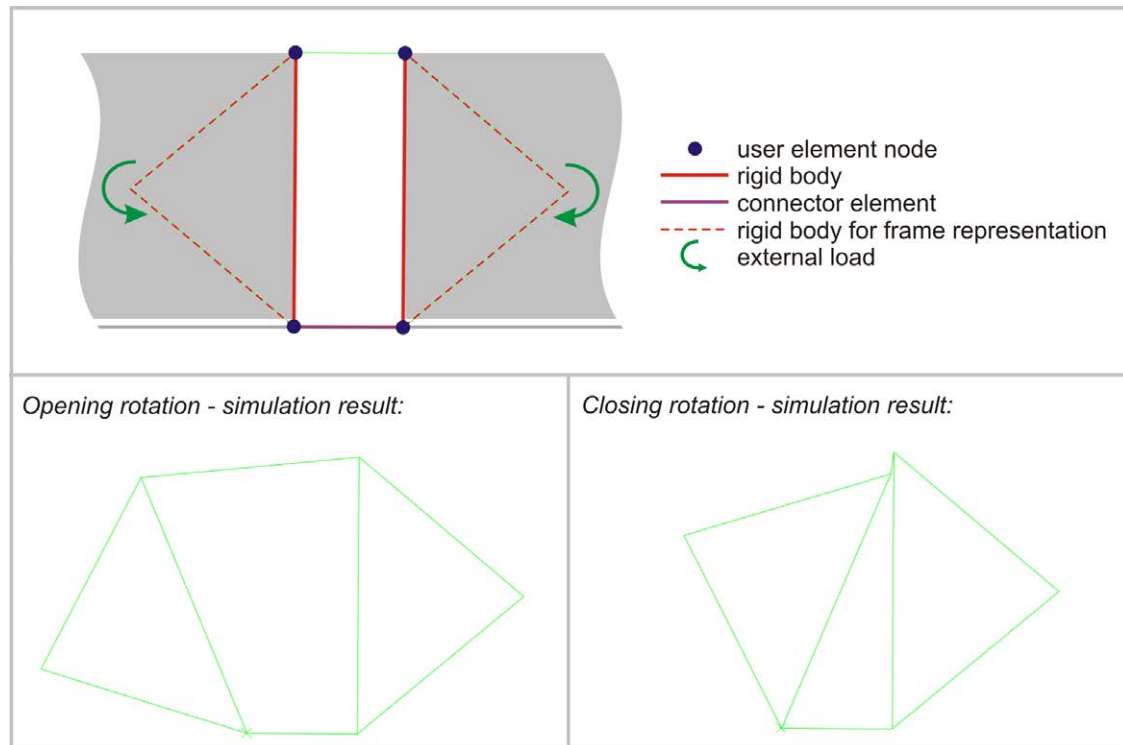


Figure 5-10: Quasi-single element model for the verification

The verification of the coordinate transformation routine was conducted with a parameterised version of this quasi-single element model that can be rotated arbitrarily with respect to the global coordinate system. The coordinate transformation routine was verified regarding all combinations of quadrants of both transformation angles Θ and Φ , see Figure 5-7. This verification ensures that in a fuselage section model the kinematic hinge can be positioned arbitrarily with respect to roll and pitch angle. The simplified assumption of $\Psi = 0$, discussed in paragraph 5.1, implicates a negligible yaw angle.

Further verification considered the calculation of the moment-rotation behaviour. The potential load paths and unloading/ reloading combinations were verified with the quasi-single element model. Figure 5-11 depicts an exemplary user element output of the verification procedure. The graphs show details like unloading during the transition from elastic behaviour to the post-failure curve, unloading with zero crossing as well as different unloading/reloading combinations including unloading during reloading phases.

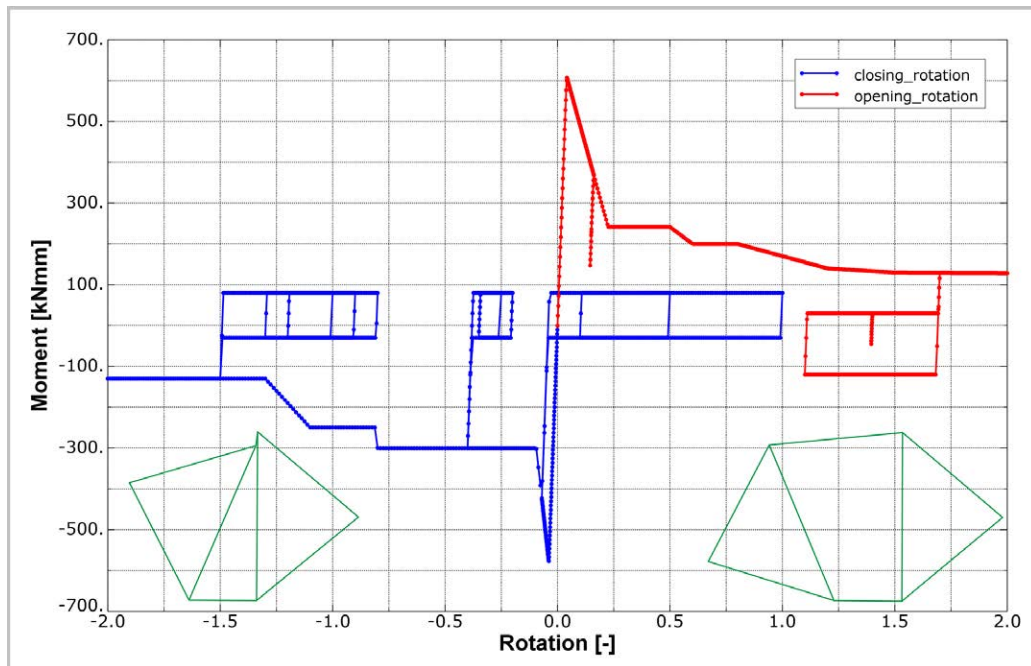


Figure 5-11: User element output of the moment-rotation behaviour

The verification on the quasi-single element level identified a correct functionality of the user element with respect to all element internal calculation procedures. Nevertheless, some bugs were identified which are located in the ABAQUS solver respectively in the interface between solver and user element.

One bug refers to the output of the internal energy [142]. After the export of the element internal energy to the solver this value is included in the ‘whole model internal energy’. Nevertheless, the requested internal energy output exclusively of the user element is written as null-energy to the output data base (.odb) of the solver. This bug was solved in ABAQUS V6.9.

Another bug was identified in the import of rotational displacements of the user element nodes [143]. In combination with several constraints (e.g. rigid body, multi-point constraint, etc.) which are defined at the user element nodes, the solver transfers incorrect nodal rotations to the user element subroutine. Generally, additional nodal mass can help to solve such problems. Nevertheless, any solution failed to solve this problem especially in combination with rigid body constraint. A solution of this bug was implemented in the subsequent solver version ABAQUS V6.8-EF1 respectively V6.8-2. In the meantime, to avoid this bug in (at that time) current solver versions, rotational degrees of freedom of the 4-node user element were derived from translational degrees of freedom with the scalar product.

Finally, another discrepancy was identified in the export of internal loads to the solver. In combination with some constraints at the user element nodes, moment loads calculated from the user element are not applied to the model. Although correct moment history is written to the data

base as desired, the solver does not apply these moments to the nodes. Despite of extensive investigation and discussion with the FE solver developer this bug is not solved completely yet. Nevertheless, one solution to by-pass this bug was found in using multi-point constraints (*MPC) instead of rigid body formulations to constrain the user element nodes within the kinematic hinge architecture. This modified kinematic hinge architecture worked well in the quasi-single element model. The moment loads were applied to the user element nodes and the kinematic hinge behaviour was identified as intended.

Unfortunately, this solution with modified kinematic hinge architecture using multi-point constraints does not work successfully on a reference model level which is discussed in the next paragraph. The transfer of the same kinematic hinge architecture from the quasi-single element model to a frame-stringer-skin model led to the well-known discrepancy with missing applied moment load on the user element nodes as described above.

5.4. Verification on the reference model level

Further verification after the quasi-single element level was conducted on a reference model level. The reference model corresponds to a frame-stringer-skin model which is similar to the models used in the investigations of chapter 4. A detailed definition of the reference model is given in Appendix A3.4.

The frame-stringer-skin model enables a user element verification which is implemented in a reference structure with typical dynamic behaviour. Instead of rigid body motions as used on the quasi-single element level, a more realistic elastic behaviour leads to dynamic oscillation loading of the user element. Stable element calculation under typical short-duration unloading/reloading can be verified.

In addition, the requirements of the user element with respect to the elastic behaviour can be verified in the reference model. Whereas the post-failure behaviour with its unloading/ reloading options was verified intensively on the quasi-single element level, the elastic behaviour up to failure was verified mainly on the reference model level. This is in more detail the strain-based triggering as well as the user element behaviour under low bending-compression ratios.

As discussed in paragraph 5.3, an unsolved bug regarding applied moment loads hindered the verification on the reference model level. Whereas a solution was found to run the user element successfully on the quasi-single element level, the calculated moment loads are not applied by the solver on the reference model level. To verify the elastic behaviour of the user element despite of this bug, the assembly of internal loads on the right hand side was modified in the user subroutine. Instead of moments on the outer user element nodes, forces on the inner user element

nodes were applied. These forces in combination with the moment arm induce the same moment on the outer user element nodes, as shown in Figure 5-12. This modification is accurate for small rotation angles, hence, is an appropriate solution to verify the elastic behaviour.

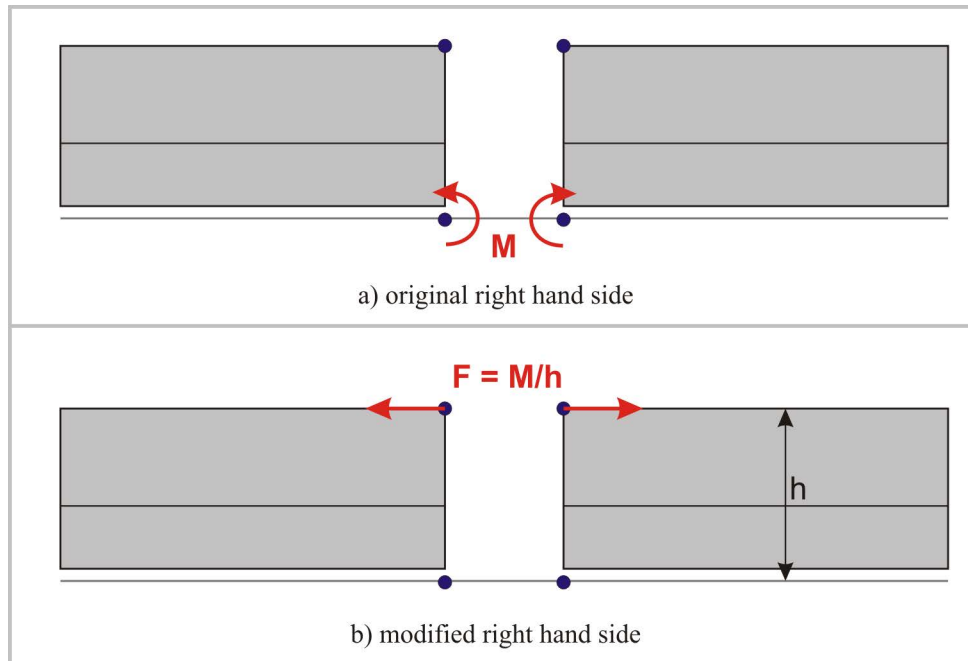


Figure 5-12: Modified right hand side in the user subroutine without applied moments

The verification procedure is illustrated in Figure 5-13. For a better understanding the internal loads of the user element are illustrated with respect to the original right hand side. In a first step, the rotational elastic stiffness is calibrated based on the frame inner flange strain, Figure 5-13a). Pure moment is applied on the model in this step. With calibrated rotational stiffness, applied load with low bending-compression ratio leads to a discrepancy similar to the kinematic hinge with a standard connector element, Figure 5-13b). In a next step, the distribution of normal forces over the frame height of the user element is adapted so that the kinematic hinge strain agrees with the structural frame behaviour with respect to the frame inner flange, Figure 5-13c). This final setup of calibrated rotational stiffness and normal force distribution leads to the required accuracy in the representation of the elastic behaviour for low bending-compression ratios, Figure 5-13c), as well as for high bending-compression ratios, Figure 5-13d).

In addition, the strain based trigger criterion in Figure 5-13 illustrates the required behaviour. In this example, a trigger strain of $\varepsilon = -2000$ microstrain was defined in the user element input deck. Independently of the bending-compression ratio, the kinematic hinge triggered accurately at this defined trigger strain level, Figure 5-13a) – d).

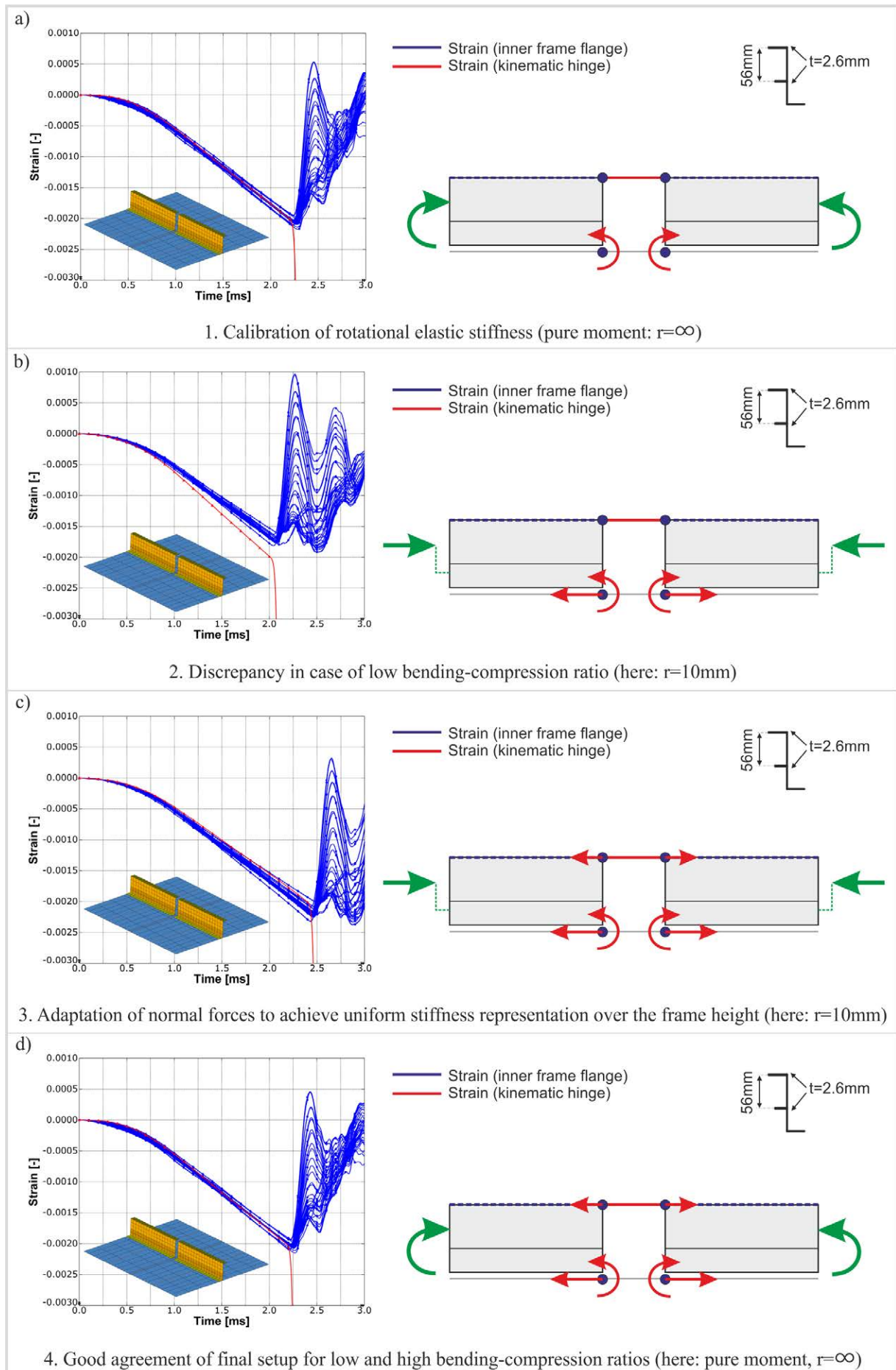


Figure 5-13: Verification on the reference model level

5.5. Summary and outlook

The discussion of the kinematic hinge architecture based on standard macro elements identified limitations in the frame failure representation which are caused by restrictions of the standard macro element. On the basis of a catalogue of further requirements, a user element was implemented to achieve improved frame failure representation by the usage of a user-defined macro element instead of the standard macro element.

Enhanced unloading/ reloading behaviour as well as an improved triggering on the basis of frame inner flange strains was implemented in the user-defined macro element. Further improvement could be achieved by an accurate representation of the frame failure behaviour for very low bending-compression ratios.

The verification of the user element on the quasi-single element level and the reference model level demonstrated the fulfilment of all requirements which were defined in paragraph 5.1. All functionalities of the user element could be proved.

Unfortunately, a solver bug with missing applied moment loads on the user element nodes could neither be definitely clarified with the FE solver developer nor solved in a subsequent solver version. Due to this circumstance, the improved kinematic hinge architecture on the basis of the implemented user element could not be implemented in the Kinematics Model for the aircraft section. Hence, the Kinematics Model applications, which are discussed in the following chapters are based on the final kinematic hinge architecture with the standard connector element, as defined in paragraph 4.7.

However, the discussed limitations of the standard connector element mainly refer to load cases which differ from the standard crash scenario¹. Thus, the usage of the standard connector element had minor impact on the development of a crashworthy fuselage design which is discussed in the following chapters 6 and 7.

Nevertheless, with the foresight beyond the scope of this thesis, a final solution of the bug situation is awaited to use the enhanced kinematic hinge architecture in the Kinematics Model.

¹ Within this thesis, the 'standard crash scenario' specifies impact conditions of a vertical impact with $v_i = 6.7$ m/s, fully loaded overhead bins, occupied seats, zero pitch and roll angle. Cargo loading is not considered in this case.

6. Development of a crashworthy composite fuselage design

– crash scenario assessment

The fundamentals of the Kinematics Model were developed and discussed in the previous chapters. The following chapters deal with the approach to develop a crashworthy composite fuselage design based on numerical simulations using the Kinematics Model. In this approach basic principles were established for the investigation and development of crash kinematics for composite fuselage structures. Figure 6-1 gives an overview of this approach.

The considered method of development of crashworthiness is based on the general idea to install discrete crash devices in the fuselage structure which control the crash behaviour. Figure 1-4 in chapter 1 already illustrated this concept. The definition of the crash behaviour in particular includes the crash kinematics of a fuselage section. In contrast to traditional fuselage structures fabricated of aluminium material, the crash kinematics of composite fuselages should not develop uncontrolled. Hence, the definition of a favourable crash kinematics, which should be ensured by an appropriate activation of the individual crash devices, is the first step in the development of a crashworthy composite fuselage design. To identify the most favourable crash kinematics of a fuselage section, an assessment of crash scenarios was performed based on numerical simulation with the Kinematics Model. Chapter 6 deals with this general investigation of crash scenarios.

Based on the selection of the most favourable crash kinematics, the detailed development of such a crash scenario was conducted by numerical simulation using the Kinematics Model. The basis of this crash scenario development is a statically pre-sized CFRP narrow-body fuselage structure. The final target of this investigation is the definition of an optimised crash scenario which includes the characterisation of local crash devices in a way that reduced loads, which act on the passengers and the fuselage structure, can be realised. In a subsequent step the reduction of crash loads induces a reduction of the structural mass. Chapter 7 discusses this development process.

The optimised crash device characteristics, load-deformation relations which are outcomes of the Kinematics Model, can be used as basis for the development of local crash devices. In several experimental investigations on the design of crash devices, axial crush absorbers as well as generic frame components were tested under crash related loads. Appropriate test setups were

developed to investigate the general characteristics of technological concepts. These experimental investigations are discussed in chapter 8.

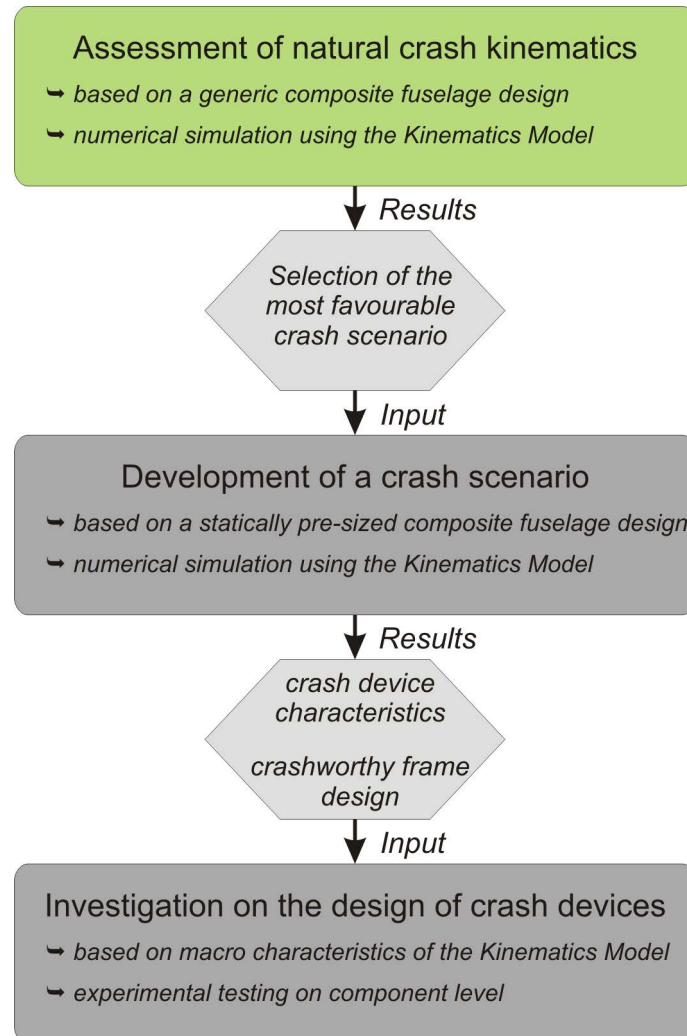


Figure 6-1 : Approach for the development of a crashworthy composite fuselage design

The present chapter deals with the investigation of crash kinematics in general. Several known drop tests of fuselage sections and structural components, conducted in the past by different research facilities, were assessed to derive natural crash kinematics of typical fuselage structures from the test results. The natural crash kinematics were analysed with the Kinematics Model. Based on these simulation results, an assessment of the crash scenarios identified main benefits and drawbacks with respect to the differences in the crash kinematics and led to the selection of a most favourable crash scenario.

6.1. Natural crash kinematics

With respect to the development of a crash concept, a lightweight design solution aligns to the natural crash kinematics of a fuselage structure. Consequently, it is important to understand the

natural crash behaviour. All attempts to achieve a crash kinematics differing from the natural structural behaviour will lead to an additional weight penalty.

In the past, several tests of fuselage structures were performed with respect to crash relevant loads. Fuselage section drop tests performed in the last decades have given valuable information about the natural crash kinematics of typical fuselage structures [15-19,24-26,30-32].

In addition, several detailed investigations of different research projects provided useful data, too. The NASA research on composite frame structures, already discussed in chapter 4, shows valuable results with respect to typical crash kinematics of frame as well as fuselage structures [46-51].

Further experimental and numerical studies on simplified fuselage structures are documented in [132,133]. The influence of the vertical passenger crossbeam position on the crash scenario was investigated in these studies. The results provide basic information with respect to typical crash kinematics of different fuselage section designs.

Other valuable results regarding general crash kinematics are given in [117]. Experimental, analytical and numerical studies were performed considering semi-circular frame structures which were pressed against a rigid plane. The formation of plastic hinges as well as their kinematics was investigated which contributed to the definition of typical kinematics of semi-circular frames under crash related loads.

Experimental studies on simplified fuselage section models, loaded under crash related conditions, are documented in [118,119]. Crash kinematics of typical fuselage section designs can be derived from these experimental results.

A numerical study on the influence of different vertical support strut configurations is given in [115]. Plastic hinge locations in the frame were identified in dependence of the vertical support strut position. Based on the plastic hinge locations typical crash kinematics can be derived.

Based on this range of empirical and analytical results two general crash kinematics of typical fuselage structures could be identified. Figure 6-2 illustrates both kinematics and compares the schematic scenarios with exemplary results from documented experiments.

The first natural crash kinematics, called “scenario A”, describes three main locations of frame failure. The first frame failure occurs in the lower centre at $\alpha_1 = 0^\circ$, the point of the first impact. Induced by this first failure a second frame failure develops between $\alpha_2 = \pm 45$ to $\pm 60^\circ$. Details on these failure locations were already discussed in chapter 4.1. With these three main locations of frame failure an unrolling crash kinematics develops with an upwards movement of the lower fuselage shell. This scenario was identified as typical crash kinematics of fuselage structures

with quasi-circular geometry and lateral stiffness provided by a passenger crossbeam. Figure 6-2I) illustrates examples with a crash kinematics of scenario A which are of different fuselage size respectively different structural design. In Figure 6-2a), the crash kinematics is shown after the drop test of an A230 fuselage section which provides a narrow-body fuselage design with vertical support struts. Figure 6-2c) displays a B707 fuselage section after the drop test with similar crash kinematics. This narrow-body fuselage structure is designed without vertical support struts. A NAMC YS-11 fuselage section is depicted in Figure 6-2e) after the drop test. The YS-11 is a short-range aircraft of smaller size compared to typical narrow-body fuselage aircraft. Figure 6-2e) pictures the fuselage structure after removal of dummies and seats. Finally, a component test of a 1.8 m (6 ft) diameter circular CFRP frame is illustrated in Figure 6-2g) which shows the crash kinematics according to scenario A.

Besides scenario A, one further typical crash kinematics was identified, which develops when different factors hinder the formation of scenario A. This so-called “scenario B” describes multiple frame failure locations in the lower fuselage shell, as illustrated in Figure 6-2II). Instead of an unrolling with an upwards movement, a flattening of the lower fuselage shell occurs in scenario B. One potential factor that can lead to scenario B is illustrated in Figure 6-2b). This figure pictures the same A320 drop test as in Figure 6-2a), but the opposite side of the tested fuselage section. On this side, the passenger crossbeams failed and provided no further lateral stiffness. This effect led to higher lateral flexibility in the lower fuselage shell that induced a flattening with multiple failures in the lower frame. Besides failure of the passenger crossbeam a fuselage design with reduced stiffness at the crossbeam connection may similarly lead to a crash kinematics according to scenario B. Another factor that potentially effects a crash kinematics according to scenario B is cargo loading. In case of cargo loading the upwards movement of the lower fuselage shell can be hindered by the cargo mass, or in case of container loading by the cargo rigidity. Figure 6-2d) illustrates a B737 fuselage section with bulk loading after the drop test. In Figure 6-2f), a B737 fuselage section with an auxiliary fuel tank is depicted after the drop test. Figure 6-2f) pictures the fuselage structure after removal of dummies, seats and passenger crossbeams. Both examples of B737 drop tests show the flattening effect that is caused by constraints of the lower shell unrolling. Finally, a scaled drop test of a simplified subfloor fuselage section is shown in Figure 6-2h). In this scaled test, the frame stiffness was smeared in the skin so that the fuselage structure was represented only by a comparably stiff skin. Further examples are known where the frame stiffness is smeared in the skin for scaled fuselage section drop tests [119]. In these tests, perfect flattening of the lower fuselage shell occurred in combination with travelling plastic hinges. In contrast to a smeared representation of fuselage shell stiffness, local frame failure of a real fuselage structure leads to significantly reduced

bending stiffness compared to the adjacent shell structure. This is the postulate for the formation of local hinges. A smeared stiffness represented exclusively by a stiffer skin cannot represent such local stiffness reduction, hence cannot represent the rotation of undamaged structural parts around a location with reduced stiffness caused by damage. The given example of a scaled model test in Figure 6-2h) shall clarify that a crash kinematics according to scenario B can occur exclusively in combination with travelling hinges respectively (in case of a frame-skin structure) with multiple frame failure.

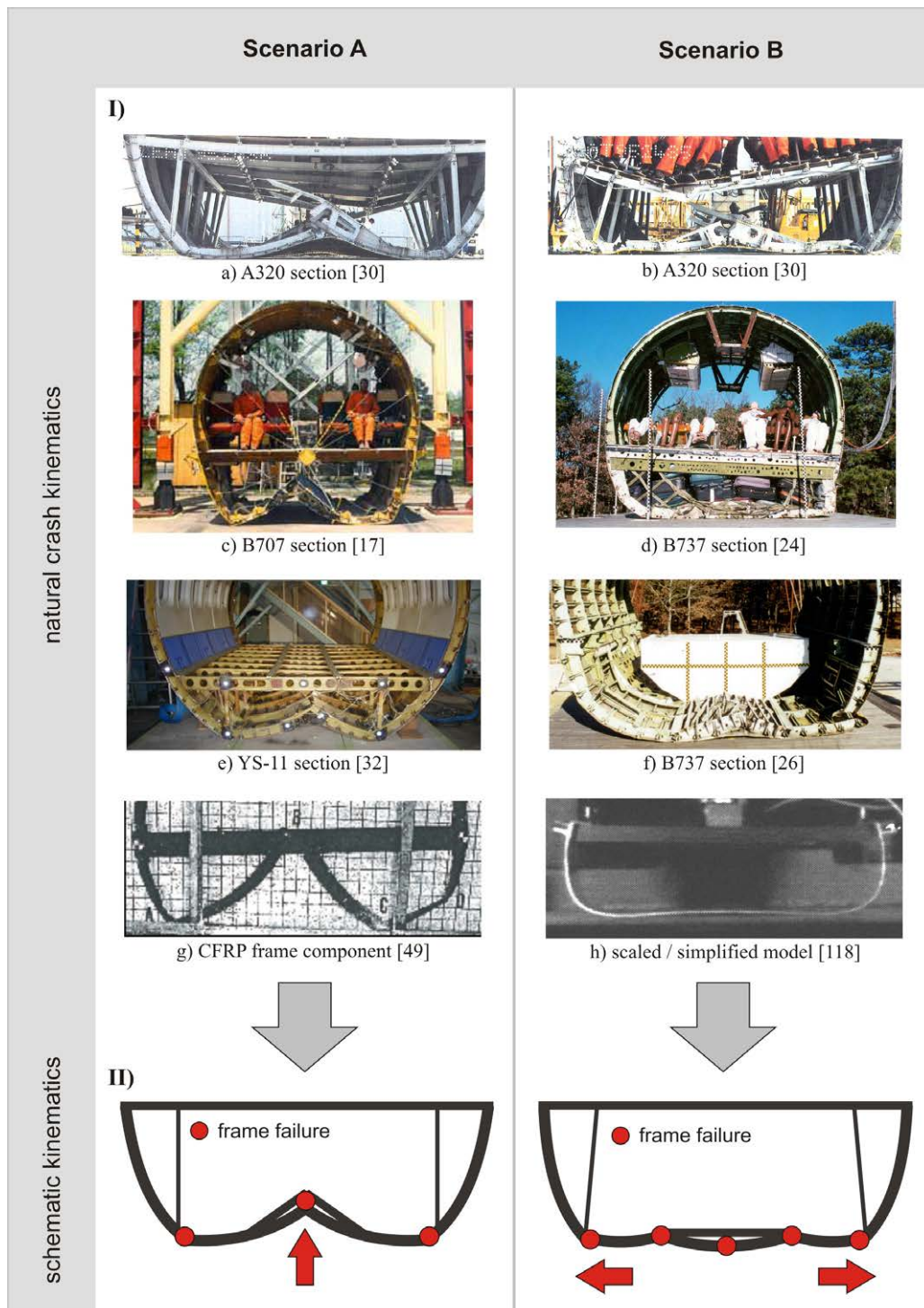


Figure 6-2: Natural crash kinematics

Both crash kinematics, scenario A and B, were identified as natural crash kinematics of typical fuselage structures. Further crash kinematics of typical fuselage sections could not be identified in the review of experimental and analytical studies which were considered in this investigation. However, in case of non-typical fuselage sections, such as cargo-door installation or tapered fuselage section, some differing crash kinematics could be identified. For instance, cargo door installation can lead to asymmetric crash kinematics. In a tapered fuselage section, frame failure can develop as shear failure instead of hinge failure with according differences in the crash kinematics. However, these untypical crash kinematics are generally based on the above described typical scenarios A and B and are expected to be controllable by the considered crash devices. Finally, the development of a crashworthy fuselage design concentrates on the typical fuselage section for what reason untypical crash kinematics are not considered in the design process.

The results of documented experimental and analytical studies discussed above exemplarily show that both crash kinematics, scenario A and B, can occur independently of different typical fuselage designs or fuselage sizes. Hence, with respect to the development of a crash concept for a CFRP fuselage structure both scenarios have to be considered.

6.2. Development of crash scenario A & B

Based on the identified natural crash kinematics, both scenarios A and B were developed and assessed using the Kinematics Model.

A generic procedure was selected for this assessment of crash scenarios:

- With respect to the fuselage structure a generic CFRP design of a typical fuselage section was used to compare the crash scenarios. The generic CFRP structure was exclusively used for the comparison of several effects without structural adaptation during the assessment procedure.
- Regarding structural loads generic strain limit criteria were used to assess differences in both crash scenarios. These strain criteria exclusively consider the most critical frame inner flange. Tensile and compressive limit strains were defined with respect to simplified assumptions regarding material failure respectively instability failure. The tensile strain limit in the frame inner flange was defined as $\varepsilon_t = +10,000$ microstrain. The compressive strain limit was defined as $\varepsilon_c = -6000$ microstrain.
- The Kinematics Model used in this scenario assessment represents an early generation version with comparably coarse FE mesh particularly with respect to the frame structure.

Due to this discretisation, full accuracy of the frame bending behaviour as discussed in chapter 4.5 was not provided in this model version. However, the model accuracy was reasonably evaluated with respect to an assessment of crash scenarios on the generic level.

The basis for the assessment is a generic CFRP structure of a typical fuselage section of narrow-body size with LCF-shaped frame design. This generic fuselage design provides a specific sub-cargo structure with a stiff cargo-crossbeam that enables to absorb energy in a first crash phase by the crushing of the sub-cargo structure (bend-frame concept) [120]. Based on this fuselage design the schematic crash kinematics of Figure 6-2 were adapted to idealised kinematics as illustrated in Figure 6-3.

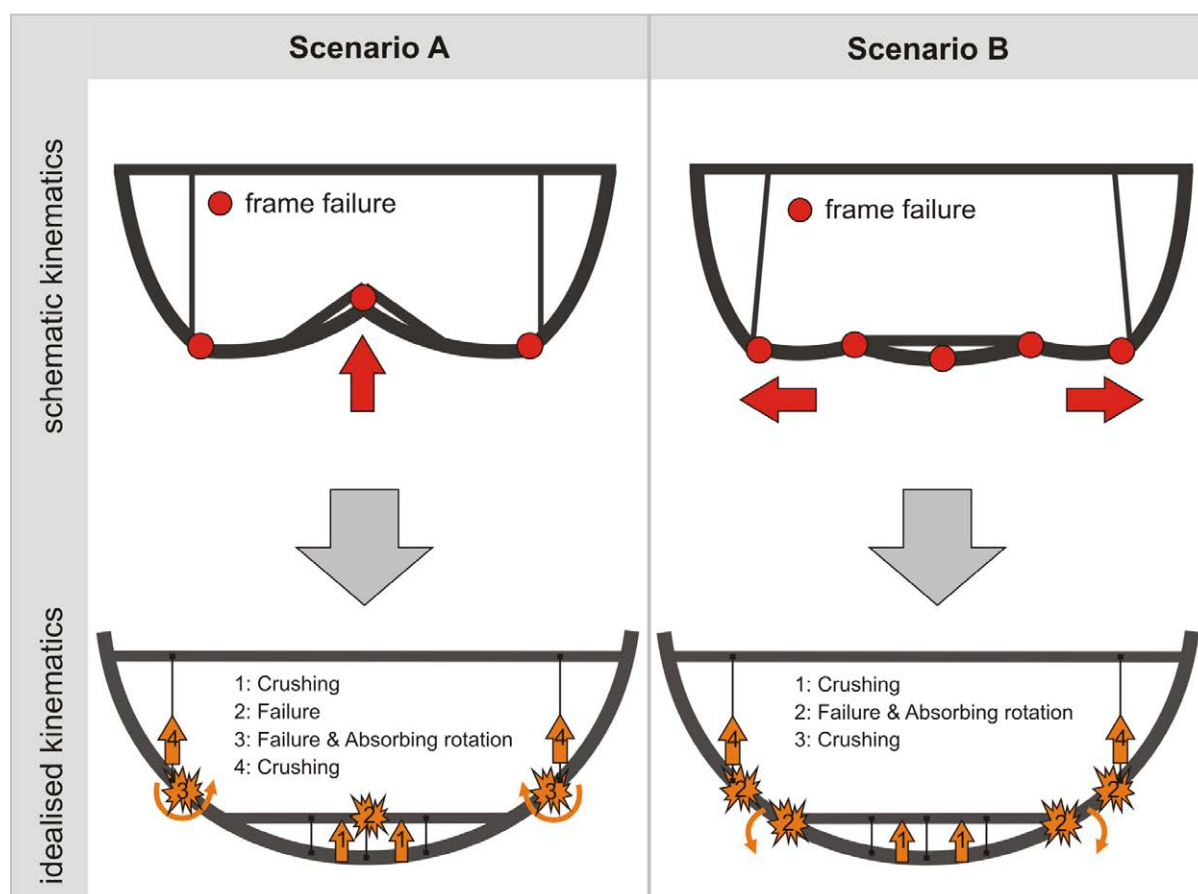


Figure 6-3: Idealised crash kinematics for a fuselage design with a stiff cargo-crossbeam

In both scenarios the idealised crash kinematics specify a first crash phase with energy absorption by a crushing process below the cargo-crossbeam.

In a second phase, frame failure occurs along the lower fuselage shell and specifies different crash scenarios dependent on the failure locations. In scenario A, crash devices in the frame, located directly below the connection of the vertical support strut, as well as in the cargo-crossbeam shall trigger and initiate an appropriate crash kinematics. Energy has to be absorbed

by a closing bending rotation of the crash devices in the frame. In scenario B, failure in the cargo-crossbeam is not specified. In addition to the frame failure located directly below the vertical support strut, further frame failure is specified at the coupling of frame and cargo-crossbeam in this scenario. According to the desired crash kinematics, closing frame bending is specified at the vertical support strut connection whereas opening frame bending is specified at the frame coupling to the cargo-crossbeam. Energy shall be absorbed by frame bending rotation of the opening frame hinge as the development of an opening bending absorption mechanism was expected to be less complex.

In both scenarios the last phase of the crash sequence is specified by the crushing of the vertical support struts.

According to the specification of the idealised crash kinematics, the Kinematics Model was built up with a refined modelled sub-cargo area, as discussed in paragraph 3.4.1, to allow the crushing of the sub-cargo structure without kinematic constraints. The main crushing characteristic of the sub-cargo structure is described by axial macro elements. Two macro elements at each cargo-crossbeam, at a lateral position of $y = \pm 150$ mm, represent the crash absorbers. A typical crush characteristic was assumed in this study which was derived from several known test results of CFRP crush absorbers [136]. This force-deflection characteristic describes a linear slope up to the triggering with a following constant force plateau at 80 % of the trigger load. Figure 6-4a) illustrates this characteristic. During the assessment study the trigger load of the axial macro elements was the parameter for the variation of the sub-cargo crush behaviour.

The kinematic hinges in the frame were positioned similarly to the discussion of paragraph 4.1. With the exception of the active kinematic hinges all other hinges were defined with trigger moments that correspond to the strain limit criteria of the frame structure. Hence, passive kinematic hinges triggered at frame inner flange strains of $\varepsilon_t = +10,000$ microstrain for opening bending and $\varepsilon_c = -6000$ microstrain for closing bending. The active kinematic hinges were allowed to trigger in the range between static sizing and material failure respectively instability failure. With respect to opening bending, the range of potential hinge triggering was specified between $\varepsilon_{tr_min} = +4000$ microstrain and $\varepsilon_{tr_max} = +10,000$ microstrain. The range of potential hinge triggering for closing bending was specified between $\varepsilon_{tr_max} = -4000$ microstrain and $\varepsilon_{tr_min} = -6000$ microstrain. The moment-rotation characteristic for absorbing hinge rotation was based on detailed analysis which was conducted by the project partner ONERA [121]. In this analysis an absorber mechanism in the frame inner flange was considered. A maximum absorbing force level in the frame inner flange was determined over the bending rotation angle, based on the strength and the lateral stability of the defined LCF-shaped frame design. The

outcome of this analysis is a moment-rotation characteristic with decreasing absorbing moment level over the hinge rotation, as illustrated in Figure 6-4b). During the assessment study the trigger moment was the parameter for the variation of the frame failure behaviour. In case of an absorbing kinematic hinge the absorption levels in the moment-rotation characteristic were defined fix, independently of the trigger moment.

In addition to the kinematic hinges in the frame, bending failure macro elements were positioned in the cargo-crossbeam to allow brittle failure of this crossbeam as specified in scenario A. During the assessment study the trigger moment was the parameter for variation of the cargo-crossbeam failure behaviour.

The crushable vertical support struts were described by axial macro elements. The force-deflection characteristic was defined according to experimental investigations on a crushable strut design concept, conducted by the project partner EADS-IW [122]. The failure characteristic is illustrated in Figure 6-4c). During the assessment study the trigger force of the axial macro element was the parameter for variation of the strut failure behaviour. The failure characteristic after triggering was defined fix according to the experimental results.

Details of the generic fuselage structure, the Kinematics Model definition as well as the assumptions on the macro input characteristics are documented in Appendix A4.1.

The basis of the scenario development is a so-called ‘standard crash case’ that specifies impact conditions with an initial velocity of $v_i = 6.7$ m/s (22 ft/s) and a zero pitch and roll angle. All seats are occupied with a passenger mass of $m_p = 77$ kg, cargo loading is not considered. The overhead bins were loaded with a distributed mass of $m_H = 47.5$ kg/m on each side. An acceleration field of $a_z = -9.81$ m/s² was applied on the model. This load case definition is based on well-known fuselage section drop tests, which were performed in the past (e.g. A320 section drop test [30]) and represent the metallic equivalent.

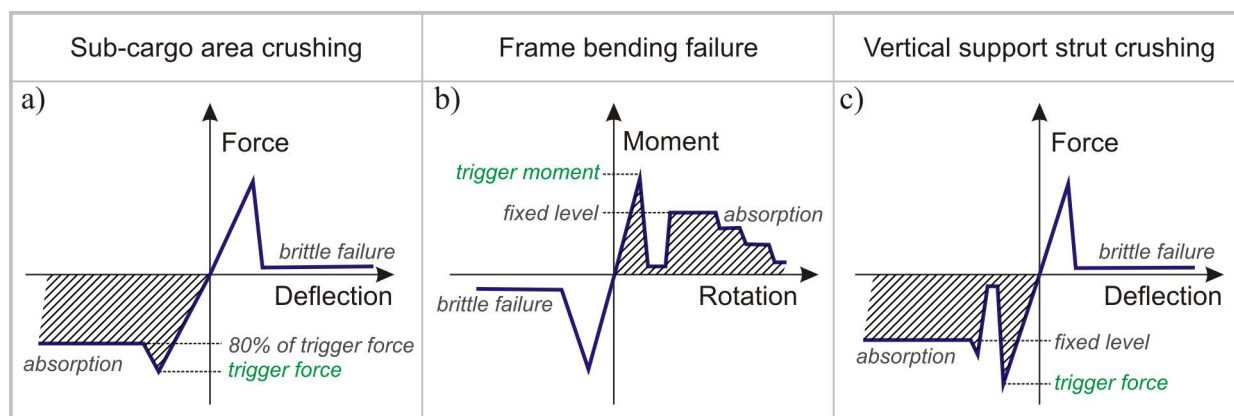


Figure 6-4: Characteristic input for the macro elements

In a first step the Kinematics Model simulations started with a sub-cargo study. As the structural design of the fuselage section was fixed, the maximum possible energy absorption of the sub-cargo crushing had to be identified with respect to the load carrying capacity of the above fuselage structure. In this simulation step all kinematic hinge trigger moments were set to the maximum strain limit values and the trigger forces of the sub-cargo absorber macros were varied stepwise between $F_{\min} = 5 \text{ kN}$ and $F_{\max} = 25 \text{ kN}$ per crush absorber. The frame inner flange strains and the cargo-crossbeam flange strains were checked against the limit criteria. The reached crushing distance inside the strain limit criteria was measured for each force level to identify the absorbed energy. Figure 6-5 illustrates this approach. The diagram of the crushing distance illustrates the results of the individual trigger force levels. The upper fuselage structure could withstand trigger forces up to $F = 15 \text{ kN}$. Higher trigger forces in the sub-cargo absorber macro could not be supported by the fuselage structure, hence, the macro elements did not trigger and frame failure was initiated, instead. As expected, the highest crushing distance occurred with the lowest trigger force level. Nevertheless, the highest energy absorption, as an integral of force level over crushing distance, was achieved with a trigger force of $F = 10 \text{ kN}$ respectively a crushing force plateau of $F = 8 \text{ kN}$. Regarding the above fuselage structure the strains in the cargo-crossbeam lower flange reached the limit strain of $\epsilon_{\min} = -6000$ microstrain with the variant of $F = 10 \text{ kN}$ trigger force. Hence, further safety margin is not provided in this variant. For that reason a trigger force of $F = 5 \text{ kN}$ was selected as final setting for the sub-cargo crash absorbers although this value is very low and significantly more energy could be absorbed with the $F = 10 \text{ kN}$ variant. It is obvious that a trigger force of $F = 5 \text{ kN}$ is low and may conflicts with static loads. Nevertheless, this approach is reasonable against the background of a generic assessment of crash scenarios.

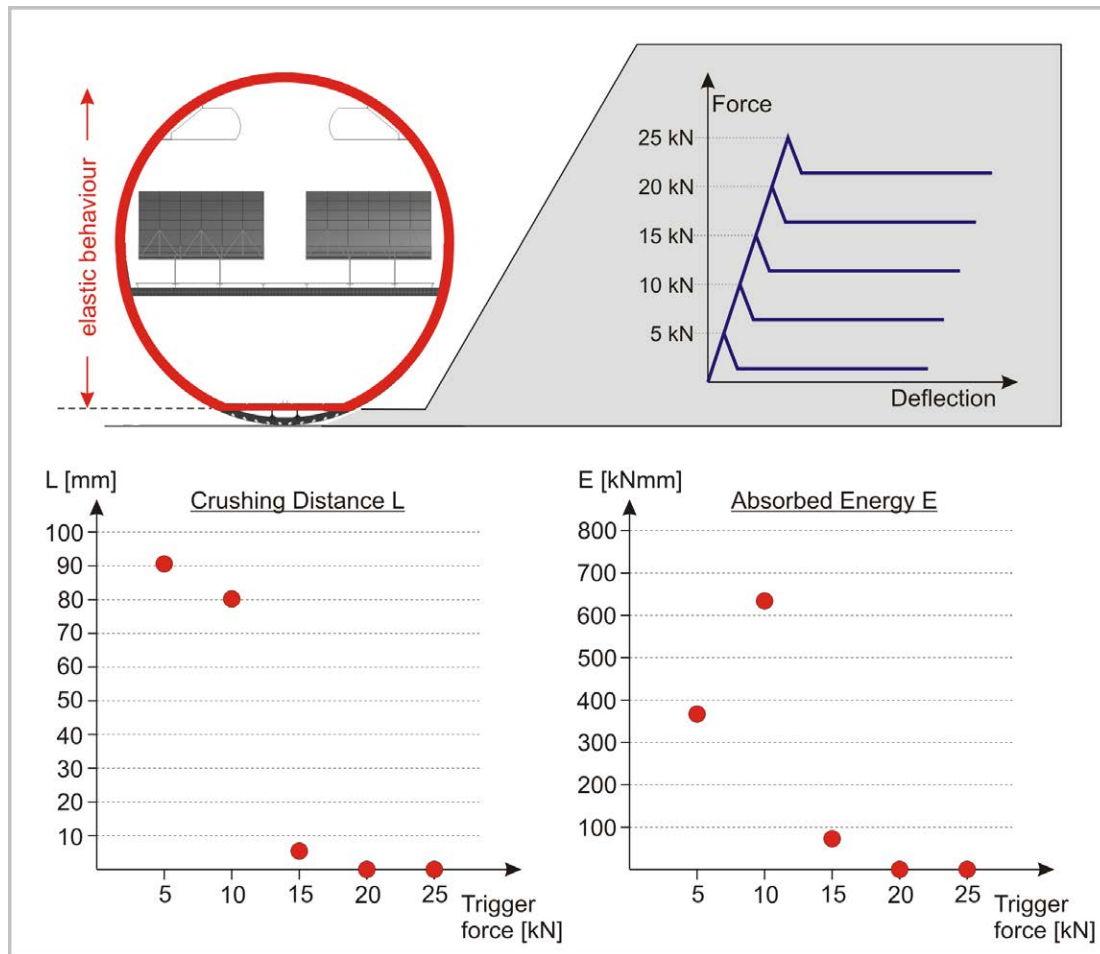


Figure 6-5: Sub-cargo study

With the final setting of the sub-cargo absorber macros the development of the different crash scenarios was realised with the determination of the individual kinematic hinge characteristics. In an iterative process the trigger moments of the active hinges were adapted so that the desired crash kinematics could be achieved and, in a further proceeding, improved with respect to the crash performance. Both scenarios A and B were developed with the same simulation model only by varying of the kinematic hinge characteristics.

Figure 6-6 illustrates the final model developed for scenario A. The kinematic hinge characteristics are given in Figure 6-6a). A trigger strain of $\epsilon_{tr} = 4000$ microstrain in the cargo-crossbeam flange was defined to achieve a smooth transition from the sub-cargo crushing phase to the frame failure phase. Higher trigger moments would lead to a delayed triggering of the second crash phase with a high amount of elastic energy stored in the fuselage structure. After cargo-crossbeam failure a trigger strain in the frame inner flange of $\epsilon_{tr} = -6000$ microstrain is sufficient to achieve controlled frame failure at the kinematic hinges located directly below the vertical support strut connection. These kinematic hinges describe an absorbing characteristic as illustrated in Figure 6-4b). The calculated crash sequence of scenario A is depicted in Figure 6-6b).

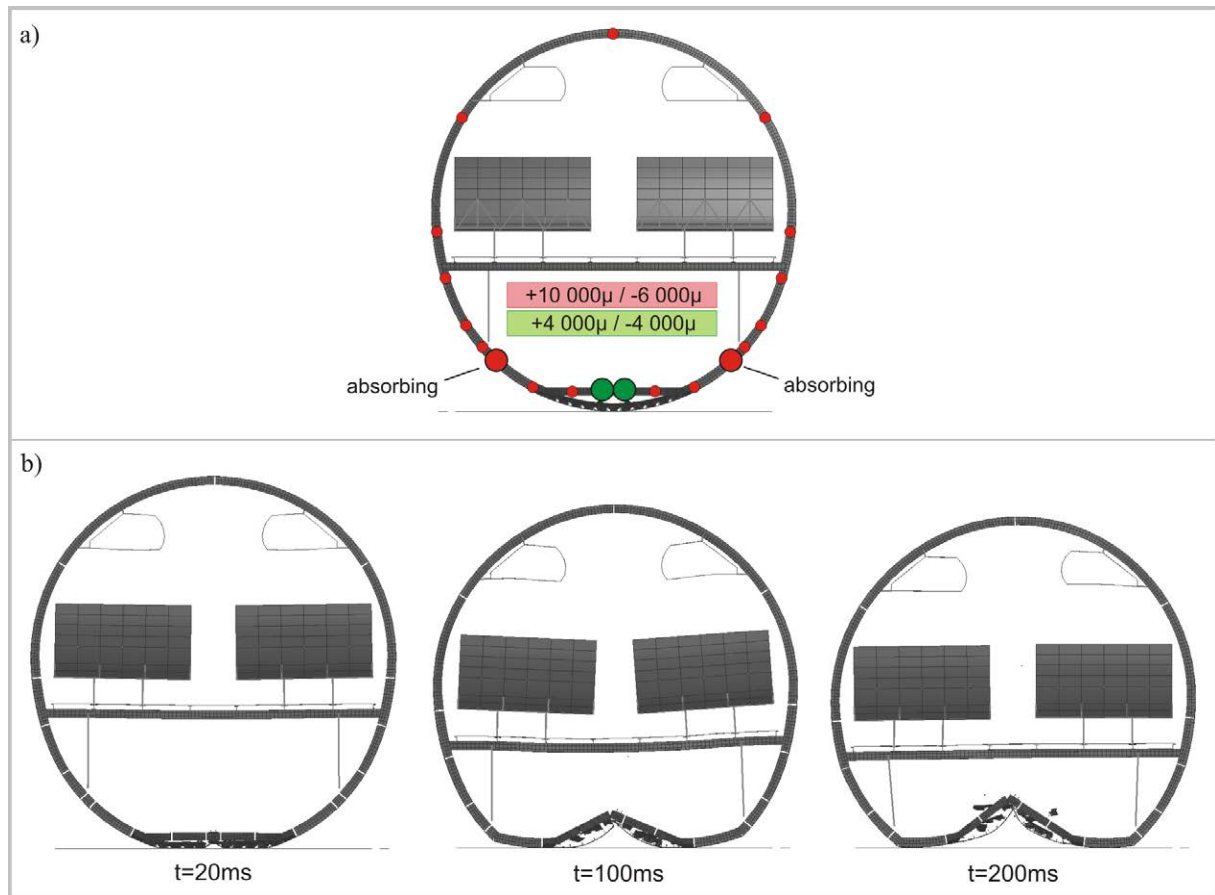


Figure 6-6: Scenario A - developed with the Kinematics Model

Figure 6-7 illustrates the final scenario B. The kinematic hinge characteristics are given in Figure 6-7a). As the cargo-crossbeam failure load was set to the strain limit values, first failure in the frame occurred at the critical location directly below the vertical support strut connection. A trigger strain of $\epsilon_{tr} = -6000$ microstrain was sufficient to achieve controlled frame failure at these kinematic hinges. For further initiation of the desired flattening effect, frame failure at the cargo-crossbeam connection had to occur directly after the first frame failure. In this crash phase the frame experiences a change of sign in the moment load from closing direction to opening direction at this location which is caused by frame failure of the kinematic hinge above. This effect is clarified in more detail in Appendix A4.2.1. To achieve a smooth transition into the flattening effect, a trigger strain of $\epsilon_{tr} = +4000$ microstrain was defined at the frame inner flange of the kinematic hinges positioned at the cargo-crossbeam connection. These kinematic hinges describe an absorbing characteristic as displayed in Figure 6-4b). The crash sequence of scenario B is given in Figure 6-7b).

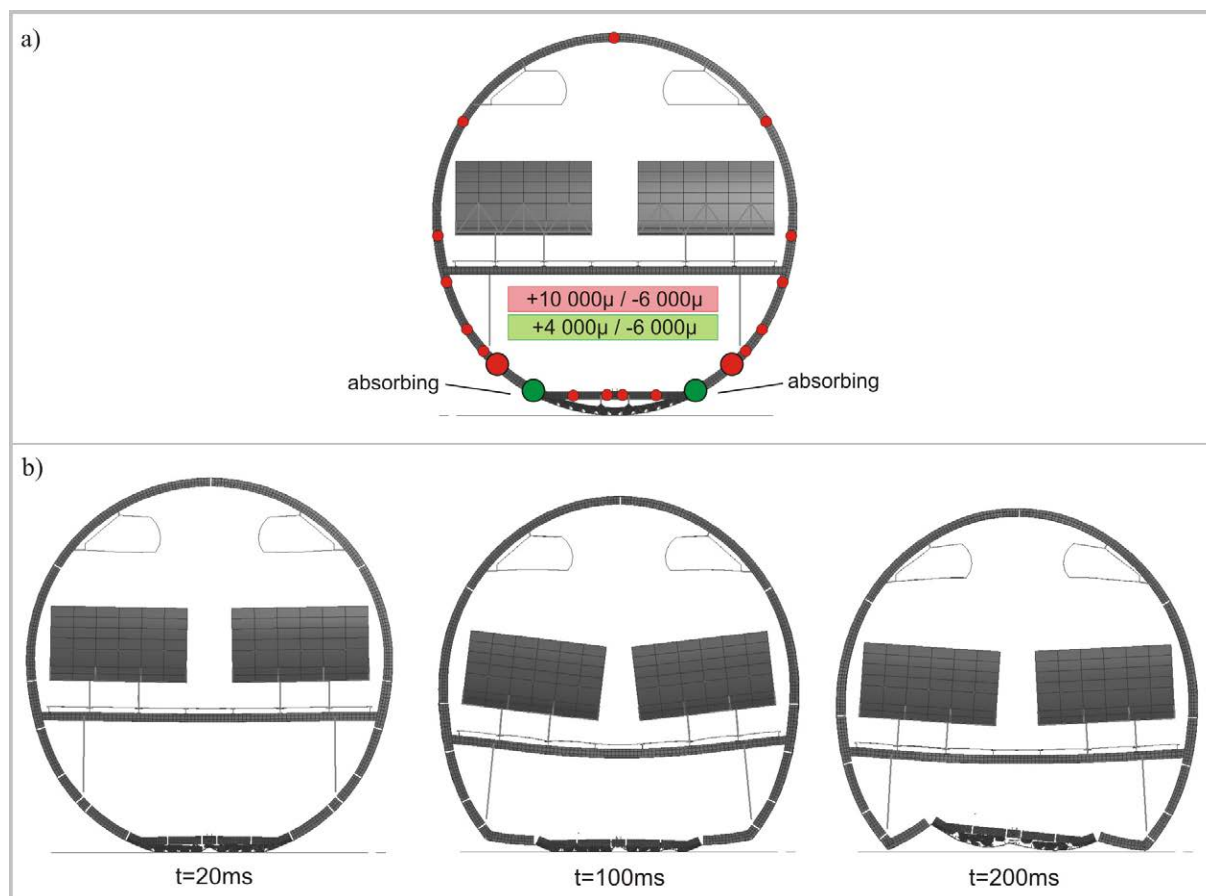


Figure 6-7: Scenario B - developed with the Kinematics Model

6.3. Assessment of crash scenario A & B

The basis of the scenario assessment is the ‘standard crash case’ that is defined in detail in paragraph 6.2 and that aligns to boundary conditions of well-known fuselage section drop tests performed in the past.

In addition, further crash load cases were considered in this assessment to determine the robustness of both scenarios (A/B). These load cases differ from the standard crash case in:

- A/B 1. a higher initial velocity of $v_i = 9.1 \text{ m/s}$ (30 ft/s),
- A/B 2. one-sided loading with occupied triple seat and loaded overhead bins at one side combined with free triple seat and unloaded overhead bins at the other side,
- A/B 3. cargo loading represented by a flat plate with a distributed mass of $m = 745 \text{ kg}$,
- A/B 4. a roll angle of $\phi = 5^\circ$.

With respect to the standard crash case, Figure 6-8 displays the energy plot of both scenarios. As expected the comparison of both diagrams illustrates a similar first crash phase, the crushing of the sub-cargo area. After the crushing of the sub-cargo structure the storage of elastic energy in

the fuselage structure increases up to failure of the cargo-crossbeam respectively the frame. This elastic storage is visible in the plots of total kinetic and internal energy.

In the further sequence of scenario A, the kinematic hinges rotate with energy absorption up to the impact of the vertical support struts on the ground. With that impact the crushing of the struts is initiated and further energy is absorbed. The total kinetic energy of scenario A altogether shows a steady decrease during the crash sequence, except a little elastic storage effect in the transition from sub-cargo crushing to the frame failure phase. 70 % of the initial kinetic energy was absorbed by the crash devices respectively material failure in the sub-cargo area. The remaining energy (kinetic and potential energy) was stored elastically in the fuselage structure respectively remained kinetically.

After the crushing of the sub-cargo structure, the further sequence of scenario B also shows kinematic hinge rotation with energy absorption. In contrast to scenario A significantly higher rotation angle of the absorbing kinematic hinge must be reached to fulfil the required kinematics. Based on the defined absorbing characteristic of the kinematic hinge according to Figure 6-4b), the absorption capacity was exceeded and further non-absorbing hinge rotation followed up to the impact of the vertical support struts. This non-absorbing rotation phase is obvious in the energy plot where in the sequence of approximately $t = 100\text{-}125$ ms the total kinetic energy increases. A steep decrease of the total kinetic energy at approximately $t = 125\text{-}130$ ms indicates the impact of the vertical support struts on the ground. This steep decrease of the kinetic energy is equivalent to high acceleration loads on the passengers. In the following phase, the crushing of the vertical support struts could not be realised due to tensile failure of these struts in the previous phase of the crash sequence. According to the crash kinematics of scenario B the struts are loaded in tension during the frame bending phase. At about $t = 110$ ms these tensile loads exceed the strength of the defined strut characteristic as displayed in Figure 6-4c). In Figure 6-7b) the crash sequence at $t = 100$ ms illustrates the kinematic with oblique strut positions which leads to tension loading of the vertical struts. Although tensile failure could be avoided by the definition of a higher tensile failure load in the axial macro element, a modification of the basic macro characteristics was not the objective in this assessment study as the defined characteristic of the vertical support struts is based on experimental test results. In fact, the tensile failure can be seen as a general indication of high tension loads acting in the vertical support struts in case of a crash kinematics according to scenario B. Altogether, about 60 % of the initial kinetic energy was absorbed by the crash devices respectively material failure in the sub-cargo area. The remaining energy (kinetic and potential energy) was stored elastically in the fuselage structure respectively remained kinetically.

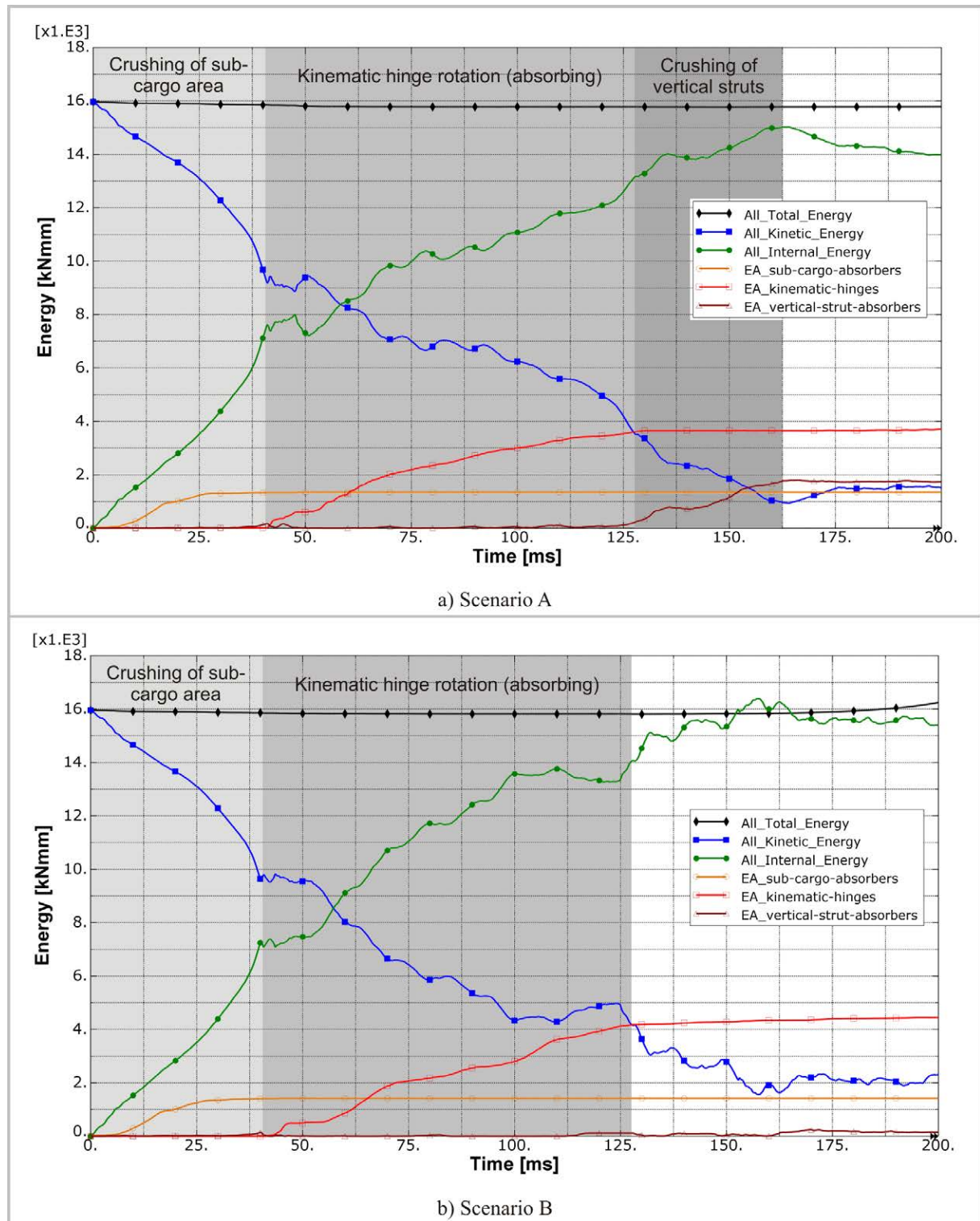


Figure 6-8: Energy plot of scenario A and B in the standard crash case

Finally, the assessment identified the following benefits and drawbacks of both crash scenarios:

The general crash kinematics leads to significantly higher frame bending rotation in case of scenario B. The simulation results of scenario B show a maximum hinge rotation of about $\varphi = 43^\circ$ of the absorbing opening hinge. In contrast to this, the absorbing closing hinge of scenario A experienced a maximum rotation angle of about $\varphi = 34^\circ$. With respect to a crash device concept that considers energy absorption by frame bending, significantly higher complexity is expected

when high absorbing rotations are required. Hence, a reduced frame bending rotation in scenario A is clearly a benefit. Appendix A4.2.2 provides a comparison of both kinematic hinge rotations.

The simulation results provided strain values along the frame inner flange that indicate tendencies of higher frame loading in case of scenario B during the whole hinge rotation phase. The spectrum of strain values in scenario B reaches the tensile as well as the compressive limit criteria whereas the spectrum of scenario A is clearly less critical. A more massive frame design is expected in case of scenario B according to these simulation results. A comparison of the frame inner flange strains is given in Appendix A4.2.3.

The tensile failure of the vertical support struts in scenario B clearly indicates higher tensile loads compared to scenario A where the crash kinematics does not result in an oblique strut position. Especially with respect to the trigger mechanism of a crushable vertical strut high tensile loads are complex to withstand. Reduced strut loads during the first crash phases up to ground impact of the strut are a clear benefit of scenario A. Appendix A4.2.4 compares the tensile loads in the vertical struts of scenario A and B.

With respect to the robustness load cases one obvious drawback of scenario A is a high interaction with potential cargo loading. As mentioned in the discussion of the natural crash kinematics in paragraph 6.1, cargo loading can hinder the developing of scenario A. In that case of cargo loading (A3) the simulation results indicated a high risk of failure at the frame coupling to the cargo-crossbeam. Failure at this location could potentially lead to scenario B. Another robustness case (A4: roll angle of $\varphi = 5^\circ$) indicates risk of frame failure at this location, too. Hence, a drawback of scenario A is the needful requirement of additional crash devices in the coupling of frame and cargo-crossbeam if a robust crash concept is desired.

On the other hand, some robustness load cases of scenario B identified frame failure above the passenger crossbeam (B1: $v_i = 9.1$ m/s; B3: cargo loading). Failure of the frame in the cabin area is assessed critical and therefore a clear drawback of scenario B.

Detailed results of the robustness analyses are given in Appendix A4.2.5 and A4.2.6.

Finally, the summation of benefits and drawbacks identified scenario A as the most favourable crash kinematics. Nevertheless, a potential change to a crash kinematics according to scenario B, caused by effects such as cargo loading constraints, has to be considered secondarily to ensure the development of a robust crash concept.

Summarising the investigations of the crash scenario assessment, natural crash kinematics of typical fuselage sections were identified on the basis of a review of documented experimental and analytical results which were generated in several research projects in the past. The

identified natural crash kinematics were developed in the Kinematics Model on the basis of a generic CFRP fuselage design. The crash kinematics were analysed and assessed regarding several identified effects. The outcome of the assessment is the selection of scenario A as the preferred crash kinematics which has to be considered primarily in the following steps of the crash scenario development.

7. Development of a crashworthy composite fuselage design

– crash scenario development

The crash kinematics assessment in chapter 6 identified scenario A to be the most favourable crash kinematics. Based on this selection, the detailed development of a crash scenario is discussed in this chapter. Figure 7-1 again illustrates the scope of the development of a crashworthy composite fuselage design and highlights this detailed development step. The basis of the crash scenario development is a CFRP narrow-body fuselage structure which was statically pre-sized with respect to relevant flight and ground loads by the project partner Airbus. Based on this pre-sized fuselage structure the final target of this investigation is the definition of an optimised crash scenario which includes the characterisation of local crash devices to achieve an optimised crash kinematics, as well as the adaptation of the fuselage structure to these optimised crash loads. Hence, the outcome of this investigation is a crashworthy fuselage design which includes information about additional mass penalty between statically sized and crashworthy frame structure regarding the selected crash concept.

The statically pre-sized narrow-body fuselage structure which is considered in this investigation differs in some parameters from the generic fuselage design which was used in the crash kinematics assessment in chapter 6. Main differences are the length of the 2-bay fuselage section and, as a consequence of the increased section length, the definition of two seat rows instead of one. Nevertheless, the main fuselage design is similar and the same crash concepts shall be used here. Details on the fuselage design as well as the Kinematics Model definitions are given in Appendix A5.1.

In the following, paragraph 7.1 deals with the structural allowables which were used in this scenario development. In contrast to the crash kinematics assessment of chapter 6 more precise criteria were used, especially for the representation of compressive failure limits.

In paragraph 7.2 an analytical estimation for the crash scenario development is described. The individual crash zones as well as the crash loads in the individual phases are discussed.

Paragraph 7.3 gives a detailed overview on the approach which was used for the crash scenario development.

The crash scenario development in detail is presented in paragraph 7.4. The adaptation of the crash kinematics as well as of the fuselage structure are described in this paragraph. Finally, as an outcome of the crash scenario development, the final crash scenario is discussed.

In paragraph 7.5 a further investigation of a modified final crash scenario is presented. With an additional crash device in the passenger crossbeam connection, this investigation illustrates how the Kinematics Model can be used efficiently for crash analyses in a preliminary design phase.

Finally, the determined macro characteristics are given in paragraph 7.6 which can be used as a basis for the development of local crash devices.

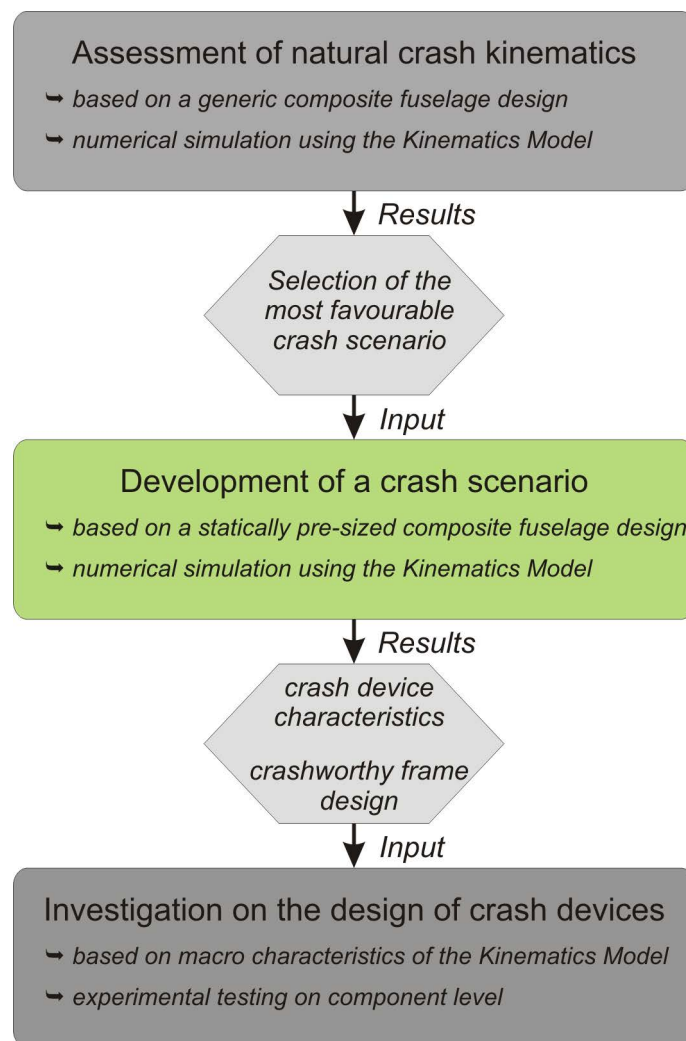


Figure 7-1 : Approach for the development of a crashworthy composite fuselage design

7.1. Definition of structural allowables

The crash kinematics assessment, described in chapter 6, used simplified criteria to describe the structural load limits of the frame structure - which is the main structural part in case of crash. Here, in the detailed development of a crash scenario, more precise criteria are required to represent the structural limits.

The tensile strain limit is based on material failure and was defined similarly to the crash kinematics assessment with $\epsilon_t = +10,000$ microstrain. Different criteria were defined for the compressive strain limits which are based on structural instability failure. The basis for the definition of compressive strain limits is the assumption of crippling failure in the flanges of the LCF-shaped frame. Crippling failure is characterised by a local distortion of the cross-sectional shape. With the beginning of buckling the more stable portions of a cross-section take additional load and support the already buckled portions. This leads to a typical stress distribution of a buckled structure as displayed in Figure 7-2 for a LCF-shaped frame with compressive loaded inner flange, e.g. caused by closing frame bending. With further increase of the compressive load, material failure stress is exceeded in the more stable portions of the cross-section and complete collapse of the structure may occur. This failure mode, characterised by local material failure in the more stable portions of a cross-section, is called crippling failure.

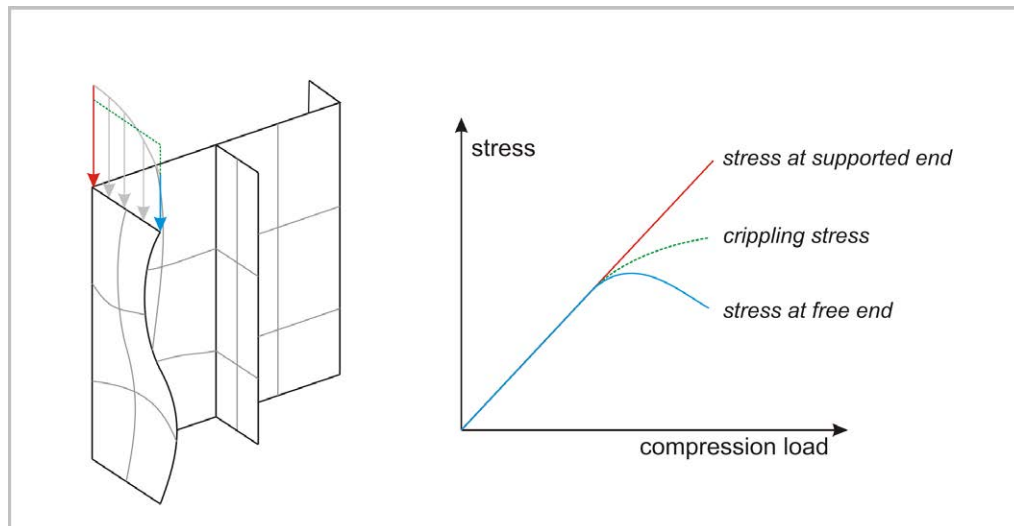


Figure 7-2: Stress distribution along a buckled inner flange of a LCF-shaped frame just before crippling

The use of crippling failure criteria for the definition of compressive strain limits allows the occurrence of frame flange buckling during the crash phase. Hence, the frame structure is well utilised and a massive frame design caused by conservative strain limit criteria can be avoided.

With respect to crippling failure, no satisfactory theory exists for the prediction of the cross-sectional average stress at failure, which is called ‘crippling stress’. Thus, it is necessary to rely on test results or empirical methods. Empirical formulations based on tests of different carbon composite material layups are given in the MIL-HDBK-17 [123]. In these formulations the crippling stress is related to the laminate strength. Figure 7-3a) compares one of these empirical formulations with test results for the ‘one-edge free’ variant. The ‘one-edge free’ formulation describes test results of flat laminates under compression load which are supported only at one

edge. This setup is comparable with the flanges of an LCF-frame design. The ‘one-edge free’ formulation recommended for preliminary design is

$$\frac{F_{cc}}{F_{CII}} = 1.63 * \left(\frac{b}{t} \right)^{-0.717}, \quad (7.1)$$

where F_{CC} is the crippling stress and F_{CII} is the laminate compression strength. b/t is the ratio of flange width to flange thickness. Assuming linear-elastic material behaviour up to failure this formulation can be described as

$$\frac{F_{cc}}{F_{CII}} = \frac{\varepsilon_{cc}}{\varepsilon_{cII}} = 1.63 * \left(\frac{b}{t} \right)^{-0.717}. \quad (7.2)$$

With this formulation the crippling failure strain ε_{CC} can be determined based on the laminate compression failure strain ε_{CII} . This crippling failure strain is the average strain over the cross-section at failure. Figure 7-3b) illustrates a ‘one-edge free’ test setup after crippling failure. Further discussions about post-buckling and crippling effects are given in [124-126].

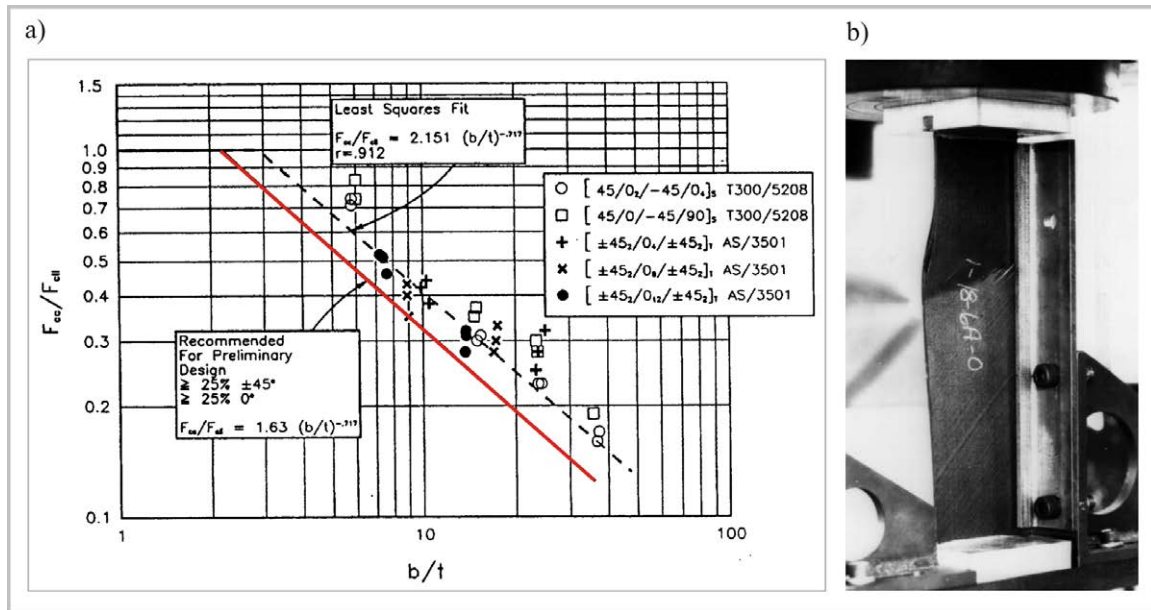


Figure 7-3: Normalised crippling data of the 'one-edge free' tests [123]

With respect to the Kinematics Model the structural frame loads are measured with strain bar elements, as discussed in paragraph 3.3.2. These bar elements are positioned at the corners of the inner flange respectively the outer flange and the web, and measure the local strains along the frame. Thus, an average strain over the frame flange cross-sections, which could be used directly for a check against the crippling strain, is not measured.

On the other hand, the strain measured with bar elements in the more stable frame corners can be checked directly against laminate failure strain according to the crippling theory. The

investigations on the accuracy of the Kinematics Model approach in paragraph 4.5 identified good agreement of the elastic frame behaviour compared to detailed FEM analysis. The buckling modes could be resolved acceptably in the Kinematics Model. Nevertheless, the Kinematics Model approach does not aim to represent buckling modes in detailed accuracy. Thus, it is not recommended to use this procedure in the Kinematics Model.

Instead, a conservative assumption was used which checks the bar element strains of the frame section corners against the average crippling strain. The check of locally increased strain values measured at the frame corners against average crippling strains represents a conservative estimation which is reasonable in a preliminary design process.

Accordingly, the structural allowables used in this crash scenario development for the frame structure are defined as illustrated in Figure 7-4. Tensile failure is assumed at a strain of $\epsilon_{t1} = +10,000$ microstrain. The static sizing was conducted with maximum tensile strain of $\epsilon_{t2} = +6000$ microstrain. Regarding compression loads, the minimum allowed compression strain for static sizing, ϵ_{c2} , depends on the frame laminate. This static strain allowable includes several parameters like open-hole reduction, b-values or hot-wet conditions. Compressive failure is assumed by crippling, the failure strain ϵ_{c1} depends on the frame flange layup thickness according to the ‘one-edge free’ crippling formulation. Potential trigger mechanisms in the frame are allowed to trigger in the range between static sizing and material tensile respectively structural instability failure.

Similar structural allowables were used for the design of the cargo-crossbeam.

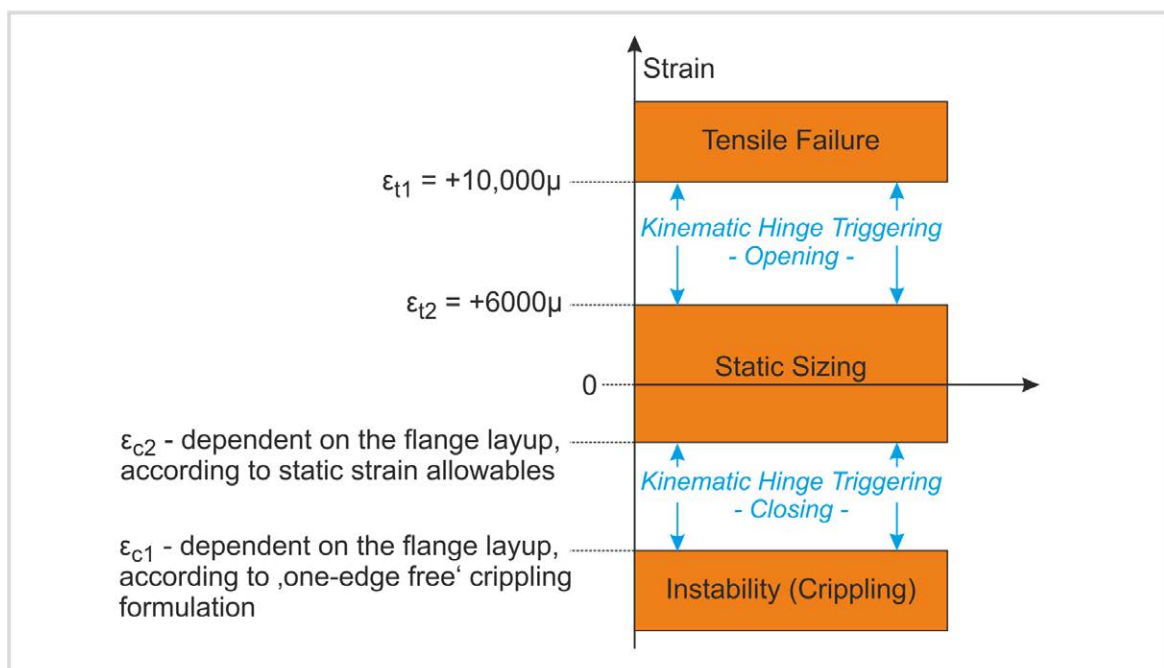


Figure 7-4: Structural allowables used in the crash scenario development

7.2. Analytical consideration of the crash zone

In one of the first steps of the crash scenario development a general estimation of the required energy absorption capacity in the individual crash zones of a fuselage section shall provide a basic understanding that can be used in the following simulation procedure.

In general, a common basis for comparison of crashworthiness is the ‘standard crash case’ of a vertical drop test with an initial velocity of $v_i = 6.7$ m/s (22 ft/s), according to several drop tests which were performed in the past. Regarding this standard crash case one potential analytical approach considers the Emergency Landing Conditions of the Federal Aviation Regulations, FAR Part 25.561, which specifies a crashworthiness that is verified by a quasi-static crash approach: *“The structure must be designed to give each occupant every reasonable chance of escaping serious injury in a minor crash landing when... the occupant experiences the following ultimate inertia forces... downward, 6.0g”* [10]. The crash load case is covered in this regulation by a quasi-static load which specifies a vertical acceleration of $a_z = 6.0$ g.

According to these regulations, one conceivable approach is the development of a crash concept which enables an average acceleration of less than $a_z = 6.0$ g with respect to the standard crash case of $v_i = 6.7$ m/s (22 ft/s). Considering the narrow-body soft section of this development process the sub-cargo area specifies a crushable height of about $H_1 = 150$ mm, as illustrated in Figure 7-5. A concept which specifies only the usage of this crash zone for the standard crash case would lead to an average acceleration of about $a_{z1} = 15.0$ g. Therefore, further crash concepts are necessary in the fuselage structure above the sub-cargo area to reduce the average acceleration. Considering additionally the crash zone between cargo floor and vertical support struts the crushable height is about $H_{1+2} = 450$ mm. A concept which specifies the usage of these two crash zones for the standard crash case would lead to an average acceleration of about $a_{z1+2} = 5.0$ g, and would fulfil the quasi-static crash approach which is specified in the FAR. With respect to this approach passive vertical support struts could be defined for the standard crash case. Further energy absorption capacity could be provided in these struts for robustness crash cases, e.g. with a higher initial velocity. This theoretical approach identified the necessity of energy absorbing crash devices above the cargo floor and gives a first estimation of a potentially necessary crash distance with respect to the standard crash case.

In this approach specified acceleration levels are considered and not the energy absorbing capacity of a typical fuselage structure. For that reason, the crashworthiness of novel CFRP fuselage structures is not verified against this regulation. Instead, an equivalent crashworthiness has to be demonstrated based on certified fuselage structures of the same size that are traditionally fabricated from metallic material [11]. Hence, higher acceleration levels than the

average values discussed above are supposable if the metallic equivalent shows such crash behaviour.

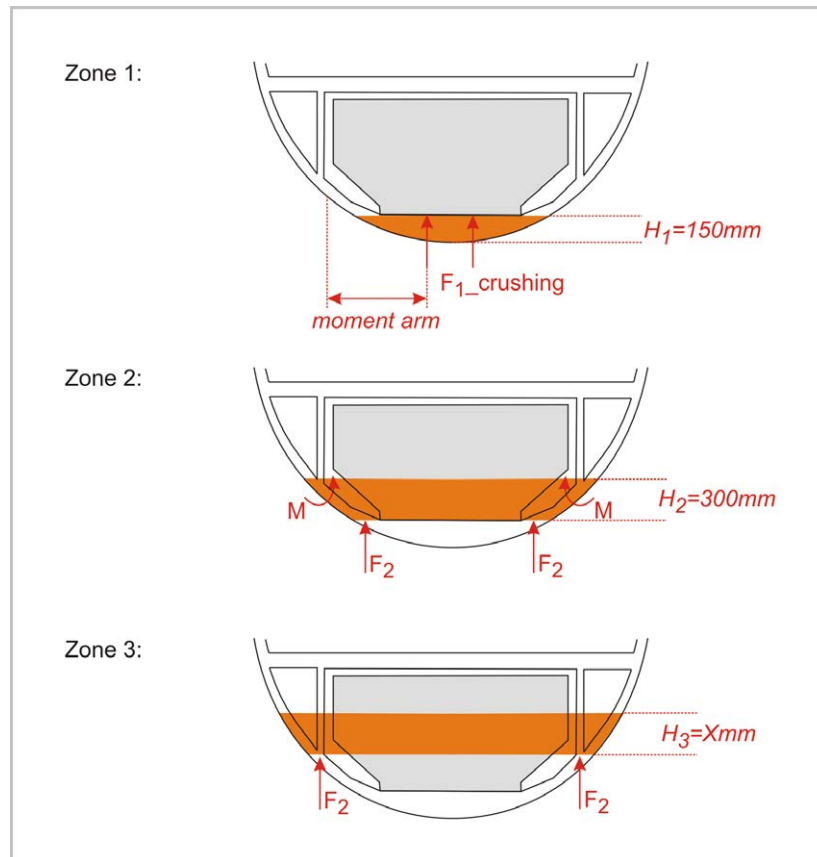


Figure 7-5: Crash zones of a typical narrow-body fuselage section

The outcome of the above discussion is a general estimation of the required energy absorption. Looking at the individual crash zones of a fuselage section, different issues are discussed in the following.

A theoretically optimised crash design offers constant accelerations and therefore constant and minimised crash loads during the whole crash sequence. In the different phases during the crash of a fuselage structure the crash load is associated with different moment arms and different critical structural parts as illustrated in Figure 7-5.

In the first crash phase, the crushing of the sub-cargo structure, a high moment arm acts with respect to the frame in the lower side shell and induces high loads. Furthermore, the cargo-crossbeam is highly loaded with moment and compression loads. A massive crossbeam and frame design is expected which strongly depends on the crushing force level of the sub-cargo structure. Hence, it is expected that the usage of a comparably small crash height of $H_1 = 150\text{ mm}$ would lead to significant mass increase of the crashworthy fuselage structure.

In the second phase, the frame bending phase, the moment distribution along the frame differs from phase 1 due to the specified failure of the cargo-crossbeam in scenario A. The moment arm

of the average crash load is reduced compared to phase 1. It is expected that this crash phase is less critical for the backing structure and will not affect the frame sizing. The crash distance of zone 2 is approximately twice the height of zone 1. Considering a constant acceleration level during the whole crash sequence, the energy absorption of the frame bending mechanism in the kinematic hinges has to be twice the energy which is absorbed in the sub-cargo area. The challenge here is to develop a frame bending concept which provides this high energy absorption capacity. It is expected that an absorbing bending concept will not be able to achieve such a high mass specific energy absorption as it is feasible in a crushing process of the CFRP structure in zone 1.

In a last crash phase, a high crash distance of zone 3 can be used in case of several robustness cases. In Figure 7-5, the illustration of this crash distance is limited to the lower part of the Bermuda triangle without a specific length. Regarding zone 3 the typical fuselage section has to be considered in the scope of a full-scale fuselage structure. Structural parts like the centre wing box and the landing gear bay influence the crash behaviour of a typical fuselage section. Therefore, it is expected that the height of the Bermuda triangle can not be used completely in a real crash scenario. Nevertheless, the lower part of the Bermuda triangle can be defined as a realistic crash zone. In this final crash phase, the moment arm of the average crash load is small and little mass penalty is expected to achieve a crashworthy backing structure above this crash zone. The limiting factor of this crash zone is the kinematic behaviour of the Bermuda triangle. A crushing of the vertical support struts has to be supported by the frame structure, otherwise the stiff frame structure may carry the crash load with a limited crushing capability, and accordingly high accelerations may act on the structure. In addition, it is expected that a disintegration of the Bermuda triangle may lead to critical crash kinematics which has to be controlled by the local crash device.

The analytical consideration explained above showed benefits and drawbacks in all individual crash zones. None of the crash zones was identified as a clear favourite. Hence, it is not reasonable to differ from the strategy of an optimised crash kinematics with constant crash loads during the whole crash phase. In case of a clear favourite, a compromise of theoretical kinematics optimisation and realisation of a crash concept could specify a higher energy absorption in the favoured crash zone compared to the other zones with the price of a certain deviation of the optimised constant acceleration level.

7.3. Approach for the crash scenario development

The effects of crash loads in the individual phases of a crash sequence were discussed in paragraph 7.2. In general, it is expected that the crash loads will clearly exceed the load carrying capacity of the statically pre-sized fuselage structure, in particular on the basis of a bend-frame concept as it is considered in this study.

Hence, an adaptation of the statically pre-sized frame structure was foreseen in this crash scenario development to adapt the frame sizing to the finally identified crash loads. The adaptation of the frame structure was conducted on the basis of a frame profile catalogue which was provided by a static analysis of the project partner Airbus. The frame profile catalogue offers LCF-shaped frame profiles of similar design with increasing stiffness respectively flange thicknesses and frame heights. The smallest frame profile of this catalogue represents the statically sized frame design with a frame height of $H_f = 92$ mm and a flange thickness of $t_f = 2.6$ mm. The stiffest frame profile provides a frame height of $H_f = 120$ mm and a flange thickness of $t_f = 9.2$ mm. In total 15 different profile definitions were provided, Figure 7-6a) shows examples.

Regarding the cargo-crossbeam a similar profile catalogue was provided. A total number of 12 τ -shaped profiles was given in this catalogue. The smallest profile of this catalogue provides a crossbeam height of $H_{CCB} = 55$ mm and flange thicknesses of $t_{UF} = 3.4$ mm as well as $t_{LF} = 5.5$ mm. The stiffest profile specifies a crossbeam height of $H_{CCB} = 100$ mm and flange thicknesses of $t_{UF} = 5.5$ mm as well as $t_{LF} = 8.75$ mm. Figure 7-6b) shows examples of the cargo-crossbeam profile catalogue.

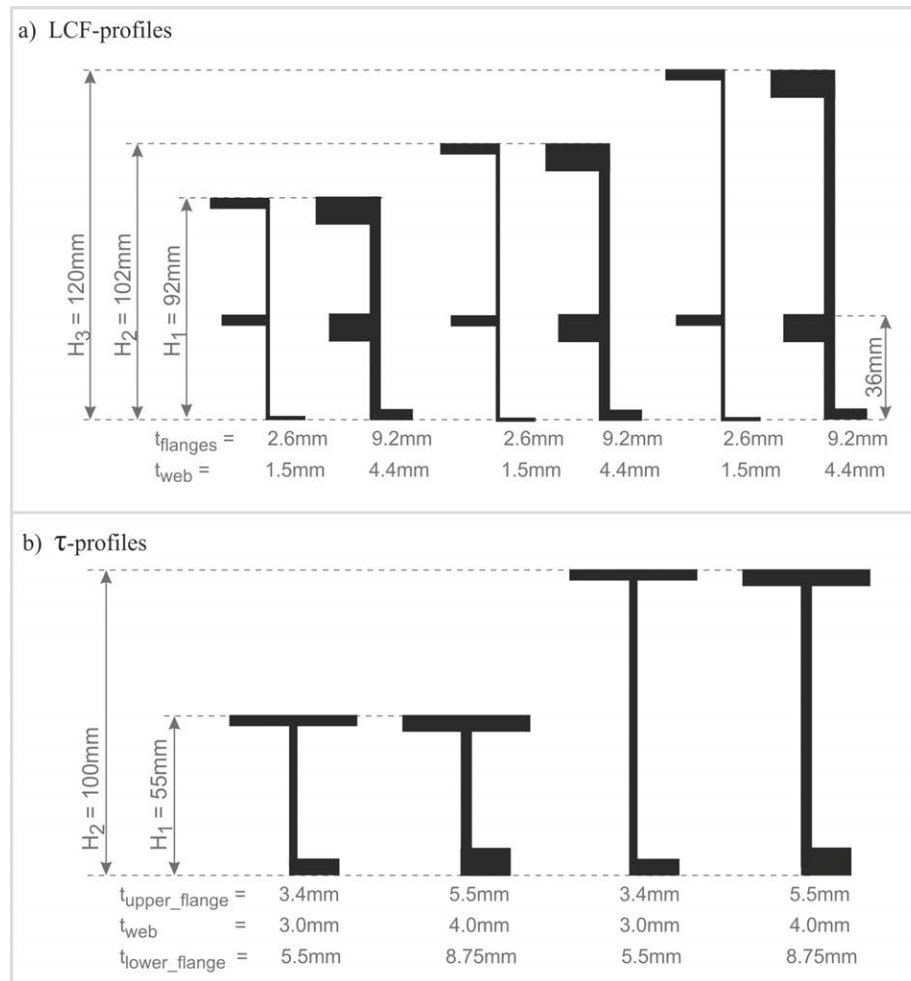


Figure 7-6: Examples of a) the frame and b) the cargo-crossbeam profile catalogue

The approach for the crash scenario development starts with a frame and cargo-crossbeam definition according to the stiffest profile to avoid instability failure and strain limit exceeding during the development process. A subsequent adaptation of the frame and cargo-crossbeam structure is conducted downwards based on the stiffest profile.

Figure 7-7 provides an overview on this approach. The starting point of the development procedure is a maximum structural frame and cargo-crossbeam design according to the profile catalogues. In addition, the trigger loads of all crash devices above the cargo floor were set to the maximum values according to the strain criteria discussed in paragraph 7.1. Based on this starting point a sub-cargo study was conducted in the first step of the crash scenario development. The outcome of this study is the maximum energy value which can be absorbed in the sub-cargo area with the given maximum frame and cargo-crossbeam structure. Based on the specified fuselage geometry this energy value is equivalent to a specific crushing force level. As the bend-frame concept specifies a crushing of the sub-cargo structure without failure of the above fuselage structure, this sub-cargo study could be performed independently from the following crash kinematics.

In the second step of the scenario development the crash kinematics were optimised by the determination of appropriate input characteristics for the kinematic hinges in the frame region between cargo-crossbeam and vertical support struts, as well as in the cargo-crossbeam. These macro input characteristics were determined in a way that an optimised crash kinematics according to scenario A was achieved. The outcome of this development step are optimised crash loads with respect to a scenario A kinematics and the given fuselage structure, as well as the input characteristics in the kinematic hinges which are necessary to achieve the requested crash kinematics.

With this optimised crash kinematics the maximum frame design was adapted to the crash loads in a further step. The outcome of this adaptation is a more filigree frame design compared to the maximum design. Nevertheless, this crashworthy frame design will be significantly more massive compared to the filigree design after the static sizing.

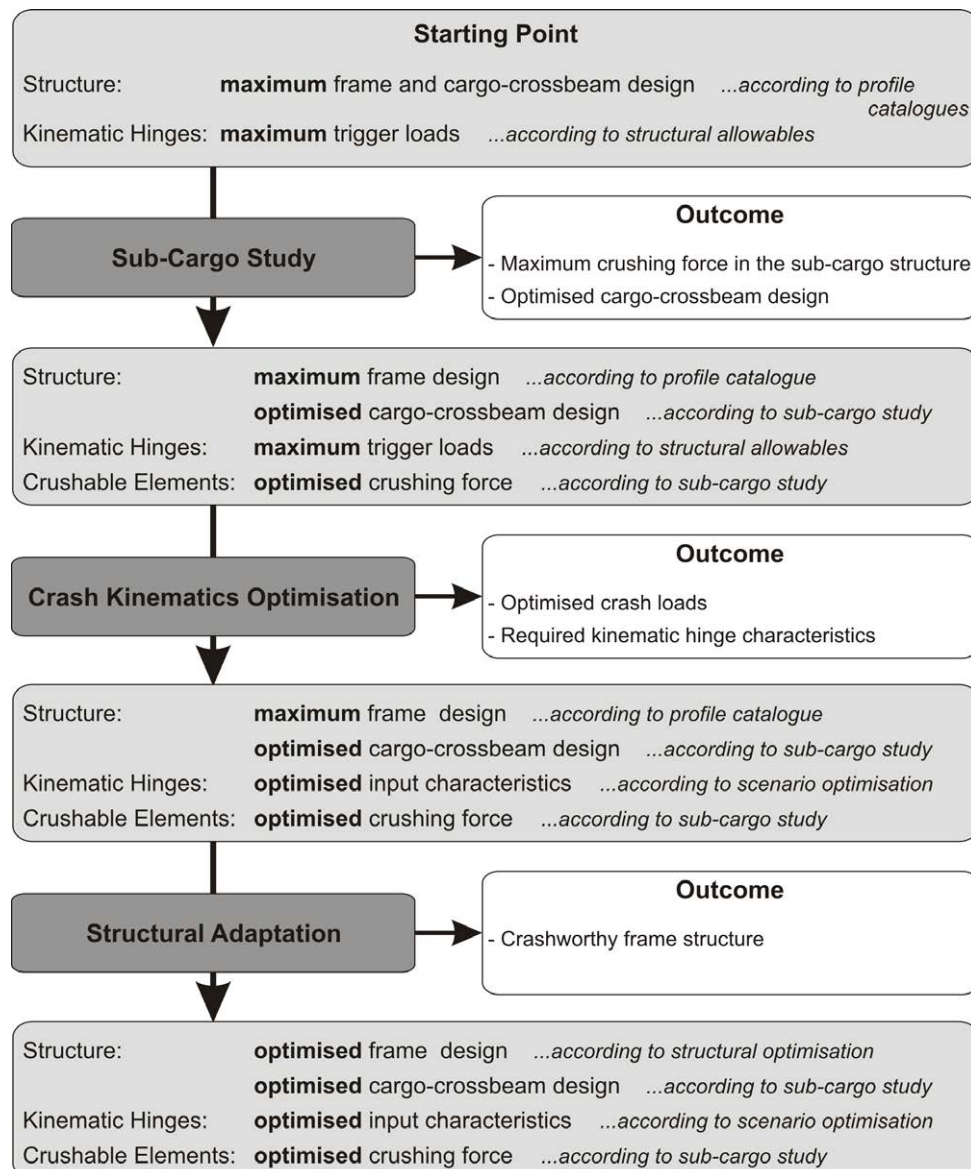


Figure 7-7: Approach for the crash scenario development

In the following crash scenario development, the basic characteristic input of the macro elements was defined similarly to the crash kinematics assessment discussed in chapter 6. One exception is the input characteristic of the kinematic hinges. In chapter 6, the absorption levels in the moment-rotation characteristic were defined at fixed values. These moment levels were based on the lateral stability behaviour of the generic frame structure during a frame bending process. Here, the crash scenario development includes a structural adaptation. Hence, the frame design can vary and with the frame design the lateral frame stability varies, which leads to different maximum possible moment levels during frame bending. To take this into account, the absorbing moment level of the kinematic hinge was defined in dependence of the trigger moment. A basic assumption was used here which describes the absorption level at 50 % of the trigger level. Although this assumption is generic, the general dependence of the absorbing moment level on the lateral frame stability is considered. In addition, the maximum absorbing rotation was defined more conservative compared to the crash kinematics assessment of chapter 6. The complex absorption characteristic of different moment levels used in the kinematics assessment was replaced by a constant moment level and the maximum absorbing rotation was reduced to $\varphi = 20^\circ$.

Figure 7-8 illustrates the general characteristic macro input for the individual macro elements which were used in this crash scenario development. For all macro elements the trigger load is the independent parameter for the variation of the crash device behaviour.

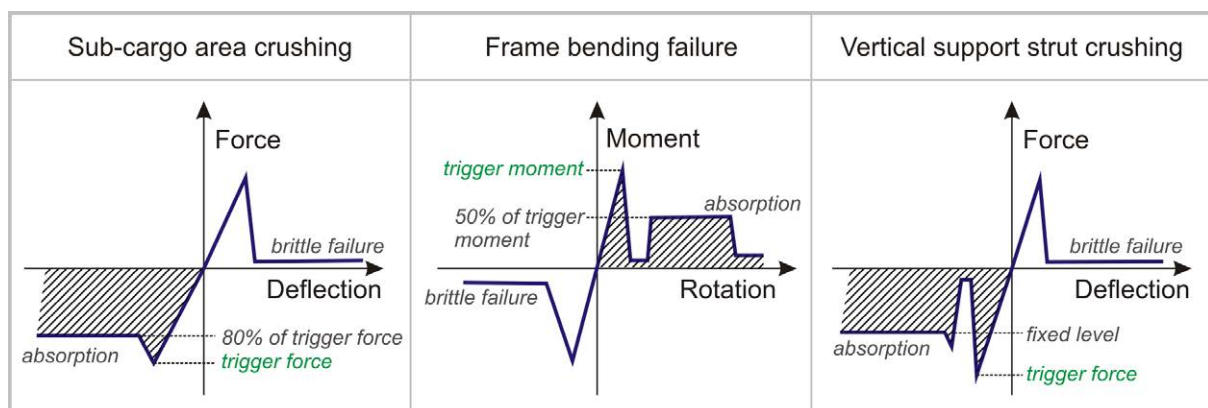


Figure 7-8: Characteristic input for the macro elements

7.4. Crash scenario development

The crash scenario development started with a sub-cargo study, similar to investigations on sub-cargo crushing described in paragraph 6.2. The maximum possible energy absorption by the crushing of the sub-cargo floor structure was analysed, based on the given profile catalogues. The investigation started with the stiffest of the given τ -profile for the cargo-crossbeam.

Simulation runs with different trigger loads in the sub-cargo crushing macro elements identified the individual crushing distances respectively amounts of absorbed energy.

The structural allowables in this sub-cargo study were checked by the longitudinal strains along the frame as well as the cargo-crossbeam, which were measured with the strain bar elements. The strain limit criteria were defined according to the discussion of paragraph 7.1.

The outcome of the sub-cargo study is an optimised trigger force for the sub-cargo absorbers of $F = 15 \text{ kN}$ in combination with the stiffest crossbeam profile according to the profile catalogue.

Based on these results of the sub-cargo study the crash kinematics optimisation is presented in paragraph 7.4.1. The subsequent structural adaptation of the frame structure is discussed in paragraph 7.4.2. The results of the final crash scenario are summarised in paragraph 7.4.3.

7.4.1. Crash kinematics optimisation

The crash kinematics optimisation starts with the investigation of the maximum possible crash scenario. Based on the maximum frame structure according to the frame profile catalogue as well as the outcomes of the sub-cargo study, the input characteristics of the kinematic hinges were defined in a way that the trigger strains in the frame reach the structural allowables. Based on the characteristic macro input, given in Figure 7-8 of paragraph 7.3, this scenario provides the maximum possible energy absorption for the given fuselage structure.

All active kinematic hinges, which describe the crash kinematics, are defined here with an absorbing characteristic. The crash sequence of the standard crash case, $v_i = 6.7 \text{ m/s}$ (22 ft/s), is given in Figure 7-9. With maximum possible energy absorption in the kinematic hinges a remaining distance of $\Delta z \approx 170 \text{ mm}$ was identified at the end of the crash between the vertical support struts and the ground. Figure 7-10 illustrates the output of the active kinematic hinges. The cargo-crossbeam experienced a maximum rotation of more than $\varphi_{\text{CCB}} = 35^\circ$. Hence, the energy absorbing capacity, defined over a rotation of $\varphi_{\text{abs}} = 20^\circ$, was utilised completely. The kinematic hinges in the frame, located below the vertical support struts, experienced a maximum rotation of about $\varphi_{\text{Frame}} = 17^\circ$ on each fuselage side. Here, the energy absorbing moment plateau was not used up completely.

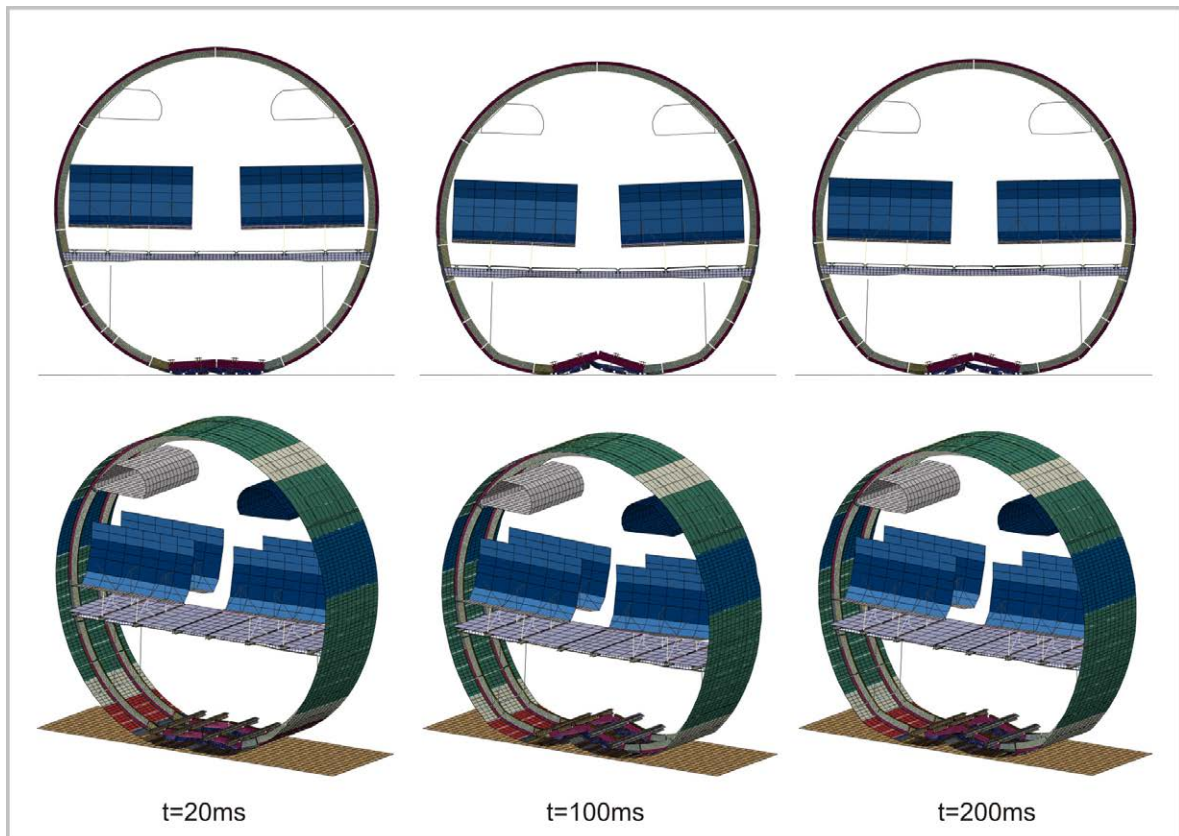


Figure 7-9: Crash sequence of the 'standard crash case' with maximum possible energy absorption

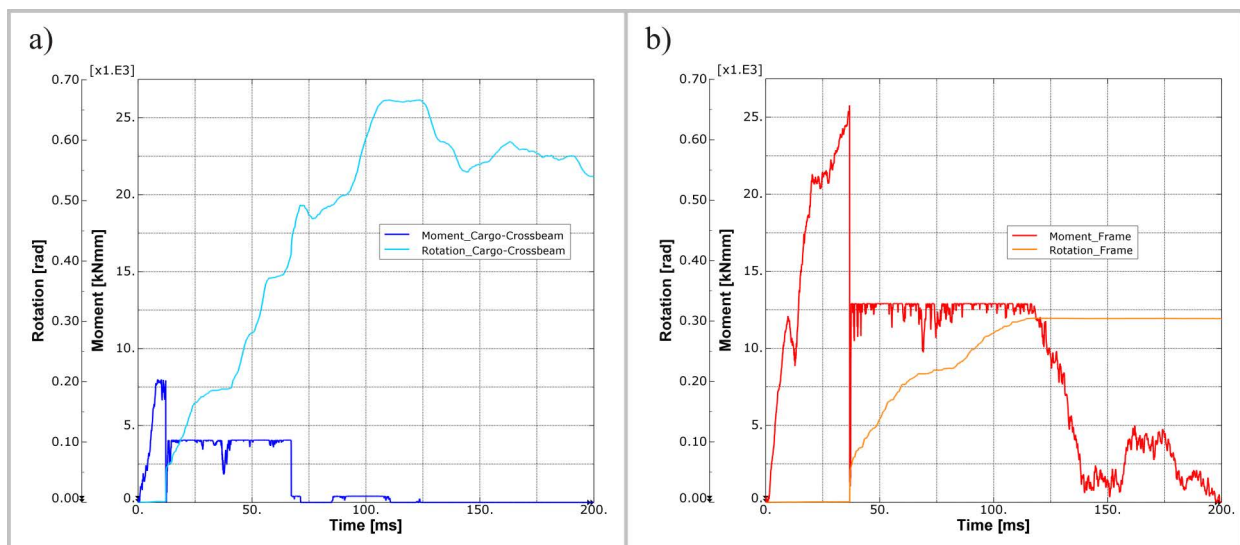


Figure 7-10: Kinematic hinge output of the 'standard crash case' with maximum possible energy absorption

This variant of maximum possible energy absorption implicates high acceleration loads for the passengers as the kinetic energy is absorbed over a minimum crash distance. Figure 7-11 shows the passenger accelerations in the Eiband diagram. The results of the front seat-row for the passengers A-F are given. The second seat-row in the simulation model shows similar acceleration values. All passengers experience high accelerations which are close to the limit of severe injury.

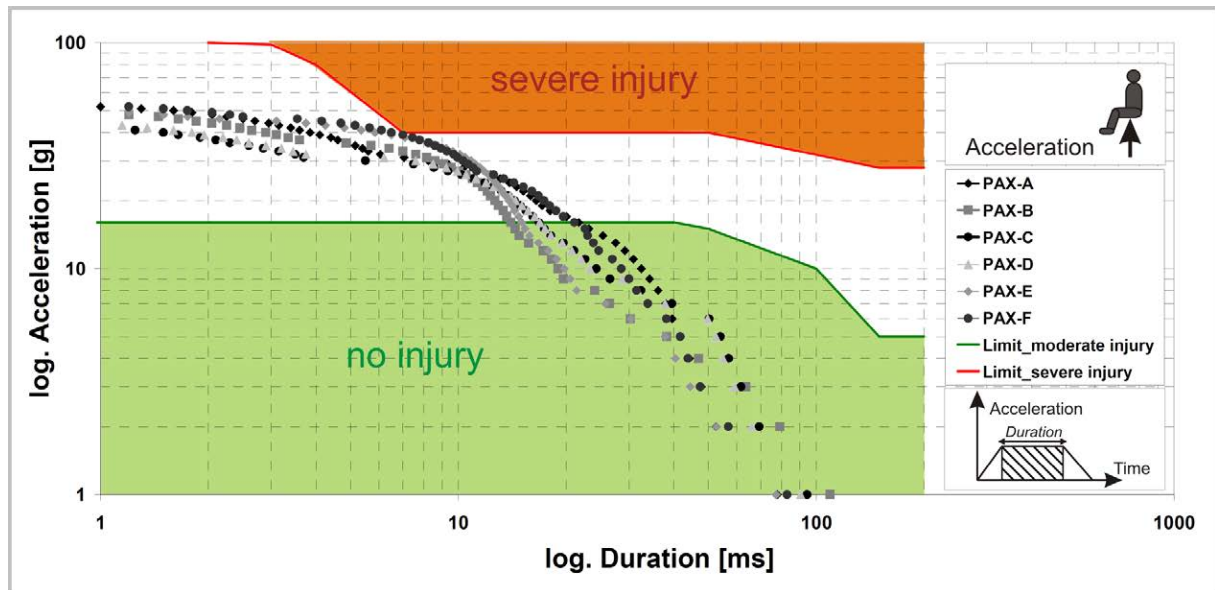


Figure 7-11: Passenger accelerations of the first seat row – ‘standard crash case’ with maximum possible energy absorption

In the following, the kinematic hinge input characteristics were modified stepwise to utilise the remaining distance of $\Delta z \approx 170$ mm between the vertical support struts and the ground for a smoother crash kinematics. Nevertheless, passive vertical struts are still foreseen for the standard crash case. Hence, the total kinetic energy has to be absorbed up to the ground contact of the struts. The trigger moments respectively the absorbing levels of the frame kinematic hinges were stepwise reduced to 75 %, 60 % and 50 % of the maximum possible level.

Figure 7-12 compares plots of the total internal energy of these three variants with the ‘100 % variant’ investigated above. The first crash phase, the crushing of the sub-cargo structure, shows identical curves for all variants, as expected. In the following, the frame failure, more precisely the kinematic hinge triggering, can be identified by a small decrease of the internal energy which is caused by the partly release of elastically stored energy. The plots illustrate the influence of the trigger moment on the triggering time. With decreasing trigger moment, the kinematic hinges trigger accordingly earlier. Whereas in the ‘100 % variant’ the kinematic hinges trigger at $t = 35$ ms, the ‘50 % variant’ shows a trigger time of $t = 14$ ms. After triggering of the kinematic hinges in the frame different absorbing moment levels in the individual variants are indicated by different averaged slopes of the internal energy curves. In the further progress of the curves a reduction of the averaged slope indicate the exceedance of absorbing bending in the cargo-crossbeam. The absorbing rotation of $\varphi_{CCB} = 20^\circ$ is reached at that time. A further reduction of the averaged slope indicates the end of energy absorbing rotation in the frame hinges. In the further progress of the energy curves the averaged slope is almost horizontal.

The final progress of the curves is of interest in this investigation, too. Here the curves give valuable information about potential ground contact of the vertical support struts as well as the amount of remaining kinetic energy at that time. As already discussed above, the '100 % variant' with maximum possible energy absorption shows no ground contact of the vertical support struts. A remaining distance of $\Delta z \approx 170$ mm was determined in that variant. The internal energy curve of this variant illustrates in the last crash phase a smooth progress to a horizontal level which indicates the end of the crash sequence. In contrast to this, the variants with decreasing energy absorption show a more distinct increase of internal energy in the final crash phase which finally decreases again. This curve progression is caused by an elastic rebound effect of the fuselage structure. The reduction of energy absorption leads to a higher crash distance with the utilisation of the remaining distance of $\Delta z \approx 170$ mm. With further reduction of energy absorption in the kinematic hinges, the vertical support struts hit the ground with an increasing amount of remaining kinetic energy. Hence, the '50 % variant' shows a very distinct rebound effect. In this variant the energy absorption in the frame is not sufficient for the standard crash case. The '60 % variant' shows a small rebound effect whereas in the '75 % variant' a rebound effect is hardly visible.

In this crash kinematics optimisation, the trigger force of the vertical support struts was defined artificially high to indicate the ground contact and to obtain valuable information as discussed above.

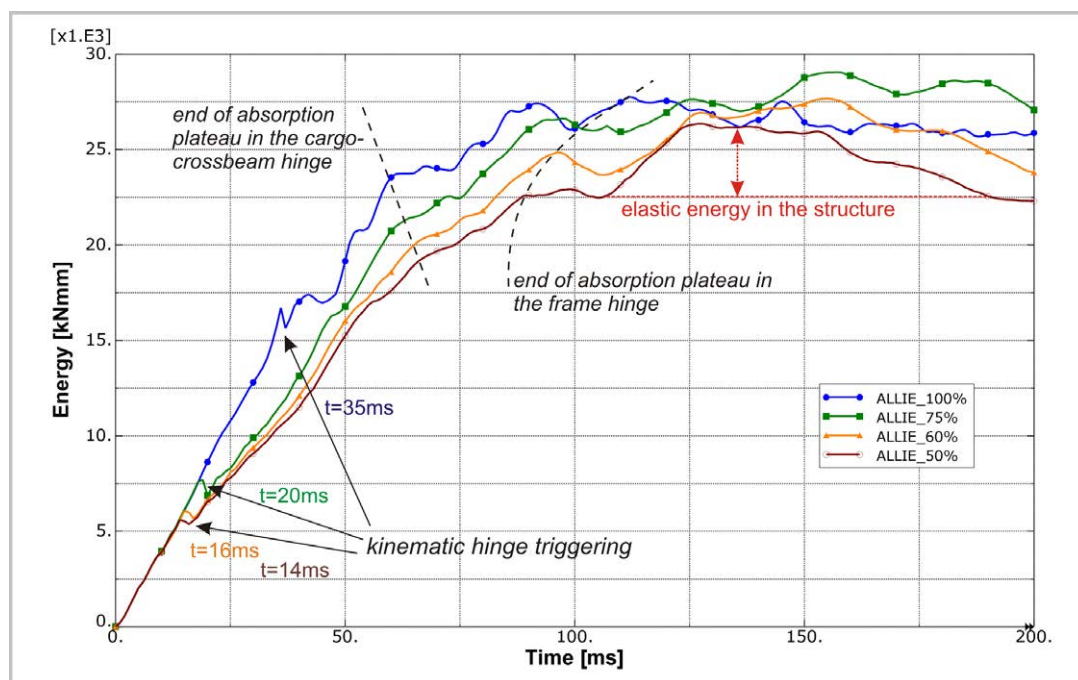


Figure 7-12: Internal energy (ALLIE) with reducing energy absorption capacity in the frame

The structural loads of the '75 %' and the '60 % variant' are presented in Figure 7-13. The strains along the most critical frame inner flange are displayed over the crash duration. The first negative peak is at the time of kinematic hinge triggering in the frames. The crash loads in the frames abruptly reduce to a lower, constant level which is the absorbing moment level of the kinematic hinges. After the exceedance of energy absorbing rotation the strain values drop again, followed by a further increase up to a second negative peak. This second peak is the ground contact of the vertical support struts. The elements showing the strain values of the first peak are located in the most critical frame region between cargo-crossbeam and vertical support struts. The elements showing the strain values of the second peak are located in the vertical orientated frame region of the Bermuda triangle and above the passenger floor.

The comparison of both diagrams in Figure 7-13 clearly shows a reduction of the first peak value for the '60 % variant' compared to the '75 % variant'. This reduction is equivalent to the reduced trigger moment in the kinematic hinge. In addition, the second peak in Figure 7-13b) shows higher absolute values compared to the '75 % variant' in Figure 7-13a). This increase of absolute strain value indicates a more distinct impact of the vertical support struts.

Regarding the analysed variants the utilisation of the remaining distance of $\Delta z \approx 170\text{mm}$ was achieved most favourable with the '75 % variant'. Hence, a reduction of 25 % of the maximum possible energy absorption was found to be an improved solution.

The passenger accelerations of this optimised crash kinematics are given in Figure 7-14. Compared to the accelerations of the maximum possible scenario, displayed in Figure 7-11, the acceleration values could be reduced significantly, with a larger margin to the limit of severe injury.

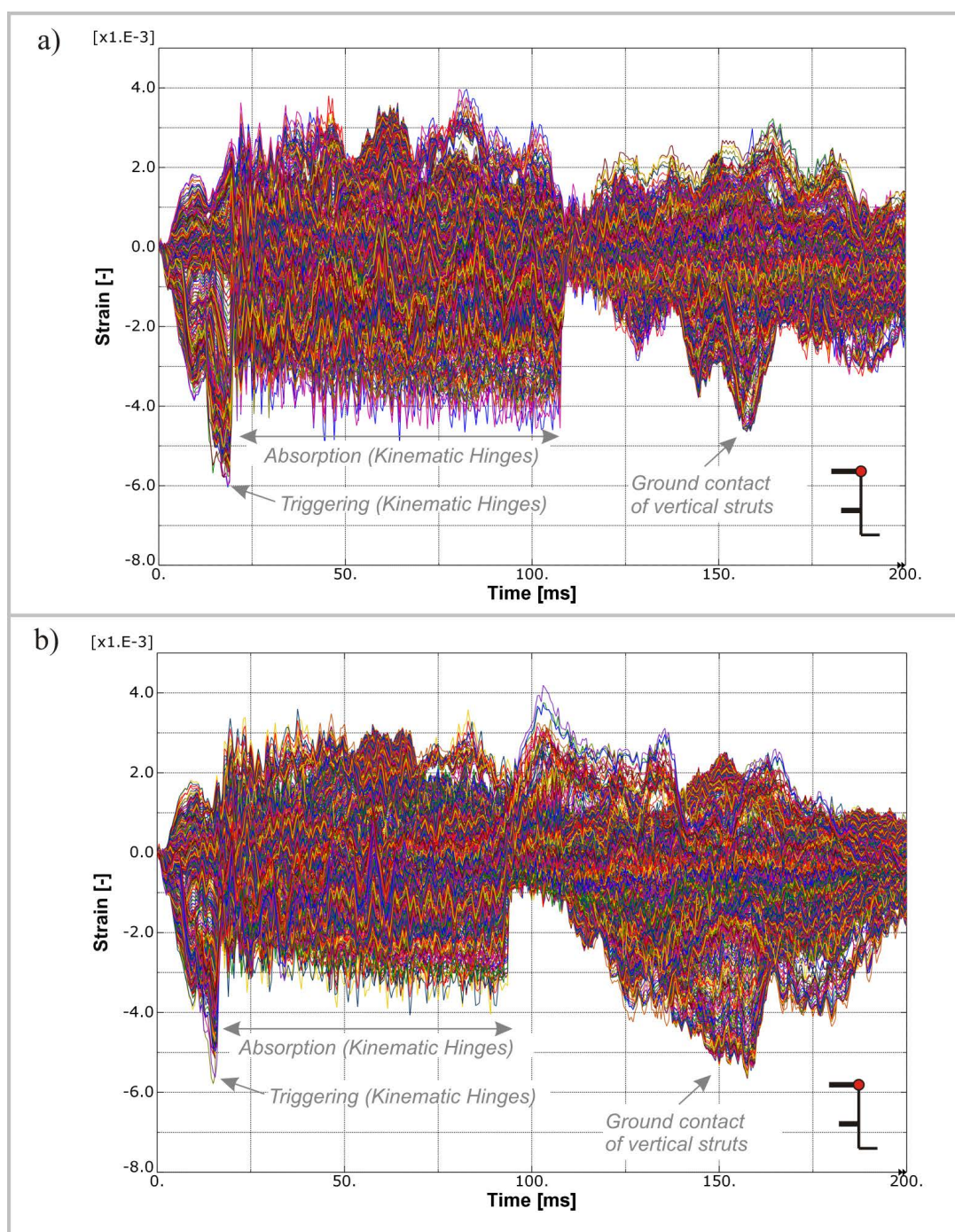


Figure 7-13: Frame inner flange strains of a): 75 % variant, and b): 60 % variant

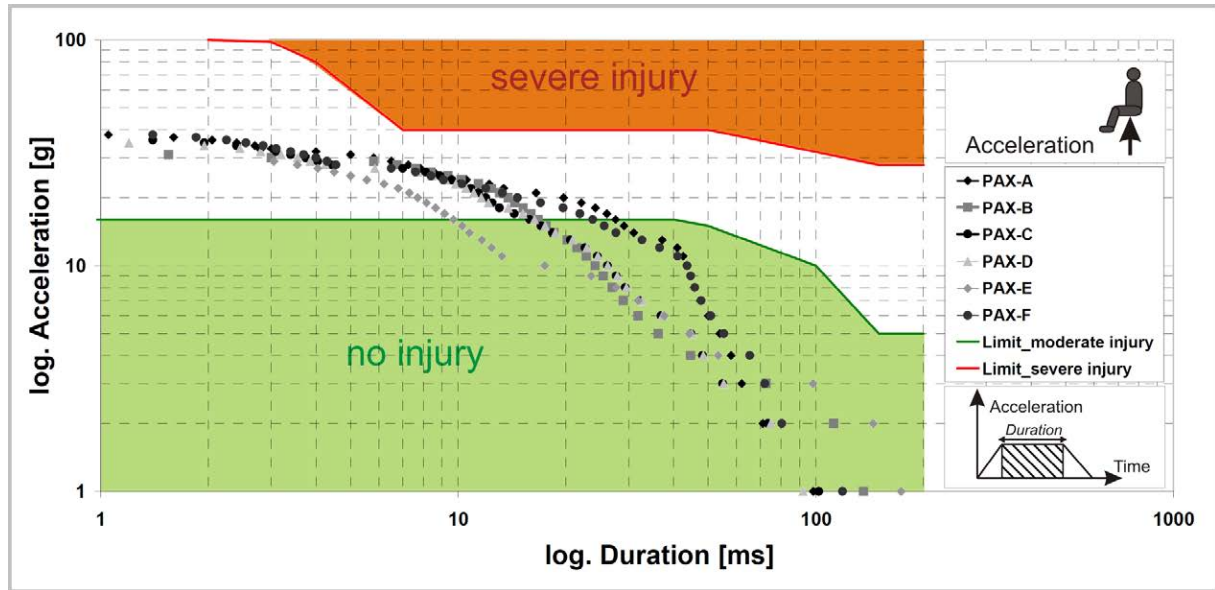


Figure 7-14: Passenger accelerations of the first seat row – ‘standard crash case’ with optimised crash kinematics

7.4.2. Structural adaptation

With the outcomes of the sub-cargo study as well as of the crash kinematics optimisation all macro element characteristics, except the vertical support strut macro characteristic, were defined and the crash kinematics was optimised with respect to the standard crash case. In this further step, the fuselage structure was adapted to the optimised crash loads. The most critical structural part with respect to typical crash loads is the frame structure, followed by the crossbeam structure. The fuselage skin as well as the stringers are less critical. The cargo-crossbeam structure was already defined in the sub-cargo study. The passenger crossbeam was not considered in this structural adaptation.

The adaptation of the frame structure is based on the most critical frame inner flange strains which were measured in the above discussed optimised crash kinematics, the ‘75 % variant’. Structural reserve factors were determined which compare these strain values with the structural allowabels according to the following formulation:

$$RF = \frac{\varepsilon_{FrameInnerFlange}}{\varepsilon_{Allowable}} \quad (7.3)$$

The reserve factors were determined for local frame regions. Figure 7-15 shows the results of the optimised crash kinematics with the maximum frame profile. The distribution of the reserve factors is as expected and shows the highest loaded frame region between cargo-floor and vertical support struts. The reserve factors increase in the upper fuselage region. One exception is the frame region below the overhead bins. Inertia effects of the loaded overhead bin mass

induce higher loads in that frame region. In addition, poor lateral frame support is existent here, due to a large distance between the kinematic hinges. This effect was discussed in paragraph 4.4.

With respect to the frame adaptation a desired reserve factor of $RF = 1.0$ is used instead of the typical factor of $RF = 1.5$. The standard crash load case considered here is not within the envelope of flight and ground loads which is the basis for static sizing. In addition, the mass penalty which is caused by a crashworthy frame design should be as low as possible. A reserve factor of $RF = 1.0$ leads to the full utilisation of the frame structure in the standard crash case and as a result leads to minimised mass penalty.

The distribution of reserve factors in Figure 7-15 shows a minimum value of $RF = 1.5$. Hence, the current frame design with maximum profile according to the frame profile catalogue can be reduced in all frame regions.

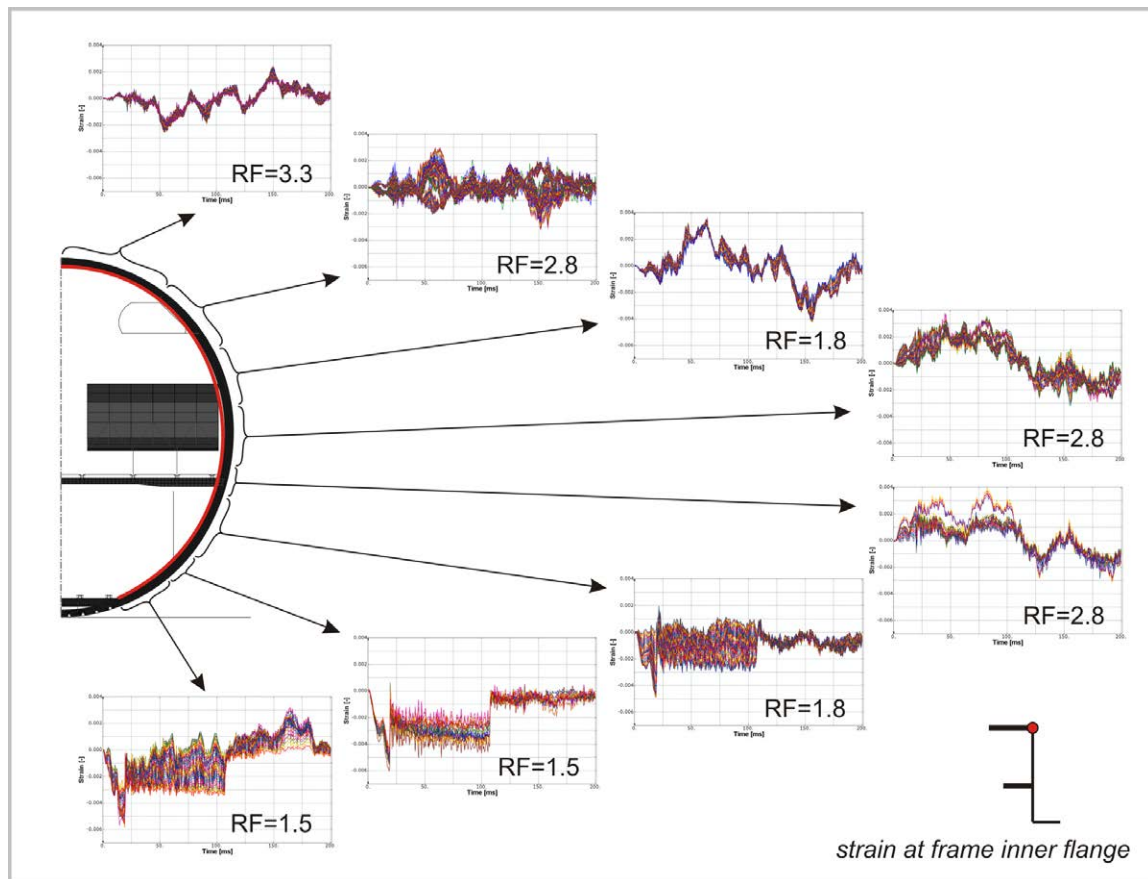


Figure 7-15: Structural reserve factors of the optimised crash kinematics with the maximum frame profile

The adaptation of the frame structure was conducted iteratively as the reduction of frame stiffness directly influences the overall crash behaviour. In addition, the adaptation of the frame design was conducted in sections. Inside these frame sections a constant frame design was specified. The sections were defined according to general local crash effects. The first section is between the cargo-floor and the vertical support struts (stringer #31-#26). The frames in this region experience high loads during the sub-cargo crushing phase. The second section is between

the vertical support struts and the passenger crossbeam connection and covers the Bermuda triangle (stringer #26-#20). A third section is defined above the passenger floor (stringer #20-#13) and finally the last section starts above the window area (stringer #13-#1).

In a first step, the most critical frame section between the cargo-floor and the vertical struts was adapted. In this step, the frame design of the upper sections was kept maximal. The results of this adaptation are given in Figure 7-16. The structural reserve factors in the considered frame section were reduced from $RF = 1.5$ to $RF = 1.2$ respectively $RF = 1.1$. In the following iteration the frame profile of the upper sections were adapted stepwise as illustrated in Figure 7-16.

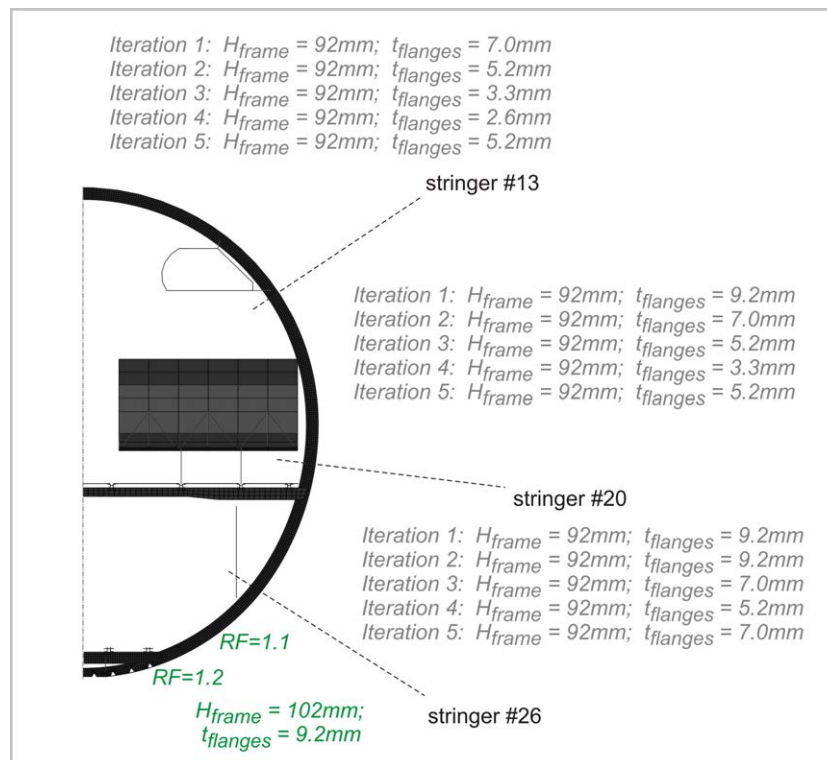


Figure 7-16: Adaptation of the frame design

The final frame distribution is given in Figure 7-17. Although the reserve factors could be reduced significantly compared to the maximum frame design, the final reserve factors show a wide range between $RF = 0.8$ and $RF = 1.8$. The lowest reserve factor of $RF = 0.8$ is located in the window area. Inertia loads of the overhead bins act in this frame region. The distance between the kinematic hinges is comparably high in that region. Hence, lateral support provided by the kinematic hinge macro architecture is marginal. This fact is important as lateral frame support by cleats is not modelled. In chapter 4.4 sufficient lateral frame support by the kinematic hinges was determined for typical distances between the hinge macros. In the upper fuselage area, this distance is significantly higher and the influence of less lateral support is obvious. A detailed view on the window region identified little frame buckling caused by the overhead bin

loads. Considering lateral frame support by cleats a reserve factor above $RF = 1.0$ is expected here.

The adaptation of the frame design was conducted exemplarily and on a rough basis as it is reasonable for a preliminary design. Further optimisation of the fuselage structure can be performed in a detailed design phase.

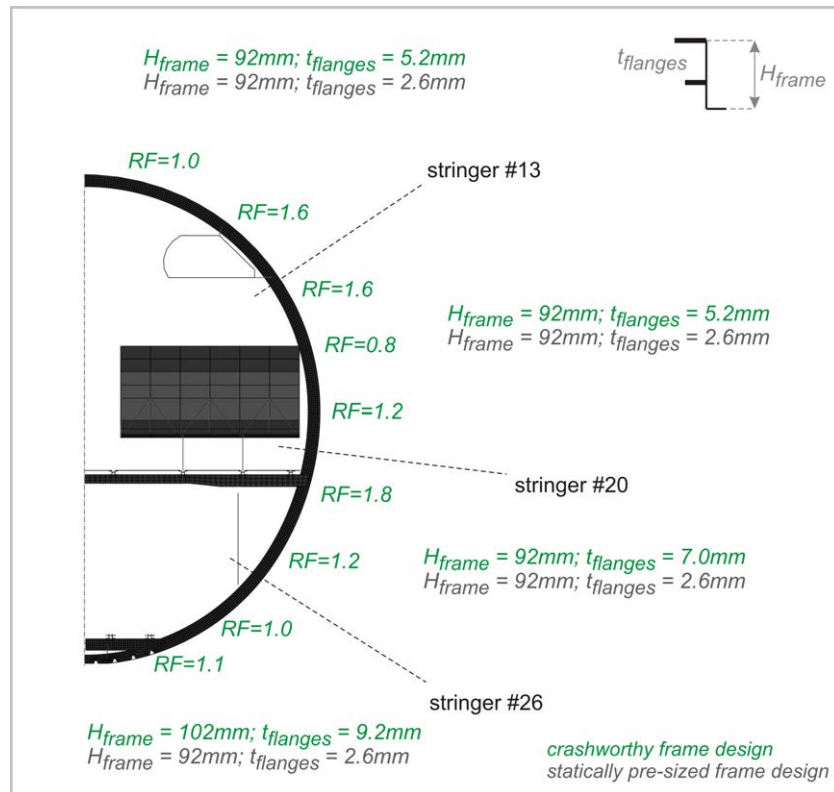


Figure 7-17: Final frame distribution of the structural adaptation (grey: static sizing)

In Figure 7-17 the frame distribution of the final crashworthy frame design is compared to the frame design of the static pre-sizing. Regarding the structural weight the increase of mass from static sizing to maximum frame design is about +257 % with respect to the frame mass. The structural adaptation leads to a mass reduction from maximum frame design to optimised frame design of about -140 %. Hence, compared to the statically sized frame structure, the crashworthy frame structure of this crash concept leads to a mass penalty of +117 %.

The energy plot in Figure 7-18 compares the optimised crash kinematics with maximum frame profile to the structurally optimised scenario. The macro input characteristics of both variants are identical. The variants distinguish only in the frame stiffness distribution. The total kinetic energy as well as the internal energy curves show the same overall behaviour. Nevertheless, a detailed view on the curves identifies differences in the time of the kinematic hinge triggering in the frames. The stiffer maximum frame profile leads to higher moments at a certain crash distance compared to the structurally optimised frame design. Hence, the trigger moment in the

kinematic hinges is reached at a bit later time with the stiffness reduced, structurally optimised frame profile distribution. Despite of the observed difference in the kinematic hinge trigger time, the differences of the crash kinematics optimisation is marginal in this structurally optimised variant.

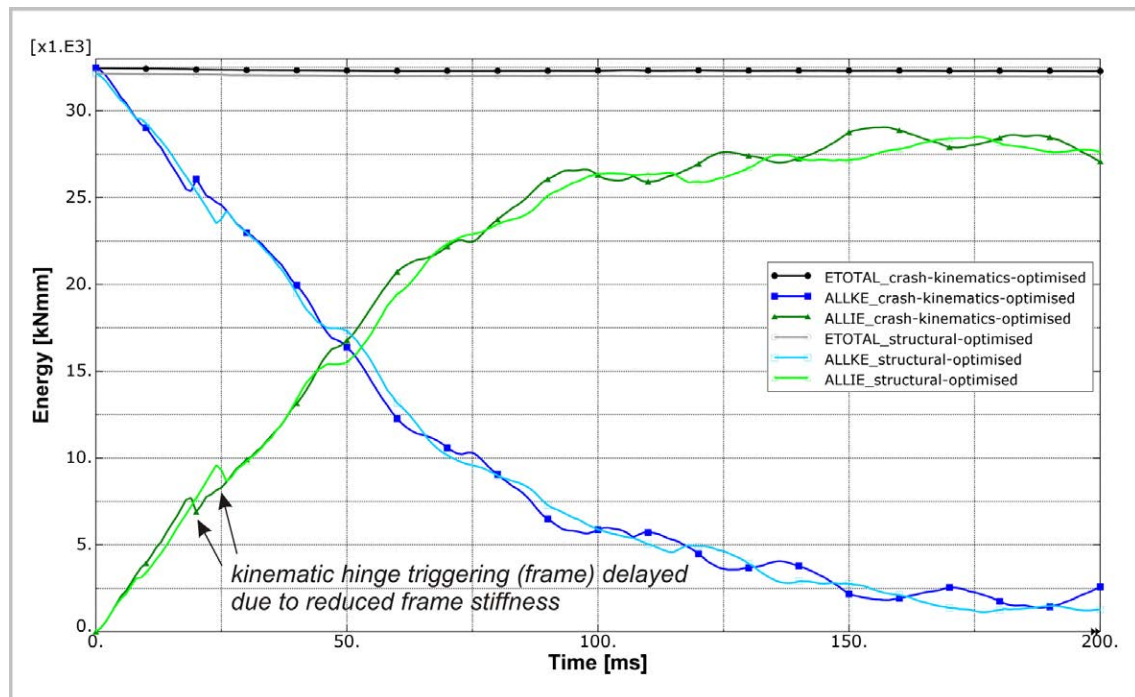


Figure 7-18: Comparison of 'crash kinematics optimised' and 'structurally optimised' scenario

7.4.3. Final crash scenario

The final crash scenario represents the outcomes of the sub-cargo study, the crash kinematics optimisation as well as the structural adaptation. Figure 7-19 illustrates the sequence of the 'standard crash case' with $v_i = 6.7$ m/s (22 ft/s). The energy plot in Figure 7-20 shows a smooth and steady increase of the internal energy (ALLIE) which indicates approximately constant energy absorption. Unsteadiness in the curve progression is caused by crossbeam and frame failure which leads to a partly release of elastically stored energy due to the differences between trigger and absorption moment level. This release of elastic energy is described by a spring back effect of the surrounding structure with further structural oscillations. Hence, the released elastic energy converts directly to kinetic energy which can be seen in the plot of total kinetic energy (ALLKE).

In Figure 7-20 the plot of external work (ALLWK) represents the effect of the gravity field. The loss of potential energy, caused by the vertical translation of the structural mass in the gravity field, leads to an additional amount of energy which has to be absorbed. In this scenario the amount of external work is approximately 20 % of the initial kinetic energy.

Besides the absorption of the kinetic energy by the fuselage structure, further energy is absorbed by frictional effects, mainly between fuselage skin and the ground. A friction coefficient of $\mu = 0.4$ was specified here. This value aligns to recent outcomes of research projects and is significantly higher compared to test results of previous research [127,128]. About 21 % of the initial kinetic energy could be absorbed by friction in this crash scenario (ALLFD).

Finally, the numerical energies show marginal values in Figure 7-20. The artificial strain energy (ALLAE), representing the energy to control hourglass effects, reaches approximately 2 % of the total energy (ETOTAL). This is a comparably small amount of energy which is clearly inside of common limits. Further numerical energies, applied by the solver to control contact (ALLPW) as well as constraint (ALLCW) penalties, are less than 1 % of the total energy. Hence, the small amount of numerical energies indicates a numerically acceptable modelling.

A detailed view on the energy absorption in the individual fuselage areas is given in Figure 7-21. The absorbed energy in the macro crash devices as well as the absorbed energy by material failure in the detailed modelled sub-cargo structure is illustrated in this diagram. With respect to the sub-cargo area the energy curves very clearly show the necessity of a detailed modelled sub-cargo structure including material failure formulation. The largest amount of energy, absorbed in the sub-cargo area, is attributed to material damage and failure described by detailed FEM, which is approximately 45 % of the sub-cargo energy dissipation. This high amount of energy absorption by the material is mainly founded in the bend-frame concept which specifies material crushing below the cargo-crossbeam. Other concepts without a bend-frame would lead to significantly less material failure in this lower fuselage area. Due to early failure of the cargo-crossbeam caused by interaction with the lower frame, the amount of energy absorbed by the macro crush absorbers is comparably small and reaches only 15 % of the sub-cargo energy dissipation. The remaining approximately 40 % of the sub-cargo energy dissipation are absorbed by cargo-crossbeam failure which is described with an absorbing kinematic hinge characteristics.

In total, 35 % of the total internal energy was absorbed in the sub-cargo area. In contrast to this, the kinematic hinges in the frames absorbed 52 % of the total internal energy. 13 % of the total internal energy is stored elastically in the fuselage structure. This value is comparably low, particularly with respect to a CFRP structure with its high potential to store elastic energy compared to a metallic structure. Hence, the comparably small amount of elastic energy indicates a correct modelling. The Kinematics Model approach with mainly linear-elastic material formulation did not lead to excessive strain energies in the structure.

Considering the discussion of the individual crash zones in paragraph 7.2, the crash height influenced by the frames is twice the crash height of the sub-cargo area. Hence, a constant level

of energy absorption during the crash sequence would require an appropriate ratio of absorbed energy in both crash zones. The results of the final crash scenario provide energy absorption in the sub-cargo area of 35 % of the total internal energy. Thus, 70 % of the total internal energy had to be theoretically absorbed in the second crash zone. Instead, the final crash scenario provides only 52 % energy absorption in the frames. A detailed view on the cargo-crossbeam failure clarifies this discrepancy from the desired ratio of energy absorption. The absorbing rotation of the cargo-crossbeam kinematic hinge is part of both, crash zone 1 and 2. The crossbeam fails as discussed before the complete crushing of the sub-cargo area. This absorbing rotation continues in the crash phase of zone 2. Hence, the phases of zone 1 and zone 2 overlap in this case, and therefore the ratio of absorbed energy in the individual crash zones can hardly be determined. In Figure 7-21, the absorbing rotation of the cargo-crossbeam was assigned to the sub-cargo energy absorption. Despite of this circumstance, the smooth and steady increase of the total internal energy indicates an approximately constant energy absorption which concludes to the desired ratio of absorbed energies in the individual crash zones.

Further results of the final crash scenario are presented in Appendix A5.2.

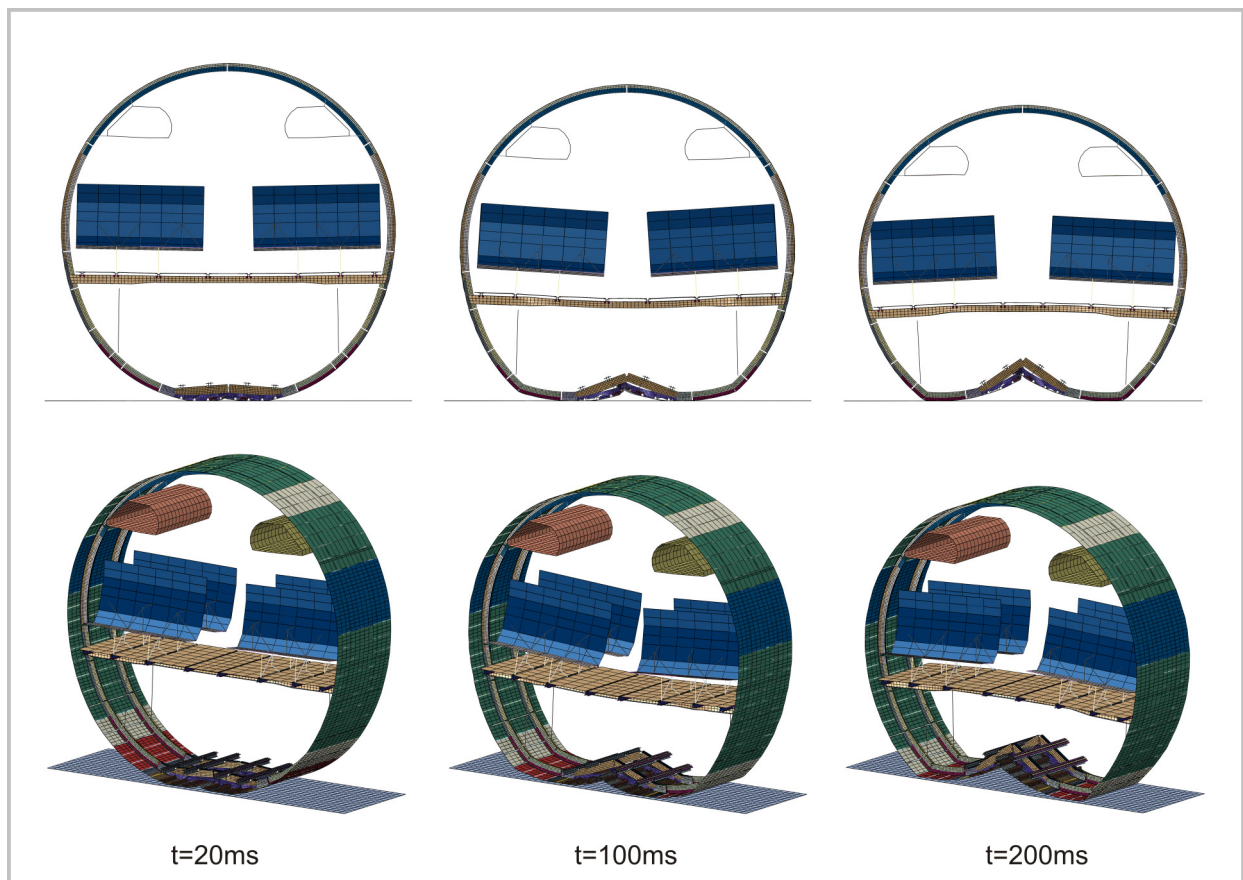


Figure 7-19: Crash sequence of the final crash scenario

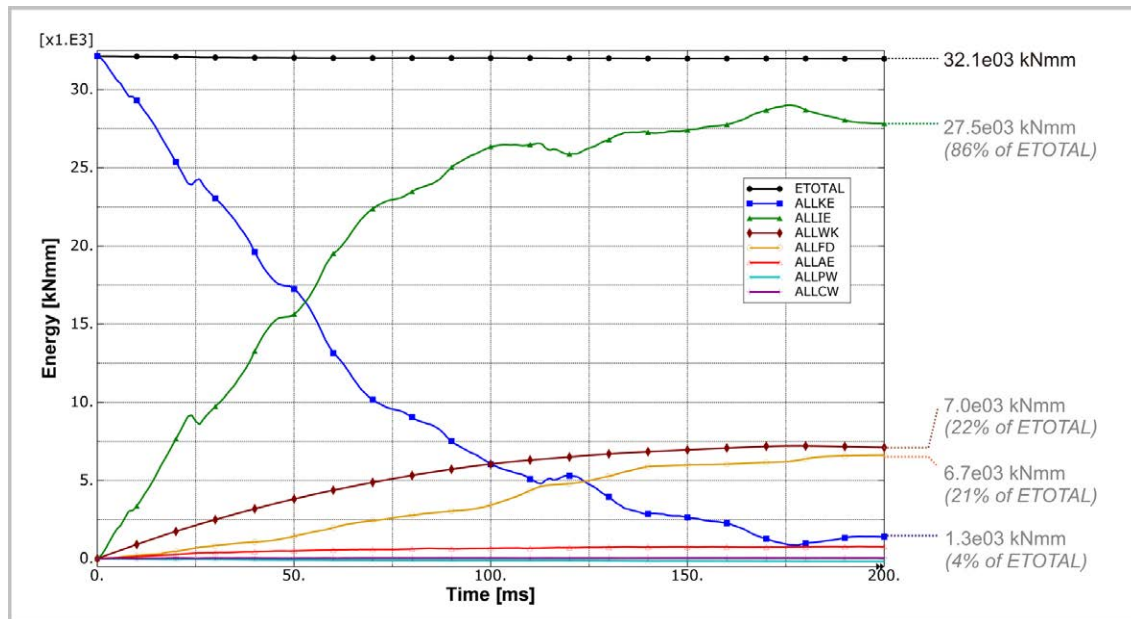


Figure 7-20: Energy plot of the final crash scenario

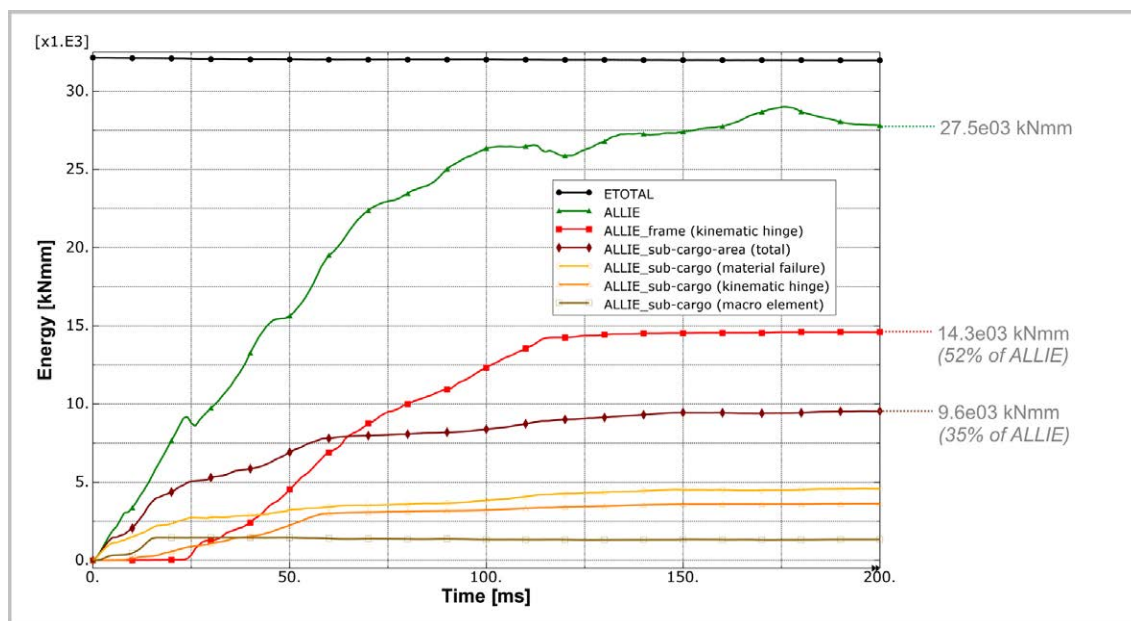


Figure 7-21: Energy absorption in the final crash scenario

7.5. Modification of the final crash scenario – the ovalisation effect

After the discussion of the final crash scenario an additional option for the final crash scenario is discussed in this paragraph and shall demonstrate the capability of the Kinematics Model.

In this investigation, an additional local crash device is installed in the connection of the passenger crossbeam to the frame structure. During the first crash phases up to the frame failure, the frame structure is elastically loaded with an oval deformation. A full development of this ovalisation is hindered by the passenger crossbeam which is tensile loaded during this crash phase. The definition of an appropriate flexibility in the connection between the passenger

crossbeam and the frame structure would assist this ovalisation effect and would lead to a certain displacement in this connection. Such a displacement could be used for further energy absorption. The advantage of this mechanism is its tensile loading direction. In general, energy absorbing concepts in tensile direction are less complex compared to compressive concepts as no risk of instability effects exists. The crossbeam connection could be equipped with a comparably simple bearing absorber which provides an ideal characteristic with an absorbing level of almost 100 % of the trigger load level.

Hence, the advantage of such an additional crash concept is obvious for what reason the option of energy absorption by an ovalisation effect was analysed in the Kinematics Model. Based on the final crash scenario, an additional macro architecture was implemented in the passenger crossbeam connection, according to paragraph 3.2.5. In this macro architecture the passenger crossbeam is linked to the frame structure with a connector element. Both structural parts are reinforced with rigid bodies for the load introduction of the connector element. The lateral displacement as well as the rotational displacement around the fuselage longitudinal axis was defined as independent degree of freedom which had to be investigated to achieve an improved crash performance. The input characteristic was defined linear-elastically for the rotational stiffness. The lateral displacement was defined with a constant force plateau after triggering which is 100 % of the trigger load.

In a first step, the tensile loads in the passenger crossbeam of the final crash scenario were analysed to determine the load progression over the crash duration and to define a potential trigger time and trigger load level. As expected, the natural crash behaviour of the fuselage section provides high tensile forces in the crossbeam after the sub-cargo crushing and before frame failure. Figure 7-22 illustrates the longitudinal loads in the passenger crossbeam of the final crash scenario.

Based on these crossbeam loads potential trigger loads could be defined for the ovalisation device. The influence of these trigger loads as well as different rotational stiffness were analysed in a parameter study. Three different trigger loads were defined as illustrated in Figure 7-22. In addition, three different rotational stiffness values were defined in this parameter study. The stiffness values of the rotational degree of freedom were defined artificially. In total, nine different variants were simulated in this study.

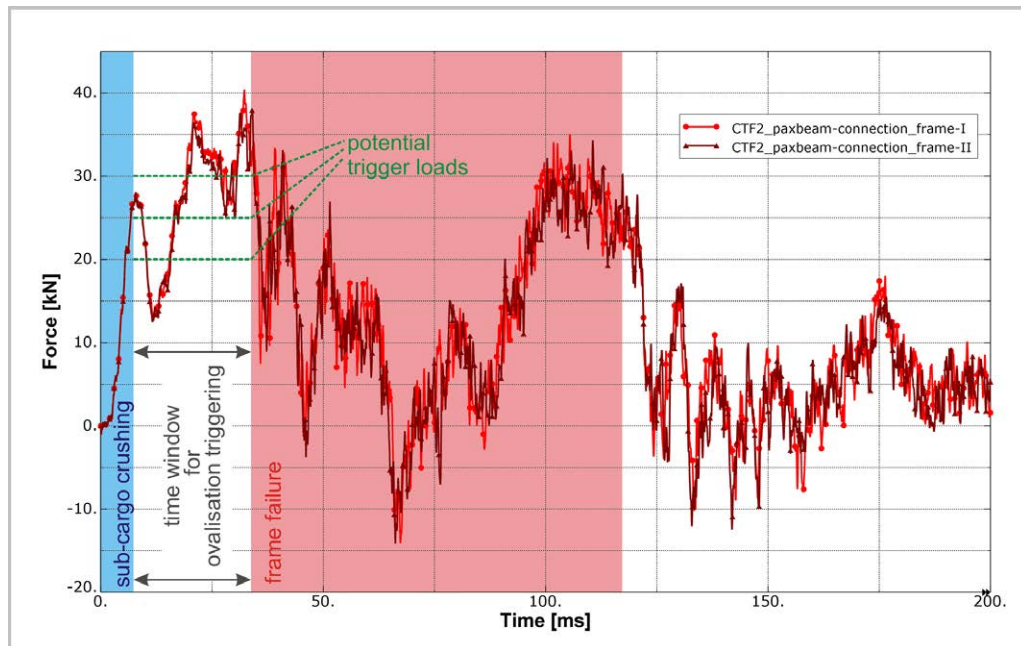


Figure 7-22: Longitudinal loads in the passenger crossbeam of the final crash scenario

A first outcome of this limited parameter study was that none of the variants led to a change in the overall crash kinematics. For all variants a crash kinematics according to scenario A could be identified. The additional ovalisation phase occurred as desired after the sub-cargo crushing and before the frame failure. Figure 7-23 illustrates macro element output data of a variant with a trigger load of $F = 20$ kN. The elongation of the macro elements is given in this diagram over the crash duration. In a first crash phase the modified cascading scenario shows the crushing of the sub-cargo area. After complete crushing, the ovalisation devices experience lateral displacement up to the triggering of the frame kinematic hinges with the following frame bending phase.

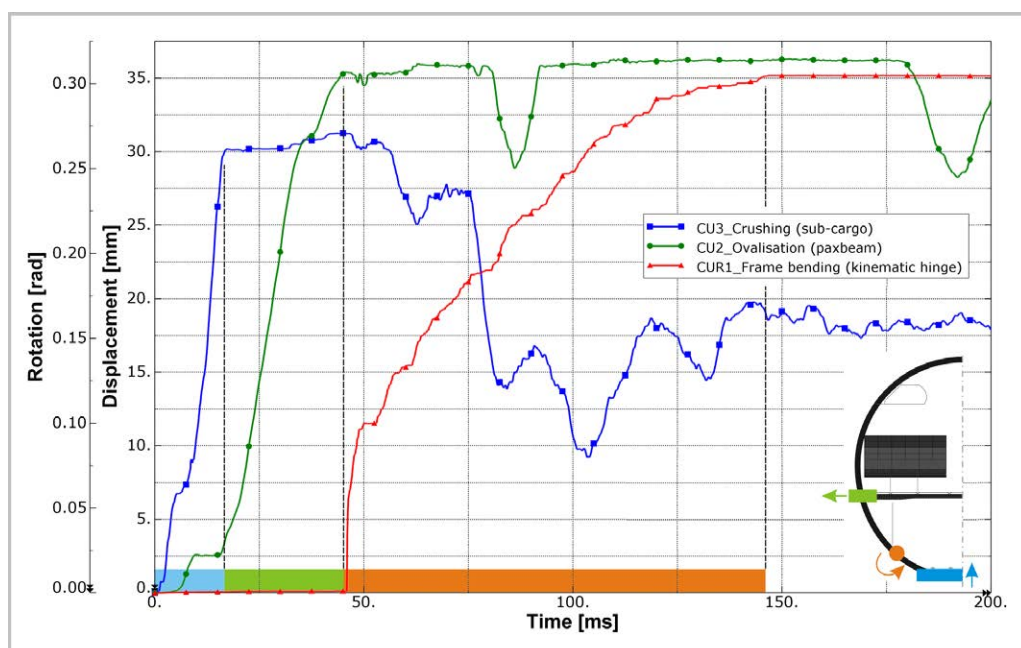


Figure 7-23: Modified cascading scenario with ovalisation ($F = 20$ kN)

The influence of the rotational stiffness was determined to be less important compared to the influence of the lateral trigger force. Figure 7-24 gives an overview on the results of this parameter study. The lateral displacement of the ovalisation device is displayed over the crash duration. The highest energy absorption in the ovalisation device is provided at a force level of $F = 20$ kN.

Regarding a force level of $F = 20$ kN approximately 9 % of the initial kinetic energy could be absorbed by the tensile mechanism in the ovalisation device. In the further crash sequence this amount of energy absorption leads to a reduced utilisation of the energy absorbing capacity of the frames. Figure 7-25 illustrates the frame kinematic hinge rotation and shows a reduction of the frame rotation of approximately $\Delta\phi = 12^\circ$. With respect to the energy absorbing capacity, defined for the frame kinematic hinges, the ovalisation device led to a rotational reduction of $\Delta\phi = 5^\circ$ due to the end of the absorption plateau in the frame hinges.

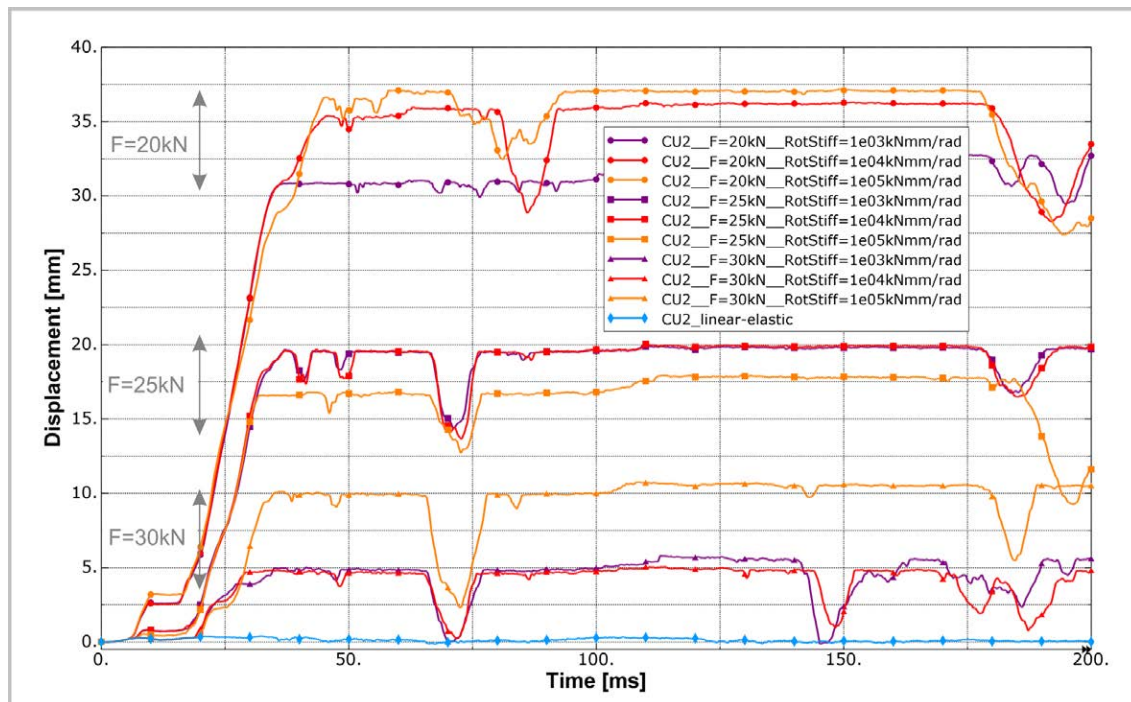


Figure 7-24: Lateral displacements of the ovalisation device

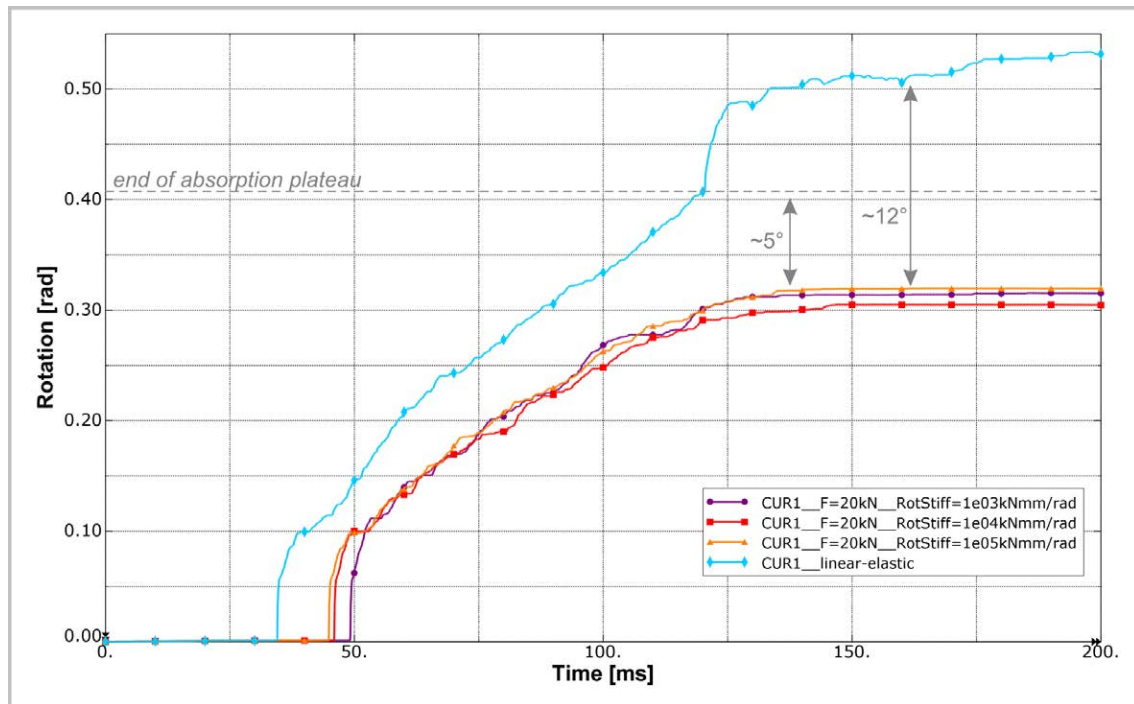


Figure 7-25: Frame kinematic hinge rotations

Using the identical macro input characteristics of the final crash scenario, the implementation of an ovalisation device with a trigger load of $F = 20$ kN led to a reduced crash distance of $\Delta z = 150$ mm. Figure 7-26 compares the final crash scenario with the option of an additional ovalisation device and illustrates the reduction of the crash distance.

The trigger load of $F = 20$ kN is an outcome of an investigation which considered exclusively crash aspects. The feasibility of such an ovalisation concept has to be checked against the static sizing. The static analysis by the project partner Airbus identified maximum static tensile loads in the passenger crossbeam connection of $F = 21$ kN with respect to all flight and ground load cases. For that reason, the final trigger load of the ovalisation device has to be increased at least to $F = 22$ kN to fulfil the static requirements. Despite of this marginal adaptation of the trigger load, the general feasibility of such a concept could be proved.

Further results on the investigation of the ovalisation effect are given in Appendix A5.3.

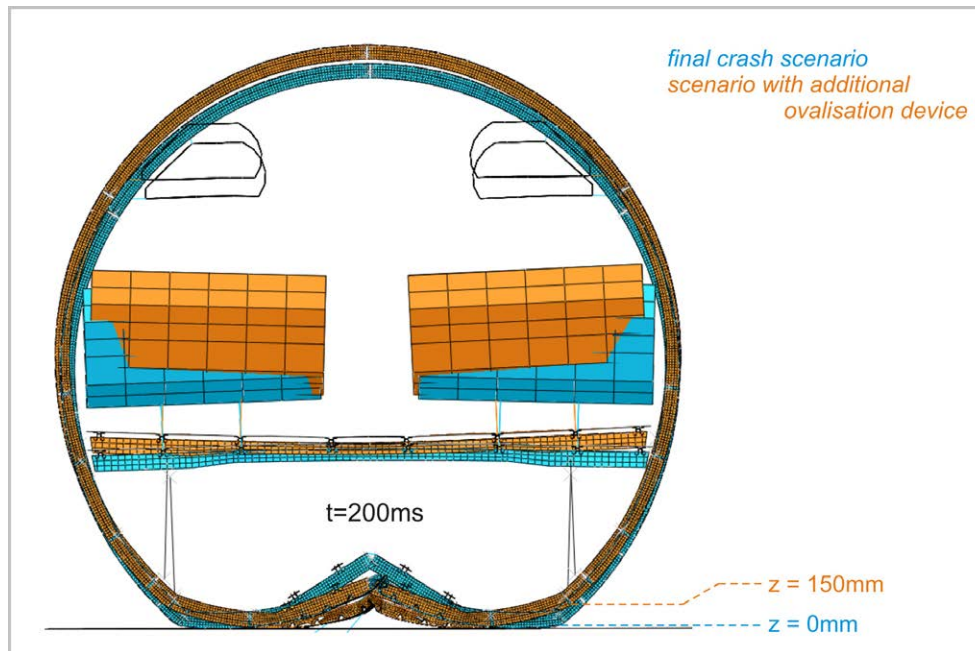


Figure 7-26: Final crash scenario vs. additional ovalisation device

7.6. Summary - definition of the final macro input characteristics

On the basis of the selected natural crash kinematics, scenario A, the development of a crash scenario was discussed in this chapter. A procedure was defined to conclude to an optimised crash kinematics as well as to an optimised fuselage structure. The development process was conducted exemplarily on the basis of a statically sized CFRP fuselage structure with a cargo-crossbeam according to the bend-frame concept. The developed final crash scenario provides valuable information about the expected crash loads, the requirements for crash devices as well as the potential structural mass penalty of the considered crash concept. In addition, the effect of frame ovalisation, using an additional crash device at the passenger crossbeam connection, could be analysed efficiently with the Kinematics Model.

The final macro input characteristics of this exemplary scenario development are given in Figure 7-27.

The sub-cargo crushing absorbers trigger at a load level of $F = 15 \text{ kN}$. With two absorbers defined per frame, the static loads in the sub-cargo framework have to be less than $F = 30 \text{ kN}$. This small load value is challenging, but regarding a bend-frame concept this requirement is expected to be feasible.

The cargo-crossbeam triggers at a moment of $M = 8000 \text{ kNmm}$. The selected τ -profile of highest stiffness according to the profile catalogue is fully utilised at this load level.

The frame structure directly below the vertical support strut connection triggers at a moment of $M = 19,000 \text{ kNmm}$. A large amount of energy has to be absorbed by this crash device in the frame. An estimation of the feasibility of such a requirement was conducted by detailed analyses of a generic frame structure. The frame region at the vertical strut connection was modelled in detail and analysed with full FEM. A metallic frame structure was defined in that detailed model with a similar frame profile compared to the final crash scenario. The moment-rotation curve of this numerical analysis, on basis of a metallic frame structure, is presented in Figure 7-28a) and is compared to the kinematic hinge output of the final crash scenario. This comparison shows almost similar behaviour of the metallic frame and the requirements of the kinematic hinge, with respect to the trigger load as well as the energy absorption capacity. Comparing both curves it is obvious that the kinematic hinge behaviour is more of generic character whereas the metallic frame provides a typical, more realistic post-failure curve. However, with respect to the required trigger load and energy absorption the outputs of the frame kinematic hinge of the final crash scenario can be used as a feasible requirement. Figure 7-28b) shows the considered kinematic hinge in the Kinematics Model whereas Figure 7-28c) displays the detailed metallic frame model. Further details on this frame model are provided in Appendix A5.4.

With respect to the vertical support struts, potential crushing could be provided in case of some robustness crash cases. Important is a smooth transition from the frame bending phase to the vertical support strut crushing phase. Appendix A5.5 discusses the axial forces in the vertical struts during the final crash scenario. According to the identified loads a trigger force of $F = 35 \text{ kN}$ is recommended for potential energy absorption in the vertical support struts.

Finally, with a modified final crash scenario using the ovalisation effect an optimised trigger force of $F = 22 \text{ kN}$ was identified for the ovalisation device which is positioned in the passenger crossbeam connection. This trigger value already considers static requirements and guarantees the feasibility of the ovalisation concept.

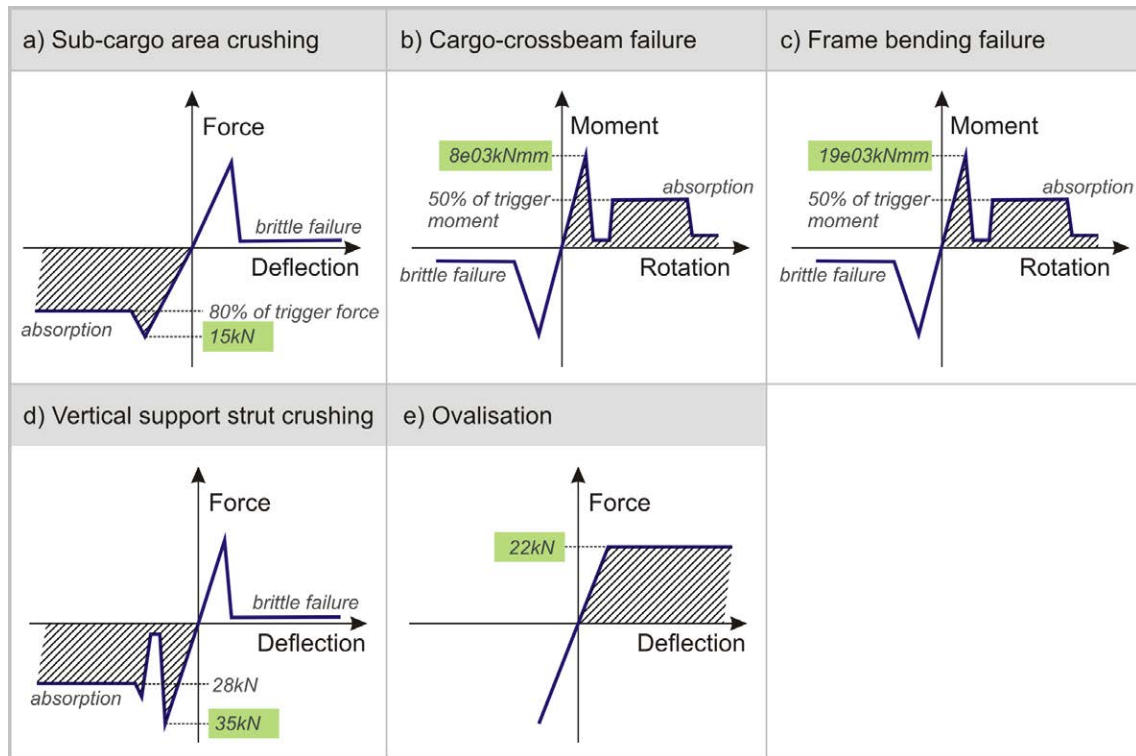


Figure 7-27: Final macro input characteristics

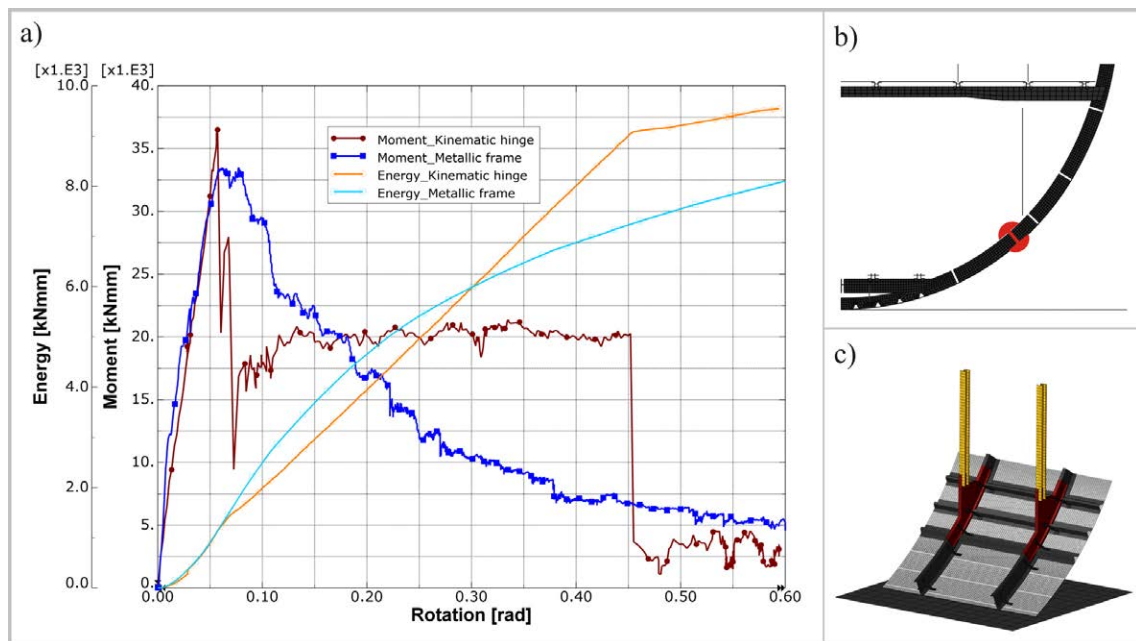


Figure 7-28: Frame bending of the kinematic hinge output and the metallic frame

8. Development of a crashworthy composite fuselage design

– experimental investigation on the design of crash devices

The crash scenario development in chapter 7 identified crash device characteristics which are required to achieve an optimised crash kinematics according to scenario A. Based on these identified requirements, general concepts of local crash devices can be developed. Figure 8-1 again illustrates the scope of the development of a crashworthy composite fuselage design and highlights this final step of investigations on the design of local crash devices.

In the scope of this thesis, the focus is on the development of the experimental methods for the investigation on potential crash devices. Appropriate test setups were developed to test local crash device concepts under reasonable conditions that consider structural loads, constraints or other effects which influence the crash device in a fuselage structure and thus have to be represented by appropriate boundary conditions in the test.

Two general kinds of experimental investigation were considered. The first one is focused on a precise representation of structural boundary conditions and aims to investigate the detailed crash device behaviour taking into account the interaction with the structural environment of the aircraft fuselage. The second one is focused on fundamental experiments that concentrate on general characteristics, such as the energy absorbing capacity of a crash device concept. In the second kind of investigations, a detailed representation of boundary conditions is secondary and a simplified, and accordingly a more efficient, test setup can be used. Both kinds of experimental investigations are discussed in this chapter.

First kind of experimental investigations are discussed in paragraph 8.1. Experiments are presented which consider the crushable absorber structure in the sub-cargo area. A detailed test setup was developed which represents important boundary effects in the sub-cargo structure on the crush absorber. With this specific test setup a wide range of absorber design variants was tested with a total number of 72 specimens [147]. However, the discussion in this paragraph concentrates on the development of the test setup to exemplarily show how experimental tests can be used to develop local crash devices, or vice versa to generate macro input data for the Kinematics Model.

Second kind of experimental investigations are dealt in paragraph 8.2. Experiments are discussed which investigate energy absorbing concepts for the frame structure. In contrast to the specific

test setup of the crush absorber test programme here a basic test setup was developed. The experiments on the frame structure concentrate on the general feasibility of energy absorption concepts in a bending failure mechanism. The test setup was defined as simple as possible to enable an efficient investigation of different bending absorption concepts.

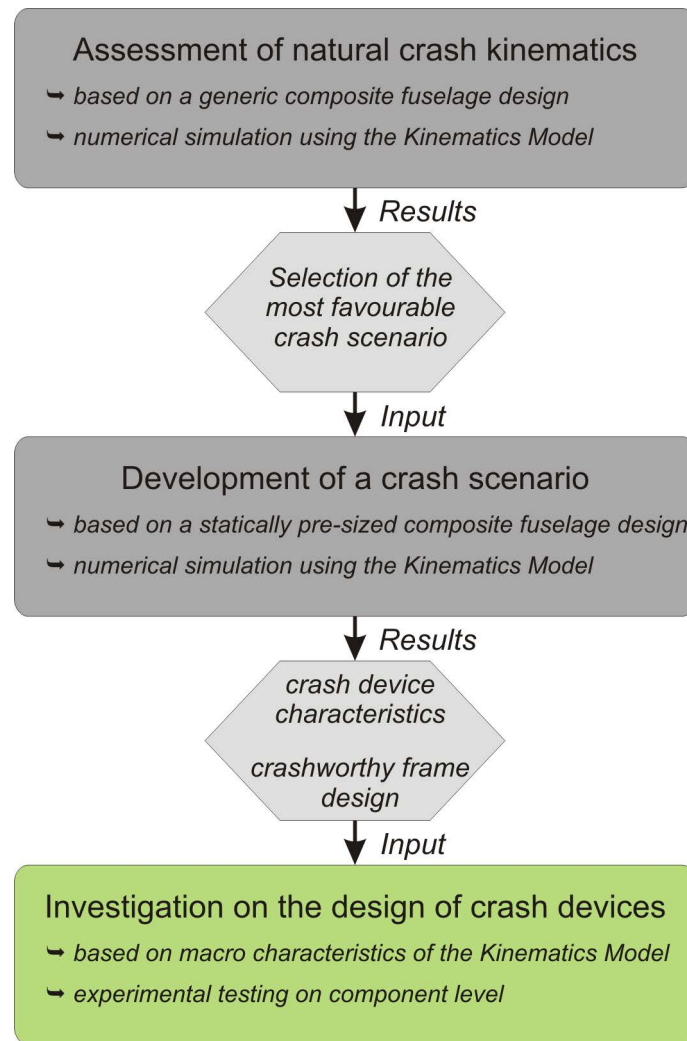


Figure 8-1 : Approach for the development of a crashworthy composite fuselage design

8.1. Axial crushing tests

The exemplary development of a crashworthy composite fuselage design in this thesis considers a so-called bend-frame concept. A stiff cargo-crossbeam provides sufficient stiffness to enable crushing of the sub-cargo structure in a first crash phase. In Figure 8-2a) such a sub-cargo structure is depicted, which is in this case a highly integrally manufactured CFRP part [120]. Similar to the sub-cargo design defined in chapter 6 and 7, two crush absorbers are installed at the centre struts of the sub-cargo structure. The conceptual idea is to mount the crush absorbers on the statically sized structure with a riveted connection. The general crush absorber design is a

CFRP structure of half-tube geometry with additional flanges for the riveting connection. Such CFRP half-tube crush absorbers are well investigated and identified an excellent crush performance respectively a high mass-specific energy absorption [41,45]. Figure 8-2b) illustrates the general design of the considered half-tube absorber mounted to the strut of the sub-cargo structure.

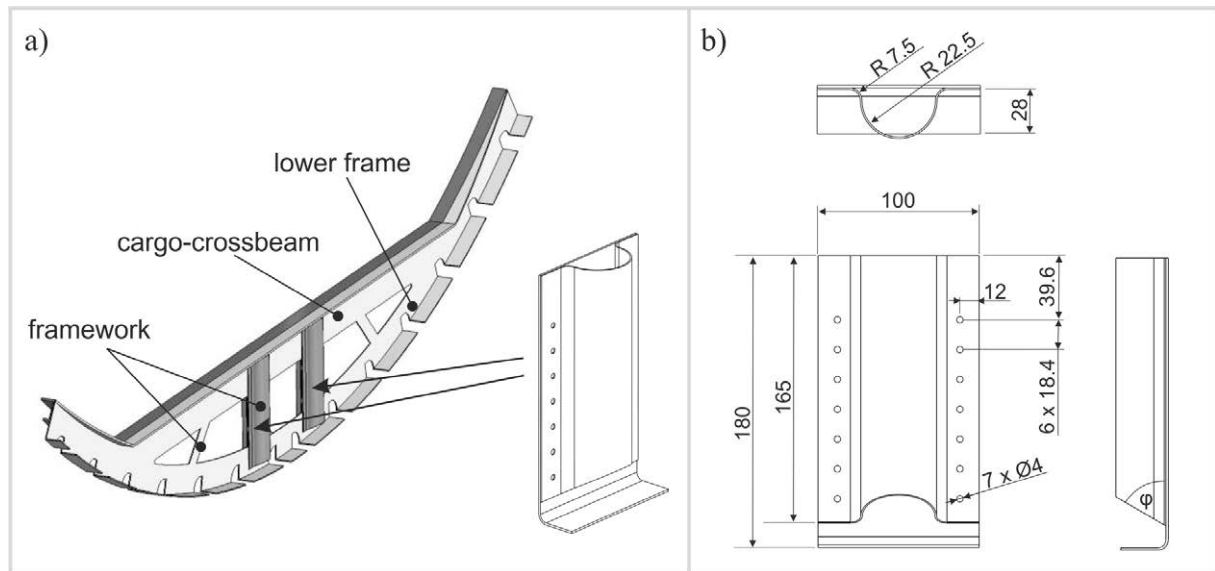


Figure 8-2: Crush absorber of a bend-frame concept in the sub-cargo structure [120]

The focus in the development of an appropriate test setup is a detailed representation of boundary conditions which may influence the crush absorber in this sub-cargo structure. The crushing behaviour of half-tube absorbers is well investigated and documented in the literature. But most of these investigations concentrate on the half-tube absorber itself as well as its material failure behaviour and neglect the influence of the adjacent structure. Regarding a crashworthy composite fuselage design, these effects cannot be neglected. Hence, the required test setup has to consider all influence of potential interaction with the fuselage structure.

To identify potential factors which influence the failure behaviour of the crush absorber, detailed finite element analyses as well as static and dynamic pre-tests were performed. A short documentation of the FE model as well as the pre-test setups is given in Appendix A6.1.

One identified factor is the influence of the strut to that the half-tube absorber is riveted. The sub-cargo design according to Figure 8-2a) specifies a flat CFRP strut. Whereas the half-tube absorber provides sufficient buckling strength to achieve stable crushing, this flat strut tends to buckling failure. Dependent on the structural stiffness of both parts, potential failure without progressive crushing is expected for the riveted combination of strut and half-tube absorber. Thus, to analyse this effect the test specimen was defined as riveted assembly of a flat strut and a half-tube absorber, as illustrated in Figure 8-2b).

A further parameter that may have an influence on the absorber crushing behaviour is the upper connection of the half-tube absorber to the cargo-crossbeam. In the specified design according to Figure 8-2a) the absorber structure is riveted also to the web of the crossbeam to provide sufficient backing strength for progressive crushing. Hence, this part of the absorber which is in the region of the crossbeam will not be crushed, but will support the crushing of the lower part of the half-tube absorber. The representation of this upper connection would lead to a complex test setup which includes a riveted connection to the test fixture or alternatively the integration of the crossbeam structure. To reduce the complexity of the test setup, the upper absorber connection was neglected. Instead, the representation of the absorber structure concentrates on the crushable region below the crossbeam. The upper end of the test specimen was embedded in a fixture that was defined in a way that clear boundary conditions for the tests are provided and potential failure in the fixture is prohibited. Therefore, the specimen was bonded into the fixture. In addition, the fixture was designed with a bleeding system to avoid an artificial increase of the crushing force by the compression of the air in this closed cross-section of the specimen. In the real structure, the upper absorber part in the region of the crossbeam provides sufficient volume to avoid any compressible effects. Figure 8-3a) compares the structural environment in the fuselage and the derived test setup. The upper fixture is pictured and illustrates the notches for a bonded fixation of the specimen as well as the central whole of the bleeding system.

Regarding the boundary condition at the lower end of the specimen the connection of the flat strut to the fuselage skin was identified as a further parameter which can influence the crushing performance of the absorber structure. According to the highly integral design pictured in Figure 8-2a), the flat strut merges with the lower frame in this lower region. The flange of the lower frame is riveted to the fuselage skin. In case of a crash, first failure is expected in the radius between the lower frame web and the flange. Hence, progressive crushing is triggered by this radius design. In the test setup, the connection of the lower frame flange to the fuselage skin cannot be neglected. Otherwise the flange would be enabled to roll up and following to fail in a different mode respectively at a different failure load. This effect could be demonstrated numerically in the FE analyses as well as experimentally in the pre-test investigations, as documented in Appendix A6.1. To consider the influence of the fuselage skin, a metallic plate was bolted to the flange. During the impact of the specimen, this plate avoids an unrolling of the flange and affects the failure initiation similarly to the influence of the fuselage skin. In combination with this metal plate, another effect was identified which showed a lateral displacement of the frame flange caused by the constraint unrolling. In a real fuselage environment the fuselage skin constraints this lateral displacement. Accordingly, a guidance system was developed that constraints the metal plate against lateral displacement. With the final

setup of this guided plate, the failure representation of the frame radius is similar to that expected in the real fuselage structure. In Figure 8-3a) the bolted connection of the flange to the metal plate is depicted. Furthermore, a circular notch in the metal plate is visible which is used for the guidance system.

The finally planned test setup is shown in Figure 8-3b). An upside-down configuration was defined due to the installation of the dynamic test machine. The guidance system was coupled with the load cell to enable the measurement of potential friction effects between metal plate and guidance.

Appendix A6.1 documents the verification of this finally planned test setup by static and dynamic pre-tests.

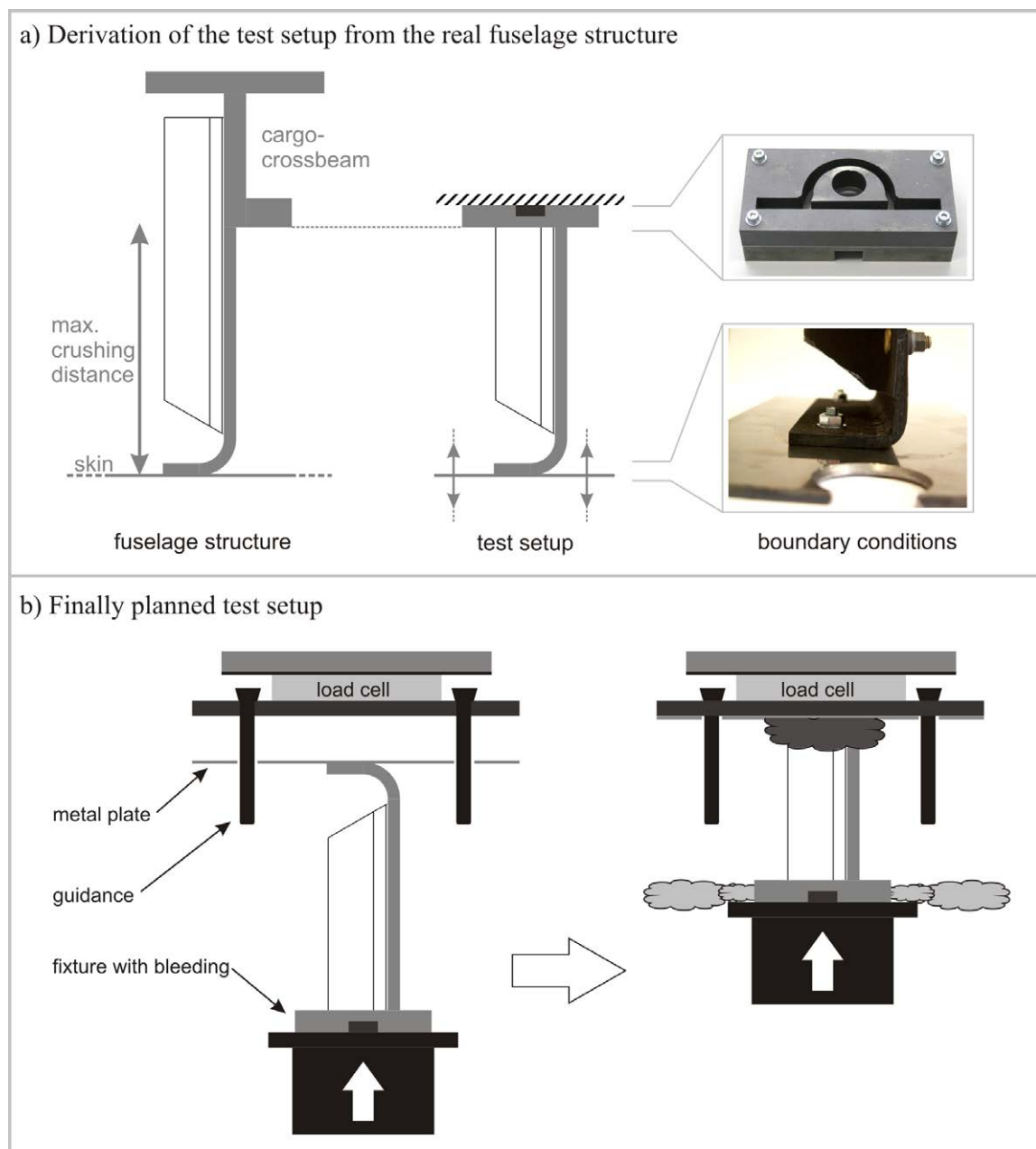


Figure 8-3: Test setup configuration

The final test setup was developed for the dynamic test machine Instron VHS (type: PLS100/20M) that is shown in Figure 8-4a) together with the data acquisition systems. In addition, the high-speed camera (FASTCAM-APX RS250K) as well as the lighting is depicted which was used for the recording of high-speed videos.

The detailed setup in the test machine is given in Figure 8-4b) and mainly corresponds to the schematic setup of Figure 8-3b). An additional wooden plate ($t = 3 \text{ mm}$) was installed on the impact plate to damp the impact of the metallic plate which is bolted to the strut flange. In addition to the path measuring by the cylinder signal, a laser system was installed which measured simultaneously the path over a distance of $L = 100 \text{ mm}$. As one of the main objectives of this test campaign is the investigation of the interaction of the flat strut and the half-tube absorber, a mirror was installed to record the front and the rear side of the specimen with the high-speed camera. Using this mirror, potential buckling failure of the flat strut at the rear side of the specimen could be identified. In general, the visualisation of CFRP specimens with video or photo systems is difficult due to the limited contrast of the black specimen. Therefore, the specimens were painted in white colour with additional black points to improve the contrast in the high-speed video records.

Finally, a modified configuration of the final test setup is given in Figure 8-4c). An oblique device was mounted between load cell and impact plate to investigate the crushing performance under an off-axis angle of $\beta = 10^\circ$. The aim of this test setup is to identify the robustness of the absorber crushing performance, similar to robustness analyses of the Kinematics Model. The off-axis crushing configuration is one of several parameters which are specified in the following.

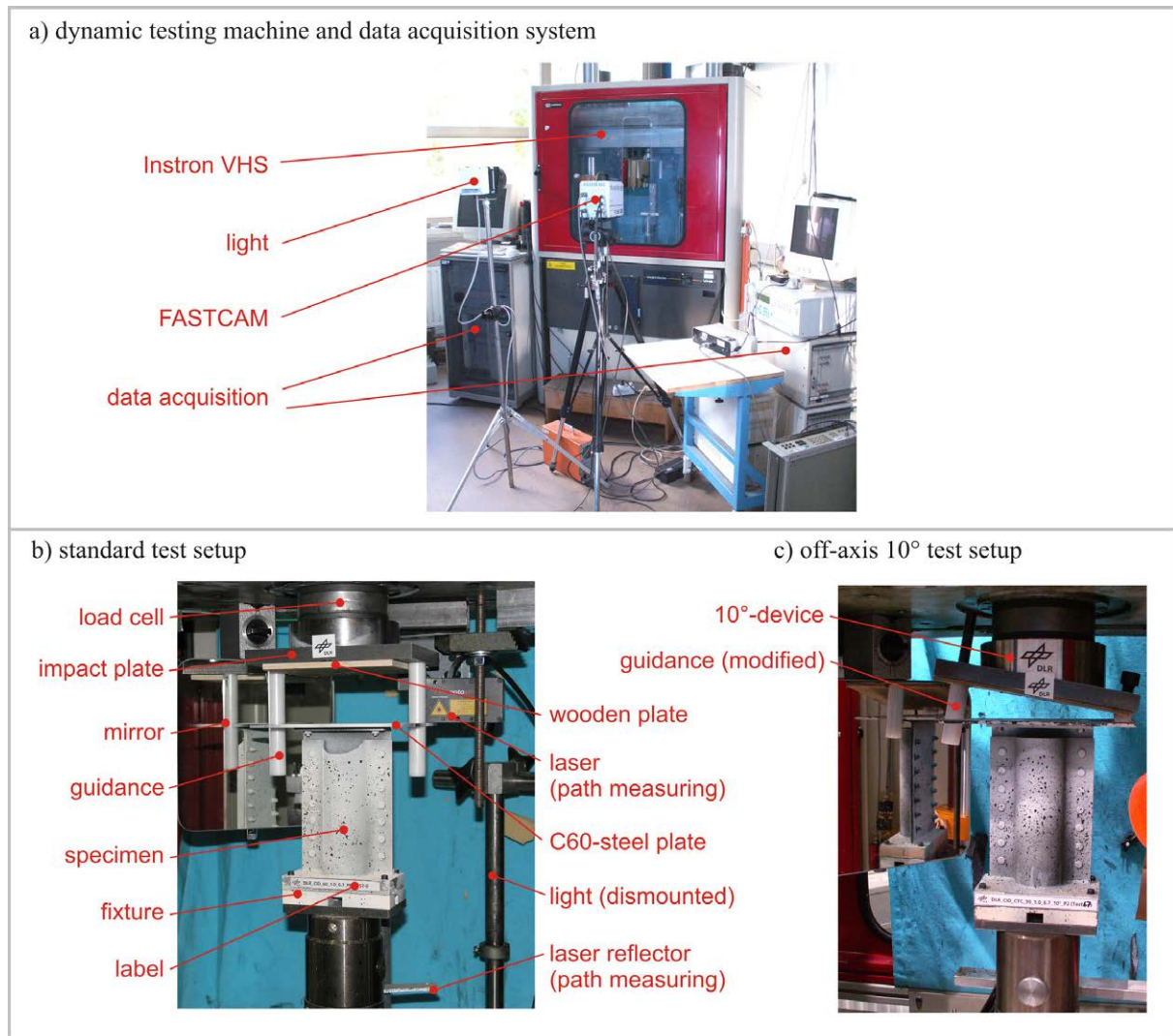


Figure 8-4: Final test setup in the dynamic test machine

A total number of 72 specimens were tested with the test setup described above. Different parameters of the crush absorber design or its loading condition were analysed in 36 test variants, each with two individual tests. The analysed parameters were:

- Different designs of the flat CFRP strut (complex layup, simplified layup)
- Different angles of the geometrical trigger of the half-tube absorber ($\alpha = 60^\circ, 75^\circ$)
- Different layup thickness of the half-tube absorber ($t = 1.0 \text{ mm}, 2.0 \text{ mm}$)
- Different laminate types of the half-tube absorber (woven fabric, biaxial-, triaxial braided laminates)
- Variants with paste bonding additionally to the riveting of the strut and the half-tube absorber
- Variants with off-axis loading (roll angle $\beta = 10^\circ$)
- Different loading rates ($v = 6.7 \text{ m/s}, v = 10 \text{ m/s}$)

An overview on the complete test matrix is presented in Appendix A6.2.

The evaluation of the test results was conducted mainly on the basis of the measured force-displacement curves, the recorded high-speed videos as well as the post-test pictures which document the absorber failure modes.

Several important effects could be identified with respect to the functionality of a robust crash absorber in its structural environment. Exemplary results are given in Figure 8-5, which illustrates two main characteristics of the identified absorber behaviour.

The results in Figure 8-5a) represent variants that show stable and progressive crushing. As expected, the first load peak is influenced by the failure of the strut radius. The following phase at a low force level is caused by the folding mechanism of the free strut length between radius and the half-tube absorber. After this distance is crushed, the absorber gets into contact and the load level increases according to the trigger angle up to the nearly constant crushing plateau. In the following crushing phase, local peaks in the load level identify the individual rivet lines.

In contrast to the results discussed above, Figure 8-5b) represents variants that show unstable crushing which also includes local or total failure of the specimens. Such failures were caused by buckling tendencies of the flat strut. In addition, the strut variant with complex layup partly induced local failure lines which led to total failure of the strut. The diagram in Figure 8-5b) illustrates the significant drop of the load level after failure of the strut, at a crushing distance of approximately $L = 45$ mm. Further stable crushing on the expected force level occurred at $L = 100$ mm where the remaining intact absorber structure gets into contact again.

Furthermore, slightly different robustness behaviour was identified for the laminate types of the half-tube absorbers. According to the results of the test programme, triaxial braided absorber specimens provided the highest robustness performance whereas the specimens with absorbers made of woven fabric showed the poorest robust crushing behaviour. The differences of the individual layups and laminate types showed significant influence on the absorber failure modes. Figure 8-6 shows exemplary post-test pictures of different tested specimens which illustrate the spectrum of the failure modes.

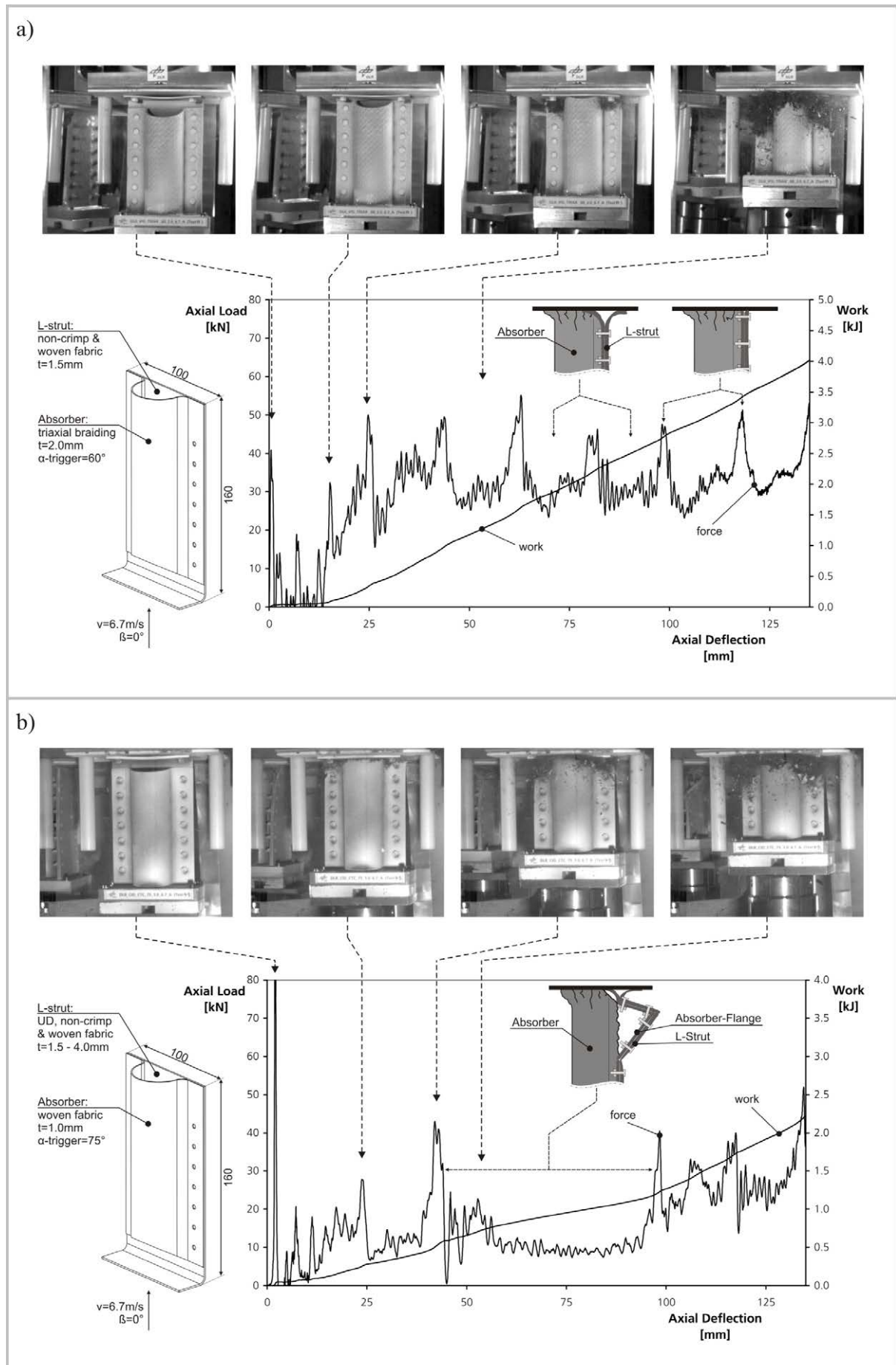


Figure 8-5: Typical characteristics identified in the absorber test programme

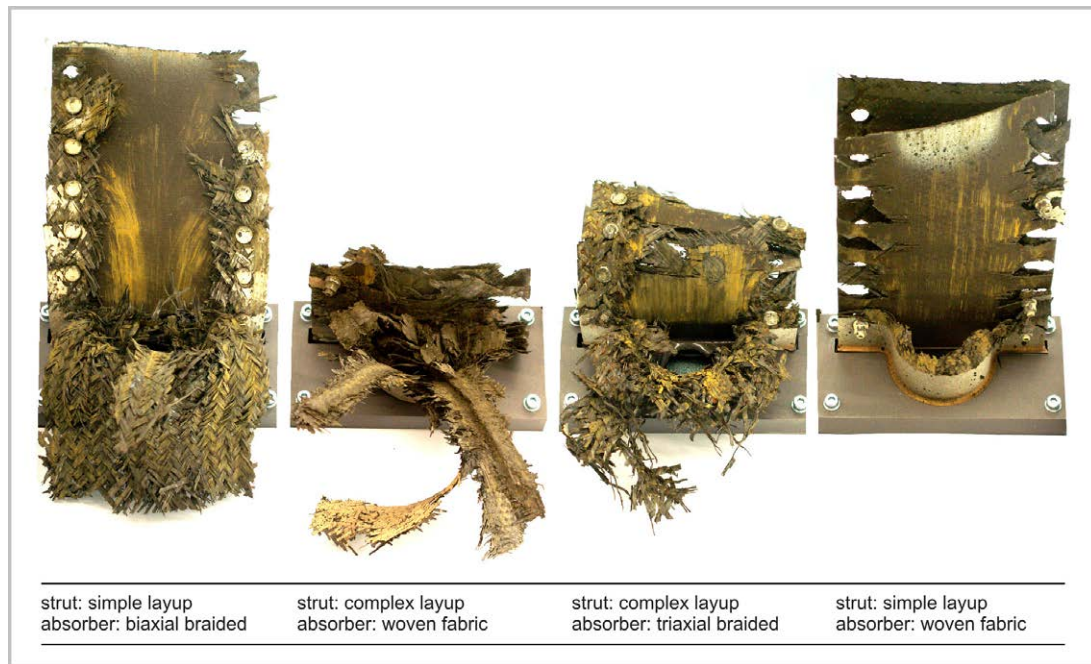


Figure 8-6: Spectrum of absorber failure modes identified in the test programme

Summarising the axial crushing tests, a test setup was developed which appropriately represents the structural fuselage environment of the considered crash absorber. In contrast to several studies on the crushing of CFRP absorbers, which analysed mainly the material failure behaviour, the developed test setup represents a structural testing with focus on the absorbers functionality in its structural environment. The test setup was verified by numerical analyses as well as by experimental pre-tests. A test series of 72 specimens was conducted using the developed test setup.

To link the test programme results with the kinematics modelling approach developed in this thesis, a comparison is presented in Figure 8-7 which depicts the test results and the required crushing characteristic based on the final macro inputs of the Kinematics Model according to paragraph 7.6. In this comparison, the selected test result represents a typical crash characteristic of stable crushing similar to Figure 8-5a). As the test setup additionally considered the lower frame structure that induced the first peak force, the macro curve starts with respect to the second peak force of the test curve which represents the triggering of the half-tube absorber. A detailed comparison of the trigger forces is hardly possible as such peak forces measured in dynamic tests are significantly influenced by inertia and other dynamic effects of the test setup and the testing machine. Nevertheless, a comparison of the crushing force plateaus identifies a good agreement in this example. Hence, sufficient energy could be absorbed according to the requirements of the final crash scenario of paragraph 7.6.

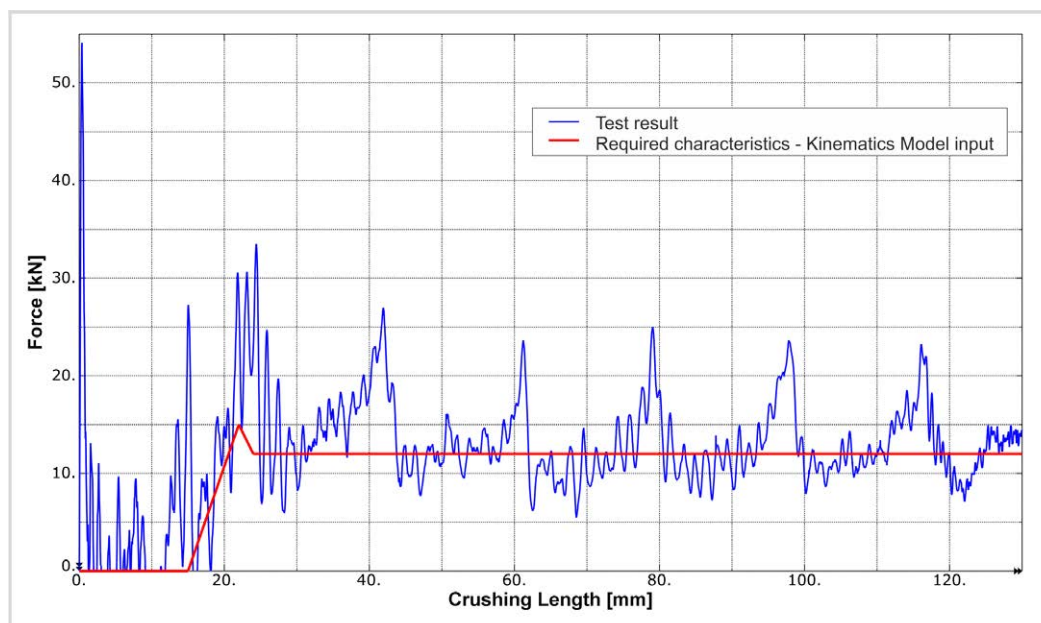


Figure 8-7: Comparison of the required absorber characteristic and the test result

8.2. Frame bending tests

The outcomes of the final crash scenario in chapter 7 identified crash characteristics in the frame kinematic hinges which have to provide a significant amount of energy absorption. With respect to the general crash concept discussed in chapter 6 and 7, one of the main challenges is the development of a structural crash device which provides sufficient energy absorption in a frame bending failure mechanism. Hence, the focus of an investigation on frame bending concepts is mainly on the energy absorbing capacity. Further design parameters such as the trigger mechanism or the detailed crash behaviour under a combined bending-compression load are of lower priority in this early development phase.

For that reason, the development of an experimental test setup concentrated on the investigation of the general feasibility to absorb the required amount of energy. To realise an efficient test method which can be used for the investigation of several absorption concepts, the test setup was defined as simple as possible.

Figure 8-8 illustrates a schematic extraction of the planned test setup out of a typical fuselage structure. Based on a LCF-shaped frame design the stiff C-frame component was considered in this setup. Instead of a curved frame component, the test setup was defined with straight C-frame segments to further reduce the complexity. A four-point bending test setup was defined to analyse the failure behaviour of the C-frame segments with respect to pure moment loads, as only a limited influence of additional compression loads on the general energy absorbing capacity is expected.

The C-profile geometry aligns to typical LCF-shaped profiles and specifies a web height of $H_{\text{web}} = 80 \text{ mm}$ and a flange width of $b_{\text{flange}} = 40 \text{ mm}$. The segment length of the C-profile is limited to $L = 600 \text{ mm}$ due to the boundary conditions of the test machine for the quasi-static bending tests as well as the drop tower for the dynamic bending tests.

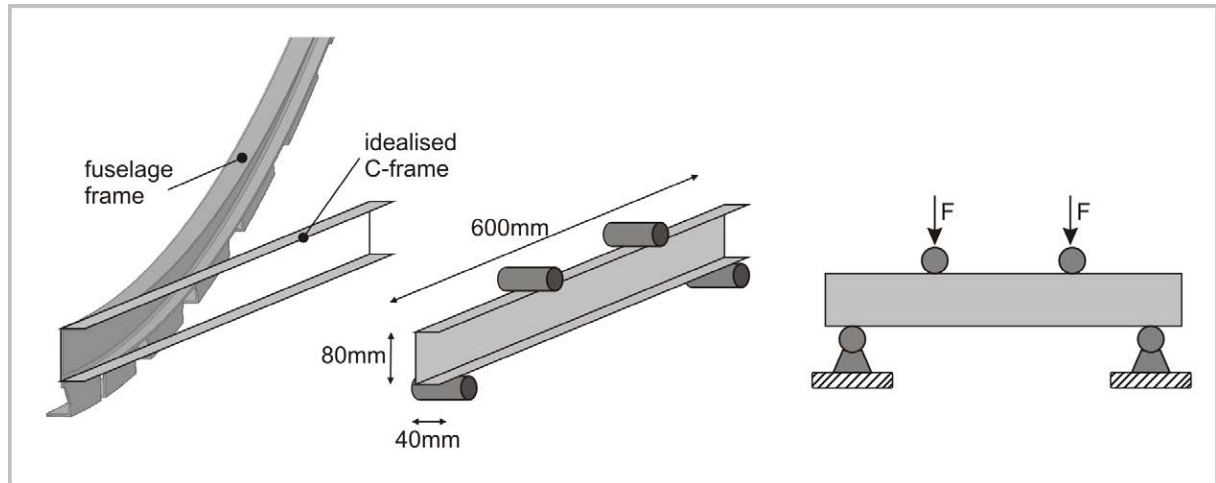


Figure 8-8: Derivation of the frame bending test setup out of a typical fuselage structure

Several investigations were performed to define an appropriate test setup configuration. Similar to the axial crushing tests, detailed finite element analyses as well as experimental pre-tests were performed to investigate effects of the test setup configuration. Appendix 6.3 provides a short documentation of the FE model as well as the pre-test setups.

One effect that was analysed in the scope of the test setup development was the influence of the bending-torsion coupling. In case of the pure bending load the C-profile segment tends to rotate around its shear centre which is located outside of the C-profile. Hence, the C-segment has to be supported against lateral displacement respectively rotation in the region of support and stamp. Another option is the combination of two C-segments to an I-segment (back-to-back C-splicing). In that case, the shear centre is located in the centre of the cross-sectional area and torsion effects with respect to pure bending loads are not expected. The manufacturing of an I-profile is more complex and potential failure or other effects in combination with a back-to-back C-splicing may influence the test results. Therefore a supported C-profile configuration was preferred.

A further investigation considered the development of an appropriate fixture which enables a smooth load introduction without local damages of the C-segment at the support and the stamp. First experimental pre-tests showed that limited support by metallic plates is not sufficient and as a consequence a robust fixture is required to avoid local material damage in the regions of the load introduction.

Another topic is the limitation of the frame segment length. Despite of the limited length of $L = 600$ mm the test setup should provide realistic frame failure behaviour. As discussed in the previous chapters, typical frame failure is initiated by crippling of the frame flanges. Hence, the free length of the test setup between the stamps has to be defined so that the compression loaded frame flange is allowed to buckle without significant stress concentration at the transition to the fixture. Finite element analyses were performed to estimate the instability behaviour of the free segment length between the stamps.

Further details about the investigations on the development of an appropriate test setup are given in Appendix A6.3.

Based on the investigation of the above discussed effects, a test fixture was developed which is pictured in Figure 8-9a) and 8-9b). Solid aluminium fittings encase the C-segment in the outer regions between stamp and support. The aluminium fittings were manufactured with an appropriate tolerance of the C-notch to enable bending tests of C-profiles within a limited range of thickness. To fix the C-profile in the C-notch the frame segment is bonded in the fixture.

Besides the realisation of a smooth load introduction without local material damage, this fixture avoids the deformation of the C-profile geometry due to the introduced load. As a result of the full casing of the C-segment in the fixture, bending-torsion coupling effects can be carried and transferred to the lateral supports, which are provided by steel brackets that were manufactured and installed between stamp and support, as pictured in Figure 8-9c).

Based on FE analyses, the free length of the C-segment was defined to be $L_f = 160$ mm. This distance is a good compromise regarding the given maximum segment length and a required minimum distance between support and stamp to introduce the moment load.

The transition from the bonded C-segment inside the fixture to the free segment length was designed with radii. In case of flange buckling, a deformation of the flange structure at the transition to the fixture is allowed and the flange can align to the fixture radii. Stress concentrations could be limited with this design.

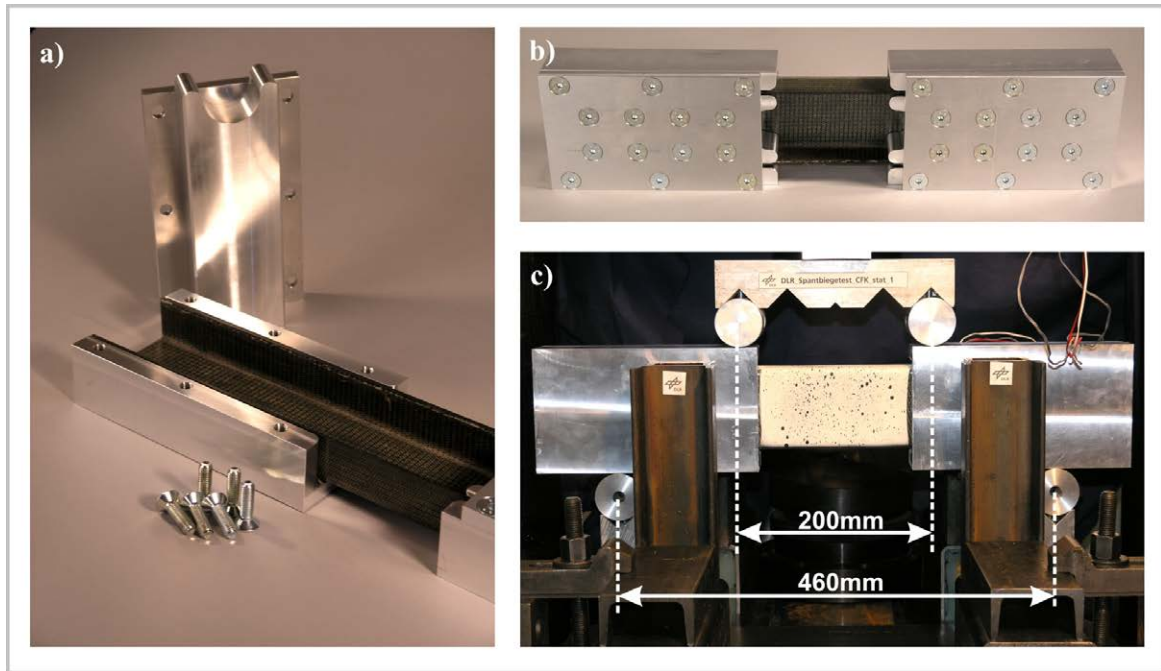


Figure 8-9: Fixture and test setup of the four-point bending test

Several frame bending tests were performed with the developed test setup. Quasi-static four-point bending tests were conducted in a universal testing machine (Zwick 1494) whereas the dynamic tests were conducted in the drop tower of the DLR Institute of Structures and Design. A test matrix of the considered frame bending tests is given in Appendix A6.4.

Regarding the energy absorption concept, the influence of hybrid laminates was analysed in this exemplary study. Besides a reference configuration, purely made of CFRP (AS4/PEEK), a hybrid configuration was tested with titanium sheets which were embedded in the flange laminate of the frame segments. Previous studies on the coupon level identified a significant potential of energy absorption regarding such hybrid laminates particularly in a bending mode [129]. Based on the coupon level results, the hybrid concept was selected for further investigation on the structural level. Figure 8-10 illustrates both frame variants.

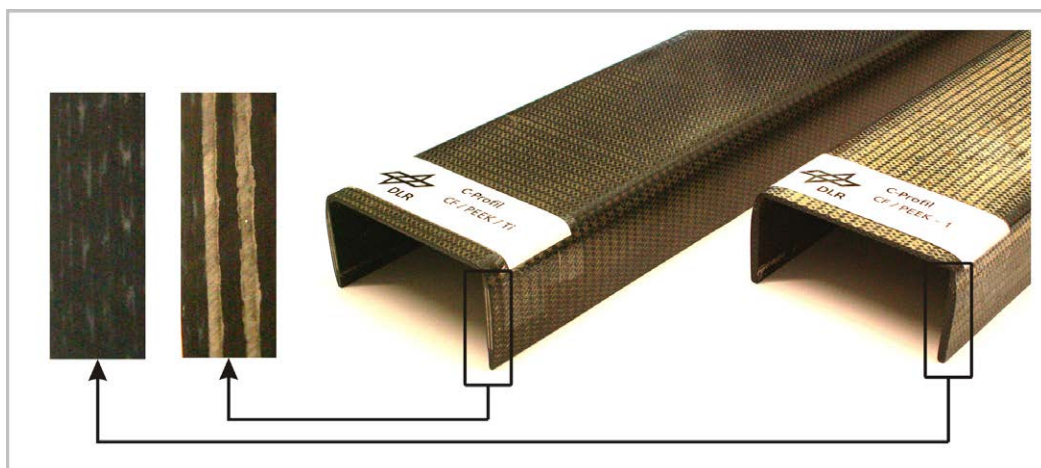


Figure 8-10: Reference variant (AS4/PEEK) and hybrid variant (titanium sheets in the flange)

Results of the quasi-static bending tests are presented in Figure 8-11. Two tests of each variant were conducted. The comparison of force-displacement curves shows similar behaviour of the reference as well as the hybrid variant. Especially the post-failure behaviour does not show any significant differences, neither in the force level nor in the energy absorption.

With the focus on the development of a frame bending test setup, the results of the quasi-static tests could be used to verify the developed test setup. The failure mode, as depicted in Figure 8-11, shows the desired typical frame failure behaviour. The compression loaded flange buckled and initiated crippling failure in the centre of the free segment length. Hence, stress concentrations at the transition to the fixture could be reduced by the radii design so that their influence is secondary and failure close to the fixture is avoided.

After failure initiation in the compressive loaded flange the failure propagated through the frame web to the lower, tensile loaded flange. Further bending rotation occurred around a pivot point which is located in the remaining lower flange.

The compression loaded, upper flange of the C-segments was recorded in the quasi-static tests with a high-speed camera (FASTCAM-APX RS250K) to allow a detailed analysis of the failure initiation. Figure 8-12 pictures the failure sequence of the reference and the hybrid variant. The sequences were recorded with a sampling frequency of 30,000 frames per second to resolve the crack propagation in the upper flange. Both sequences show a failure propagation which starts at the C-corner and propagates to the outer flange side. Hence, typical crippling failure could be identified which is initiated by material failure in the stiffer corners of the frame profile.

Despite the reduced complexity, the verification of the test setup identified realistic frame failure behaviour in the quasi-static tests.

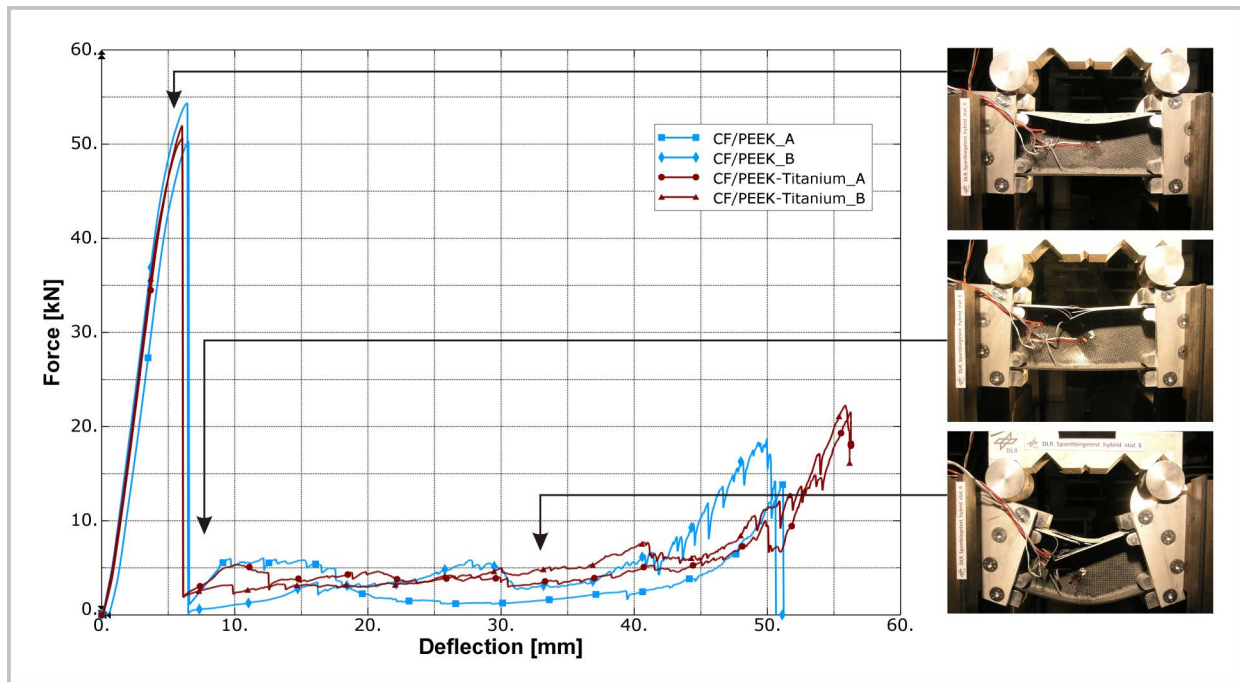


Figure 8-11: Results of the quasi-static frame bending tests

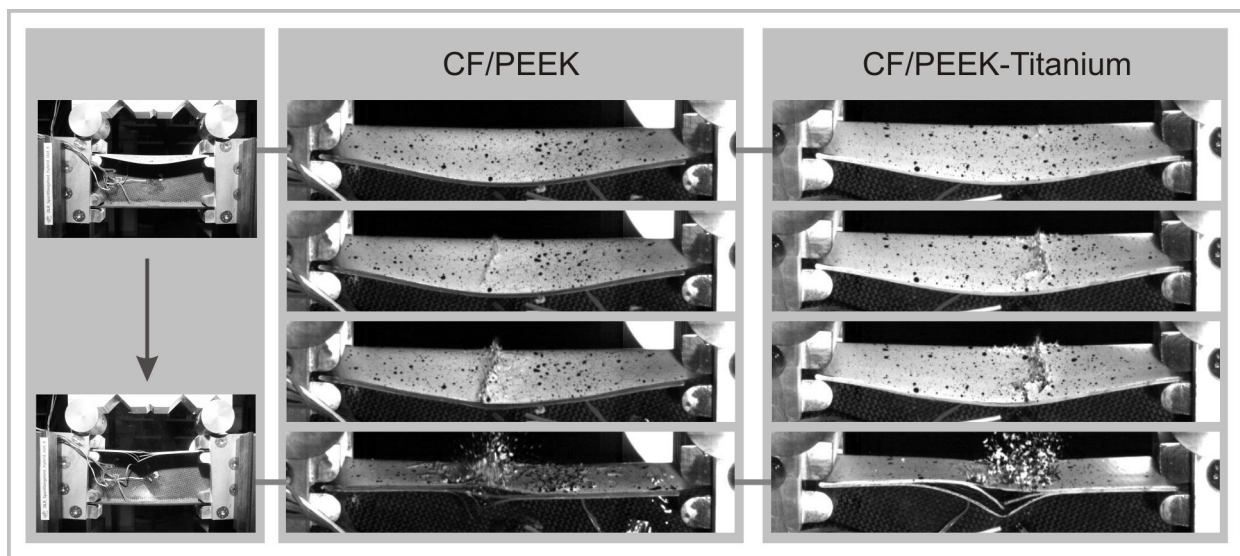


Figure 8-12: Crippling failure recorded with the high-speed camera

Further dynamic tests were performed in the drop tower at an initial velocity of $v_i = 3.4$ m/s. This loading rate corresponds to the averaged loading conditions of the frame structure in a typical crash event according to the ‘standard crash case’. Minor modifications of the test setup were conducted for the dynamic tests. Fixtures, stamps and the frame web were painted in white colour with an additional pattern in black colour. Foam stripes with negligible stiffness were bonded on the frame flanges and painted with a dispersion of black points. Both modifications were conducted to measure displacements of the individual parts on the basis of the high-speed camera records using the optical measurement system GOM ARAMIS [146].

Furthermore, in the dynamic tests unfavourable dynamic effects are expected by the impact of the stamps on the fixture with a velocity of $v_i = 3.4$ m/s. In this configuration, a sharp impulse could lead to the separation of the stamp and the fixture in the further bending sequence with accordant consequences for the measuring of displacement and load at the stamps. Furthermore, sharp impulses may lead to vibrations at the load cell which affect the measuring. To reduce this dynamic effect, a damper was installed between the stamp and the fixture to enable a smooth transfer of the dynamic loads.

The dynamic effects are obvious in the presentation of the drop test results in Figure 8-13. The force-displacement graph compares four drop tests of the hybrid and the reference frame segment variants. A stiff damper configuration was used in the bending tests of the hybrid frame segments. Oscillations are visible in the pre-failure phase which were caused by the above described dynamic effects. In the tests of the reference frame segments an optimised damper configuration led to a steady force increase up to failure but also to a higher deflection up to failure. Regarding the focus of this experimental study, the post-failure behaviour, the dynamic tests showed similar results compared to the quasi-static tests with negligible improvements of the energy absorption of the hybrid frame segment variant.

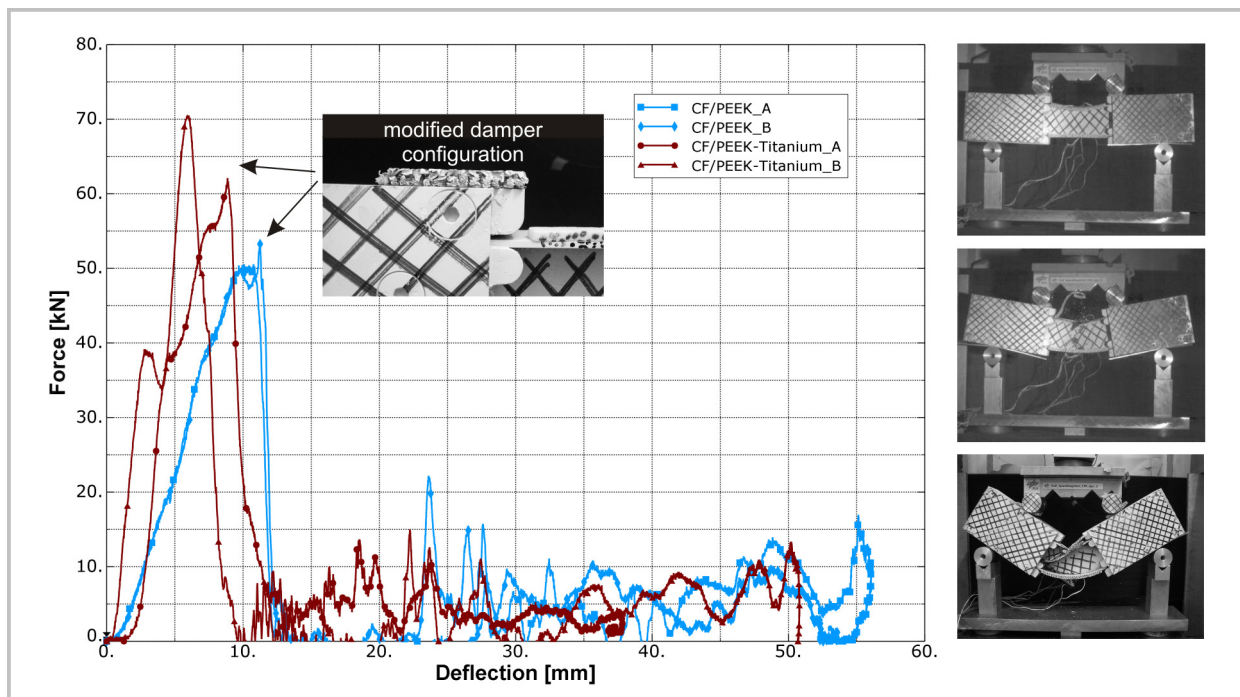


Figure 8-13: Results of the dynamic frame bending tests

Summarising the frame bending tests, a test setup was developed with the focus on the identification of the post-failure energy absorption capacity. This focal point enabled the development of a comparably simple and efficient frame testing setup which considers a four-point bending load on the stiff C-segment of a typical LCF-shaped frame design. Quasi-static

tests verified the developed test setup. Stable load introduction as well as realistic frame failure could be realised despite a limited frame segment length of $L = 600$ mm. Regarding the dynamic testing, further modifications of the test setup were defined which could be verified in the drop tests.

The exemplarily tested hybrid frame segments with ductile titanium sheets in the frame flanges provided no significant improvements in the energy absorption capacity compared to a reference variant purely made of CFRP. Due to the simplified test setup, which considers only the C-segment of a LCF-shaped profile instead of the complete frame-stringer-skin panel structure, a direct comparison of the test results with the required frame bending characteristics according to the final crash scenario is not possible. However, the final macro inputs of the Kinematics Model according to paragraph 7.6 specify a post-failure moment level which is 50 % of the failure load level. Comparing this requirement with the outcomes of the bending tests, the energy absorption capacity of the tested hybrid frame segments is clearly far below this requirement. Hence, the developed frame bending test setup can be used for further research on energy absorbing frame concepts, which is clearly essential.

9. Conclusion and outlook

The objective of the thesis is the contribution to the development of a crashworthy composite fuselage design of transport aircraft. This contribution comprises in a first part of the thesis the development of a finite element modelling approach for the investigation of crash scenarios, the so-called Kinematics Model, that combines benefits of currently used simulation modelling techniques. In a second part of the thesis, the objective is the development of a crash design methodology, on the basis of the developed Kinematics Model, that considers the design process for a composite fuselage including the verification of identified crash device requirements by experimental testing.

Paragraph 9.1 summarises the final outcomes of the development of the finite element modelling approach. Final conclusions of the methodology of the crash design process are presented in paragraph 9.2. Topics for potential future research are depicted in the outlook in paragraph 9.3.

9.1. Methodology of the finite element modelling approach

The design for crash of composite fuselages is a topic that has to be considered in the early design phases of an aircraft development. The common state-of-the-art analytical methods, which were discussed in paragraph 2.2, show drawbacks with respect to their use in a preliminary design process. Based on a beneficial combination of these common modelling methods a specification was derived that represents the foundation for the development of a new modelling approach. Chapter 3 presented this approach and dealt with the general aspects of this modelling technique. The frame was identified as the main structural part that highly affects the structural behaviour of the fuselage in case of crash. Accordingly, detailed investigations on the frame failure modelling were discussed in chapter 4 and 5 which ensure an appropriate accuracy of the developed modelling approach.

With respect to the development of the finite element modelling approach, the following conclusions can be drawn:

- A new modelling approach, the Kinematics Model, was developed that combines the advantages of current simulation techniques with the focus on a preliminary crash design tool. The main benefits are the absence of composite material formulations for damage and failure which are still hardly predictable. Besides a linear-elastic modelling of the

fuselage structure the main crash characteristics are described by macro elements. The usage of macro elements additionally enables an efficient method for the investigation of different failure characteristics in the individual structural parts. With respect to the requirements of a preliminary design tool the modelling approach provides a discretisation that considers efficient calculation without disregarding of structural effects that can influence the crash behaviour.

- Typical failure modes of transport fuselage structures caused by crash related loads were identified and assessed. With respect to failures of primary category which are of relevance for composite fuselage structures, macro architectures were developed that accurately represent the individual structural failure behaviour.
- Appropriate output definitions were developed which fulfil the specific requirements of a preliminary design tool. Of interest are efficient output data which help to quickly analyse the main results of a simulation run. Structural loads are evaluated by overall strain plots of the most critical frame structure. Passenger loads are described in Eiband diagrams which provide information about the risk of injury. The output for crash device requirements are given in load-deflection characteristics that can directly be used for the comparison with test data or other analysis results, like output data of local explicit FE calculations.
- According to the requirements of a preliminary design tool, all relevant input variables of the Kinematics Model are parameterised for the efficient conduction of various simulation runs.
- Detailed investigations of the frame structure led to an accurate and efficient representation in the Kinematics Model. Frame failure is well represented with respect to the identification of potential failure locations, the elastic pre-failure behaviour, the triggering respectively the definition of failure criteria for the frame structure, and the post-failure behaviour.
- Further improvement for the representation of the frame failure behaviour was realised by the development of a user-defined macro element in the ABAQUS environment. Improvements such as strain-based triggering, physically correct unloading/reloading behaviour as well as high accuracy with respect to loads with a low bending-compression ratio were implemented in the user-defined macro element. However, due to an unsolved bug situation, discussed in paragraph 5.5, this user element could not be proved in the crash design process.

9.2. Methodology of the crash design process

The review on crashworthiness research identified the need to modify the static design of a composite fuselage to fulfil the crash requirement. Otherwise, transport aircraft with a composite fuselage would provide significantly worse crashworthiness compared to metallic equivalents which are typically not designed for crash.

The need was identified to implement additional crash absorbers in a composite fuselage structure and to adapt the structure to the expected crash loads. Chapters 6-8 dealt with a design process that was developed to conclude to an optimised crash kinematics, to a crashworthy fuselage structure and to the definition of required crash absorber characteristics. The design process additionally considers the verification of identified crash device characteristics by experimental testing on the component level. The developed crash design process was exemplarily performed on the basis of a statically pre-sized CFRP fuselage structure of narrow-body size with a stiff cargo-crossbeam to allow the crushing of the sub-cargo structure in case of crash (bend-frame concept).

Considering the development of the crash design methodology, the following conclusions can be drawn:

- The necessity was postulated to align the crash concept with the natural crash behaviour of the considered fuselage structure. Otherwise, additional weight penalty is expected to ensure a crash kinematics that differs from the natural structural behaviour.
- Natural crash kinematics of typical fuselage structures of narrow-body transport aircraft were identified and assessed using the Kinematics Model. The assessment of natural crash kinematics provided a good understanding of the typical fuselage crash behaviour.
- The most favourable natural crash kinematics was adapted to a preliminary sized CFRP fuselage structure using the Kinematics Model. Appropriate structural allowables were defined to assess the structural loads during the design process. The crash kinematics was optimised with respect to the given fuselage design. Subsequently, the fuselage structure was adapted to the final crash loads. The structural adaptation was conducted starting with a structure of high stiffness. With respect to the final crash scenario valuable outcomes could be provided, which include information about the structural mass penalty caused by the crash related re-sizing of the frame and the cargo-crossbeam, loads on the passengers as well as final requirements for the crash device characteristics which are necessary to fulfil the optimised crash kinematics.

- Different experimental test setups were developed for the investigation of crash device concepts on the basis of the required macro characteristics. The first test setup was developed to investigate in detail the failure behaviour of axial crush absorbers in combination with an accurate representation of the fuselage boundary conditions. A comprehensive test programme of potential absorber designs for the sub-cargo structure could be tested with realistic boundary conditions. The second test setup was developed to efficiently investigate basic crash device characteristics of frame bending failure. The energy absorption capacity is in the focus of this bending test setup, which can be investigated with generic frame structures. The developed bending test setup was successfully proved by experimental bending tests with composite frame structures. Both developed test setups demonstrated options to investigate crash device concepts on different levels of complexity. In both test setup variants efficient testing was ensured by reasonable representation of structural boundary conditions instead of the definition of large component tests.
- The integration of experimental testing into the crash design process ensures model accuracy with respect to the assumptions used for the macro inputs. The feasibility of assumed crash absorber characteristics can be checked and adapted during the design process, when necessary.

9.3. Outlook

With respect to the final target to achieve improved crashworthiness for composite transport fuselage structures further research work is required that may focus on the following topics.

- An implementation of the user-defined kinematic hinge macro element into the Kinematics Model is desired. A solution of the bug situation would enable the usage of improved frame failure representation. Further options for the user-element in ABAQUS would enhance the usage of the developed macro element, e.g. to enable the storage of user-element output data in the output data base file (*.odb).
- The exemplary development of a crash scenario in this thesis was performed on the basis of a generic fuselage structure which was equipped with a stiff cargo-crossbeam to realise the bend-frame concept. This crash concept enables extensive crushing of the structure below the cargo-crossbeam similar to concepts known from rotorcraft designs. The final crash scenario developed within this thesis identified a structural mass of the frame structure which is more than twice the statically pre-sized frame mass. Research on alternative crash concepts is recommended to reduce the structural mass penalty usually

associated with crashworthiness. Alternative concepts could specify e.g. a filigree sub-cargo structure with the focus on energy absorption in the upper crash zones of the sub-floor area. Such an alternative concept could align to the consideration of a minimum required backing structure to achieve energy absorption in the individual crash zones, according to the discussion in paragraph 7.2.

- Further improvement of crashworthiness could be realised by the consideration of non-typical fuselage sections in the design process. An adaptation of the crash design for fuselage sections with cargo-door, landing gear bay, wing-box or tail cone would significantly improve the crashworthiness of the overall fuselage structure. Further enhancement of the Kinematics Model is necessary to consider fuselage sections that differ from the typical fuselage design. In particular, the kinematic hinge macro architecture has to be extended to represent the frame failure behaviour of non-typical fuselage sections. Frame shear failure or skin separation are requirements for such an enhanced kinematic hinge architecture. After the implementation of enhanced modelling options for non-typical fuselage sections, the efficient simulation technique of the Kinematics Model can be used in a subsequent step to investigate crash concepts for composite fuselages in full aircraft simulations.

A1. Appendix of chapter 2

Paragraph A1.1 provides a short overview on the finite element method and its integration schemes with the focus on explicit time integration and structural elements as used in the scope of this thesis.

A1.1. The finite element method in the scope of this thesis

There is various literature dealing with the finite element method and explaining this theory in an excellent way, e.g. in [111,113,144]. Nevertheless, a short overview on the finite element method shall be given here with the aspect on the selected calculation schemes in this thesis.

The finite element method uses several approximations to analyse structural problems. A first approximation is the discretisation which represents the considered structure by finite elements. The most complex finite element is the continuum element (solid) which represents all components of a general stress tensor. In some of the considered problems in this thesis the structure or parts of the structure behave according to the shell, beam or bar theory. Here, specific structural finite elements can be used to represent these parts in the finite element analysis. Structural elements only consider those components in the stress tensor which are affected by the structure or the structural part, while all other components are not considered. This leads to a significant improvement in the efficiency of element calculation. If the considered structure is discretised by structural finite elements which behaves similar to the real structure enormous calculation time can be saved instead of using calculation time consuming continuum elements. In the scope of the finite element analyses discussed in this thesis, the structures were discretised mainly with shell, beam and bar elements, as displayed in Figure A1-1.

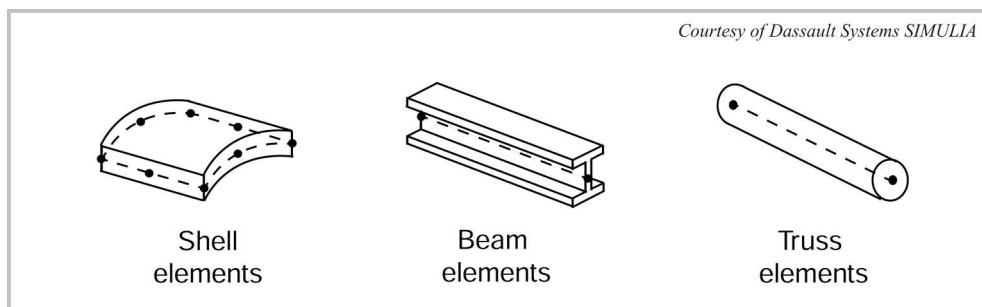


Figure A1-1: Discretisation by structural finite elements [112]

A further approximation in the finite element method is the definition of field quantities inside of a finite element. The field quantity “displacement” is defined at the element nodes whereas the field quantity “stress” is defined at the element integration points which are located inside of the element. Basic functions are used to describe the distribution of field quantities over a finite element. To calculate the stresses at the element integration points the basic functions are used to approximate the displacements, respectively the strains, at the integration points based on the known displacements at the element nodes. The order of such basic functions depends on the considered problem and on the time integration scheme which is used to solve the equation of motion. In the scope of this thesis, the finite element analyses use basic functions of first order.

The equation of motion defines the force equilibrium at each node of the discretised structure and is given as follows:

$$M\ddot{u} + C\dot{u} + R(u) = P \quad (A1.1)$$

P are the external forces which cause accelerations, velocities and displacements dependent on the mass M , the viscosity C and the stiffness R of the element respectively the elements node. Formulation (A1.1) is a system of n equations, n is the number of degrees of freedom defined for this element node.

The integration of equation (A1.1) can be solved either with implicit time integration or with explicit time integration scheme. The implicit time integration replaces the time derivation by quantities which depend on both, the current time t and the unknown values of a time $t + \Delta t$. In each time step this integration scheme requires the solution of a non-linear system of equations which is accordingly complex. The advantage of the implicit time integration is the realisation of large time steps which can be solved absolutely stable.

In contrast to the implicit integration scheme, the solution of an explicit time integration at the time $t + \Delta t$ depends only on quantities of the time t . This integration scheme is particularly efficient if the mass matrix M and the damping matrix C are lumped, which means that they are of diagonal form. In this case each equation of the system given in (A1.1) can be solved independently. The drawback of this efficient time integration scheme is the limitation of small time steps to ensure a stable solution.

If dynamic problems are considered, such as impact or shock loads, the time step has to be reduced in both integration schemes in a way that all high-frequent portions of the structural response are represented physically correct. Hence, the efficient explicit time integration is preferable compared to the complex solution of non-linear systems of equation in the implicit

time integration. The implicit integration scheme is preferable in cases where the structural response is composed mainly of the low-frequent portions.

In the case of the crash analyses of this thesis the explicit time integration is used. Equation (A1.1) is transformed in the following form:

$$\ddot{u} = M^{-1}[P - C\dot{u} - R(u)] \quad (A1.2)$$

The accelerations are calculated through time using the central difference rule, which calculates the change in velocity assuming that the acceleration is constant. The change in velocity is added to the velocity from the middle of the previous time step to determine the velocities at the middle of the current time step:

$$\dot{u} \Big|_{(t+\frac{\Delta t}{2})} = \dot{u} \Big|_{(t-\frac{\Delta t}{2})} + \frac{(\Delta t \Big|_{(t+\Delta t)} + \Delta t \Big|_{(t)})}{2} \ddot{u} \Big|_{(t)} \quad (A1.3)$$

The velocities are integrated through time and added to the displacements at the beginning of the time step to determine the displacements at the end of the time step:

$$u \Big|_{(t+\Delta t)} = u \Big|_{(t)} + \Delta t \Big|_{(t+\Delta t)} \dot{u} \Big|_{(t+\frac{\Delta t}{2})} \quad (A1.4)$$

After these nodal calculations, the displacements at each node are determined at the time $t + \Delta t$. In a following step - the element calculations - the element strains are computed. Based on these strain increments the element stresses are computed at the element integration points from constitutive equations:

$$\sigma_{(t+\Delta t)} = f(\sigma_{(t)}, d\varepsilon) \quad (A1.5)$$

Equation (A1.5) represents the material formulations of an element which describes the relationship of strain and stress for the considered material.

Finally, the element stresses are assembled to nodal internal forces at the time $t + \Delta t$ and the calculation of the current increment is concluded.

To ensure the physically correct representation of all high-frequent portions of the structural response, a stability limit is defined in terms of the highest frequency in the system. This stability limit considers a perturbation which propagates with the wave speed of the material. As a consequence, the stability limit can be defined using the element length L^e and the wave speed of the material c_d . The wave speed is calculated from the Young's modulus E and the mass density ρ of the material:

$$\Delta t_{stable} = \frac{L^e}{c_d} \quad \text{with} \quad c_d = \sqrt{\frac{E}{\rho}} \quad (\text{A1.6})$$

The finite element analyses in this thesis are used in a preliminary design tool for crash investigations which requires an efficient computation strategy. The explicit time integration method is based on efficient nodal and element calculation as these calculations recur very often due to the small time step defined by the stability limit. The approach of the developed crash design tool, which is described in chapter 3, is based on a modelling technique which reduces the calculation time considering the theory discussed above. A linear-elastically modelled structure, where all failure is described in special macro elements, allows a coarse discretisation. The structure deforms only in the scope of its linear strain limits which are defined by comparatively small failure strains of the (composite) material. These small strains allow the use of large elements to represent the structural deformations. An increased element size improves the calculation efficiency significantly. On the one hand, the stability limit increases linearly with the element size. On the other hand, an increased element size is equivalent with a reduced number of elements that represent the considered structure and have to be calculated.

As an example, a structure is considered that is discretised by shell elements. A discretisation with a shell element length which is twice the length compared to a reference discretisation reduces the calculation time by a factor $2^3 = 8$. With twice the element length, the number of elements in a plane shell discretisation is reduced by the factor 2^2 . In addition, the stability limit of the time step increases proportionally to the element length and leads to half the number of calculation cycles which are necessary for the calculation of the reference discretisation.

A2. Appendix of chapter 4

Paragraph A2.1 provides a detailed description of the numerical model that was used for investigations on the pre-failure behaviour of a frame-stringer-skin structure.

A2.1. Analysis of pre-failure behaviour – description of the numerical model

Figure A2-1 gives an overview on the numerical model of the generic frame-stringer-skin structure which was considered in the scope of the investigations of the pre-failure behaviour. One non-curved frame component is defined in this model. The radius of a standard transport aircraft fuselage is about $r_F = 2000$ mm, effects of the curvature are expected to be marginal for such high radii, especially with respect to general instability failure modes. Therefore a planar geometry was considered here. The width of the model is based on a generic frame pitch of $w_F = 635$ mm. The length of the model is $l = 700$ mm. Three omega stringers with a stringer pitch of $l_S = 168$ mm are modelled. The LCF-shaped frame corresponds to typical, integral CFRP frame designs with flange widths of $w_{IFF} = 25$ mm, $w_{MFF} = 15$ mm and $w_{OFF} = 28$ mm. The outer frame web height is $h_{OFW} = 36$ mm. The inner frame web height as well as the frame thicknesses are parameters in the present investigation. The skin thickness was defined to be constant in all simulations with $t_S = 2.125$ mm and a layup of $[10/70/20]^1$. The omega stringers were specified with a constant thickness of $t_{St} = 1.375$ mm in all simulations and a layup of $[50/40/10]$. Cleats were defined at each stringer position. All material formulations used in this model were linear-elastic, material damage and failure was not considered. Apart from the cleats, which were modelled with isotropic material behaviour, all other structural parts were modelled with orthotropic material formulations for composites. Elastic data of typical CFRP material was used. The design and layup of the frame, the stringers and the skin is based on a static pre-sizing (on fuselage section level, considering the complete envelope of flight and ground loads) which was performed by the project partner Airbus. The connection of the individual parts was assumed to be ideal so that tied constraints were used. Symmetry boundary conditions were defined on both lateral sides. Both ends of the model were clamped using rigid bodies. These rigid bodies include the frame as well as the skin. A pure rotation was specified at the reference

¹ Ratios in percent of ply orientation in the layup: $[0^\circ/\pm 45^\circ/90^\circ]$

nodes of the rigid bodies which were positioned in the centre of the cross-sectional area of frame and skin. Shell elements with reduced integration (S4R) were used. The characteristic element size is $L_E = 12$ mm. The simulations were performed on a Microsoft Windows machine with the FE solver ABAQUS, solver version V6.8-1, using explicit time integration.

Several LCF-shaped frame designs were analysed to identify the structural behaviour in dependence of different frame stiffness. All frame designs used in this investigation are based on a given static sizing and provide typical layup definitions in the webs (between $[0/75/25]^2$ and $[0/85/25]$) and the flanges (between $[45/45/10]$ and $[50/40/10]$). Flange thicknesses between $t_{FF1} = 2.5$ mm and $t_{FF2} = 9.2$ mm were considered as well as inner frame web heights between $h_{IFW1} = 56$ mm and $h_{IFW2} = 84$ mm.

This model does not conform to the standard for detailed investigation of instability problems. For instance, imperfections or mesh dependencies were not considered in the scope of this investigation. The general elastic behaviour and the derivation of potential failure criteria were the focus of these simulations.

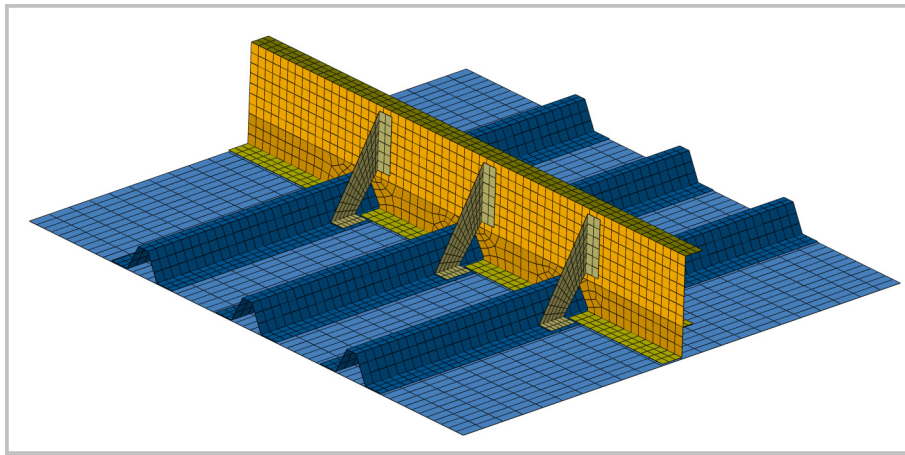


Figure A2-1: Numerical model for the analysis of the pre-failure behaviour

² With respect to layups in the frame: Ratios in percent of ply orientation in the layup: $[0^\circ/\pm 30^\circ/90^\circ]$

A3. Appendix of chapter 5

Paragraph A3.1 provides a summary of all user element property parameters that have to be defined in the ABAQUS input deck to describe the kinematic hinge behaviour. An overview of all solution-dependent variables used for internal element calculation is given in paragraph A3.2. A structogram of the calculation of internal forces is presented in paragraph A3.3. Finally, paragraph A3.4 provides a detailed definition of the reference model used for the verification of the user element.

A3.1. List of property parameters

The ABAQUS input deck of the implemented user element is given in Figures A3-1 and A3-2. A parameterised input definition was specified (Figure A3-1) that links the complex user element property definition (Figure A3-2) to a clear list of property parameters. The user element property definition requires the specification of all input in real format first and hereafter the specification of all input in integer format with eight inputs per line, separated by comma.

The following list of property parameters describes all input parameters of the user element that are defined in the ABAQUS input deck:

‘elastic_slope_pos’/ ‘elastic_slope_neg’:

rotational elastic stiffness up to triggering – independent definition for positive and negative bending rotation

‘eps_trigger_pos’/ ‘eps_trigger_neg’:

strain limit value for the initiation of triggering – independent definition for positive and negative bending rotation

‘jump_slope_pos’/ ‘jump_slope_neg’:

slope stiffness of the transition from rotational elastic stiffness to the post-failure curve – independent definition for positive and negative bending rotation

‘alpha_i_pos’/ ‘alpha_i_neg’ and ‘M_i_pos’/ ‘M_i_neg’ (i = 1-8):

tabular definition of pairs of values of the post-failure curve (max. eight pairs of values) – independent definition for positive and negative bending rotation

‘slope_pos’/ ‘slope_neg’:

unloading slope stiffness for the transition between post-failure curve, unloading curve and reloading curve – independent definition for positive and negative bending rotation

‘unload_pos’/ ‘unload_neg’:

moment level of the unloading behaviour – independent definition for positive and negative bending rotation

‘reload_pos’/ ‘reload_neg’:

moment level of the reloading behaviour – independent definition for positive and negative bending rotation

‘normal_elastic_slope_pos’/ ‘normal_elastic_slope_neg’:

translational elastic stiffness in the frame normal direction – independent definition for positive and negative bending rotation

‘history_interval’:

definition of output frequency

```

**
** -----
** KINEMATIC HINGE INPUT PARAMETER DEFINITION
** -----
**
**
*Parameter
**
** ### POSITIVE ROTATION (OPENING BENDING): ####
**
elastic_slope_pos= 1.5e05
**
alpha_1_pos=          0.00
M_1_pos=                241.50
alpha_2_pos=          0.50
M_2_pos=                241.50
alpha_3_pos=          0.51
M_3_pos=                150.00
alpha_4_pos=          0.80
M_4_pos=                150.00
alpha_5_pos=          0.90
M_5_pos=                80.00
alpha_6_pos=          1.50
M_6_pos=                80.00
alpha_7_pos=          3.00
M_7_pos=                80.00
alpha_8_pos=          3.01
M_8_pos=                80.00
**
slope_pos= 1.5e07
unload_pos= -50.
reload_pos= 20.
eps_trigger_pos= 2.0
jump_slope_pos= 5.e03
**
** ### NEGATIVE ROTATION (CLOSING BENDING): ####
**
elastic_slope_neg= 1.5e04
**
alpha_1_neg=          0.00
M_1_neg=                -300.50
alpha_2_neg=         -0.80
M_2_neg=                -300.50
alpha_3_neg=         -0.81
M_3_neg=                -250.00
alpha_4_neg=         -1.10
M_4_neg=                -250.00
alpha_5_neg=         -1.30
M_5_neg=                -130.00
alpha_6_neg=         -1.80
M_6_neg=                -130.00
alpha_7_neg=         -3.00
M_7_neg=                -130.00
alpha_8_neg=         -3.01
M_8_neg=                -130.00
**
slope_neg= 1.5e04
unload_neg= 80.
reload_neg= -30.
eps_trigger_neg= -0.1
jump_slope_neg= 5.e03
**
**
** ### NORMAL TRANSLATIONAL STIFFNESS: ####
**
normal_elastic_slope_pos= 3000.
normal_elastic_slope_neg= 3000.
**
**
** ### HISTORY OUTPUT: ####
**
history_interval= 1.e-02
**
**

```

Figure A3-1: Parameterised user element input definition

```

**
**
**
**
** ### VUEL INPUT FORMAT: ###
**
*User Element, Nodes=4, Type=VU2, Properties=47, Coordinates=6, Variables=16
1, 2, 3, 4, 5, 6
*Element, Type=VU2, Elset=myelement
50005, 5001, 6002, 6005, 5005
*Uel Property, Elset=myelement
<elastic_slope_pos>, <alpha_1_pos>, <M_1_pos>, <alpha_2_pos>, <M_2_pos>, <alpha_3_pos>, ...
...<M_3_pos>, <alpha_4_pos>,
<M_4_pos>, <alpha_5_pos>, <M_5_pos>, <alpha_6_pos>, <M_6_pos>, <alpha_7_pos>, <M_7_pos>, ...
...<alpha_8_pos>,
<M_8_pos>, <slope_pos>, <unload_pos>, <reload_pos>, <eps_trigger_pos>, <jump_slope_pos>, ...
...<elastic_slope_neg>, <alpha_1_neg>,
<M_1_neg>, <alpha_2_neg>, <M_2_neg>, <alpha_3_neg>, <M_3_neg>, <alpha_4_neg>, <M_4_neg>, ...
...<alpha_5_neg>,
<M_5_neg>, <alpha_6_neg>, <M_6_neg>, <alpha_7_neg>, <M_7_neg>, <alpha_8_neg>, <M_8_neg>, ...
...<slope_neg>,
<unload_neg>, <reload_neg>, <eps_trigger_neg>, <jump_slope_neg>, <normal_elastic_slope_pos>,
...<normal_elastic_slope_neg>, <history_interval>
**
**

```

Figure A3-2: ABAQUS input deck for the user element

A3.2. List of solution-dependent variables (SDV)

In the following, a list of solution-dependent variables, which were defined to calculate the user element behaviour, is given:

- ‘salph1’: rotational displacement of the current increment (last increment: ‘salph1Old’)
- ‘sM1’: moment magnitude of the last/current increment
- ‘loadflag’: flag for loading condition (loading/unloading/reloading/etc.) of the last/current increment
- ‘jumpflag’: flag for loading condition (untriggered/triggered) of the last/current increment
- ‘salph_j1’: rotational displacement at the increment of triggering
- ‘salph_j2’: rotational displacement at the end of transition from the rotational elastic stiffness to the post-failure curve
- ‘salphs_s1’: rotational displacement of the increment of the last unloading initiation
- ‘salph_s2’: rotational displacement at the end of the transition from the post-failure curve to the unloading curve
- ‘salph_s3’: rotational displacement at the beginning of the transition from the reloading curve to the post-failure curve
- ‘salph_s4’: rotational displacement of the first increment of the reloading after unloading along the unloading curve

- ‘salph_s5’: rotational displacement at the end of the transition from the unloading to the reloading curve
- ‘salph_s6’: rotational displacement of the first increment of the unloading after reloading along the reloading curve
- ‘salph_s7’: rotational displacement at the end of the transition from the reloading to the unloading curve
- ‘sF’: force magnitude (frame normal direction) of the last increment
- ‘seps’: strain magnitude (frame normal direction) of the last increment

A3.3. Structogram of the calculation of internal forces

The following structogram is an extraction of the calculation of internal loads and considers the determination of the moment load (‘sM1’) based on the current rotational displacement (‘salph1’). The given structogram exclusively considers positive rotational displacement. Figure A3-3 again illustrates the solution-dependent variables for calculation of the moment load for a better understanding of the following structogram.

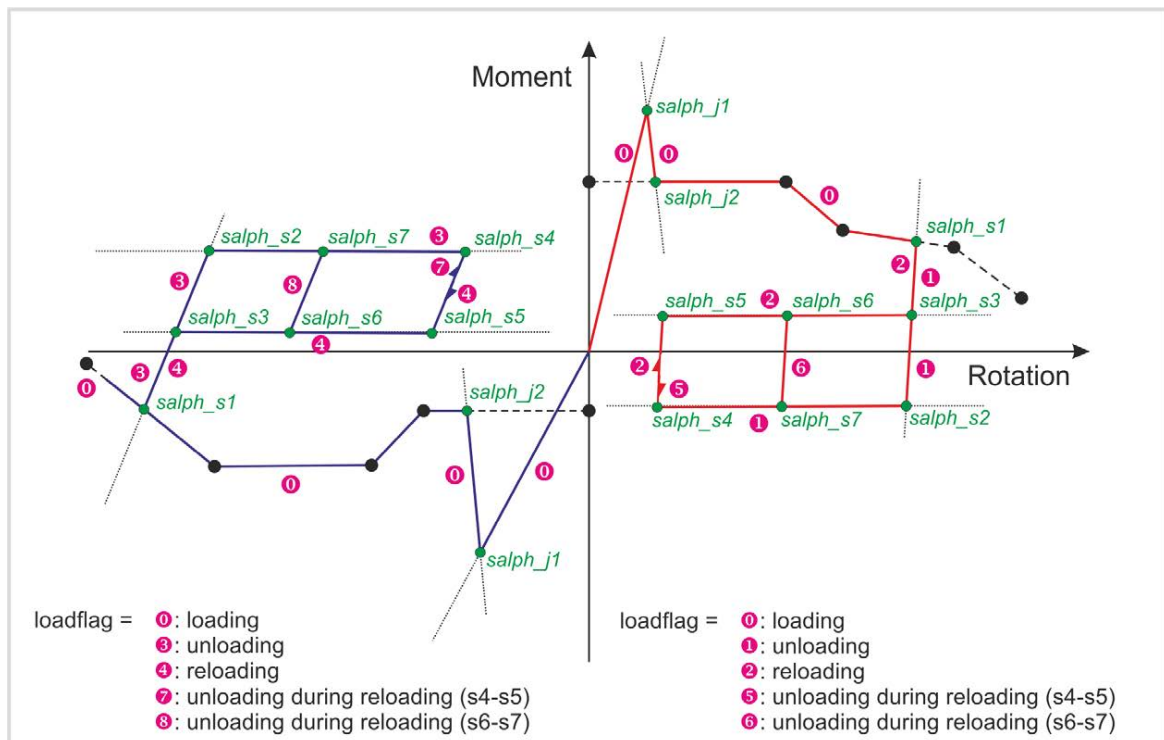


Figure A3-3: Calculation of the moment load

Extraction of the moment calculation for 'salph1' ≥ 0 :

IF (salph1 \geq salph1Old AND seps2 \leq seps_p AND loadflag = 0)	
	→ current increment on elastic-slope_positive / loading
	→ calculate sM1 on elastic-slope_positive
ELSEIF (salph1 \geq salph1Old AND seps2 > seps_p AND loadflag = 0 AND jumpflag = 0)	
	→ initiation of jump / loading
	→ jumpflag = 1
	→ calculate sM1 on elastic-slope_positive
	→ calculate salph_j1 and salph_j2
ELSEIF (salph1 \geq salph1Old AND loadflag = 0 AND jumpflag = 1 AND salph_j1 < salph1 \leq salph_j2)	
	→ on jump-slope_posistive / loading
	→ calculate sM1 on jump-slope_positive
ELSEIF (salph1 \geq salph1Old AND loadflag = 0 AND jumpflag = 1 AND salph1 > salph_j2)	
	→ on post-failure-curve_positive / loading
	→ calculate sM1 on post-failure-curve_positive
ELSEIF (salph1 < salph1Old AND loadflag = 0 AND jumpflag = 0)	
	→ on elastic-slope_postive / unloading (→ linear elastic unloading)
	→ calculate sM1 on elastic-slope_positive
ELSEIF (salph1 < salph1Old AND loadflag = 0 AND jumpflag = 1 AND salph1 \leq salph_j2)	
	→initiation of unloading on jump-slope_positive
	→ loadflag = 1
	→ calculate salph_s1, salph_s2 and salph_s3
	→ calculate sM1 on jump-slope_positive
ELSEIF (salph1 < salph1Old AND loadflag = 0 AND jumpflag = 1 AND salph1 > salph_j2)	
	→ initiation of unloading on the post-failure-curve_positive
	→ loadflag = 1

	<ul style="list-style-type: none"> ➔ calculate salph_s1, salph_s2, salph_s3 ➔ calculate sM1 on $\text{post-failure-curve_positive}$
ELSEIF ($\text{salph1} < \text{salph1Old}$ AND $\text{loadflag} = 1$ AND $\text{salph1} \geq \text{salph_s2}$)	
	➔ unloading on slope_positive
	➔ calculate sM1 on slope_positive
ELSEIF ($\text{salph1} < \text{salph1Old}$ AND $\text{loadflag} = 1$ and $\text{salph1} < \text{salph_s2}$)	
	➔ unloading on $\text{unloading-curve_positive}$
	➔ calculate sM1 on $\text{unloading-curve_positive}$
ELSEIF ($\text{salph1} \geq \text{salph1Old}$ AND $\text{loadflag} = 1$ AND $\text{salph1} < \text{salph_s2}$)	
	➔ initiation of reloading on the $\text{unloading-curve_positive}$
	<ul style="list-style-type: none"> ➔ $\text{loadflag} = 2$ ➔ calculate salph_s4 and salph_s5 ➔ calculate sM1 on $\text{unloading-curve_positive}$
ELSEIF ($\text{salph1} \geq \text{salph1Old}$ AND $\text{loadflag} = 1$ AND $\text{salph1} \geq \text{salph_s2}$)	
	➔ initiation of reloading on slope_positive
	<ul style="list-style-type: none"> ➔ $\text{loadflag} = 2$ ➔ calculate sM1 on slope_positive
ELSEIF ($\text{salph1} \geq \text{salph1Old}$ AND $\text{loadflag} = 2$ AND $\text{salph1} \leq \text{salph_s5}$)	
	➔ reloading on slope_positive (between salph_s4 and salph_s5)
	➔ calculate sM1 on slope_positive
ELSEIF ($\text{salph1} \geq \text{salph1Old}$ AND $\text{loadflag} = 2$ AND $\text{salph1} > \text{salph_s5}$ AND $\text{salph1} \leq \text{salph_s3}$)	
	➔ reloading on $\text{reloading-curve_positive}$
	➔ calculate sM1 on $\text{reloading-curve_positive}$
ELSEIF ($\text{salph1} \geq \text{salph1Old}$ AND $\text{loadflag} = 2$ AND $\text{salph1} > \text{salph_s3}$ AND $\text{salph1} \leq \text{salph_s1}$)	
	➔ reloading on slope_positive

	➔ calculate sM1 on slope_positive
ELSEIF (salph1 \geq salph1Old AND loadflag = 2 AND salph1 > salph_s1)	
	➔ back on the post-failure-curve_positive
	➔ loadflag = 0
	➔ calculate sM1 on the post-failure-curve_positive
ELSEIF (salph1 < salph1Old AND loadflag = 2 AND salph_s4 \leq salph1 \leq salph_s5)	
	➔ initiation of unloading on slope_positive (between salph_s4 and salph_s5)
	➔ loadflag = 5
	➔ calculate sM1 on slope_positive (between salph_s4 and salph_s5)
ELSEIF (salph1 < salph1Old AND loadflag = 5 AND salph_s4 \leq salph1 \leq salph_s5)	
	➔ unloading on slope_positive (between salph_s4 and salph_s5)
	➔ calculate sM1 on slope_positive (between salph_s4 and salph_s5)
ELSEIF (salph1 < salph1Old AND loadflag = 5 AND salph1 < salph_s4)	
	➔ unloading back on unloading-curve_positive
	➔ loadflag = 1
	➔ calculate sM1 on unloading-curve_positive
ELSEIF (salph1 \geq salph1Old AND loadflag = 5 AND salph_s2 \leq salph1 \leq salph_s5)	
	➔ again reloading on slope_positive (between salph_s4 and salph_s5)
	➔ loadflag = 2
	➔ calculate sM1 on slope_positive (between salph_s4 and salph_s5)
ELSEIF (salph1 < salph1Old AND loadflag = 2 AND salph_s5 < salph1 \leq salph_s3)	
	➔ initiation of unloading on reloading-curve_positive
	➔ loadflag = 6
	➔ calculate salph_s6 and salph_s7
	➔ calculate sM1 on reloading-curve_positive
ELSEIF(salph1 < salph1Old AND loadflag = 6 AND salph_s7 \leq salph1 \leq salph_s6)	

	→ unloading on slope_positive (between salph_s6 and salph_s7)
	➔ calculate sM1 on slope_positive (between salph_s6 and salph_s7)
ELSEIF (salph1 < salph1Old AND loadflag = 6 AND salph1 < salph_s7)	
	→ unloading back on unloading-curve_positive
	➔ loadflag = 1
	➔ calculate sM1 on unloading-curve_positive
ELSEIF (salph1 ≥ salph1Old AND loadflag = 6 AND salph_s7 ≤ salph1 ≤ salph_s8)	
	→ again reloading on slope_positive (between salph_s7 and salph_s6)
	➔ loadflag = 2
	➔ salph_s5 = salph_s6
	➔ salph_s4 = salph_s7
	➔ calculate sM1 on slope_positive (between salph_s6 and salph_s7)
ELSEIF (salph1 < salph1Old AND loadflag = 2 AND salph_s2 ≤ salph1 ≤ salph_s1)	
	→ unloading on slope_positive (between salph_s1 and salph_s2)
	➔ loadflag = 1
	➔ calculate sM1 on slope_positive (between salph_s1 and salph_s2)
### Additional loops for zero crossing: ###	
ELSEIF (salph1 > salph1Old AND loadflag = 3 AND salph1 ≤ salph_s2)	
	→ unloading on slope_negative
	➔ calculate sM1 on slope_negative
ELSEIF (salph1 > salph1Old AND loadflag = 3 AND salph1 > salph_s2)	
	→ unloading on unloading-curve_negative
	➔ calculate sM1 on unloading-curve_negative
ELSEIF(salph1 ≤ salph1Old AND loadflag = 3 AND salph1 < salph_s2)	
	→ initiation of reloading on unloading-curve_negative
	➔ loadflag = 4

	<ul style="list-style-type: none"> ➔ calculate salph_s4 and salph_s5 ➔ calculate sM1 on unloading-curve_negative
ELSEIF (salph1 ≤ salph1Old AND loadflag = 3 AND salph1 ≤ salph_s2)	
	➔ initiation of reloading on slope_negative
	➔ calculate sM1 on slope_negative
ELSEIF (salph1 ≤ salph1Old AND loadflag = 4 AND salphs > salph_s5)	
	➔ reloading on slope_negative
	➔ calculate sM1 on slope_negative
ELSEIF (salph1 ≤ salph1Old AND loadflag = 4 AND salph1 ≤ salph_s5)	
	➔ reloading on reloading-curve_negative
	➔ calculate sM1 on reloading-curve_negative
ELSEIF (salph1 > salph1Old AND loadflag = 4 AND salph_s5 ≤ salph1 ≤ salph_s4)	
	➔ initiation of unloading on slope_positive (between salph_s4 and salph_s5)
	<ul style="list-style-type: none"> ➔ loadflag = 7 ➔ calculate sM1 on slope_negative (between salph_s4 and salph_s5)
ELSEIF (salph1 > salph1Old AND loadflag = 7 AND salph_s5 ≤ salph1 ≤ salph_s4)	
	➔ unloading on slope_negative (between salph_s4 and salph_s5)
	➔ calculate sM1 on slope_negative (between salph_s4 and salph_s5)
ELSEIF (salph1 > salph1Old AND loadflag = 7 AND salph_s4 < salph1)	
	➔ unloading back on unloading-curve_negative
	<ul style="list-style-type: none"> ➔ loadflag = 3 ➔ calculate sM1 on unloading-curve_negative
ELSEIF (salph1 ≤ salph1Old AND loadflag = 7 AND salph_s5 ≤ salph1 ≤ salph_s4)	
	➔ again reloading on slope_negative (between salph_s4 and salph_s5)
	<ul style="list-style-type: none"> ➔ loadflag = 4 ➔ calculate sM1 on slope_negative (between salph_s4 and salph_s5)

ELSEIF ($\text{salph1} > \text{salph1Old}$ AND $\text{loadflag} = 4$ AND $\text{salph_s3} \leq \text{salph1} \leq \text{salph_s5}$)	
	→ initiation of unloading on reloading-curve_negative
	→ $\text{loadflag} = 8$ → calculate salph_s6 and salph_s7 → calculate sM1 on reloading-curve_negative
ELSEIF ($\text{salph1} > \text{salph1Old}$ AND $\text{loadflag} = 8$ AND $\text{salph_s6} \leq \text{salph1} \leq \text{salph_s7}$)	
	→ unloading on slope_negative (between salph_s6 and salph_s7)
	→ calculate sM1 on slope_negative (between salph_s6 and salph_s7)
ELSEIF ($\text{salph1} > \text{salph1Old}$ AND $\text{loadflag} = 8$ AND $\text{salph1} > \text{salph_s7}$)	
	→ unloading back on unloading-curve_negative
	→ $\text{loadflag} = 3$ → calculate sM1 on unloading-curve_negative
ELSEIF ($\text{salph1} \leq \text{salph1Old}$ AND $\text{loadflag} = 8$ and $\text{salph_s6} \leq \text{salph1} \leq \text{salph_s7}$)	
	→ again reloading on slope_negative (between salph_s7 and salph_s6)
	→ $\text{loadflag} = 4$ → $\text{salph_s5} = \text{salph_s6}$ → $\text{salph_s4} = \text{salph_s7}$ → calculate sM1 on slope_negative (between salph_s6 and salph_s7)

A3.4. Definition of the reference model

The reference model used for the verification of the user element considers a frame-stringer-skin component similar to the numerical model that was used in the scope of the investigations of chapter 4.

A non-curved frame segment is defined in this model with a LCF-shaped frame profile of typical static sizing according to the given profile in Figure 4-5e) of chapter 4. This is a frame profile with flange widths of $w_{IFF} = 25$ mm, $w_{MFF} = 15$ mm and $w_{OFF} = 28$ mm. The flange thicknesses are $t_{IFF} = 2.5$ mm for the inner and middle flange as well as $t_{OFF} = 1.5$ mm for the outer flange. The inner frame web height is $h_{IFW} = 56$ mm, the outer frame web height $h_{OFW} = 36$ mm. Typical layup definitions based on a static sizing were used in the frame web ($[0/75/25]$) as well as in the frame flanges ($[45/45/10]^1$). The width of the model is based on a generic frame pitch of $w_F = 635$ mm. The length of the model is $l = 700$ mm. Three omega stringers with a stringer pitch of $l_s = 168$ mm are modelled with beam elements according to the Kinematics Model approach. The skin thickness was defined with $t_s = 2.125$ mm and a layup of $[10/70/20]^2$. The orthotropic material formulations used in this model were defined linear-elastically. The connection of the individual parts was assumed to be ideal so that tied constraints were used. Symmetry boundary conditions were defined on lateral side. Both ends of the model were clamped using rigid bodies. These rigid bodies include the frame as well as the skin. In several verification runs pure rotation as well as a combination of rotation and translation was specified at the reference nodes of the rigid bodies which were positioned in the centre of area of the cross-section of frame and skin.

Summarising the definition of the reference model, a typical frame-stringer-skin component was modelled with a discretisation technique according to the final kinematic hinge architecture which is given in paragraph 4.7. In contrast to this kinematic hinge architecture the user element was implemented additionally for representation of the hinge behaviour. Figure A3-4 depicts the reference model.

All verification simulations of the reference model (as well as of the quasi-single element model) were performed on a Microsoft Windows machine with the FE solver ABAQUS, solver versions V6.7-3, V6.8-1 and V6.9-1, using explicit time integration and double precision. For compilation and implementation of the user element the Intel FORTRAN Compiler version 10.1.014 as well as Microsoft Visual Studio 2005 were used.

¹ With respect to layups in the frame: Ratios in percent of ply orientation in the layup: $[0^\circ/\pm 30^\circ/90^\circ]$

² Ratios in percent of ply orientation in the layup: $[0^\circ/\pm 45^\circ/90^\circ]$

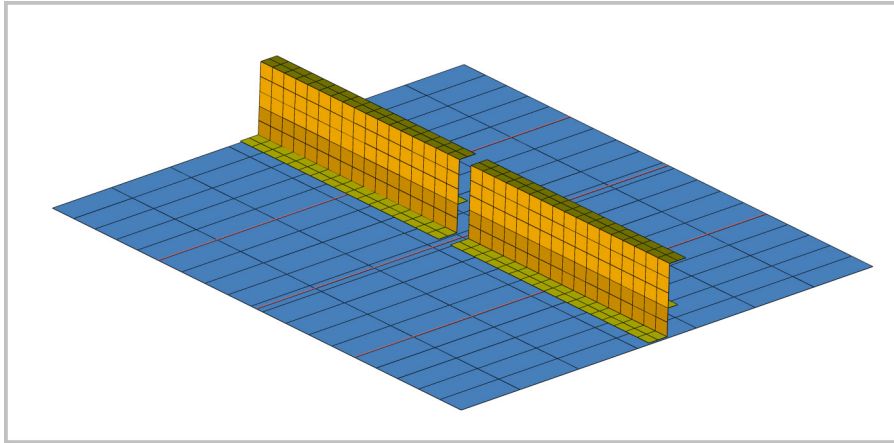


Figure A3-4: Reference model for the verification of the user element

A4. Appendix of chapter 6

Paragraph A4.1 provides a detailed definition of the simulation model used in the scenario assessment study. Further simulation results are given in paragraph A4.2, in particular results of the robustness analyses are provided here.

A4.1. Definition of the fuselage design and the Kinematics Model used for the crash scenario assessment

This paragraph provides additional data of the Kinematics Model which was used for the crash scenario assessment. Figure A4-1 displays this FE model that comprises a two-frame fuselage section. The section length is one frame pitch of $l_{FP} = 533\text{mm}$ plus 100 mm overlap at the front and rear end. Symmetry boundary conditions are defined at both ends. One row of two triple-seats is positioned in the middle of the section.

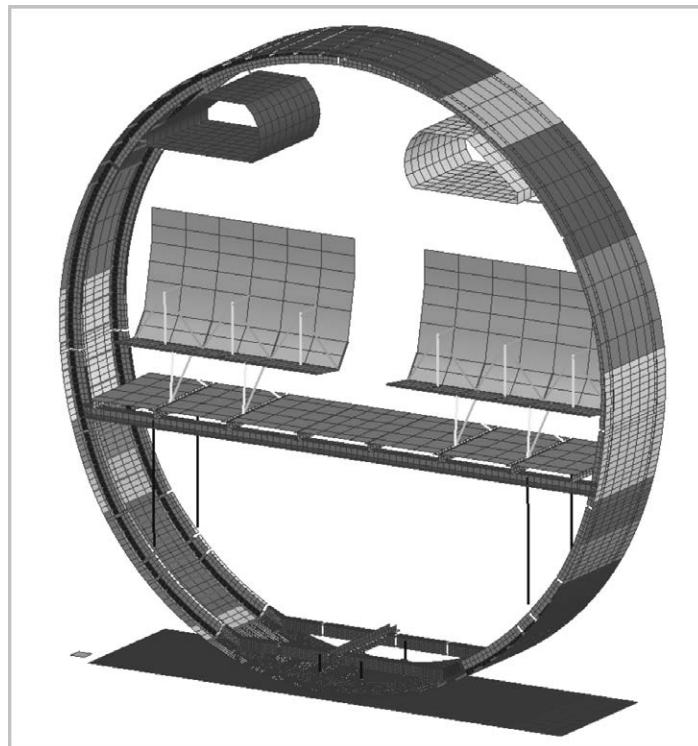


Figure A4-1: Kinematics Model used for the scenario assessment

The fuselage geometry corresponds to the cross-section of an Airbus A320 aircraft. Secondary structural parts like passenger crossbeams, seatrails, floorpanels, rollertracks and overhead bins are defined similarly to the A320 design. The primary structural parts were designed in CFRP material and sized according to several ground and flight load cases as well as dynamic load

cases. The design as well as the sizing was provided by the project partner Airbus. The skin was designed quasi-isotropic with thicknesses between $t_s = 1.6\text{--}4.0$ mm. The LCF-shaped frame design describes frame heights of the inner C-part between $H_{IFW} = 50\text{--}60$ mm. The frame inner flange width is defined between $w_{IFF} = 25\text{--}30$ mm, the frame middle flange with $w_{MFF} = 20.8$ mm. The cargo-crossbeam is designed with high stiffness to enable sub-cargo crushing. The τ -shaped cross-section has a height of $H_{CCB} = 80\text{ mm}$, an upper flange width of $w_{UF} = 60$ mm and a lower flange width of $w_{LF} = 30$ mm. The layup of the frame and the cargo-crossbeam web is defined with $[0/100/0]^1$. The layup of the frame and the cargo-crossbeam flanges is defined between $[45/55/0]$ and $[60/40/0]$. Elastic properties of CFRP UD material were used to model these structural parts:

$$E11=130\text{ GPa}, E22=9\text{ GPa}, G12=4.5\text{ GPa}, \nu=0.3, \rho=1.6\text{ kg/m}^3$$

Omega as well as blade stringers were designed of CFRP material and were represented in the simulation model by beam elements of equivalent stiffness.

The positions of the macro elements are displayed in Figure A4-2. The kinematic hinge positions correspond to potential frame failure locations according to the investigation described in paragraph 4.1. The lateral position of the vertical support struts corresponds to the A320 design and is defined with $y = \pm 1353$ mm. The sub-cargo absorbers are located at a lateral position of $y = \pm 150$ mm.

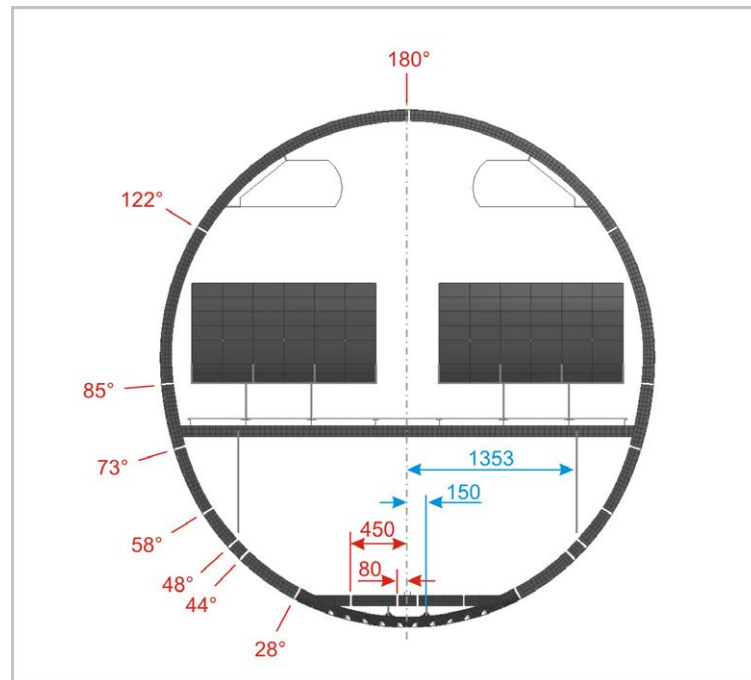


Figure A4-2: Positions of the macro elements

¹ Layup orientation in percent: $[0^\circ/\pm 45^\circ/90^\circ]$

A4.1.1. Assumptions for the macro input characteristics

The assumptions for the macro input characteristics are based on detailed numerical or experimental investigations which were performed by several project partners. The characteristic of the sub-cargo absorbers was derived from quasi-static crushing tests of half-tube segments which were performed at the DLR in the scope of the European Community funded project CRASURV. In these crushing tests the force level of progressive crushing achieved 80 % of the trigger force. The half-tube segments were equipped with a chamfer trigger. Figure A4-3 compares the macro input characteristic with the test results.

The absorbing characteristic of frame bending was investigated by ONERA using detailed numerical analyses. An energy absorbing mechanism located in the frame inner flange was assumed in this investigation. The frame stability and failure behaviour of different absorbing force levels in the frame inner flange was analysed. From these results a moment-rotation characteristic was derived which reduces the moment level with increasing bending rotation to avoid lateral frame instability. The analysis was performed for an opening hinge rotation. For comparability reasons the same macro input characteristic was used in the Kinematics Model for the closing hinge rotation. Figure A4-4 displays the detailed FE model which was developed by ONERA. In addition, the moment-rotation curve of the numerical simulation as well as the derived absorbing moment-rotation characteristic for the kinematic hinges are depicted.

The crushing characteristic of the vertical support strut is based on experimental investigations performed by EADS-IW. The crash device concept is pictured in Figure A4-5. Shear pins provide the connection between CFRP strut and the metallic crash device which is connected to the fuselage structures with a bolt. The failure of the shear pins describes the first peak in the force-deflection characteristic. A small gap inside the crash device decouples the trigger mechanism and the absorbing mechanism. This gap leads to a small crushing distance on very low force level in the characteristic. A second peak is caused by the impact of the CFRP strut on the deflection ring followed by a cutting process which describes a constant force plateau. The second force peak can be modified by the design of the deflection ring and should provide a force level which is below the first force peak. Figure A4-5 displays the crushable strut concept, the experimental force-deflection result as well as the corresponding macro input characteristic.

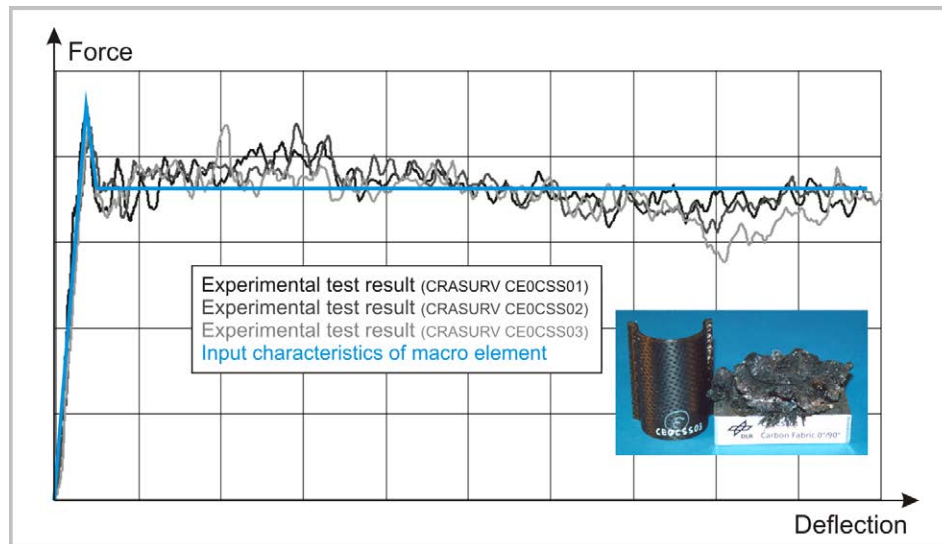


Figure A4-3: Derivation of the sub-cargo macro input characteristic from crushing test results [136]

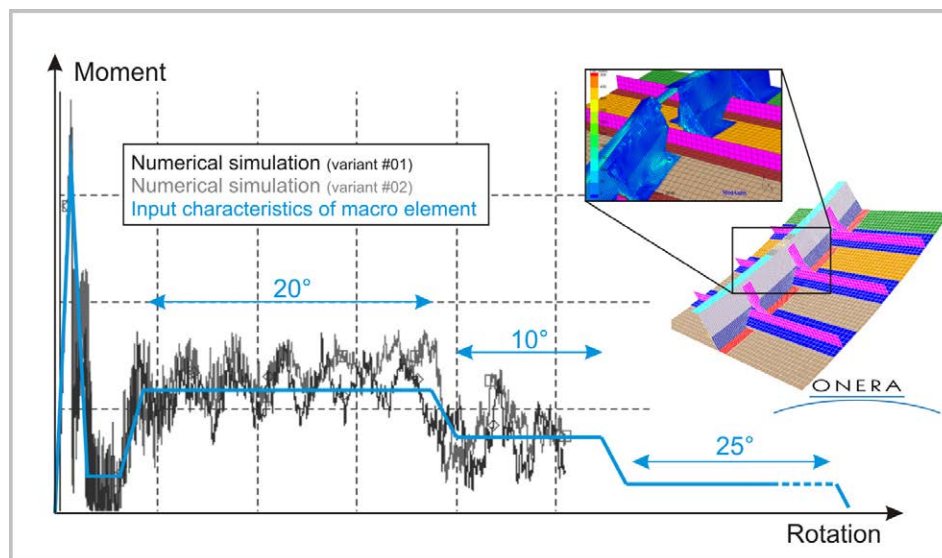


Figure A4-4: Derivation of the absorbing kinematic hinge characteristic from detailed FEM analyses [121]

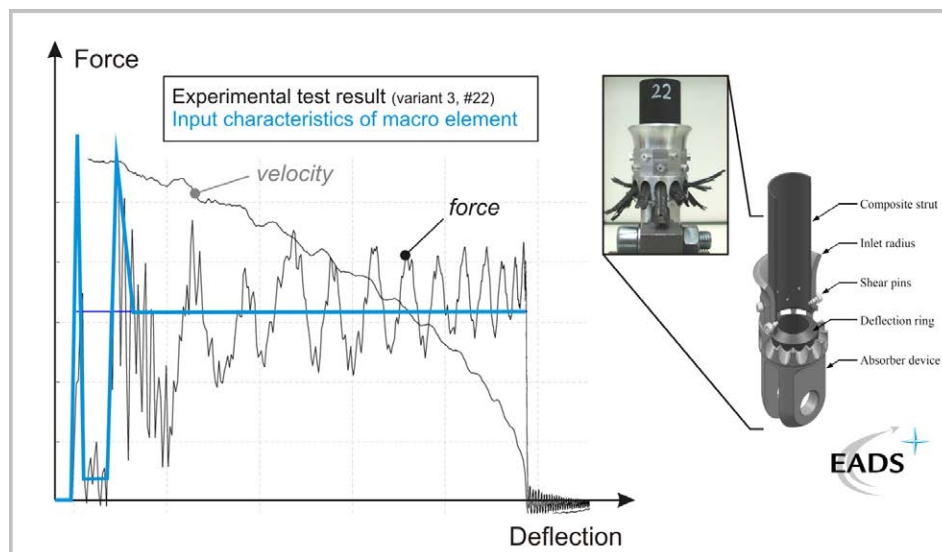


Figure A4-5: Derivation of the crushable strut characteristic from experimental test results [122]

A4.1.2. Numerical parameters

The Kinematics Model used in the crash scenario assessment study contains about 35,000 nodes as well as about 32,000 elements consisting of approximately 29,000 shell elements and approximately 3000 other elements (bars, beams, etc.).

The average mesh size of the primary (elastically modelled) parts are $l_{\text{SkinL}} = 40 \times 100$ mm for the skin of the lower fuselage shell, $l_{\text{SkinU}} = 160 \times 100$ mm for the skin of the upper fuselage shell and $l_{\text{Frame}} = 40$ mm for the frame. The stringer beam elements have an average mesh size of $l_{\text{Stringer}} = 50$ mm.

The simulations of the scenario assessment study were performed with the explicit solver PAM-CRASH V2005.0. The parameterisation of the Kinematics Model comprised 167 design parameters as well as some more dependent parameters. The parameter assignment was realised with the optimisation software PAM-OPT V2004. The simulation jobs were calculated on a Linux cluster (Opteron 250 processors) with parallel execution of four processors in the double precision mode. The simulation time was defined as $t_s = 200$ ms and led to a calculation time of $t_c \approx 27$ h.

A4.2. Further simulation results of the assessment study of the crash scenarios

Further simulation results on the discussion of the scenario assessment are provided within this paragraph. In particular results of the robustness analyses are given in the sub-paragraphs A4.2.5 and A4.2.6.

A4.2.1. Change of sign of the moment load in the frame of scenario B

In scenario B a change of sign in the moment load acting on the frame in the region of the coupling to the cargo-crossbeam is caused by the triggering of the kinematic hinge positioned below the vertical strut connection. Figure A4-6 illustrates the moment loads of both kinematic hinges. The plots identify almost simultaneously triggering of both kinematic hinges. After brittle failure of the upper kinematic hinge the moment in the lower kinematic hinge changes abruptly and leads to triggering of the lower hinge, too.

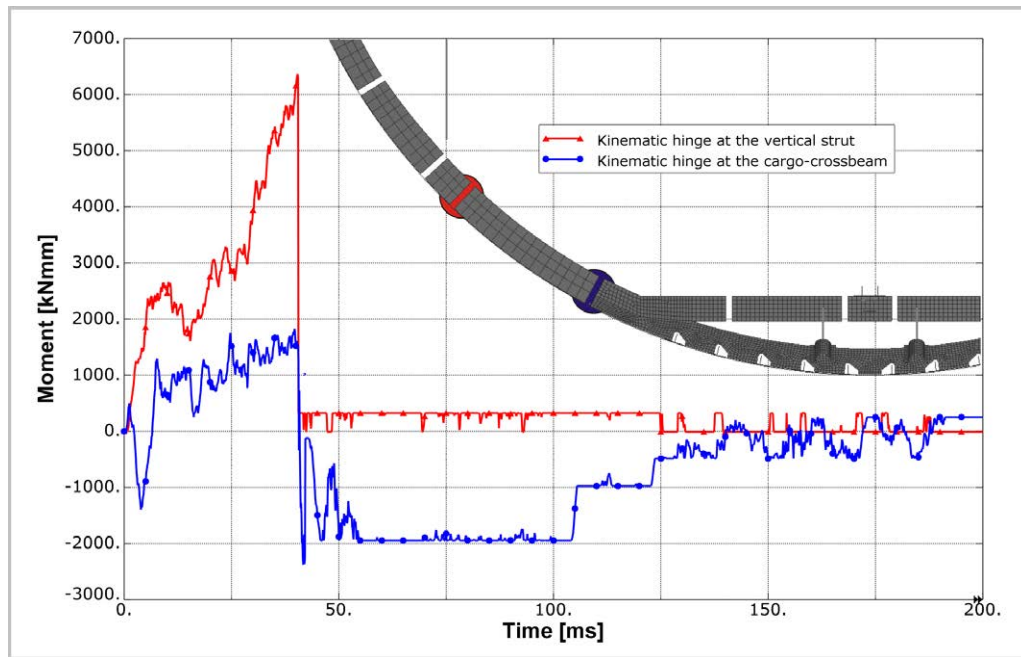


Figure A4-6: Moment loads in the active kinematic hinges of scenario B

A4.2.2. Rotation angle of the absorbing kinematic hinges in both scenarios

The difference in the maximum rotation angle of the absorbing kinematic hinges in both scenarios is depicted in Figure A4-7. The closing absorbing frame bending of scenario A reaches a maximum rotation angle of $\varphi_A = 34^\circ$ (0.59 rad). The opening absorbing frame bending of scenario B reaches a maximum rotation angle of $\varphi_A = 43^\circ$ (0.75 rad). The basis of this comparison is the ‘standard crash case’ which is precisely described in paragraph 6.2.

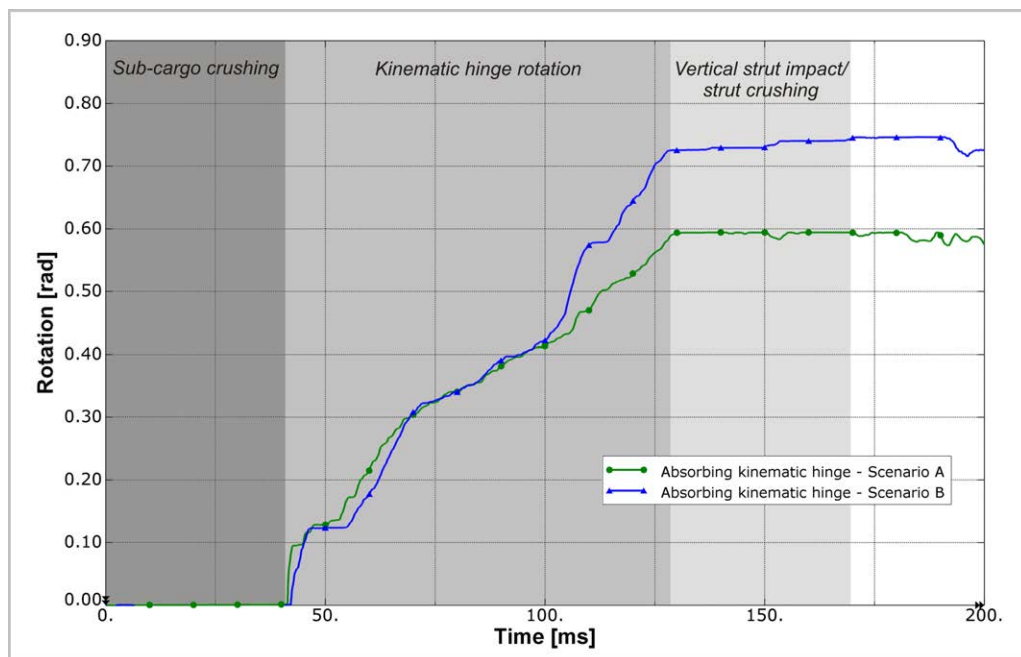


Figure A4-7: Absorbing kinematic hinge rotation of scenario A & B

A4.2.3. Structural load – frame inner flange strains of both scenarios

The frame inner flange strains, as an indicator of the structural loads, identified higher loads along the frame in scenario B. Figure A4-8 displays the frame inner flange strains along the whole frame of scenario A and B. During the first crash phase similar strain values are displayed as expected. The second phase, the frame bending phase, describes the crash sequence where the general crash kinematics develops. Higher strains in case of scenario B are obvious here.

The given strain values of the third crash phase, the vertical support strut crushing, are strongly dependent on the definition of the crushing process in the Bermuda triangle and are not dependent on the general crash kinematics. Hence, structural loads which depend on the crash kinematics have to be assessed with respect to the kinematic hinge rotation phase. The basis of this comparison is the ‘standard crash case’ which is precisely described in paragraph 6.2.

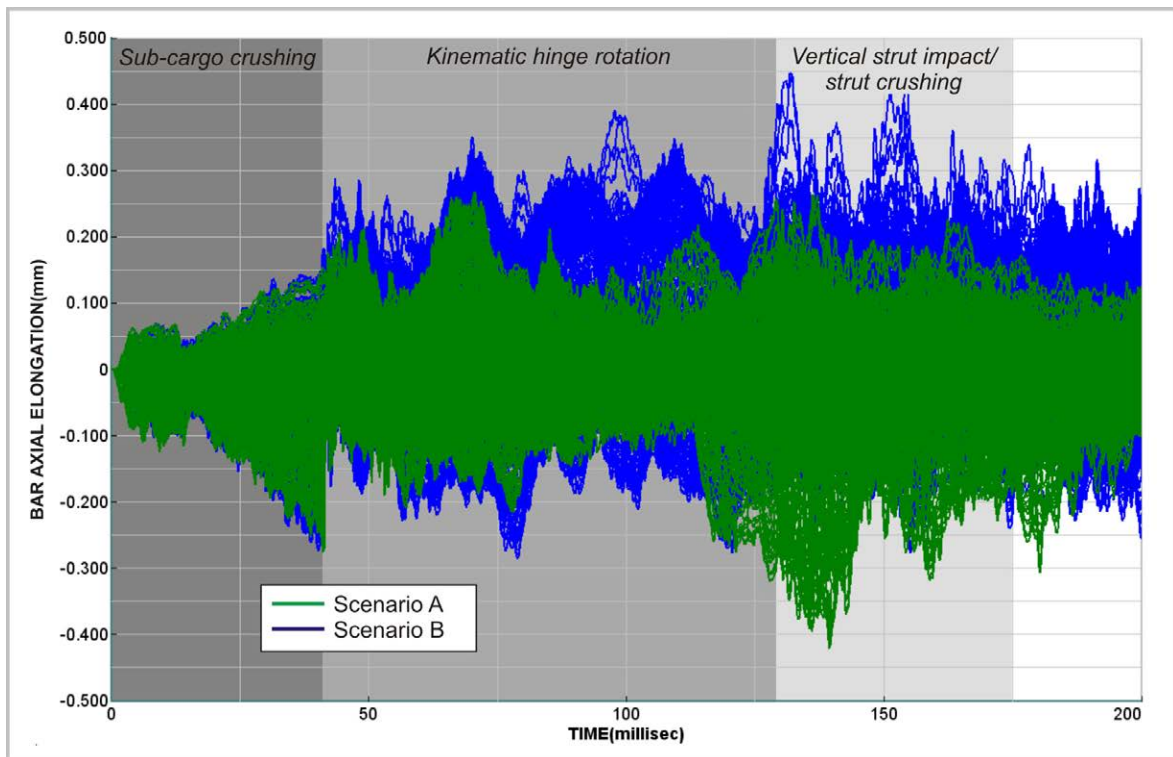


Figure A4-8: Frame inner flange strains of scenario A & B

A4.2.4. Tensile loads in the vertical support struts

In case of scenario B, high tensile loads act in the vertical support struts during the second phase of the kinematic hinge rotation. These tensile loads lead to failure of the vertical struts according to the considered input characteristic of the axial macro element. Figure A4-9 compares the axial load in the vertical support struts of scenario A and B. As the section model provides four vertical support struts, exemplary force-deflection curves of one strut are given here. The basis of this comparison is the ‘standard crash case’ which is precisely described in paragraph 6.2.

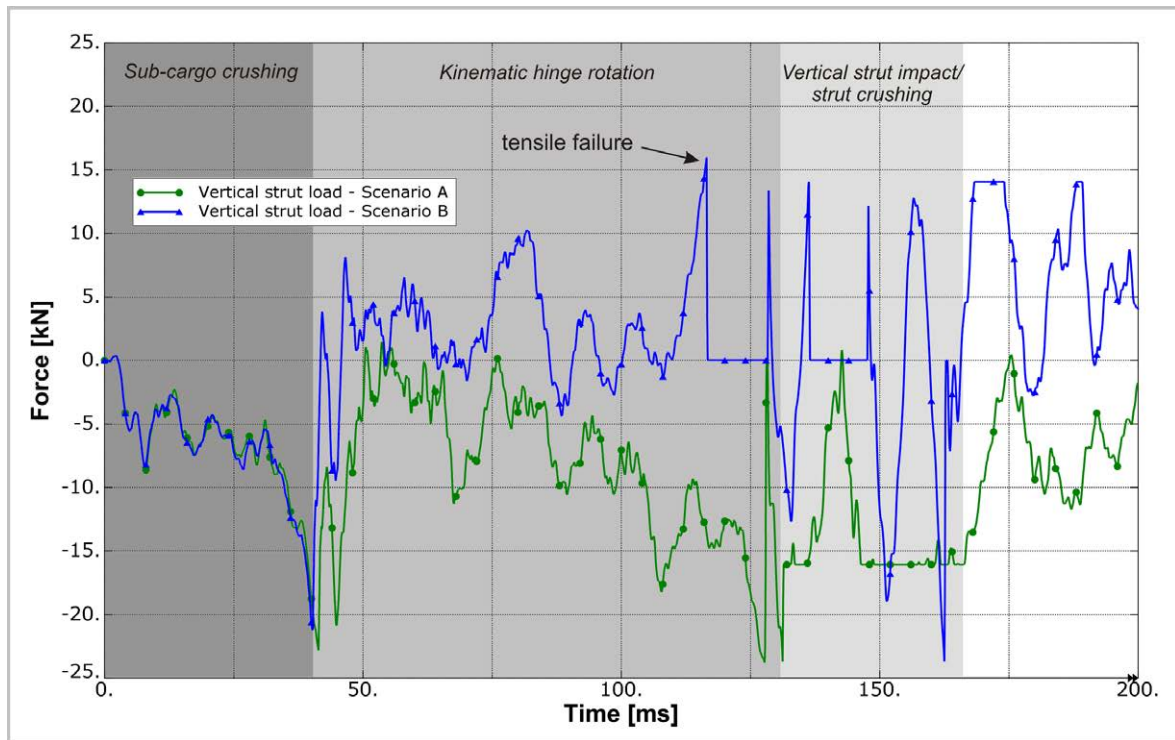


Figure A4-9: Axial load in the vertical support struts of scenario A & B

A4.2.5. Simulation results of the robustness cases for scenario A

In addition to the ‘standard crash case’, further crash load cases were considered in this assessment to determine the robustness of scenario A. These load cases differ from the standard crash case in:

- A 1. a higher initial velocity of $v_i = 9.1$ m/s (30 ft/s),
- A 2. one-sided loading with occupied triple seat and loaded overhead bin at one side combined with free triple seat and unloaded overhead bin at the other side,
- A 3. cargo loading represented by a flat plate with a distributed mass of $m = 745$ kg,
- A 4. a roll angle of $\varphi = 5^\circ$.

The robustness cases of scenario A identified the frame region of the cargo-crossbeam connection as critical with respect to potential opening bending failure. Figure A4-10 compares the moment load in this frame region of different robustness cases with the standard crash case. The robustness cases show more distinct opening bending load (negative moment) compared to the standard crash case. In one robustness case, with a roll angle of $\varphi = 5^\circ$, the moment load exceeded the limit value and frame failure occurred in this kinematic hinge. The depicted moment curves were generated by output definitions of cutting surfaces (SECFO) and consider the frame as well as the skin structure.

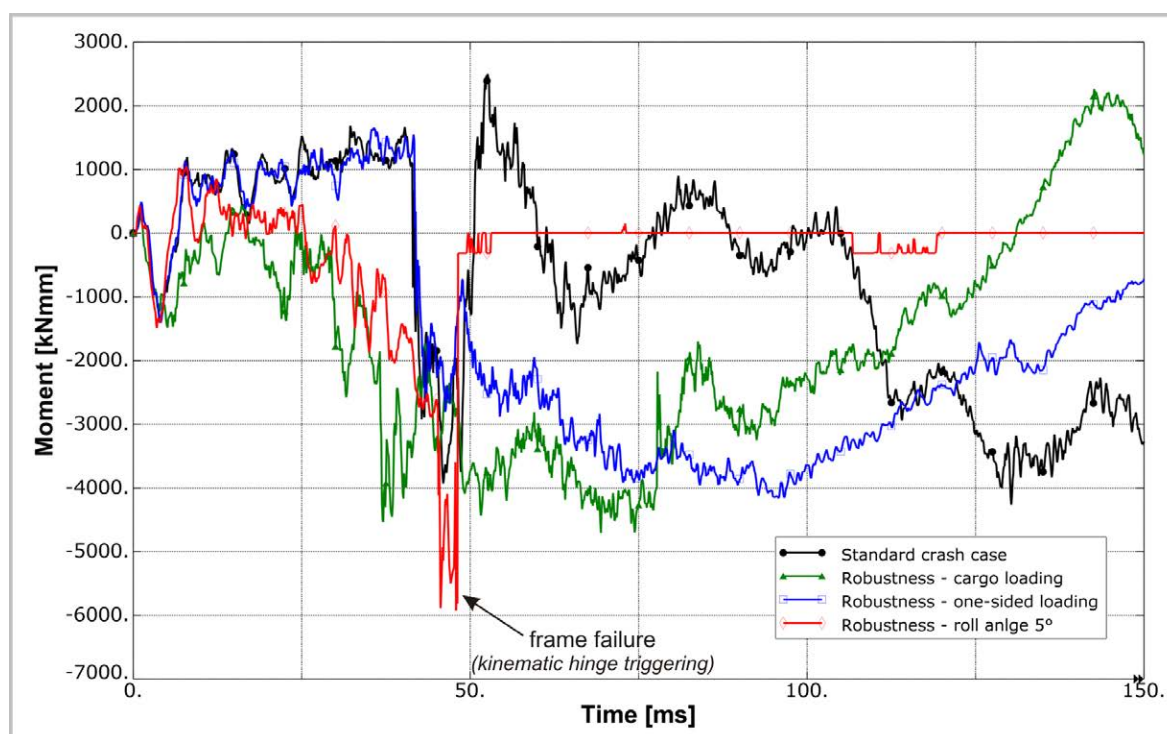


Figure A4-10: Comparison of the moment loads acting in the frame at the region of the cargo-crossbeam connection

In the following figures, the robustness cases of scenario A are briefly documented with the illustration of the crash sequence as well as the energy plot. The diagrams compare the most important energies (total, kinetic and internal energy) of the standard crash case with the energies of the individual robustness case. In particular the difference of the initial kinetic energy in some of the robustness cases compared to the standard crash case is illustrated by this comparison.

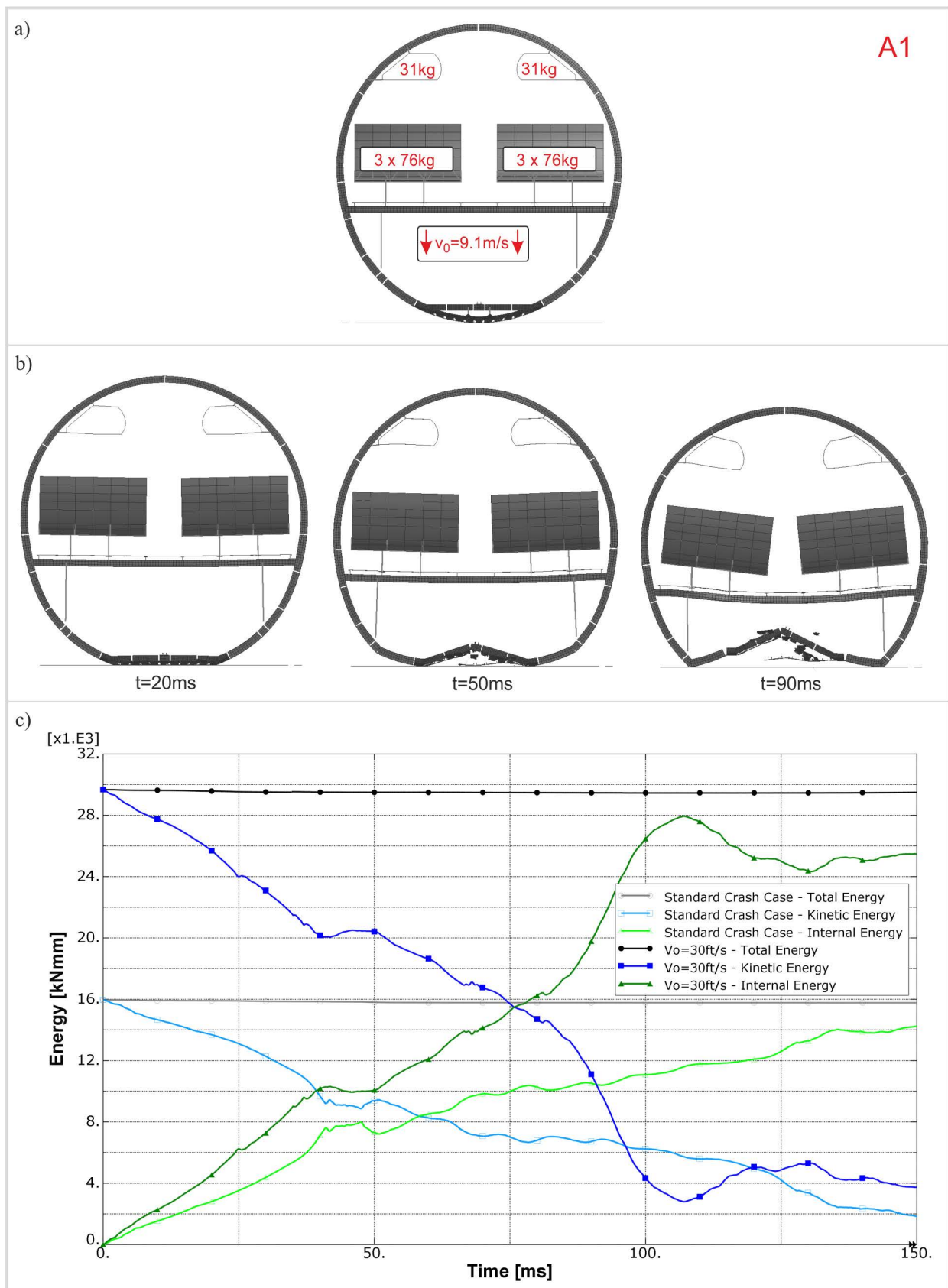
The robustness case with an initial velocity of $v_i = 9.1$ m/s (A1) is given in Figure A4-11. In this robustness case the initial total energy is 84 % higher compared to the standard crash case. A consequence of this increased initial kinetic energy is the more distinct impact of the vertical support struts which is indicated by a steeper decrease of kinetic energy in the last crash phase.

The one-sided loading crash case (A2) is illustrated in Figure A4-12. Due to the reduced mass, respectively reduced initial kinetic energy, the energy absorption capacity in the crash devices is well sufficient. The plot of the kinetic energy is very smooth and shows an elastic rebound effect in the last crash phase.

In Figure A4-13, the crash case with cargo loading (A3) shows a very steep decrease of the kinetic energy in the energy plot after the first crash phase. This decrease of kinetic energy is related to the cargo mass and does not indicate high acceleration values for the passengers. Due to the enormous cargo mass the crash absorbers in the sub-cargo structure are crushed without significant effects on the kinetic behaviour of the above fuselage structure. After this crushing phase the cargo mass impacts on the ground. Hence, a large fraction of the total mass was

decelerated abruptly and caused the steep decrease of the total kinetic energy. The following developing of the kinetic energy is roughly the same as observed in the standard crash case.

The robustness case with a roll angle of $\varphi = 5^\circ$ (A4) is depicted in Figure A4-14. The plot of the total kinetic energy indicates higher energy absorption during the hinge rotation phase compared to the standard crash case, despite of additional brittle frame failure at the cargo-crossbeam connection. The total kinetic energy shows a smooth developing and the overall crash kinematics was achieved.

Figure A4-11: Robustness case A1 - initial velocity of $v_i = 9.1 \text{ m/s}$

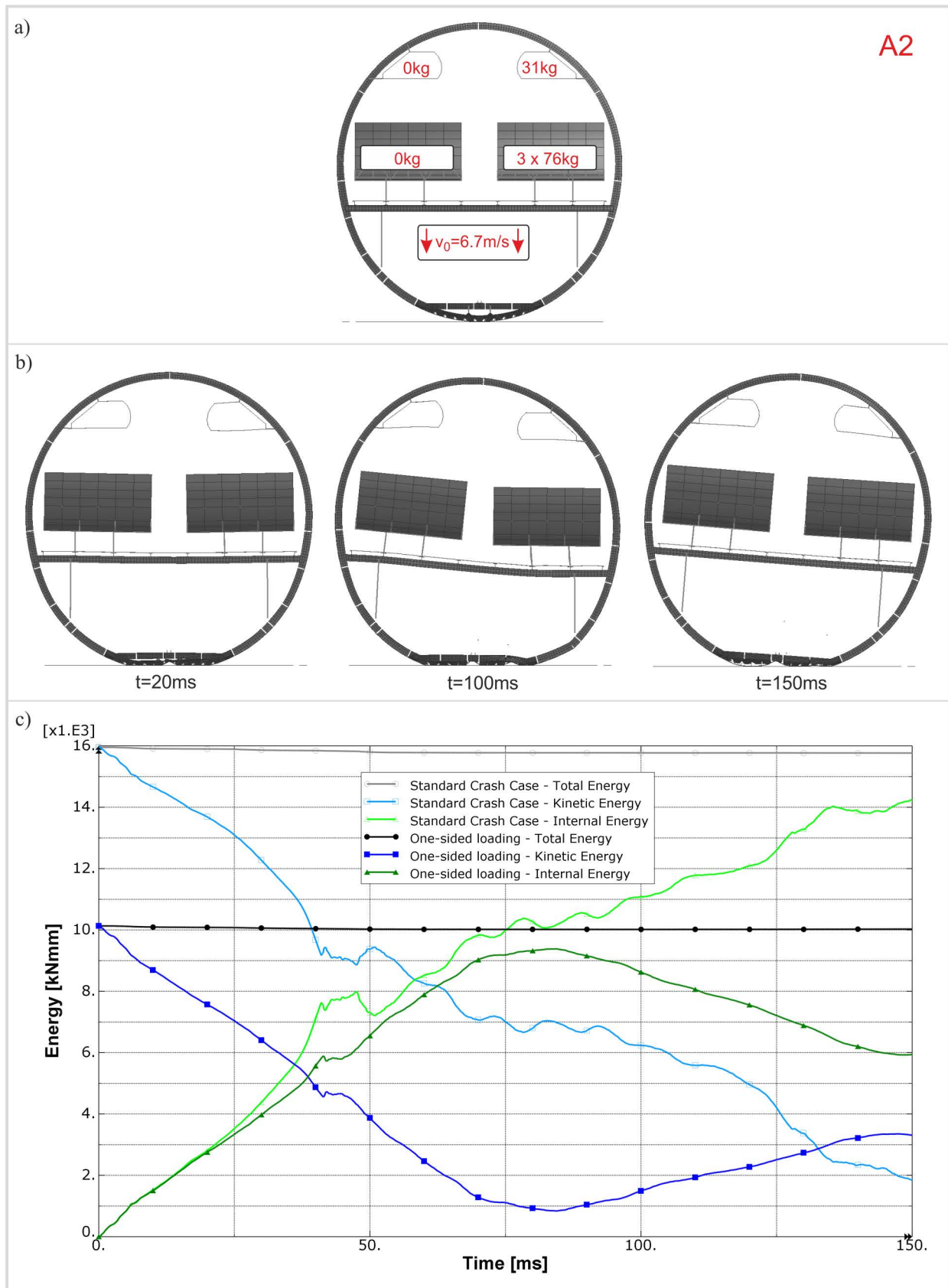


Figure A4-12: Robustness case A2 - one-sided loading

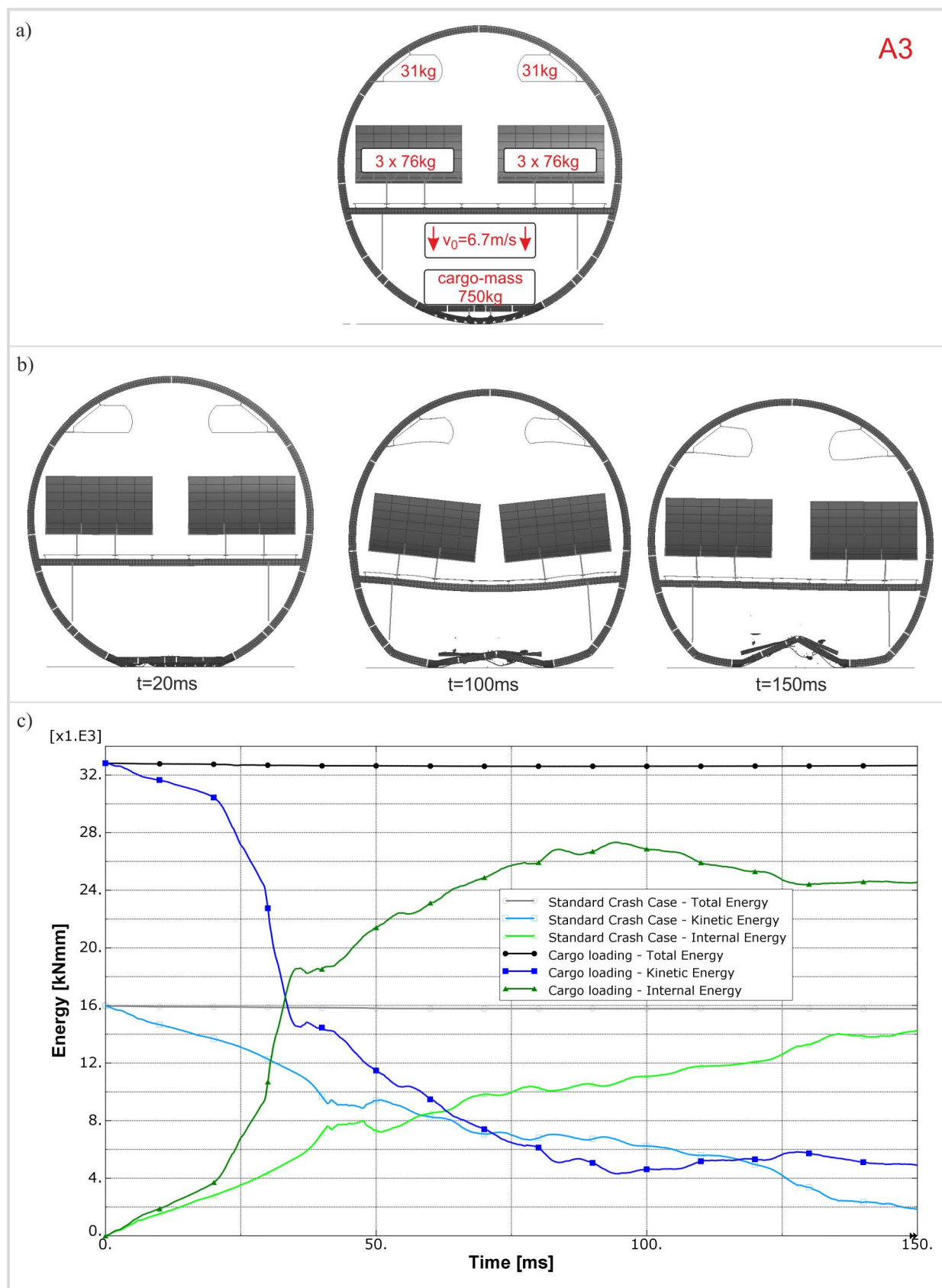
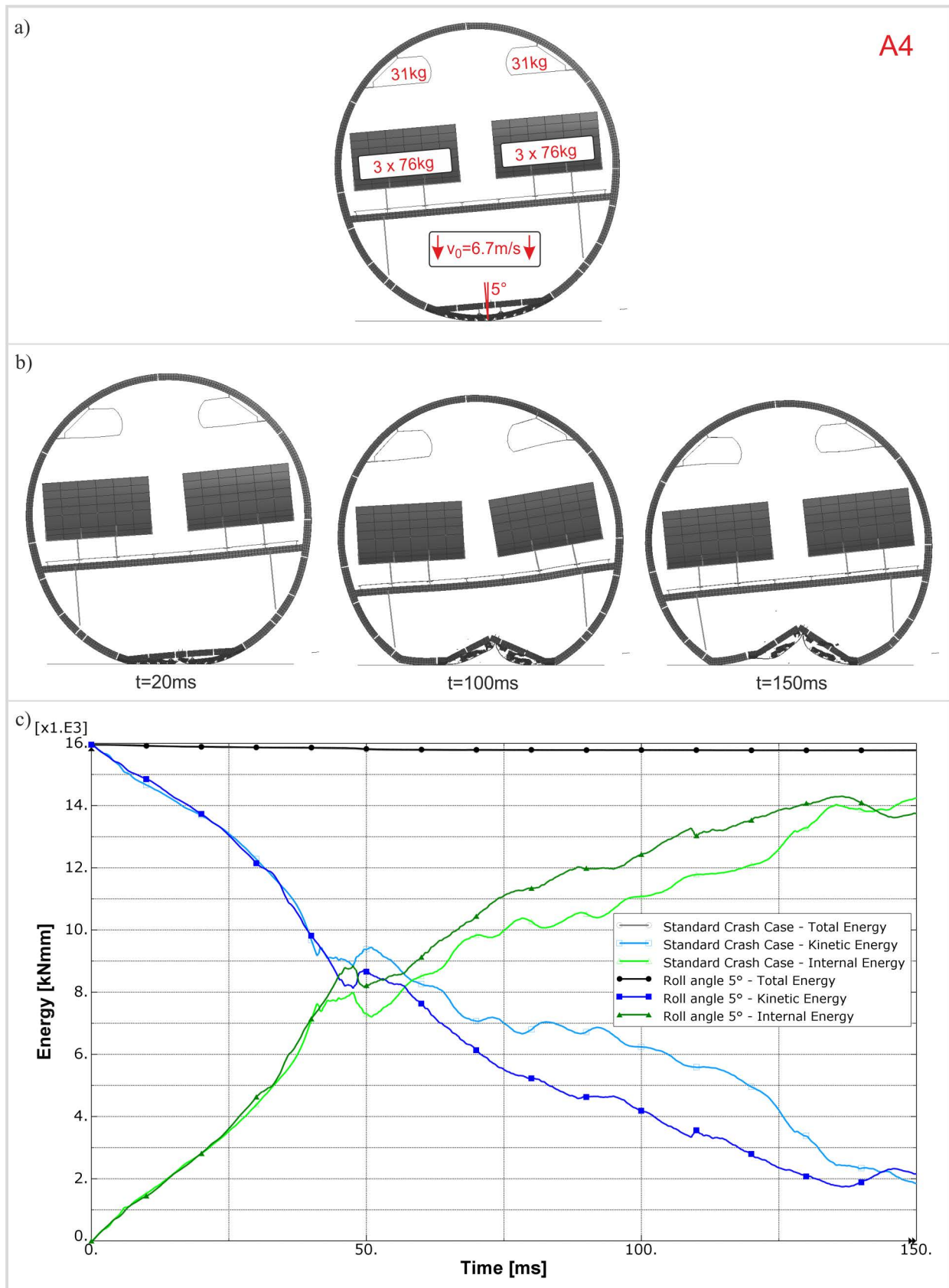


Figure A4-13: Robustness case A3 - cargo loading

Figure A4-14: Robustness case A4 - roll angle of $\varphi = 5^\circ$

A4.2.6. Simulation results of the robustness cases for scenario B

In addition to the 'standard crash case', further crash load cases were considered in this assessment to determine the robustness of scenario B. These load cases differ from the standard crash case in:

- B 1. a higher initial velocity of $v_i = 9.1$ m/s (30 ft/s),
- B 2. one-sided loading with occupied triple seat and loaded overhead bin at one side combined with free triple seat and unloaded overhead bin at the other side,
- B 3. cargo loading represented by a flat plate with a distributed mass of $m = 745$ kg,
- B 4. a roll angle of $\varphi = 5^\circ$.

In the following figures, the robustness cases of scenario B are documented similarly to the robustness cases of scenario A in paragraph A4.2.5. The illustration of the crash sequence as well as the energy plots are given. The diagrams compare the most important energies (total, kinetic and internal energy) of the standard crash case with the energies of the individual robustness case.

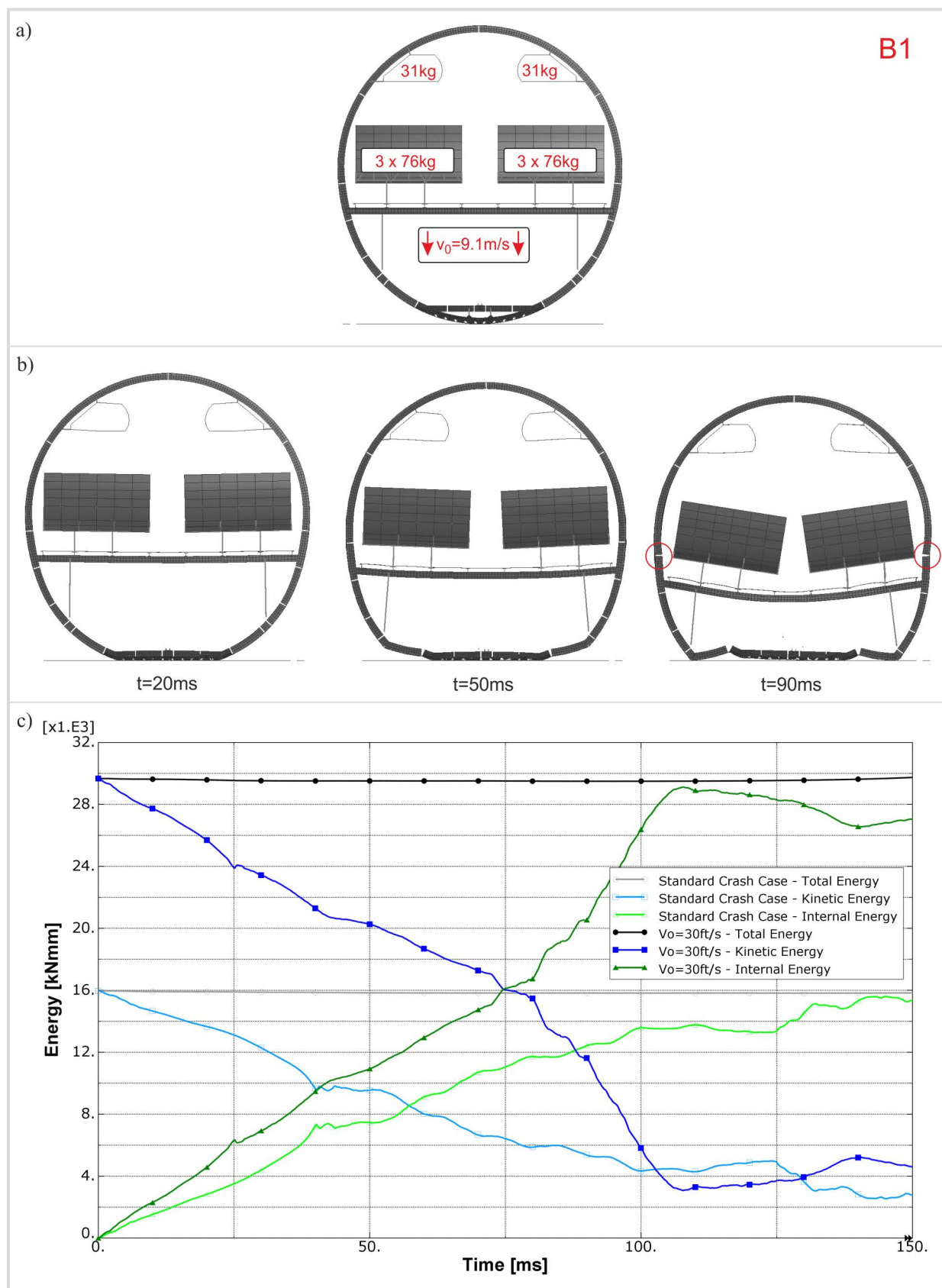
Figure A4-15 illustrates the robustness case with a higher initial velocity of $v_i = 9.1$ m/s (B1). The comparison of total kinetic energies shows approximately a similar slope during the first crash phases in the standard as well as in the robustness case. In the following phase, a steeper decrease of the kinetic energy in the robustness case indicates the impact of the vertical struts. Hence, the difference in the initial kinetic energy was compensated by the vertical support strut crushing. At $t = 90$ ms, the crash sequence in Figure A4-15b) shows opening frame failure of the kinematic hinge that is located directly above the passenger crossbeam. In this robustness case strain exceedance occurred along this fuselage side shell that indicates high danger of additional failure in the cabin area.

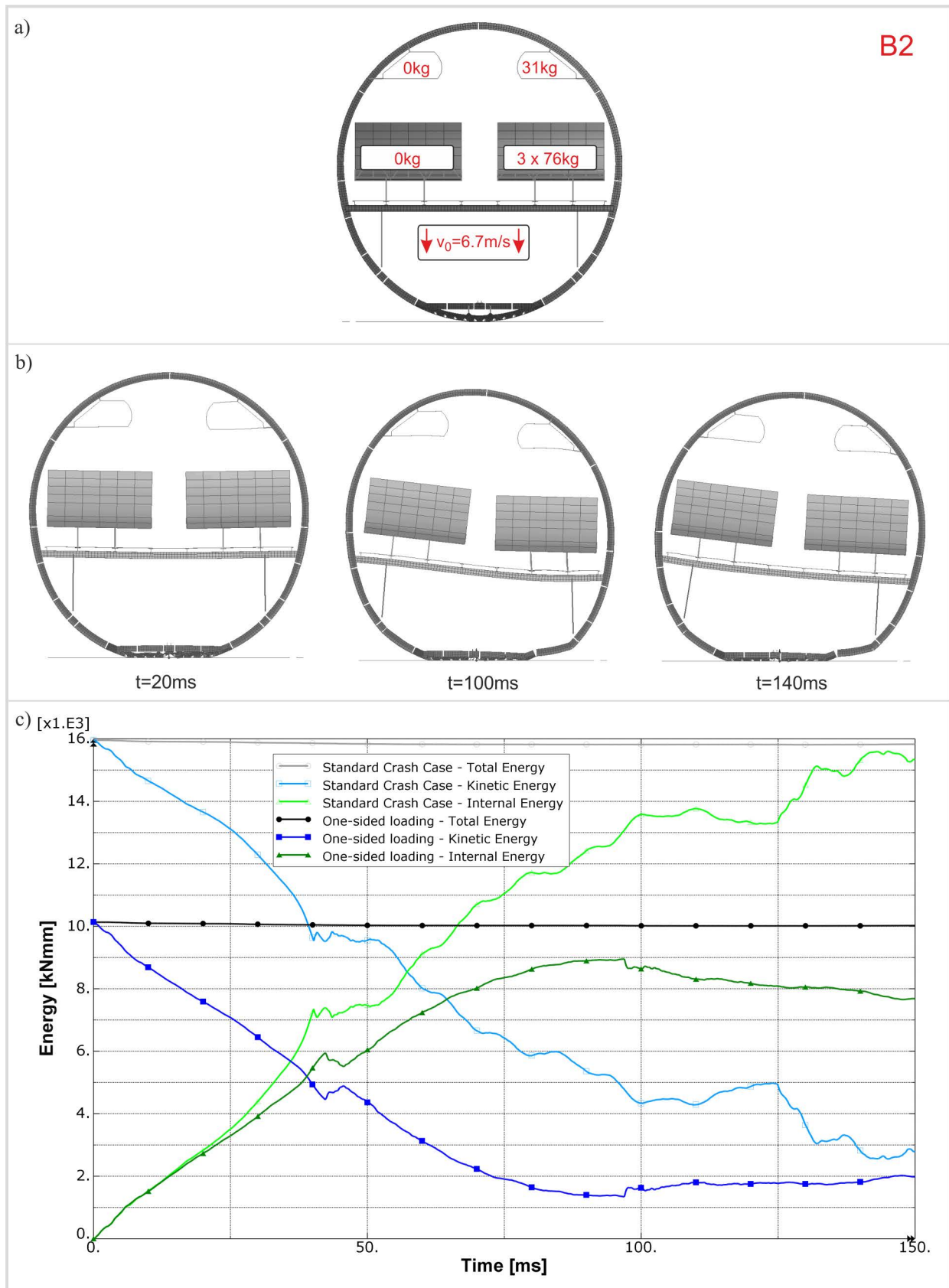
In Figure A4-16, the one-sided loading robustness case (B2) is shown. Due to the reduced mass a smooth developing of the total kinetic energy indicates a well sufficient energy absorption capacity of the crash devices.

In Figure A4-17, the robustness case with cargo loading (B3) depicts a steep decrease of the total kinetic energy which is caused by the ground impact of the cargo mass. This effect was already discussed in paragraph A4.2.5. It was clarified that this decrease of the kinetic energy does not induce high accelerations on the passengers. Nevertheless, the energy absorption of the sub-cargo structure was compensated almost completely by the cargo mass. After the crushing of the

sub-cargo structure with a subsequent ground impact of the cargo mass, the total kinetic energy provides a level that is close to the initial kinetic energy of the standard crash case. The following energy absorption by frame bending is not sufficient and the remaining additional kinetic energy has to be absorbed by vertical support strut crushing. Hence, the impact of the vertical struts is more distinct with the fixed parameter settings and strain exceedance occurred in the fuselage side shell. At $t = 150$ ms, the crash sequence in Figure A4-17b) shows opening frame failure of the kinematic hinges that are located above the passenger crossbeam.

Finally, the robustness case with a roll angle of $\varphi = 5^\circ$ (B4) is given in Figure A4-18. Although the crash sequence shows asymmetric kinematic hinge rotation the general scenario was achieved as frame failure apart of the active kinematic hinges did not occur. The comparison of energies shows similar developing of the graphs of the standard and the robustness crash case.

Figure A4-15: Robustness case B1 - initial velocity of $v_i = 9.1 \text{ m/s}$



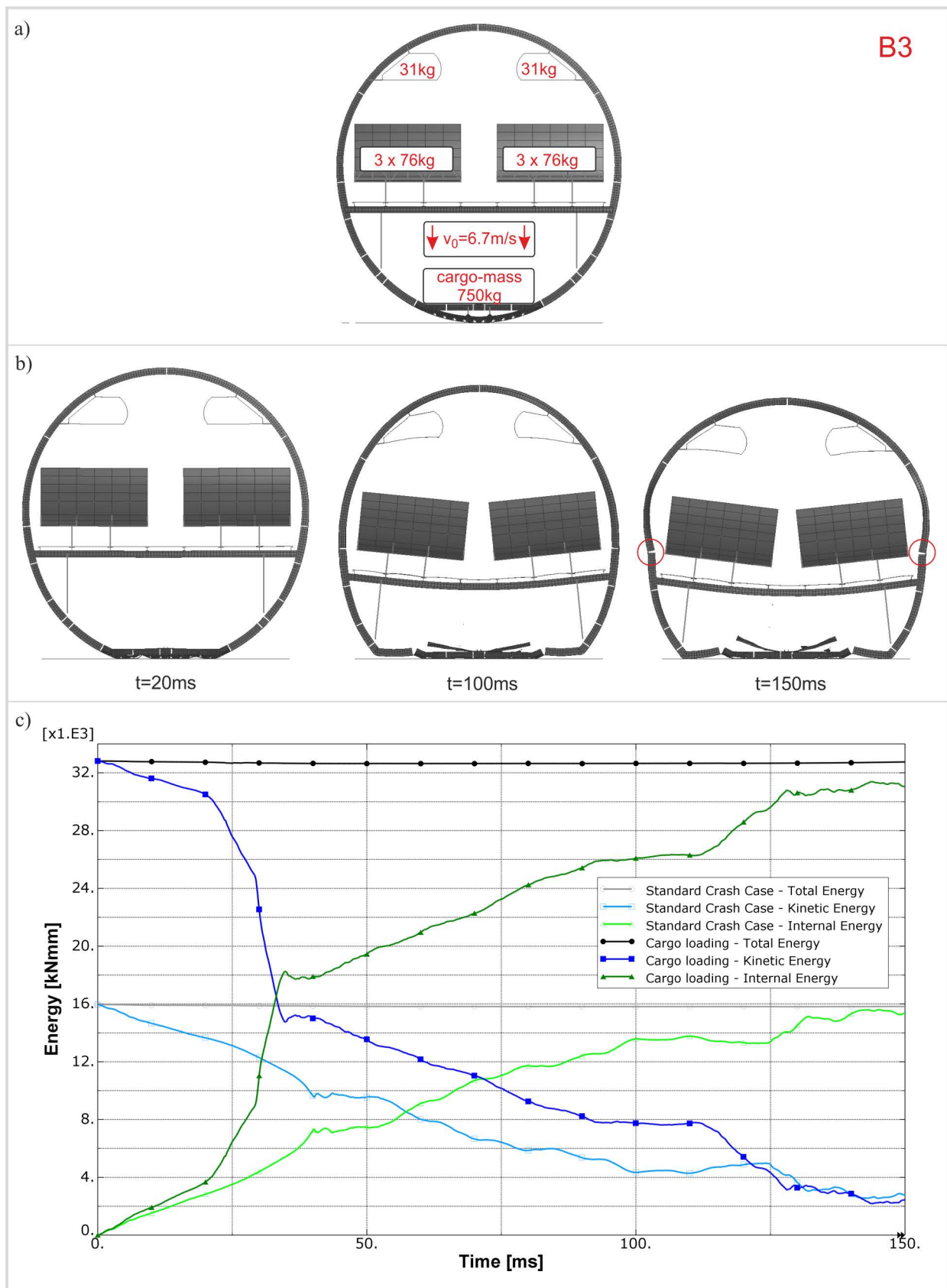
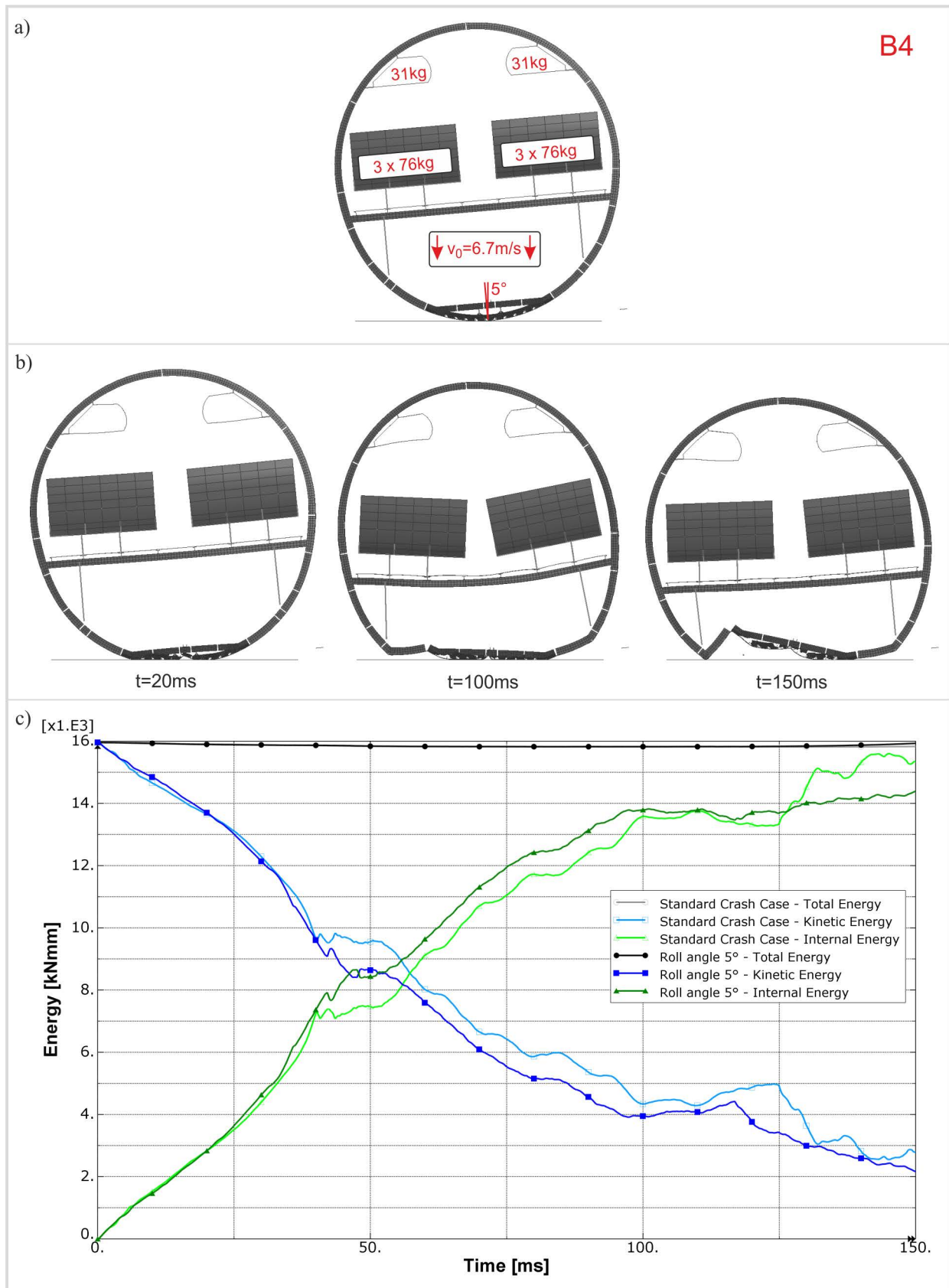


Figure A4-17: Robustness case B3 - cargo loading

Figure A4-18: Robustness case B4 - roll angle of $\phi = 5^\circ$

A5. Appendix of chapter 7

Paragraph A5.1 provides a detailed definition of the simulation model used in the crash scenario development study. Further results of the final crash scenario are given in paragraph A5.2. Paragraph A5.3 provides further results of the simulation work on the ovalisation effect. In paragraph A5.4 a detailed definition of the metallic frame model is provided which was used for the comparison of the final kinematic hinge characteristics. Finally, paragraph A5.5 discusses the axial forces in the vertical support struts of the final crash scenario to derive an appropriate trigger force for an optional energy absorbing strut crushing in some robustness cases.

A5.1. Definition of the fuselage design and the Kinematics Model used for the crash scenario development

Figure A5-1 displays the simulation model that was used for the crash scenario development. The model comprises a two-frame fuselage section. The section length is $L_s = 1270$ mm, which is twice the frame pitch of $l_{FP} = 635$ mm. Hence a full overlap at the front and rear end of half a frame pitch is modelled. Symmetry boundary conditions are defined at both ends. The minimum seat pitch for this fuselage design was defined with $l_{SPmin} = 711$ mm. To combine the frame pitch and the seat pitch in an appropriate way, two rows of triple-seats were installed in the numerical fuselage section, with passenger masses of $m_{PAX} = 68.5$ kg. This passenger mass is 89 % of the typical passenger mass and enables the adjustment of frame and seat pitch in the two-bay fuselage section model.

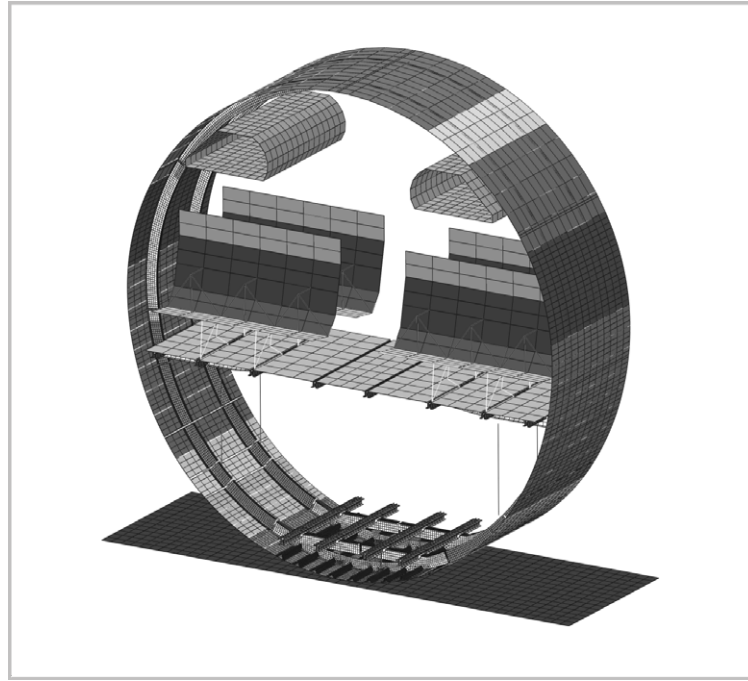


Figure A5-1: Kinematics Model used for the scenario development

The fuselage geometry is similar but not identical to the cross-section of an Airbus A320 aircraft. Secondary parts like passenger crossbeams, cargo rails, seat rails and floor panels represent a new design, partly defined in CFRP material. The overhead bins and seats are represented by standard models. The primary structural parts were designed in CFRP material and pre-sized according to relevant ground and flight load cases. The design and sizing was conducted by the project partner Airbus. The skin was designed with thicknesses between $t_s = 1.6\text{--}2.1$ mm and typical layups of about $[15/60/25]^1$. The elastic properties of the CFRP UD material used to model the skin structure are:

$$E_{11}=130 \text{ GPa}, E_{22}=8.5 \text{ GPa}, G_{12}=4.2 \text{ GPa}, \nu=0.35, \rho=1.6 \text{ kg/m}^3$$

The LCF-shaped frame design describes frame heights of the inner C-part between $H_{IFW} = 56\text{--}66$ mm. The frame inner flange width is defined with $w_{IFF} = 25$ mm, the frame middle flange with $w_{MFF} = 15$ mm. The layup of the frame web is $[0/75/25]^2$ and the frame flanges are defined with a layup of about $[45/45/10]^2$. The elastic properties of the CFRP UD material used to model the frame structure are:

$$E_{11}=135 \text{ GPa}, E_{22}=8.5 \text{ GPa}, G_{12}=4.2 \text{ GPa}, \nu=0.35, \rho=1.6 \text{ kg/m}^3$$

¹ Layup orientation in percent: $[0^\circ/\pm 45^\circ/90^\circ]$

² Layup orientation in percent (with respect to the frame only): $[0^\circ/\pm 30^\circ/90^\circ]$

The cargo-crossbeam is designed with high stiffness to enable sub-cargo crushing (bend-frame concept). The τ -shaped cross-section has a height of $H_{CCB} = 85$ mm, an upper flange width of $w_{UF} = 60$ mm and a lower flange width of $w_{LF} = 30$ mm. The layup of the cargo-crossbeam web is defined with [13/75/13]. The layup of the cargo-crossbeam flanges is defined between [55/36/9] and [63/31/6]. The elastic properties of the CFRP UD material and woven fabric material used to model the cargo-crossbeam structure are:

$$E_{11}=126 \text{ GPa}, E_{22}=9.8 \text{ GPa}, G_{12}=4.9 \text{ GPa}, \nu=0.3, \rho=1.6 \text{ kg/m}^3$$

$$E_{11}=56 \text{ GPa}, E_{22}=56 \text{ GPa}, G_{12}=4.3 \text{ GPa}, \nu=0.06, \rho=1.4 \text{ kg/m}^3$$

The stringer design describes several omega profiles with omega heights between $H_{Str} = 28$ -32 mm. The stringer thickness is defined between $t_{Str} = 1.1$ -1.4 mm with a layup between [44/44/11] and [55/36/9]. The elastic properties of the CFRP UD material used to model the stringer structure are similar to the skin material.

The positions of the macro elements are displayed in Figure A5-2. The kinematic hinge positions correspond to potential frame failure locations according to the investigation of chapter 4.1. The positions were adapted to the slightly changed fuselage section geometry compared to the generic design used in the crash scenario assessment in chapter 6. The new cargo floor design specifies a cargorail system instead of a central rollertrack. Therefore, the kinematic hinge in the cargo-crossbeam could be defined directly in the lateral centre. The lateral position of the vertical support struts corresponds to the A320 design and is defined with $y = \pm 1353$ mm. The sub-cargo absorbers are located at a lateral position of $y = \pm 200$ mm below the inner cargorails.

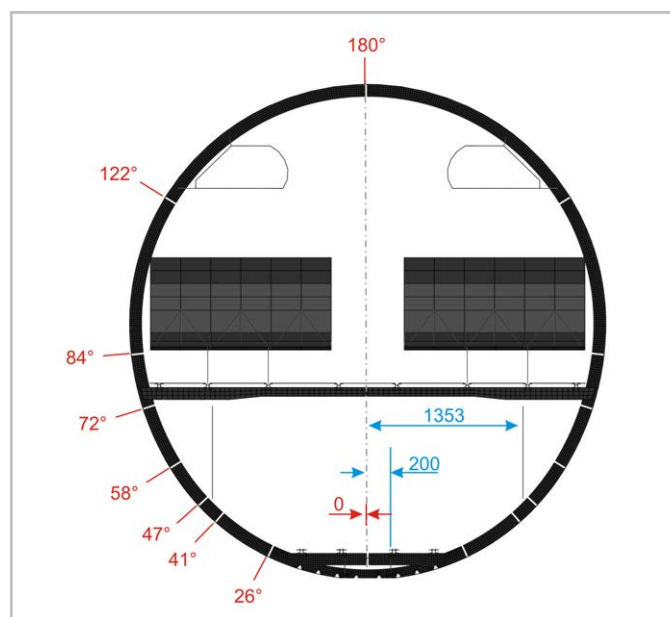


Figure A5-2: Positions of the macro elements

The Kinematics Model of the crash scenario development study is a second generation model. In contrast to the first generation model used for the crash scenario assessment study, all modelling aspects discussed in chapter 4 are implemented. Hence, full accuracy according to the outcomes of chapter 4 is guaranteed in this scenario development. With respect to the kinematic hinge modelling, this second generation model does not include the user element which is described in chapter 5. These advanced modelling capabilities could not be included due to the unsolved issues of the solver bug.

The Kinematics Model for the crash scenario development contains about 56,000 nodes and about 50,000 elements. The average mesh size of the primary (elastically modelled) parts are $l_{\text{SkinL}} = 30 \times 100 \text{ mm}$ for the skin of the lower fuselage shell, $l_{\text{SkinU}} = 190 \times 100 \text{ mm}$ for the skin of the upper fuselage shell and $l_{\text{Frame}} = 20 \text{ mm}$ for the frame. The stringer beam elements have an average mesh size of $l_{\text{Stringer}} = 50 \text{ mm}$.

The simulations for the scenario development study were performed with the explicit solver ABAQUS/Explicit V6.8-1. The parameterisation of the Kinematics Model comprised 74 design parameters as well as 773 dependent parameters. The parameter assignment was realised with the *parameter command in ABAQUS. The simulation jobs were calculated on a Windows machine:

Dell Inc. Precision WorkStation T5400

Processor EM64T Family 6 Model 23 Stepping 6 GenuineIntel ~2993 Mhz

Microsoft(R) Windows(R) Server 2003 Standard x64 Edition (Service Pack 2 Build 3790)

Microsoft Compute Cluster Pack

Parallelisation on domain-level was executed with two domains respectively two processors and double precision. The simulation time was defined with $t_S = 200 \text{ ms}$ and led to a calculation time of $t_C \approx 19 \text{ h}$.

A5.2. Further results of the final crash scenario

The detailed crash sequence of the final crash scenario is given in Figure A5-3.

The diagram in Figure A5-4 compares the moment output of the kinematic hinges with the total internal energy of the final crash scenario. This comparison illustrates the correlation between failure, respectively triggering, of the kinematic hinges and the unsteadiness in the progression of the internal energy caused by the release of elastic energy.

In addition, this diagram provides information about the chronological sequence of the absorbing frame bending. The absorbing rotation in the frame kinematic hinges of $\Delta\phi_{\text{abs}} = 20^\circ$ is spent at a crash state where about 95 % of the final internal energy is reached. Hence, the defined

absorbing rotation of $\Delta\phi_{\text{abs}} = 20^\circ$ corresponds well with the required bending deformation of this crash kinematics.

Finally, the individual moment curves of the kinematic hinges show a good correlation. Thus, the final crash scenario provides a good symmetrical crash kinematics with identical bending mechanisms in both cargo-crossbeams as well as in the frames on both sides.

The structural loads in the frames are presented in Figures A5-5 and A5-6. The bar element strains in the frame inner flange are illustrated in Figure A5-5 for both frames. The diagrams display the strains along the whole frame. The strains of both frames show a good correlation, both frames are loaded similarly. This correlation indicates a correct modelling method of the two seat-rows which leads to consistent load introduction in the frame structure.

The most critical loading direction in the frame inner flange is clearly the compression direction. The progression of the minimum strain values shows a first peak at about $t = 25$ ms. This peak reaches values of about $\epsilon_{\text{min}} = -8000$ microstrain in the most critical frame region between the cargo floor and the vertical support strut connection. In the final frame design, the crippling strain of the frame inner flange in this region is $\epsilon_{\text{cc}} = -8290$ microstrain. At this time of the first peak, the kinematic hinges in the frame trigger. The strain values of the frame structure decrease to a constant level which represents the energy absorbing frame bending phase. The second minimum peak value occurs at about $t = 170$ ms and represents the ground contact of the vertical support struts. The elements showing the maximum strain values of this second peak are located in the vertically orientated frame regions of the fuselage side shell.

The elements showing the positive maximum strain values can be found in the upper fuselage area as well as in the region of the passenger crossbeam connection. All maximum strain values are clearly below the allowable of $\epsilon_t = +10,000$ microstrain.

The frame outer flange strains are given in Figure A5-6. Again, the strains of both frames show a good correlation, both frames are loaded similarly. In contrast to the frame inner flanges, the strain values are clearly smaller in the frame outer flanges. However, due to the lower thickness in the outer flange these strain values might be critical. In fact, the elements showing the minimum strain values in Figures A5-6a) and A5-6b) are located in the upper fuselage area where the frame outer flange provides a thickness of $t_{\text{OFF}} = 2.6$ mm and a width of $w_{\text{OFF}} = 28$ mm in the final crash scenario. Hence, the crippling strain in this flange region is $\epsilon_{\text{c1}} = -3300$ microstrain. The minimum strain values in Figures A5-6a) and A5-6b) are $\epsilon_{\text{min}} = -4000$ microstrain. Hence, the strain limit criterion is clearly exceeded and the outer flange had to be adapted to this maximum crash load. In this exemplary application of the Kinematics Model, the focus of the structural adaptation was on the loads in the frame inner flange based on a specified

frame profile catalogue. Further adaptation of the frame outer flange would require the definition of individual frame profiles in addition to the given profile catalogue which is beyond the scope of this exemplary application. Hence, the loads in the frame outer flange were checked against the flange design and potential exceeding was identified, but further adaptation was not conducted.

Finally, the passenger loads in the final crash scenario are illustrated in Figure A5-7. The accelerations are given in the Eiband diagram and are illustrated separately for both seat-rows. In general, the passenger accelerations are similar to the values shown in chapter 7 for the variant with optimised crash kinematics and maximum frame design. The values are clearly below the limit of severe injuries.

In the range of the most critical duration ($\Delta t = 6-11$ ms), the correlation of both seat-rows shows a more distinct scattering of passenger A-F in the second seat-row. Despite of that both seat-rows show similar acceleration values over the acceleration duration. Again, this good correlation indicates a correct modelling method with the two seat-rows.

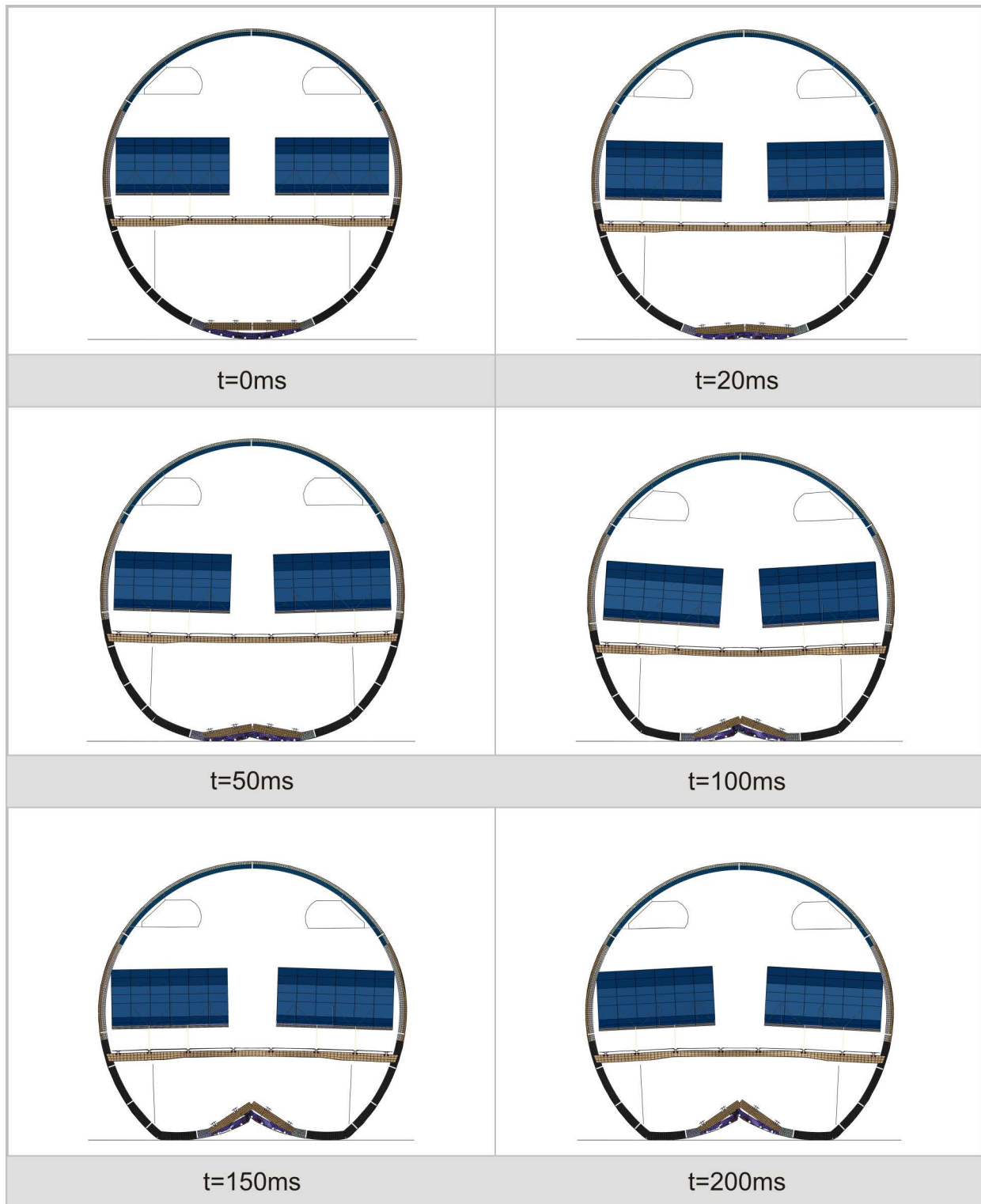


Figure A5-3: Detailed crash sequence of the final crash scenario

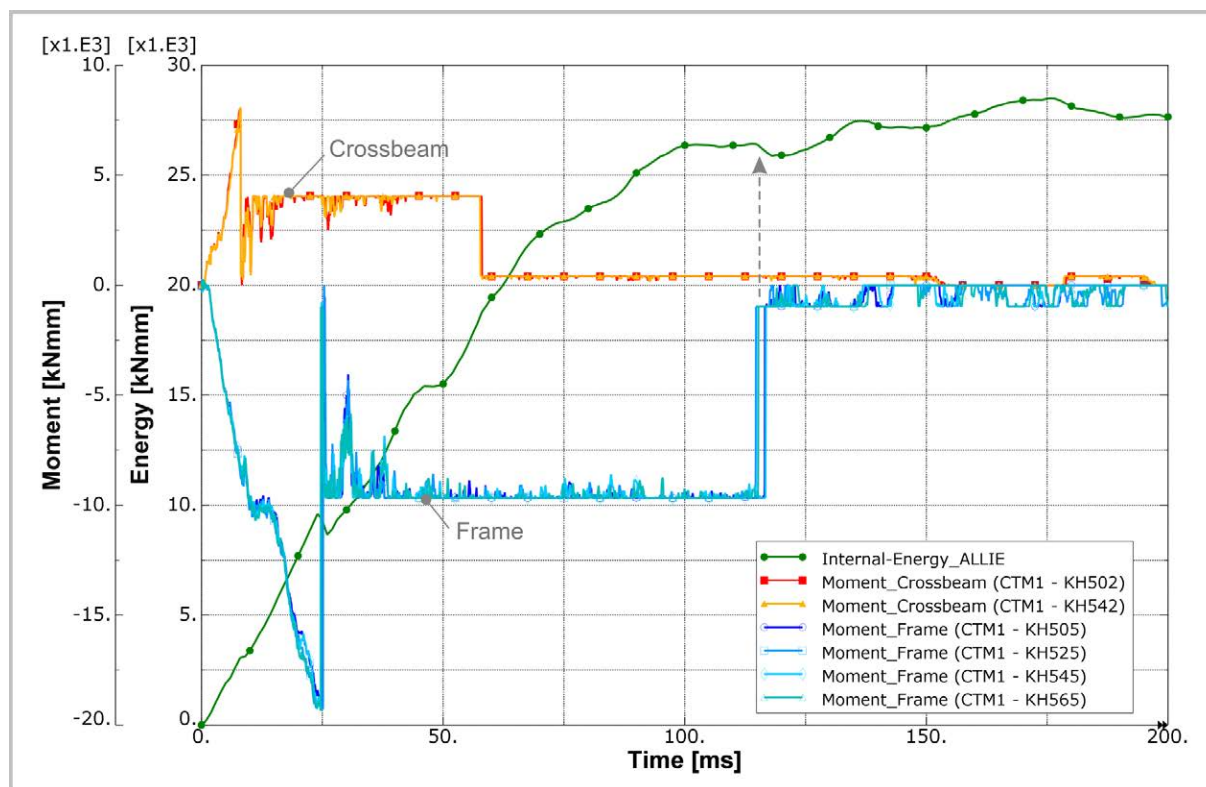


Figure A5-4: Kinematic hinge moment output versus total internal energy

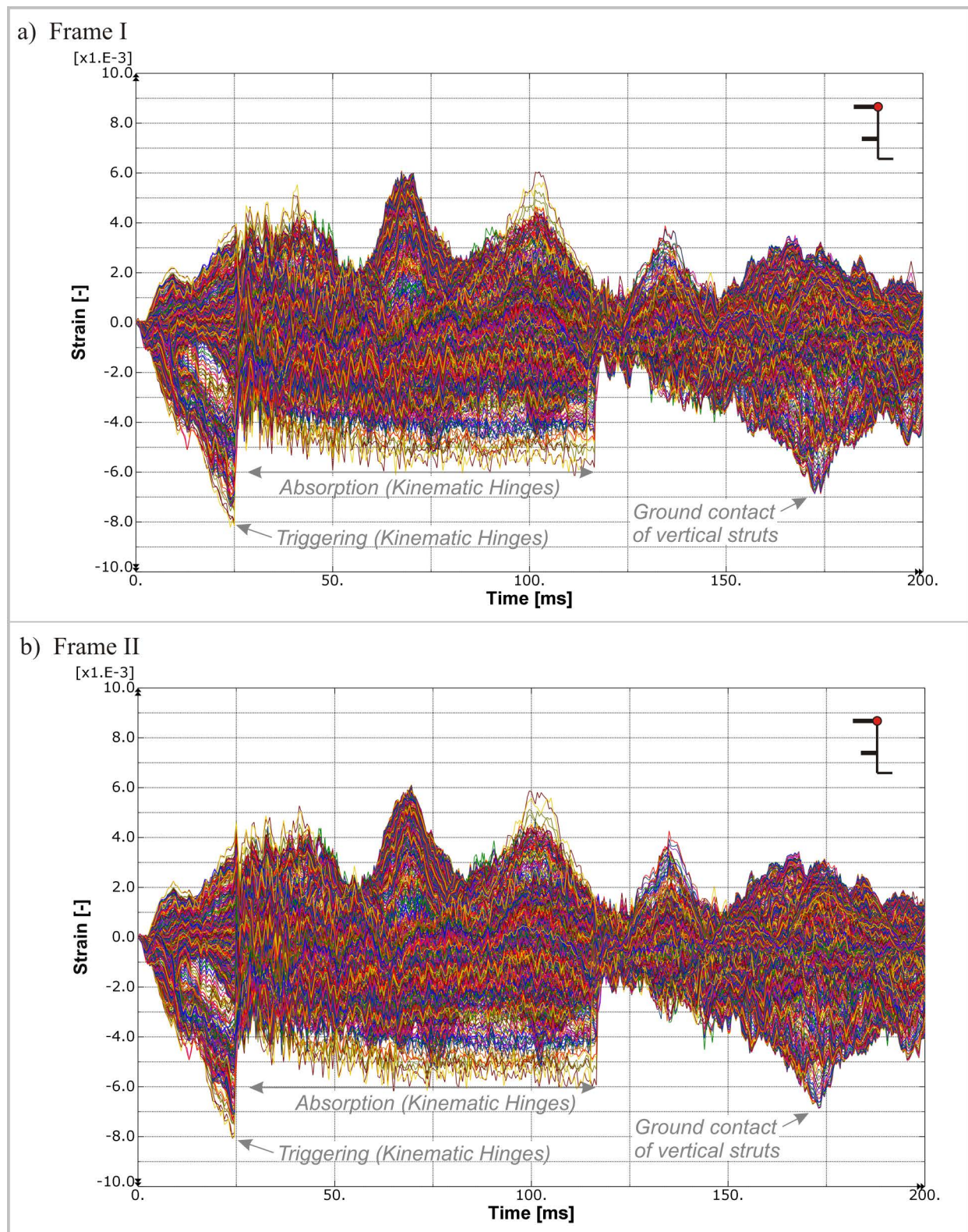


Figure A5-5: Strains along the frame inner flange

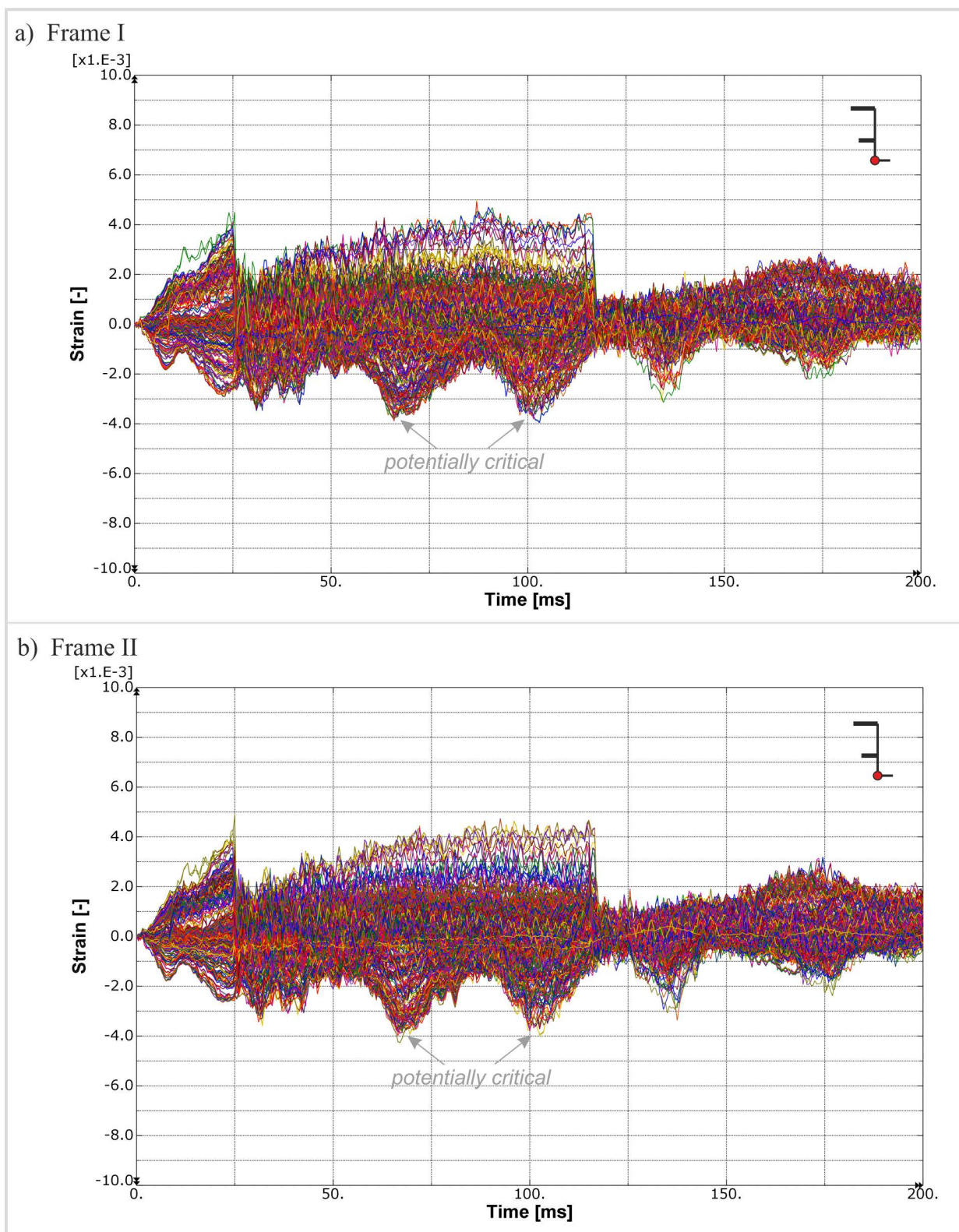


Figure A5-6: Strains along the frame outer flange

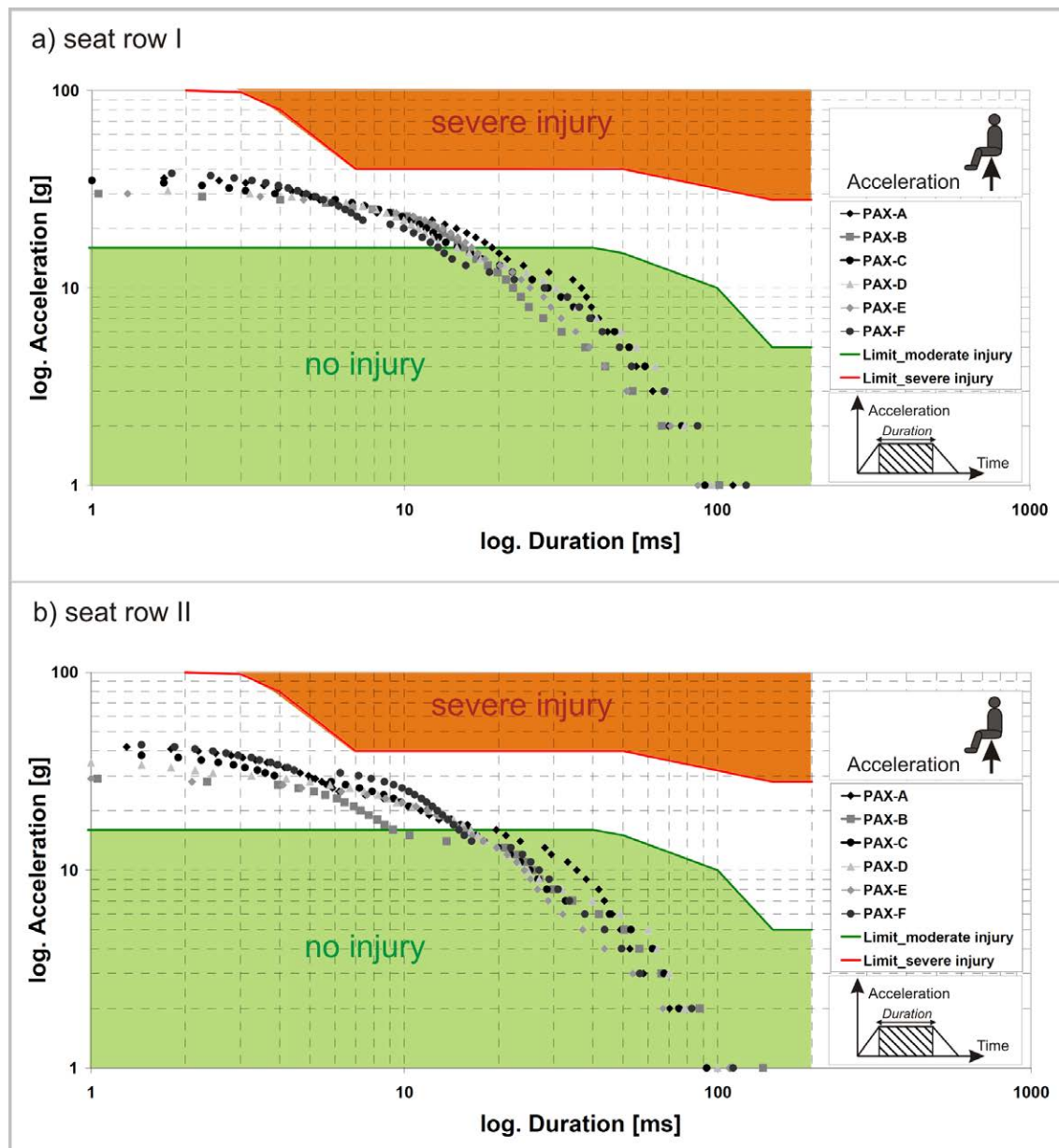


Figure A5-7: Passenger accelerations of the final crash scenario in the Eiband diagram

A5.3. Further results of the ovalisation effect

Based on the identified tensile forces in the passenger crossbeam, as illustrated in Figure 7-22, the definition of the parameter study was selected as shown in Figure A5-8.

None of these nine variants identified significant divergences in the general crash kinematics. The total internal energies in Figure A5-9 compare these variants. In addition, the total internal energy of the final crash scenario that represents a rigid crossbeam connection is given in this diagram. As expected, the curves are identical up to the triggering of the ovalisation device. Depending on the amount of energy absorbed by the ovalisation device, the internal energy curve reaches different levels respectively leads to a different trigger time of the frame kinematic hinges. Nevertheless, the overall shape of the curves is similar which indicates similar crash

kinematics. The finally selected variant describes a trigger force of $F = 20 \text{ kN}$ as well as a rotational stiffness of $K = 1.0\text{e}04 \text{ kNmm/rad}$, which is highlighted in Figure A5-8 in red colour.

Figure A5-10 compares the longitudinal force in the passenger crossbeam of the final crash scenario as well as the finally selected ovalisation variant. This diagram clearly illustrates the load limiting effect of such a crash device. During the sequence a maximum ovalisation of $\Delta y = 37 \text{ mm}$ (at each side of the crossbeam) could be found.

The frame inner flange strains in the most critical frame region between the cargo floor and the vertical support struts are plotted in Figure A5-11. The final crash scenario is compared with the finally selected ovalisation variant. The minimum strain values at the time of frame failure in that region are slightly reduced. This is an indication for a potential to reduce the structural mass due to reduced crash loads in the frame structure in case of an ovalisation concept.

Finally, the crash sequence of the finally selected ovalisation variant is shown in Figure A5-12. The sequence is compared with the final crash scenario and highlights the main differences at $t = 40 \text{ ms}$ as well as $t = 200 \text{ ms}$.

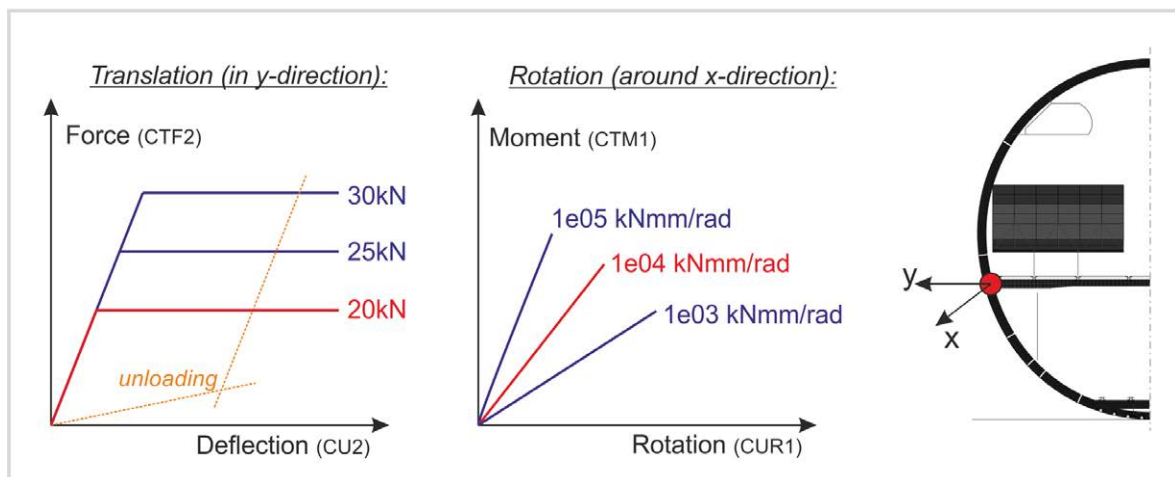


Figure A5-8: Input characteristics of the ovalisation device, analysed in the parameter study

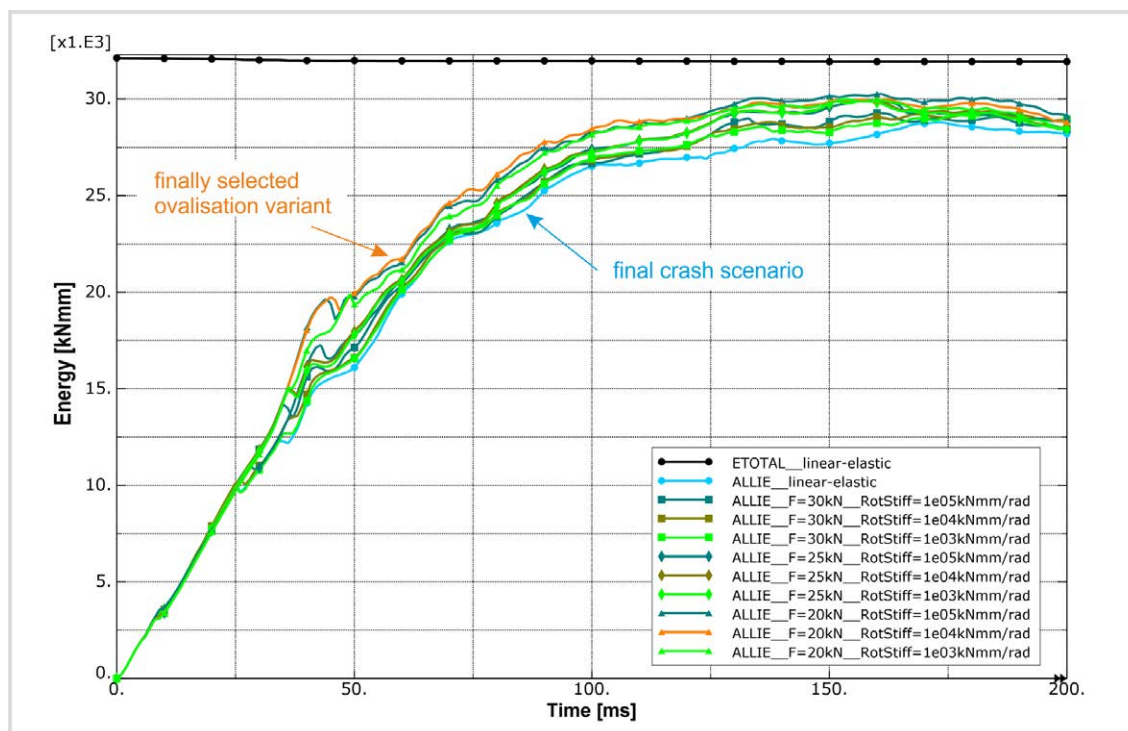


Figure A5-9: Total internal energies of the parameter study variants

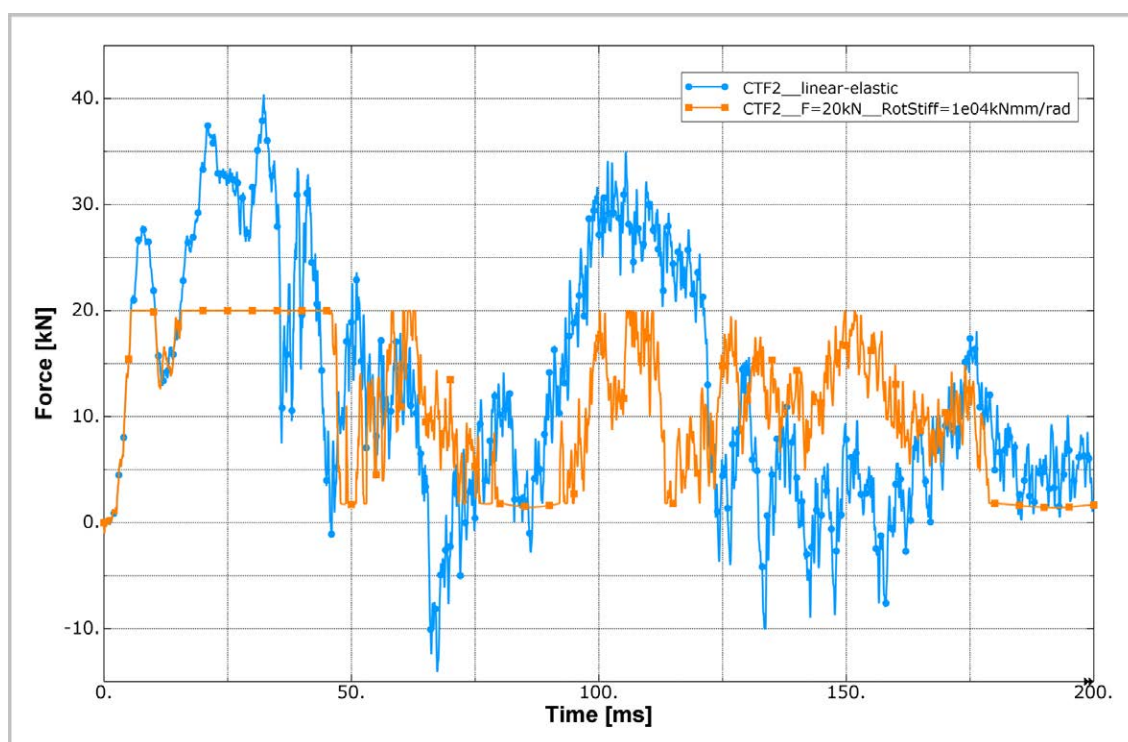


Figure A5-10: Longitudinal forces in the passenger crossbeam of the final crash scenario and the finally selected ovalisation variant

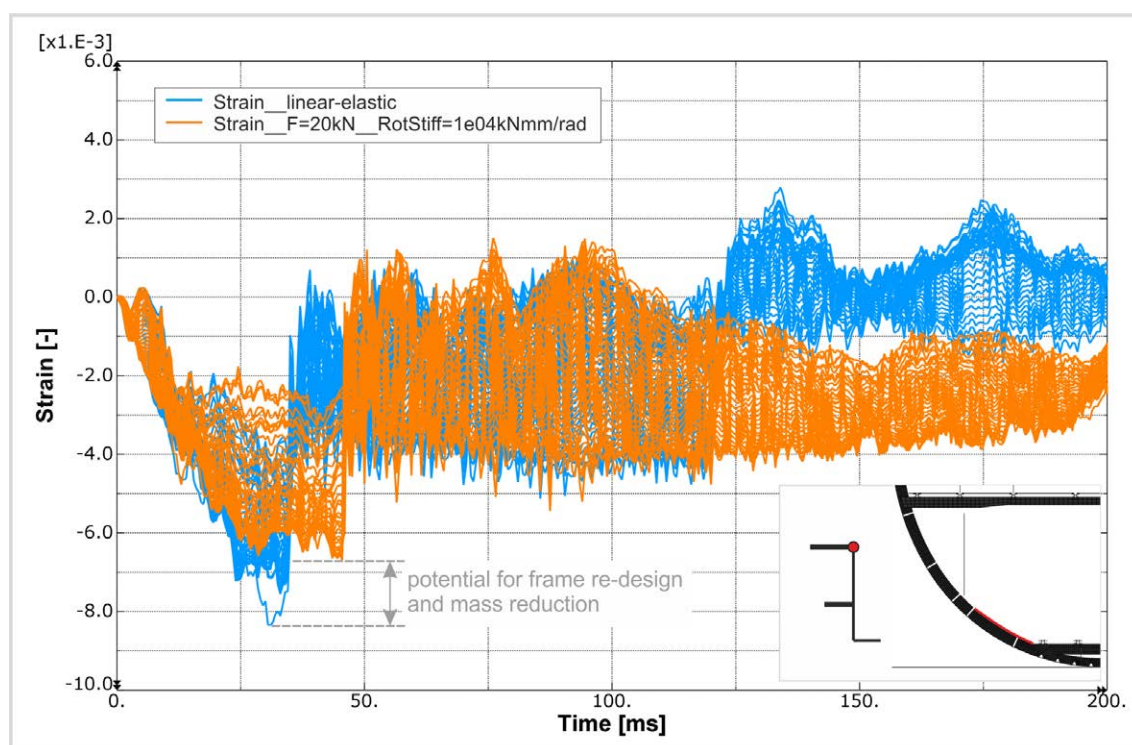


Figure A5-11: Frame inner flange strains in the most critical frame region of the final crash scenario and the finally selected ovalisation variant

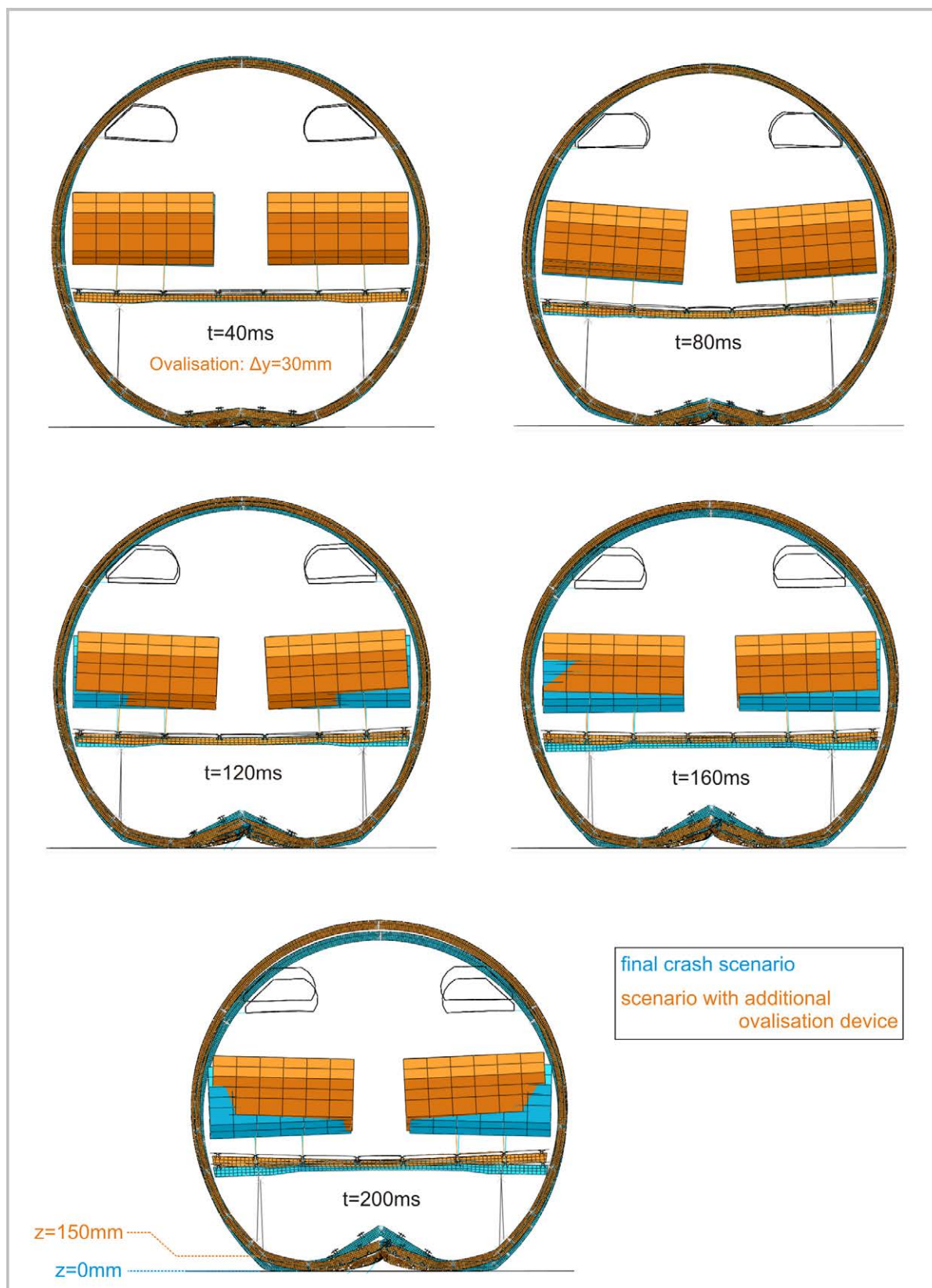


Figure A5-12: Crash sequence of the final crash scenario and the finally selected ovalisation variant

A5.4. Further details of the metallic frame model

A small study was performed to analyse exemplarily the energy absorbing capacity of the final frame design between the cargo-floor and the vertical support strut, using metallic instead of CFRP material. The detailed FE model of the metallic frame structure is shown in Figure A5-13. In the region of expected frame failure, located directly below the vertical support struts, the CFRP frame is replaced by a metallic frame structure which connects both CFRP frame parts as well as the vertical support strut. This metallic frame structure provides a similar LCF-shaped profile as the surrounding CFRP structure which is based on the final crash scenario. For assembly reasons, the frame middle and outer flange is defined on the opposite web side. Despite of this difference, the flange widths and thicknesses are identical to the CFRP frame profile. The frame inner and middle flanges describe a thickness of $t_{\text{IFF}} = 9.2 \text{ mm}$, whereas the frame web as well as the frame outer flange have a thickness of $t_{\text{OFF}} = 4.42 \text{ mm}$. The definition of the skin and the stringer design is according to the final crash scenario. The cleat design as well as the vertical support strut are similar to the A320 design.

An isotropic elastic-plastic material formulation was used for the representation of the metallic parts. The material data used for the metallic frame structure as well as the cleats is according to aluminium 2024 properties. The material data used for the vertical struts is according to aluminium 7075 properties. The CFRP parts (frame, stringers, skin) were modelled orthotropic linear-elastically.

Besides symmetry boundary conditions at the front and rear end of the model, the open cross-sections of the frame-skin structure were reinforced using rigid body formulations. In addition, the upper end of the frame-skin structure as well as the vertical support strut is constraint with fix boundary conditions. An impact plate with a constant velocity of $v = 6.7 \text{ m/s}$ applies the crash loads on the frame-skin structure. This model setup corresponds to an experimental test setup which was performed with an A320 structure in the former European Community funded project “Crashworthiness for Commercial Aircraft” [28].

The FE model size comprises 28,400 elements as well as 31,800 nodes. The simulation was performed with the explicit solver ABAQUS/Explicit V6.8-1. The simulation job was calculated on a Windows machine:

Dell Inc. Precision WorkStation T5400

Processor EM64T Family 6 Model 23 Stepping 6 GenuineIntel ~2993 Mhz

Microsoft(R) Windows(R) Server 2003 Standard x64 Edition (Service Pack 2 Build 3790)

Microsoft Compute Cluster Pack

Parallelisation on domain-level was executed with two domains respectively two processors and double precision. The simulation time was defined with $t_s = 80$ ms and led to a calculation time of $t_c \approx 8$ h.

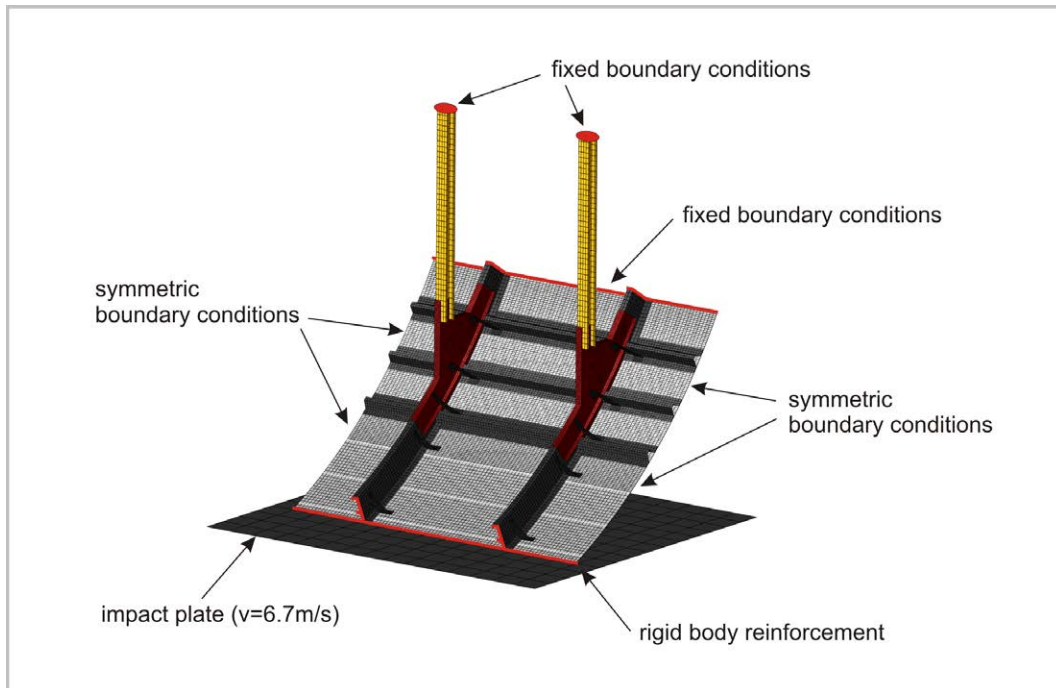


Figure A5-13: FE model of the metallic frame variant

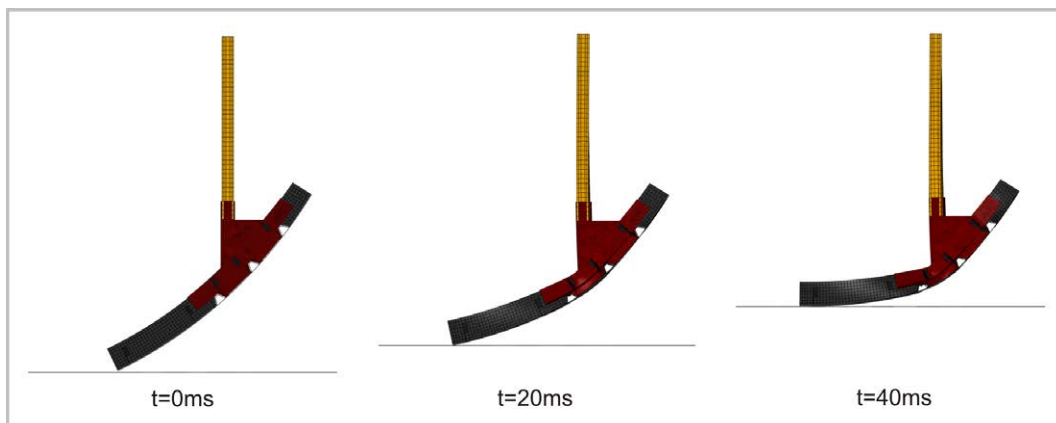


Figure A5-14: Sequence of the metallic frame bending under crash loads

A5.5. Determination of an optional trigger load level for the vertical support struts

In the investigations based on the ‘standard crash case’ passive vertical support struts were foreseen and the trigger load level was defined artificially high. With respect to other crash cases with higher initial kinetic energy or unfavourable loading conditions further energy absorption capacity in the vertical support struts could significantly improve the crashworthiness of the considered fuselage structure. For that reason, the definition of an appropriate trigger level for

the vertical struts is essential to ensure a stable crash kinematics respectively to ensure a cascading scenario with a final vertical strut crushing phase.

Figure A5-15 shows the axial forces in the vertical support struts of the final crash scenario (standard crash case). In addition, the kinematic hinge moments as well as the total internal energy are plotted over the crash duration in this diagram to give an overview of the crash sequence. The graphs of all four vertical struts show an increase of the compression force up to values between $F = 33\text{--}42\text{ kN}$. These maximum compression forces occur at a state when approximately two thirds of the energy absorption capacity in the frame kinematic hinges are reached. A smooth transition from the frame bending phase to the vertical strut crushing phase can be achieved by a trigger load level which initiates the strut crushing at this state. With respect to the considered crash scenario such an appropriate trigger force can be defined as $F = 35\text{ kN}$.

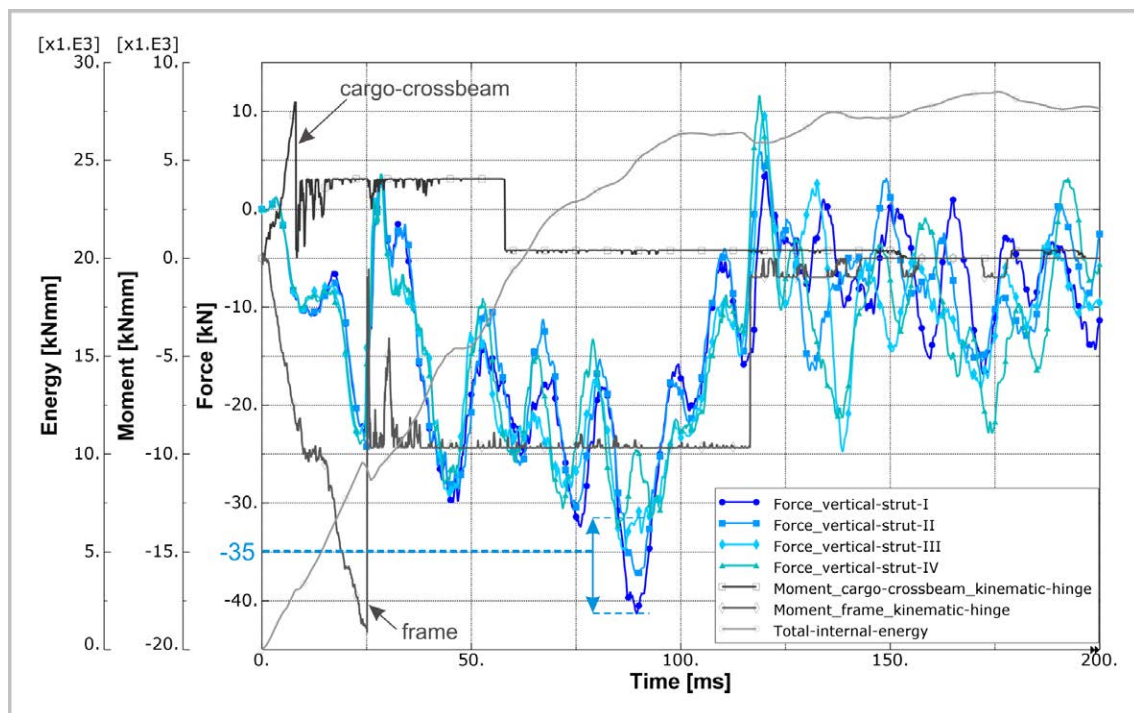


Figure A5-15: Axial forces in the vertical support struts of the final crash scenario

A6. Appendix of chapter 8

Details about the development of a test setup for axial crushing are provided in paragraph A6.1. The test matrix of the axial crushing test programme is given in paragraph A6.2.

Further details about the development of a test setup for frame bending tests are provided in paragraph A6.3 before the test matrix of the frame bending test programme is shortly presented in paragraph A6.4.

A6.1. Remarks to the development of a test setup for axial crushing tests

The development of the test setup for axial crushing tests was supported by detailed finite element analyses as well as experimental pre-tests. Different factors were identified which influence the failure behaviour of the considered crash absorber. Some of these factors are driven by the structural environment of the fuselage.

The detailed FE model is illustrated in Figure A6-1. A multi-layered shell approach is used with shell elements of reduced integration (S4R elements). The CFRP material is modelled using an ABAQUS built-in user subroutine for fabric ply modelling (VUMAT 'fabric_ply'). The rivet connection between the half-tube absorber and the strut is modelled with connector elements and appropriate failure models. The mesh independent fastener option (*fastener) is used to position the connector elements at the specified rivet locations. The connection of the metallic skin plate and the strut flange is modelled using a tied connection (*tie). The model size is 13,973 elements and 15,361 nodes. The simulations were performed with the explicit solver ABAQUS/Explicit V6.8-1. The simulation jobs were calculated on the following Windows machine:

Dell Inc. Precision WorkStation T5400

Processor EM64T Family 6 Model 23 Stepping 6 GenuineIntel ~2993 Mhz

Microsoft(R) Windows(R) Server 2003 Standard x64 Edition (Service Pack 2 Build 3790)

Microsoft Compute Cluster Pack

Parallelisation on domain-level was executed with two domains respectively two processors and single precision. The simulation time was defined as $t_S = 20$ ms and led to a calculation time of $t_C \approx 22$ h.

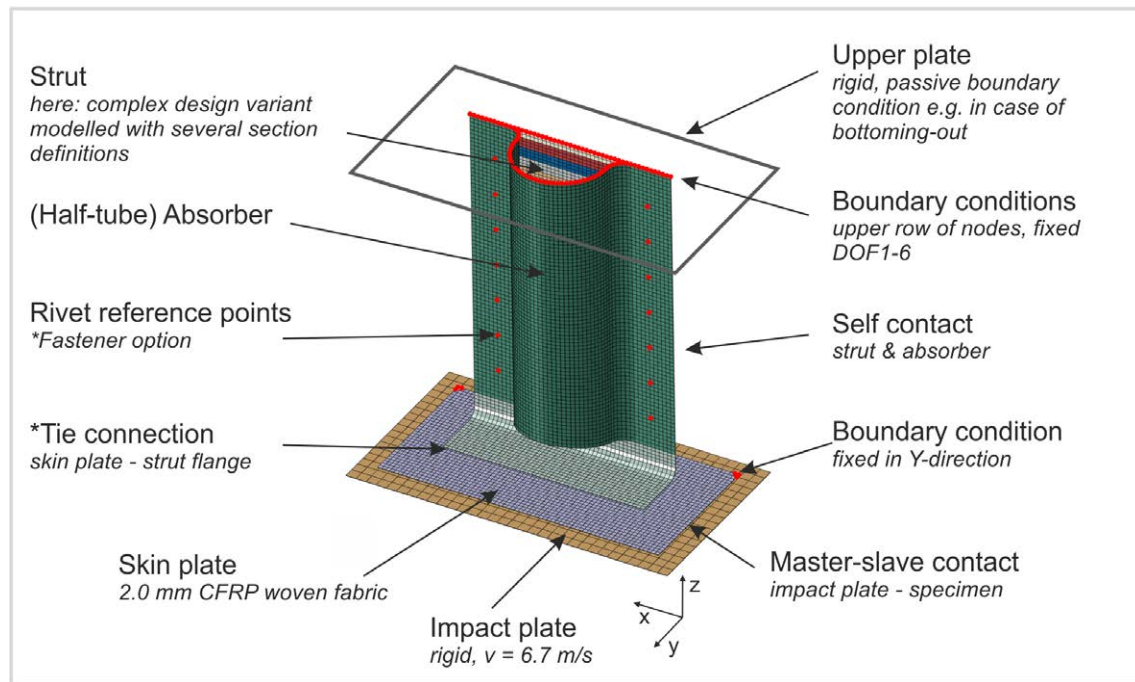


Figure A6-1: FE model of the axial crushing test

Based on the outcomes of the finite element analyses a first pre-test was conducted statically in a universal test machine (Zwick 1494). According to the identified tendency of the strut flange to roll up in a first phase of the crushing sequence, a metallic plate was bonded to the strut flange which is additionally guided to avoid further lateral displacement. Figure A6-2 pictures the prepared absorber structure for pre-test I. The pictured upper fixture represents the clamping part in which the specimen is embedded. This clamping part is bolted to a further fixture part which provides the bleeding channels. In the quasi-static pre-test I, the peeling effect of the above discussed roll up tendency induced high stresses which finally initiated failure of the bonded connection. As predicted in the finite element analyses without the modelling of the plate, the strut flange rotated after the bonding failure around its radius and separated from the plate. Figure A6-3 depicts the quasi-static pre-test I and compares this effect with outcomes of the finite element analyses.

A second pre-test was conducted with a modified connection of the strut flange and the metallic plate. The bonding connection was replaced by a bolted one, as illustrated in Figure A6-4. After the general feasibility of the guidance system was proved in pre-test I, the second pre-test was performed dynamically ($v = 6.7 \text{ m/s}$) in the test machine Instron VHS, similarly to the specified test conditions of the planned test programme. Results of pre-test II are presented in Figure A6-5. The failure modes of the absorber specimen are as expected, Figure A6-5a) and A6-5b). Besides the crushing of the specimen, rupture of the strut near the flange radius occurred as well as pull-through failure of the rivets. The inspection of the upper test fixture identified no failure of the absorber specimen on this side, Figure A6-5c). Hence, the bonding connection in the fixture is

sufficient and potential crushing at this side of the specimen is not expected. The metallic skin plate showed little plastic deformation which was caused by the constraint roll up effect of the strut radius, Figure A6-5d).

In a final pre-test a hardened steel plate (C60-steel) was used to achieve higher yield strength and to avoid any plastic deformation. Pre-test III was conducted dynamically similar to pre-test II. Figure A6-6 depicts the specimen after the test and illustrates the metallic plate without plastic deformation. Hence, in pre-test III the final test setup could successfully be verified.

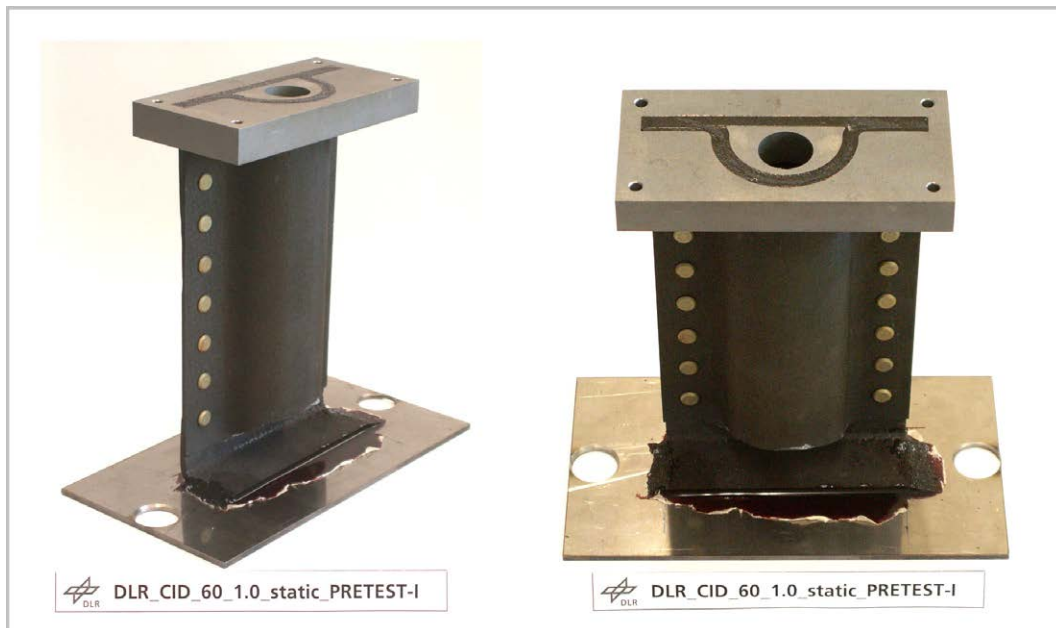


Figure A6-2: Prepared specimen of pre-test I

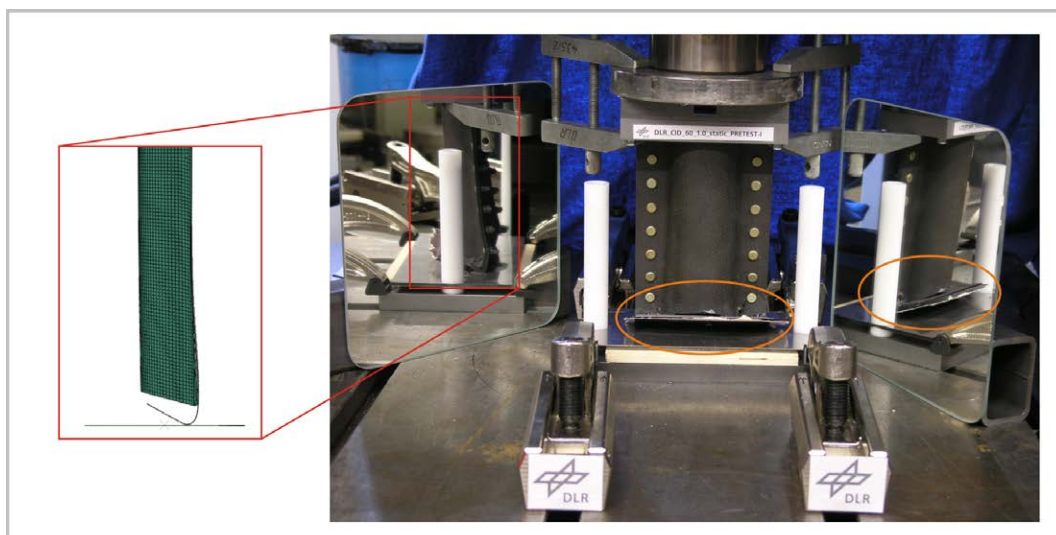


Figure A6-3: Unrolling effect of the strut flange - comparison of the FE analysis and the test (pre-test I)

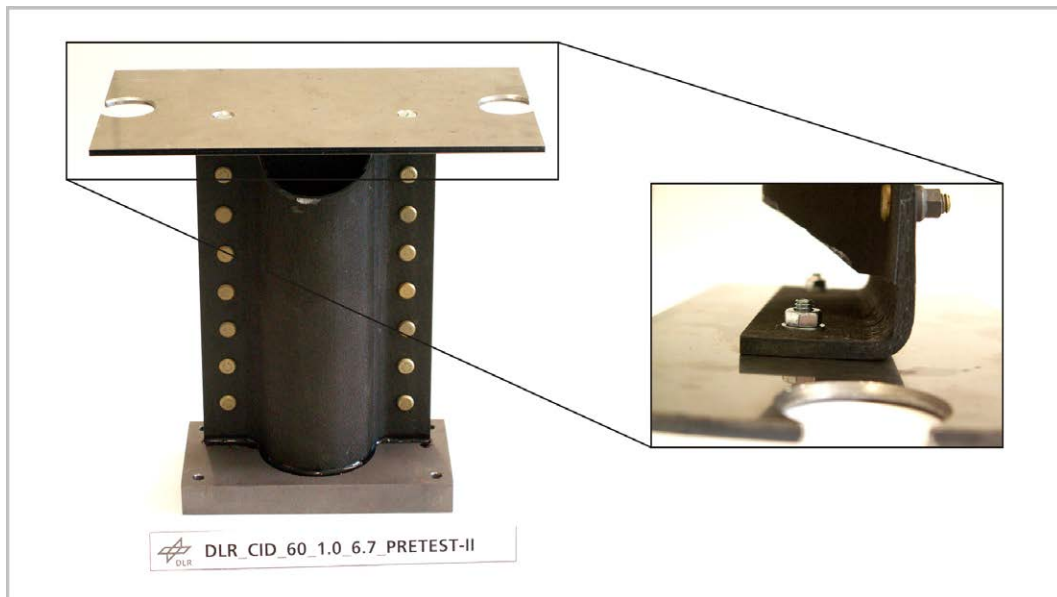


Figure A6-4: Prepared specimen of pre-test II

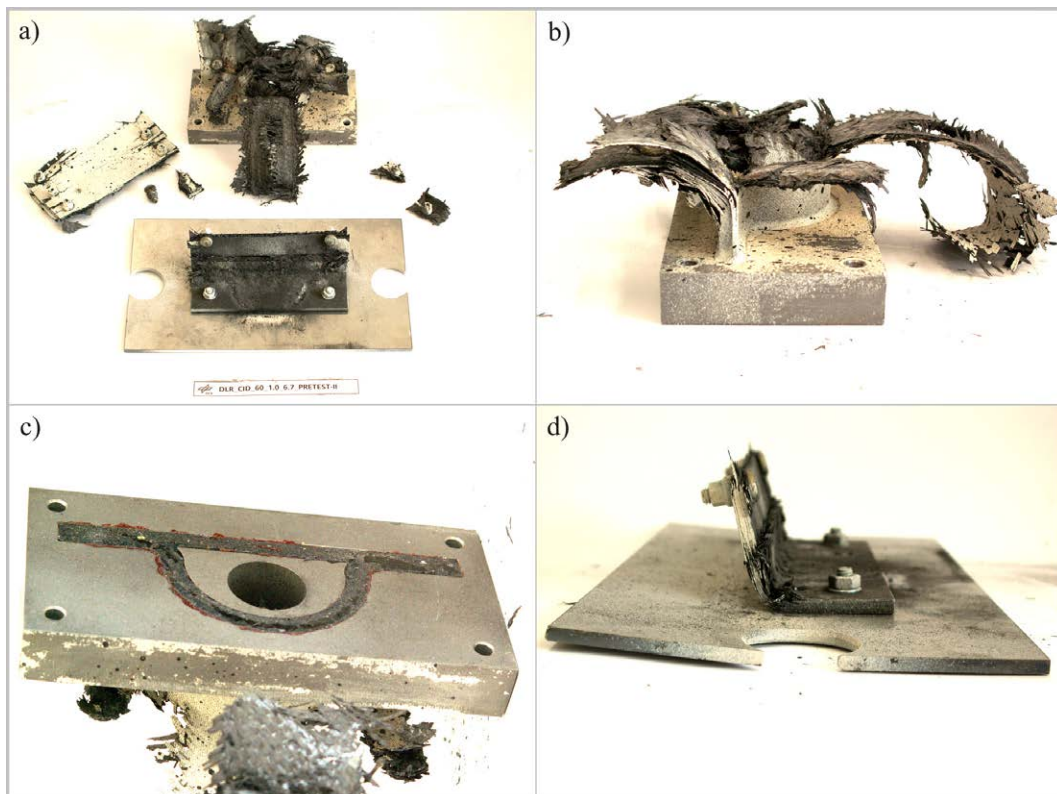


Figure A6-5: Specimen after the test (pre-test II)

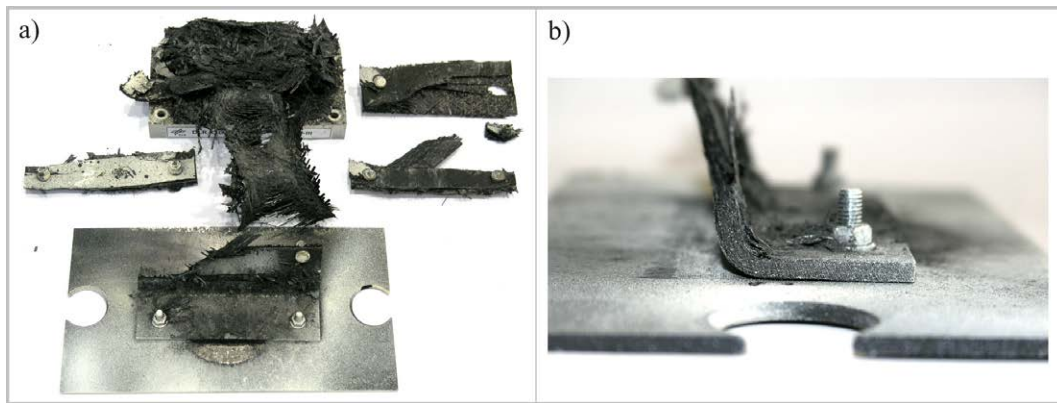


Figure A6-6: Specimen after the test (pre-test III)

A6.2. Test matrix of the axial crushing test programme

The test matrix with a total number of 72 dynamic absorber tests is given in Table A6-1.

In the following, the test parameters are briefly explained to get an overview on the investigated effects.

Two different designs of the flat strut were tested. Besides a simple geometry with a constant thickness of $t = 1.5$ mm, a complex design was considered that corresponds to a statically sized sub-cargo structure with a complex layup respectively thickness distribution along the strut.

The influence of the half-tube absorber design was regarded with several parameters. Considering the geometry, two different angles of the geometrical trigger were tested. The definition of the trigger angle is important to achieve a robust initiation of the crushing mode.

A further defined absorber design parameter is the thickness of the absorber laminate. The thickness of the absorber significantly influences the crushing force level. In addition, an increased absorber stiffness could avoid potential instability failure which is initiated by the flat strut. Hence, the influence of the absorber thickness on the global stability behaviour was of interest.

Furthermore, different materials respectively fabrications of the absorber structure were investigated. Besides absorbers made of CFRP woven fabrics, variants of CFRP braided absorbers were tested.

Another parameter considers the connection of the half-tube absorber and the flat strut. The reference variant is defined with a riveted connection. Additionally, a further variant was tested with a combination of riveted and paste bonded connection. Using additionally paste bonding, it was expected to reduce the oscillations on the force-displacement curves which are caused by the rivets. Instead a constant, increased force level was expected.

Finally, two parameters considered the influence of the loading condition. Besides the standard load case of vertical crushing with $v = 6.7$ m/s, a loading rate of $v = 10$ m/s as well as an off-axis angle (roll angle) of $\beta = 10^\circ$ was tested.

Variant Parameter	1	2	3	4	5	6	7	8	9	10	11	12
Strut design	simple	simple	simple	simple	simple	simple	complex	complex	complex	complex	complex	complex
Absorber trigger angle	$\alpha = 60^\circ$	$\alpha = 60^\circ$	$\alpha = 75^\circ$	$\alpha = 75^\circ$	$\alpha = 75^\circ$	$\alpha = 75^\circ$	$\alpha = 60^\circ$	$\alpha = 60^\circ$	$\alpha = 75^\circ$	$\alpha = 75^\circ$	$\alpha = 75^\circ$	$\alpha = 75^\circ$
Absorber thickness	$t = 1.0\text{mm}$	$t = 2.0\text{mm}$	$t = 1.0\text{mm}$	$t = 2.0\text{mm}$	$t = 1.0\text{mm}$	$t = 2.0\text{mm}$	$t = 1.0\text{mm}$	$t = 2.0\text{mm}$	$t = 1.0\text{mm}$	$t = 2.0\text{mm}$	$t = 1.0\text{mm}$	$t = 2.0\text{mm}$
Off-axis	0°	0°	0°	0°	0°	0°	0°	0°	0°	0°	10°	10°
Paste Bonding	-	-	-	-	yes	-	-	-	-	-	-	-
Loading rate	$v = 6.7\text{m/s}$	$v = 6.7\text{m/s}$	$v = 6.7\text{m/s}$	$v = 6.7\text{m/s}$	$v = 6.7\text{m/s}$	$v = 10\text{m/s}$	$v = 6.7\text{m/s}$	$v = 6.7\text{m/s}$	$v = 6.7\text{m/s}$	$v = 6.7\text{m/s}$	$v = 6.7\text{m/s}$	$v = 6.7\text{m/s}$
Woven Fabric Absorber Number of Tests	2	2	2	2	2	2	2	2	2	2	2	2
Biaxial Braided Absorber Number of Tests	2	2	2	2	2	2	2	2	2	2	2	2
Triaxial Braided Absorber Number of Tests	2	2	2	2	2	2	2	2	2	2	2	2

Table A6-1: Test matrix of the absorber test programme

A6.3. Remarks to the development of a test setup for frame bending tests

The development of the test setup for frame bending tests was supported by detailed finite element analyses as well as experimental pre-tests [130].

The detailed FE model of [130] is illustrated in Figure A6-7. A multi-layered shell approach is used for the representation of the frame segment with shell elements of reduced integration (S4R elements). The CFRP material is modelled using an ABAQUS built-in user subroutine for fabric ply modelling (VUMAT ‘fabric_ply’). The fixture is modelled using solid elements with reduced integration (C3D8R) and elastic material input according to aluminium data. A tied connection (*tie) is used to describe the bonded connection between fixture and frame segment. The model size is 12,426 elements and 17,015 nodes. The simulation was performed in a multi-step analysis to consider thermal stresses in the hybrid frame segments which are introduced in the structure during the thermoplastic manufacturing process. The simulations were performed with the explicit solver ABAQUS/Explicit V6.8-1. The simulation jobs were calculated on a Windows machine:

Dell Inc. Precision WorkStation T5400

Processor EM64T Family 6 Model 23 Stepping 6 GenuineIntel ~2993 Mhz

Microsoft(R) Windows(R) Server 2003 Standard x64 Edition (Service Pack 2 Build 3790)

Microsoft Compute Cluster Pack

Parallelisation on domain-level was executed with two domains respectively two processors and double precision. The simulation time of the complete multi-step analysis was defined as $t_s = 65$ ms and led to a calculation time of $t_C \approx 7$ h.

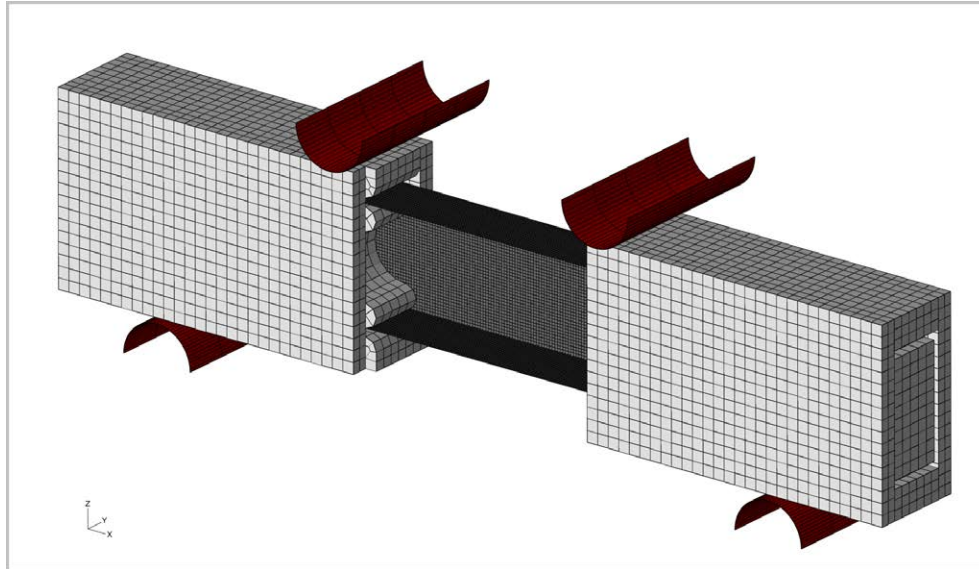


Figure A6-7: FE model of the frame bending test [130]

Several experimental pre-tests were performed to develop an appropriate test setup. Initial pre-tests were conducted with wooden inserts which were bonded in the C-frame segment in the region between the supports and the stamp. In addition, metallic plates (aluminium, $t = 3$ mm) were positioned at the supports and the stamp to smoothen the load introduction into the C-frame segment. This setup was identified to be non-sufficient. Distortion of the C-profile as well as local material damages at the supports and the stamp were observed, Figure A6-8a). Similar results of local damage by the load introduction were identified in the numerical analysis, Figure A6-8b). According to these results the test setup was modified and a solid aluminium fitting was designed which encase the C-profile in the region between the stamp and the supports.

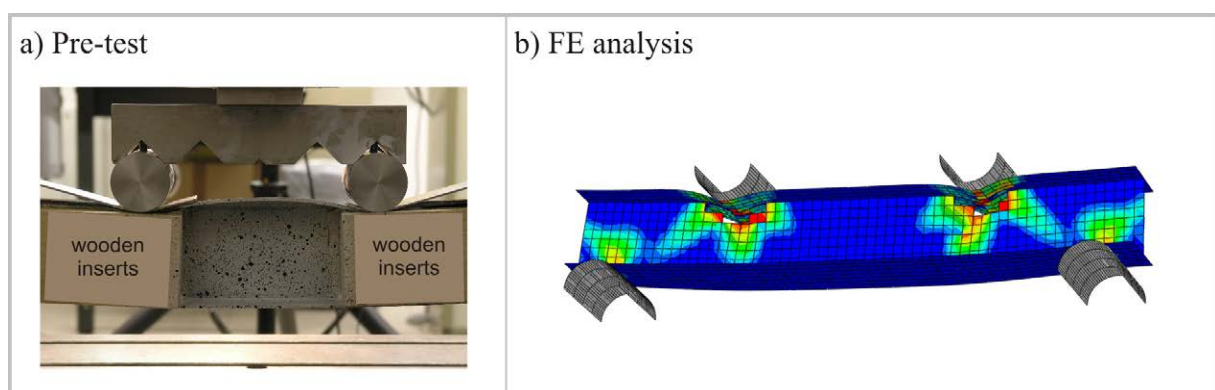


Figure 8: Damage by the load introduction of the supports and the stamp [130]

Further finite element analyses, according to the final FE model depicted in Figure A6-7, were used to estimate the instability mode of the compressive loaded flange in dependence of the free length between the stamps. To achieve failure of the frame segment in the centre of the free length an instability mode of first order was desired. The simulation results identified a free length of $L = 160$ mm as sufficient to allow the compressive loaded flange to buckle in a mode

of first order, as displayed in Figure A6-9. The vertical displacement is pictured in this figure and highlights the buckling mode of the upper, compressive loaded flange.

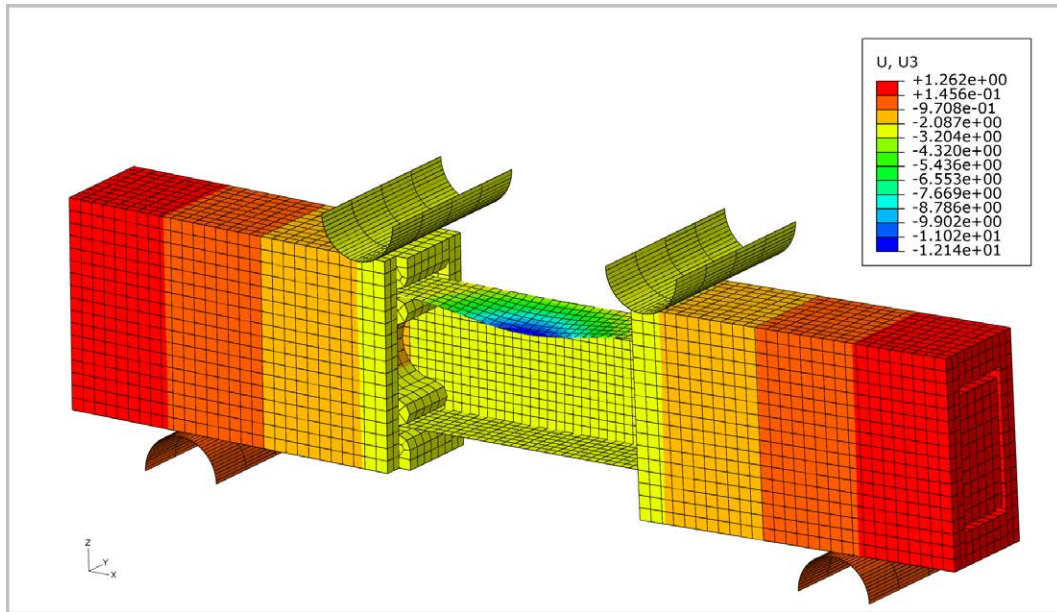


Figure A6-9: Instability mode of first order in the compressive loaded flange, displacement in z-direction [130]

A6.4. Test matrix of the frame bending test programme

The test matrix of the frame bending test programme is given in Table A6-2. A total of eight tests were conducted with the developed test setup. Hybrid frame segments with titanium sheets embedded in the flanges were tested and compared with tested reference frame segments which were made purely of CFRP. Figure A6-10 depicts the layups of both variants and illustrates the replacement of UD-plyies by titanium sheets in the hybrid variant.

The frame segments were tested quasi-statically in an universal testing machine (Zwick 1475) as well as dynamically in the DLR drop tower facility with an initial velocity of $v_i = 3.4$ m/s.

Variant Parameter	1	2	3	4
Flange design	CFRP	Hybrid	CFRP	Hybrid
Loading rate	quasi-static	quasi-static	dynamic	dynamic
Number of tests	2	2	2	2

Table A6-2: Test matrix of the frame bending test programme

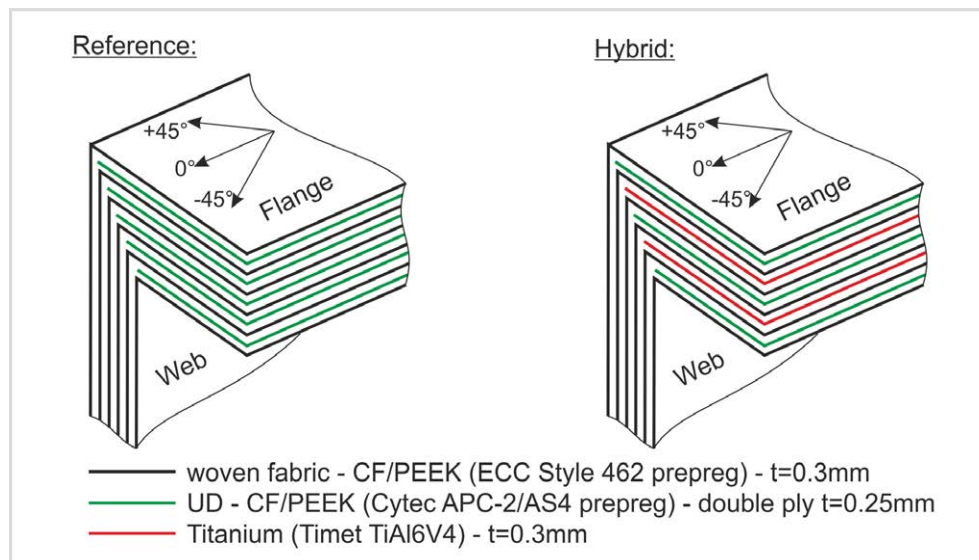


Figure A6-10: Flange and web layup of the reference and the hybrid variant

Bibliography

- [1] Boeing Commercial Airplanes: Statistical summary of commercial jet airplane accidents – worldwide operations 1959-2009, Boeing Commercial Airplanes, 2010
- [2] R. H. W. M. Frijns, J. F. W. Wiggeraad, A. T. M. Schaefer: Assessment of survivable crash scenarios – an evaluation of crash scenarios during the period 1980-1992, Sub-task 1.2 of the European Community funded research project ‘Crashworthiness for commercial aircraft’, 1994
- [3] R. G. Thomson, C. Caiafa: Structural response of transport airplanes in crash situations, NASA TM85654, 1983
- [4] US National Transportation Safety Board: Survivability of accidents involving part 121 U.S. air carrier operations – 1983 through 2000, Safety report NTSB/SR-01/01, 2001
- [5] W. Widmayer, O.B. Brende: Commercial jet transport crashworthiness, NASA CR165849, 1982
- [6] M. C. Y. Niu: Composite airframe structures – second edition / fifth published, Hong Kong Conmilit Press Ltd., 2008
- [7] A. C. Jackson, M. C. Campion, G. Pei: Study of utilization of advanced composites in fuselage structures of large transports, NASA CR172404, 1984
- [8] R. W. Johnson, L. W. Thomson, R. D. Wilson: Study of utilization of advanced composites in fuselage structures of large transports, NASA CR172406, 1985
- [9] A. C. Jackson, F. J. Balena, W. L. LaBarge, G. Pei, W. A. Pitman, G. Wittlin: Transport composite fuselage technology – impact dynamics and acoustic transmission, NASA CR4035, 1986
- [10] Federal Aviation Administration: Federal aviation regulations, part 25: airworthiness standards: transport category airplanes, 1997
- [11] Federal Aviation Administration: Special conditions: Boeing model B787-8 airplane; Crashworthiness, US Federal register Vol.72 No.111 Docket No.NM368 special conditions No. 25-07-05-SC, 2007

- [12] G. M. Preston, G. J. Pesman: Accelerations in transport-airplane crashes, NACA TN4158, 1958
- [13] W. H. Reed, S.H. Robertson, L. W. T. Weinberg, L. H. Tyndall: Full-scale dynamic crash test of a Lockheed Constellation model 1649 aircraft, FAA-ADS-38, 1965
- [14] W. H. Reed, S.H. Robertson, L. W. T. Weinberg, L. H. Tyndall: Full-scale dynamic crash test of a Douglas DC-7 aircraft, FAA-ADS-37, 1965
- [15] M. S. Williams, R. J. Hayduk: Vertical drop test of a transport fuselage center section including the wheel wells, NASA TM85706, 1983
- [16] E. L. Fasanella, E. Alfaro-Bou: Vertical drop test of a transport fuselage section located aft of the wing, NASA TM89025, 1986
- [17] M. S. Williams, R. J. Hayduk: Vertical drop test of a transport fuselage section located forward of the wing, NASA TM85679, 1983
- [18] S. M. Pugliese: B-707 fuselage drop test report, Arvin/Calspan report No. 7252-1 prepared for FAA technical center Atlantic City N.J., 1984
- [19] D. Johnson, A. Wilson: Vertical drop test of a transport airframe section, DOT/FAA/CT-TN 86/34, 1986
- [20] Arvin/Calspan: DC-10 fuselage drop test report, Arvin/Calspan report No. 7251-2 prepared for FAA technical center Atlantic City N.J., 1984
- [21] R.J. Hayduk: Full-scale transport controlled impact demonstration, NASA CP2395, 1985
- [22] Federal Aviation Administration: Summary report – full-scale transport controlled impact demonstration program, DOT/FAA/CT-87/10, 1987
- [23] K. E. Jackson, R. L. Boitnott, E. L. Fasanella, L. E. Jones, K. H. Lyle: A history of full-scale aircraft and rotorcraft crash testing and simulation at NASA Langley Research Center, Fourth triennial international fire & cabin safety research conference, 2004
- [24] A. Abramowitz, T. G. Smith, T. Vu, J. R. Zvanya: Vertical drop test of a narrow-body transport fuselage section with overhead stowage bins, DOT/FAA/AR-01/100, 2002
- [25] T. V. Logue, R. J. McGuire, J. W. Reinhardt, T. Vu : Vertical drop test of a narrow-body fuselage section with overhead stowage bins and auxiliary fuel tank on board, DOT/FAA/CT-94/116, 1995

- [26] A. Abramowitz, T. G. Smith, T. Vu: Vertical drop test of a narrow-body transport fuselage section with conformable auxiliary fuel tank onboard, DOT/FAA/AR-00/56, 2000
- [27] M. M. Sadeghi, S. M. R. Hashemi: An overview of the aircraft crashworthiness study project 'A European programme', Second triennial international fire & cabin safety research conference, 1998
- [28] R. Hashemi: Sub-component dynamic tests on an Airbus A320 rear fuselage, Cranfield Impact Centre Limited, Sub-task 2.4 of the European Community funded research project 'Crashworthiness for commercial aircraft', 1994
- [29] R. Hashemi: Sub-component quasi-static tests on an Airbus A320 rear fuselage, Cranfield Impact Centre Limited, Sub-task 2.4 of the European Community funded research project 'Crashworthiness for commercial aircraft', 1994
- [30] F. LePage, R. Carciente: A320 fuselage section vertical drop test – part 2 test results, CEAT test report S95 5776/2, European Community funded research project 'Crashworthiness for commercial aircraft', 1995
- [31] I. Kumakura, H. Sashikuma, et al.: Summary of vertical drop tests of YS-11 transport fuselage sections, SAE technical paper 2003-01-3027, 2003
- [32] I. Kumakura, H. Sashikuma, et al.: Vertical drop test of a transport fuselage section, SAE technical paper 2002-01-2997, 2002
- [33] A. Abramowitz, S. Soltis: Summary of the FAA's commuter airplane crashworthiness program, Fifth triennial international fire & cabin safety research conference, 2007
- [34] A. Abramowitz, T. Vu: Vertical impact response characteristics of four commuter/regional airplanes, DOT/FAA/AR-08/20, 2008
- [35] R. J. McGuire, W. J. Nissley, J. E. Newcomb: Vertical drop test of a Metro III aircraft, DOT/FAA/CT-93/1, 1993
- [36] R. McGuire, T. Vu: Vertical drop test of a Beechcraft 1900C airliner, DOT/FAA/AR-96/119, 1998
- [37] A. Abramowitz, P. A. Ingraham, R. McGuire: Vertical drop test of a Shorts 3-30 airplane, DOT/FAA/AR-99/87
- [38] A. Abramowitz, T. G. Smith, T. Vu, J. R. Zvanya: Vertical drop test of an ATR 42-300 airplane, DOT/FAA/AR-05/56, 2006

- [39] J. D. Cronkhite, V. L. Berry: Crashworthy airframe design concepts – fabrication and testing, NASA CR3603, 1982
- [40] J. D. Cronkhite, T. J. Haas, R. Winter, G. T. Singley: Investigation of the crash impact characteristics of composite airframe structures, American Helicopter Society – 34th annual forum, 1987
- [41] C. M. Kindervater, H. Georgi: Composite strength and energy absorption as an aspect of structural crash resistance, in Structural Crashworthiness and Failure: 189-235, 1993
- [42] G. L. Farley: Energy absorption of composite materials, Journal of composite materials Vol.17: 267-279, 1983
- [43] A. G. Mamalis, M. Robinson, D.E. Manolakos, G.A. Demosthenous, M.B. Ioannidis, J. Carruthers : Review – crashworthy capability of composite material structures, Composite structures Vol.37 : 109-134, 1997
- [44] P. Feraboli, B. Wade, F. Deleo, M. Rassaian: Crush energy absorption of composite channel section specimens, Composites: Part A Vol.40: 1248-1256, 2009
- [45] A. Jackson, S. Dutton, A. J. Gunnion, D. Kelly: Effect of manufacture and laminate design on energy absorption of open carbon-fibre/epoxy sections, International conference on composite materials ICCM-17, 2009
- [46] H. D. Carden: Unique failure behaviour of metal/composite aircraft structural components under crash type loads, NASA TM102679, 1990
- [47] H. D. Carden, M. P. Robinson: Failure behaviour of generic metallic and composite aircraft structural components under crash loads, NASA RP1239, 1990
- [48] R. L. Boitnott, E. L. Fasanella: Impact evaluation of composite floor sections, SAE 891018, 1989
- [49] R. L. Boitnott, E. L. Fasanella, L. E. Calton, H. D. Carden: Impact response of composite fuselage frames, SAE 871009, 1987
- [50] H. D. Carden, R. L. Boitnott, E. L. Fasanella: Behaviour of composite/metal aircraft structural elements and components under crash type loads – what are they telling us?, NASA TM102681, 1990
- [51] R. L. Boitnott, C. Kindervater: Crashworthy design of helicopter composite airframe structures, European Helicopter Society – 15th European rotorcraft forum, 1989

- [52] A. L. P. J. Michielsen, J. F. M. Wiggendaad: Review of crashworthiness research of composite structures - part I, D.2.1.1 of the European Community funded research project 'CRASURV', 1997
- [53] A. F. Johnson, C. M. Kindervater: Review of crashworthiness research on composite structures - part II, D.2.1.1 of the European Community funded research project 'CRASURV', 1997
- [54] J. F. M. Wiggendaad, D. Santoro, F. LePage, C. Kindervater, H. Climent Manez: Development of a crashworthy composite fuselage concept for a commuter aircraft, NLR-report TP-2001-108, 2001
- [55] F. Le Page: Presentation of the commuter sub-passenger floor structure drop test, CEAT test report S98/4449000 part 2, D.4.3.1 of the European Community funded research project 'CRASURV', 1998
- [56] F. Le Page: Results of the commuter sub-passenger floor structure drop test, CEAT test report S98/4449000 part 3, D.4.3.2 of the European Community funded research project 'CRASURV', 1999
- [57] F. Le Page: Results of the airliner sub-cargo floor structure drop test, CEAT test report S98/4449000 part 1, D.4.1.7 of the European Community funded research project 'CRASURV', 1998
- [58] F. Le Page: Presentation of the airliner sub-passenger floor structure drop test, CEAT test report S98/4449000 part 4, D.4.3.3 of the European Community funded research project 'CRASURV', 1997
- [59] F. Le Page: Results of the airliner sub-passenger floor structure drop test, CEAT test report S98/4449000 part 5, D.4.3.4 of the European Community funded research project 'CRASURV', 1997
- [60] J.-M. Souquet, B. Beral: Design airliner sub-passenger floor structure, D.2.4.1 & D.2.4.2 of the European Community funded research project 'CRASURV', 1998
- [61] M. Mahe, H. Ribet, F. LePage: Composite fuselage crash FE modelling dedicated to enhance the design in correlation with full scale drop test, *Mechanique & Industries* Vol.2 Issue 1: 5-17, 2001
- [62] E. Moas, R. L. Boitnott, O. H. Griffin: An analytical and experimental investigation of the response of the curved, composite frame/skin specimens, *Journal of the American Helicopter Society* Vol.39 Issue 3, 1994

- [63] M. B. Woodson, E. R. Johnson, R. T. Haftka: Optimal design of composite fuselage frames for crashworthiness, *International Journal of Crashworthiness* Vol.1 No.4: 369-380, 1996
- [64] J. G. Perez: Energy absorption and progressive failure response of composite fuselage frames, Master thesis – Virginia Polytechnic Institute and State University, 1999
- [65] L. O. Pilkington: Impact response and failure of a textile composite fuselage frame, Master thesis – Virginia Polytechnic Institute and State University, 2004
- [66] A. O. Bolukbasi, T. R. Baxter, T. A. Nguyen, M. Rassaian, K. R. Davis, W. Koch, L. C. Firth: Energy absorbing structure for aircraft, Patent application GB 2 444 645 A, 2008
- [67] <http://www.flightblogger.blogspot.com>
- [68] P. E. Nikraves, I. S. Chnong, R. L. Benedict: Plastic hinge approach to vehicle crash simulation, *Computers & Structures* Vol.16 No.1-4: 395-400, 1983
- [69] J. Ambrosio, J. Dias: A road vehicle multibody model for crash simulation based on the plastic hinges approach to structural deformations, *International Journal of Crashworthiness* Vol.12 No.1: 77-92, 2007
- [70] L. Sousa, P. Verissimo, J. Ambrosio: Development of generic multibody road vehicle models for crashworthiness, *Multibody System Dynamics* 19: 133-158, 2008
- [71] H.-S. Kim, S.-Y. Kang, I.-H. Lee, S.-H. Park, D.-C. Han: Vehicle frontal crashworthiness analysis by simplified structure modeling using nonlinear spring and beam elements, *International Journal of Crashworthiness* Vol.2 No.1: 107-117, 1997
- [72] G. Biakeu, L. Jezequel: Simplified crash models using plastic hinges and the large curvature description, *Multibody System Dynamics* 9: 25-37, 2003
- [73] J. P. Dias, M. S. Pereira: Optimization methods for crashworthiness design using multibody models, *Computers & Structures* Vol.82: 1371-1380, 2004
- [74] G. Wittlin, B. LaBarge: KRASH parametric sensitivity study – transport category airplanes, DOT/FAA/CT-87/13, 1987
- [75] M. Lützenburger: Simulation of the A320 section drop test using the hybrid code KRASH, DLR-report IB 435-95/24, Sub-task 3.1 of the European Community funded research project ‘Crashworthiness for commercial aircraft’, 1995

- [76] F. Invernizzi, E. Masiero, S. Poggi, M. Anghileri, L.-M. L. Castelletti, E. Francesconi, A. Milanese: Helicopter subfloor structure design adopting a combined ABAQUS/Explicit – KRASH approach, 6th International KRASH users` seminar, 2009
- [77] M. Lützenburger: KRASH related research projects at DLR, 6th International KRASH users` seminar, 2009
- [78] A. K. Noor, H. D. Carden: Computational methods for crashworthiness, NASA CP3223, 1992
- [79] S. J. Soltis: Overview of usage of crash dynamic analytical methods in civil aircraft research and certification programs, Fifth triennial international fire & cabin safety research conference, 2007
- [80] L. G. Maia, P. H. I. A. de Oliveira: A review of finite element simulation of aircraft crashworthiness, Publication of Advanced Composites Solutions, 2005
- [81] K. H. Lyle, L. W. Bark, K. E. Jackson: Evaluation of test/analysis correlation methods for crash applications, American Helicopter Society – 57th annual forum, 2001
- [82] A. Adams, H. M. Lankarani: A modern aerospace modelling approach for evaluation of aircraft fuselage crashworthiness, International Journal of Crashworthiness Vol.8 No.4: 401-413, 2003
- [83] E. L. Fasanella, K. E. Jackson, Y. T. Jones, G. Frings, T. Vu : Crash simulation of a Boeing 737 fuselage section vertical drop test, NASA Langley Research Center, 2004
- [84] K. E. Jackson, E. L. Fasanella: Crash simulation of vertical drop tests of two Boeing 737 fuselage sections, DOT/FAA/AR-02/62, 2002
- [85] D. Kohlgrüber: Numerical simulation of dynamic test II, DLR-report IB 435-94/31, Sub-task 2.2 of the European Community funded research project ‘Crashworthiness for commercial aircraft’, 1995
- [86] E. Haug, G. Milcent, G. Munck: Thirty sixth month periodic progress report, ESI SA - AERO-CT92-0030-4, in the European Community funded research project ‘Crashworthiness for commercial aircraft’, 1996
- [87] E. L. Fasanella, K. E. Jackson: Best practices for crash modeling and simulation, NASA TM-2002-211944, 2002
- [88] K. E. Jackson, E. L. Fasanella: Development and validation of a finite element simulation of a vertical drop test of an ATR 42 regional transport airplane, DOT/FAA/AR-08/19, 2008

- [89] M. A. McCarthy, C.G. Harte, J. F. M. Wiggendaad, A. L. P. J. Michielsen, D. Kohlgrüber, A. Kamoulakos: Finite element modelling of crash response of composite aerospace sub-floor structures, *Computational Mechanics* Vol.26: 250-258, 2000
- [90] J. F. M. Wiggendaad, A. L. P. J. Michielsen, D. Santoro, F. LePage, C. Kindervater, F. Beltran, M. Al-Khalil: Finite element methodologies development to simulate the behaviour of composite fuselage structure and correlation with drop test, *Air & Space Europe* Vol.3 No.3/4, 2001
- [91] M. Mahe, H. Ribet: Post-test simulation of the sub-passenger floor structure, D.3.4.3 of European Community funded research project 'CRASURV', 2000
- [92] M. Mahe, H. Ribet, J. Kleinwechter: Pre-test simulation of the sub-passenger floor structure, D.3.4.2 of European Community funded research project 'CRASURV', 1999
- [93] D. Kohlgrüber, A. Kamoulakos: Validation of numerical simulation of composite helicopter sub-floor structures under crash loading, *American Helicopter Society – 54th annual forum*, 1998
- [94] D. Kohlgrüber: Improved simulation methodologies to model the crash behaviour of composite structures, *DLR research project 'Schwarzer Rumpf'*, 2002
- [95] K. E. Jackson, E. L. Fasanella, S. Kellas: Crash simulation of a 1/5-scale model composite fuselage concept, *MSC aerospace users` conference*, 1999
- [96] K. E. Jackson: Impact testing and simulation of a crashworthy composite fuselage concept, *International Journal of Crashworthiness* Vol.6 No.1: 107-121, 2001
- [97] E. L. Fasanella, K. E. Jackson: Impact testing and simulation of a crashworthy composite fuselage section with energy-absorbing seats and dummies, *American Helicopter Society – 58th annual forum*, 2002
- [98] K. E. Jackson, E. L. Fasanella, R. L. Boitnott, K. H. Lyle: Full-scale crash test and finite element simulation of a composite prototype helicopter, *NASA TP-2003-212641*, 2003
- [99] E. Haug, A. De Rouvray: Crash response of composite structures, in *Structural Crashworthiness and Failure*: 237-294, 1993
- [100] M. David: Analysis of crushing response in composite crashworthy structures, *10th ONERA-DLR aerospace symposium ODAS*, 2009
- [101] A. F. Johnson, M. David: Failure mechanism in energy-absorbing composite structures, *Philosophy magazine* Vol.90 Issue 31&32: 4245-4261, 2010

- [102] C. M. Kindervater: Aircraft and helicopter crashworthiness: design and simulation, Crashworthiness of transportation systems: structural impact and occupant protection: 525-577, 1997
- [103] D. Kohlgrüber: SECTMESH V5 – Description of a tool to automatically generate finite element meshes of transport aircraft sections, DLR-report IB435-2008/18, 2008
- [104] ABAQUS: ABAQUS analysis user's manual V6.8, SIMULIA Dassault Systèmes, 2008
- [105] K. E. Jackson, E. L. Fasanella, R. Boitnott, J. McEntire, A. Lewis: Occupant response in a full-scale crash test of the Sikorsky ACAP helicopter, Journal of the American Helicopter Society Vol.49 Issue 2, 2004
- [106] R. G. Thomson, H. D. Carden, R. J. Hayduk: Survey of NASA research on crash dynamics, NASA TP2298, 1984
- [107] D. H. Glaister: Human tolerance to impact acceleration, Injury Vol.9 Issue 3: 191-198, 1978
- [108] A. M. Eiband: Human tolerance to rapidly applied accelerations: A summary of the literature, NASA MEMO5-19-59E, 1959
- [109] Federal Aviation Administration: Federal aviation regulations, part 27.562: airworthiness standards: normal category rotorcraft, Emergency landing dynamic conditions, 1989
- [110] G. L. W. M. Knops: Supporting Test Work – Aircraft Seat Component Tests, Subtask 2.4 of the European Community funded research project “Crashworthiness for commercial aircraft”, TNO-report No.: 94.OR.BV.011.1/GKN, 1994
- [111] ABAQUS: ABAQUS theory manual V6.8, SIMULIA Dassault Systèmes, 2008
- [112] ABAQUS: Getting started with ABAQUS: Keywords Edition V6.8, SIMULIA Dassault Systèmes, 2008
- [113] P. Wriggers: Nichtlineare Finite-Element-Methoden, Springer-Verlag, 2001
- [114] A. Haufe: Theory and application of explicit simulation methods, DYNAmore GmbH, 2007
- [115] Y. Ren, J. Xiang: A comparative study of the crashworthiness of civil aircraft with different strut configurations, International Journal of Crashworthiness Vol.15 No.3: 321-330, 2010
- [116] ABAQUS: ABAQUS user subroutines reference manual V6.8, SIMULIA Dassault Systèmes, 2008

- [117] X. W. Zhang, J. L. Yang, T. X. Yu: Elastic-plastic behaviour of a semicircular frame being pressed against a rigid plane, *Acta Mechanica Sinica* Vol.24: 419-432, 2008
- [118] F. X. Meng, Q. Zhou, J. L. Yang: Improvement of crashworthiness behaviour for simplified structural models of aircraft fuselage, *International Journal of Crashworthiness* Vol.14 No.1: 83-97, 2009
- [119] A. Adams, C. K. Thorbole, H. M. Lankarani: Scale modelling of aircraft fuselage: an innovative approach to evaluate and improve crashworthiness, *International Journal of Crashworthiness* Vol.15 No.1: 71-82, 2010
- [120] P. Westphal, W.-D. Dolzinski, T. Roming, T. Schröer, D. Kohlgrüber, M. Lützenburger: Strukturbauteil mit Spant- und Querträgererelement, Patent application DE 10 2007 030 026 A1, 2009
- [121] D. Delsart: Technical report 3/11921 DMSE, ONERA, 2007
- [122] S. Heimbs, F. Strobl, P. Middendorf, J. M. Guimard: Composite crash absorber for aircraft fuselage applications, *WIT transaction on the built environment* Vol.113: 3-14, 2010
- [123] U.S. Department of Defense: Composite materials handbook volume 3, MIL-HDBK-17-3F, 1997
- [124] D. Bushnell: Buckling of shells – pitfall for designers, AIAA 80-0665R, 1981
- [125] E. E. Spier: Postbuckling fatigue behaviour of graphite-epoxy stiffeners, AIAA-1982-779, 1982
- [126] M. C. Y. Niu: Airframe stress analysis and sizing – second edition / fourth published, Hong Kong Conmilit Press Ltd., 2007
- [127] K. E. Jackson: Friction and wear behaviour of aluminium and composite airplane skins, NASA TP2262, 1984
- [128] H. D. Carden: Impact dynamics research on composite transport structures, NASA TM86391, 1985
- [129] P. Wild: Untersuchung hybrider Werkstoffkombinationen zur Verbesserung des Crashverhaltens von Transportflugzeugen, DLR-report IB435-2009/18, 2009
- [130] R. Reiß: Untersuchung hybrider Biegeträger zur Verbesserung des Crashverhaltens von Transportflugzeugen, DLR-report IB435-2010/08, 2010

- [131] J. Jakobi, M. Roeder, M. Biella, J. Teutsch: Economic aspects of advanced surface movement guidance and control systems (A-SMGCS), Conference on air traffic management economics, 2009
- [132] I. Kumakura, M. Minegishi, K. Iwasaki: Impact simulation of simplified structural models of aircraft fuselage, SAE technical paper 2000-01-5586, 2000
- [133] T. Hosokawa, I. Kumakura, M. Minegishi, K. Iwasaki: Drop test simulation of simplified structural models of aircraft fuselage, ISSN 0289-260X, Vol. 44: 191-196, 1999
- [134] D. Kohlgrüber, H. Weissinger: Crash behaviour of composite commuter sub-floor components – report on dynamic tests, DLR-report IB 435-98/21, D.4.1.9 of the European Community funded research project ‘CRASURV’, 1998
- [135] D. Kohlgrüber, H. Weissinger: Crash behaviour of composite sub-floor components – final report on component tests, DLR-report IB 435-97/38, D.4.1.4 of the European Community funded research project ‘CRASURV’, 1998
- [136] D. Kohlgrüber: Initial materials data of carbon and aramid fabric materials, DLR-report IB 435-97/24, D.1.1.1 of the European Community funded research project ‘CRASURV’, 1997
- [137] D. Kohlgrüber, H. Weissinger: Results of dynamic tests of composite sub-floor boxes – final report, DLR-report IB 435-98/22, D.4.2.2 of the European Community funded research project ‘CRASURV’, 1998
- [138] D. Kohlgrüber: Verification and calibration of material models on cruciform elements, DLR-report IB 435-99/34, D.3.2.1 of the European Community funded research project ‘CRASURV’, 1999
- [139] M. C. Y. Niu: Airframe structural design – second edition / third published, Hong Kong Conmilit Press Ltd., 2006
- [140] Arbeitskreis Messdatenverarbeitung Fahrzeugsicherheit: Crash-Analyse Beschreibung der Kriterien - Version 1.6.2, 2005
- [141] ABAQUS: Request for enhancement – element output to odb for user-defined elements, ABAQUS RFE #11822, 2010
- [142] ABAQUS: Bug – output energy for vuel, ABAQUS bug v67_2406, 2008
- [143] ABAQUS: Bug – displacements/rotations passed in vuel, ABAQUS bug v67_2413, 2008
- [144] K.-J. Bathe: Finite-Elemente-Methoden, Springer-Verlag, 2002

- [145] <http://www.dri-krash.com>
- [146] Gesellschaft für Optische Messtechnik: Benutzerhandbuch Software ARAMIS v6, GOM mbH, 2007
- [147] M. Waimer, D. Kohlgrüber, D. Hachenberg, H. Voggenreiter: Dynamic component tests on CFRP crash absorbers of a transport aircraft sub-cargo structure, 12th ONERA-DLR Aerospace Symposium, 2012

Curriculum Vitae

Personal data

Name	Matthias Waimer
Date of Birth	February 07, 1979
Place of Birth	Schorndorf, Germany
Marital Status	Married
Nationality	German

University Education

2000 – 2006	Diplom-Ingenieur, Aero- and Astronautics Engineering, Faculty of Aerospace Engineering and Geodesy, University of Stuttgart
2009 – 2013	Doctoral Candidate, Institute of Structures and Design, German Aerospace Center (DLR), Stuttgart

Experience

since 2006	Research Associate, Institute of Structures and Design, German Aerospace Center (DLR) <i>Investigation of crash concepts for the second generation CFRP fuselage of transport aircraft within several industrial and publicly (National & European Community) funded research projects:</i> <ul style="list-style-type: none">– 2006-2008: Development of FE modelling methods for the assessment of crash kinematics (industrial research project)– 2007-2010: Experimental investigations and numerical simulations on the failure behaviour of hybrid frame bending concepts (DLR research project)– 2008-2011: Development of a crashworthy CFRP fuselage design by numerical crash simulations (industrial research project)– 2008-2011: Experimental investigations on the failure behaviour of CFRP crash absorber components (industrial research project)– 2008-2013: Development and validation of FE modelling methods for the simulation of crushing of CFRP crash absorbers (European Community funded research project)– 2012-2015: Development of improved crash concepts & -kinematics for the second generation CFRP fuselage of transport aircraft (National funded research project)
------------	--